

**Contact Erosion and Nozzle Ablation
in
Gas Blast Circuit Breakers**



UNIVERSITY OF
LIVERPOOL

Thesis submitted in accordance with the requirements of the
University of Liverpool for the degree of Doctor in Philosophy

by

Wen Wang

November 2017

Department of Electrical Engineering and Electronics
University of Liverpool

Acknowledgement

Undertaking this PhD has truly changed my life and it could not be completed without the support of the people around me. First of all, I would like to express my sincerest gratitude to my supervisor Professor J D Yan for his continuous support, patience, guidance, immense knowledge and rigorous training over the years. He encourages me never to give up no matter what difficulties lie ahead. I would forever be thankful for the inspirational discussions which help me broaden my research horizons. I hope that I could be a person as enthusiastic, energetic and kind as him.

My sincere appreciation also extends to Dr L Jiang, who influenced me a lot from his insightful feedbacks and inspiration. I would also greatly appreciate the support and comments from Professor J W Spencer. I am also grateful to my colleagues Dr Y Pei and Dr Q Zhang for all the valuable discussions and their friendship.

I would like to express my gratitude to all my friends for their selfless support. Special thanks to all my family members, my father and mother who love and care me unconditionally. Furthermore, I truly thank my fiancé for supporting and encouraging me. I love all of them forever and appreciate their help. Without the insightful guidance from them when I hesitated for taking the PhD, I would not have such a memorable experience.

Last but not least, I would like to thank the Department of Electrical Engineering and Electronics for providing me the resources to carry out my research work and also the staff in the Department for their support.

Abstract

Circuit breaker is key protection equipment in the conventional and smart grid to isolate a faulty part of the network and maintain system stability. The physical characteristics of arc plasma in the presence of contact erosion and nozzle ablation are studied in the present work with the aim to produce optimised design of circuit breakers with extended service time, minimised maintenance cost, and adequate intelligence for using in smart grid. It is achieved by using a differential arc model in two-dimensional axisymmetric coordinate system and the model is implemented in a commercial Computational Fluid Dynamics (CFD) software package, PHOENICS.

The thermodynamic properties and transport coefficients of pure copper vapour under local thermodynamic equilibrium (LTE) and non-equilibrium conditions are calculated first in Chapter 2, which can be used in the near electrode layer to determine the energy flux towards the cathode bulk. The non-equilibrium thermophysical properties of pure copper vapour have not been calculated before. The composition and thermophysical properties are obtained according to fundamental theory from 300 K to 30,000 K at 4 pressure levels of 0.1 MPa, 0.4 MPa, 0.8 MPa and 1.0 MPa. Non-equilibrium degree ranging from 1 to 4 is considered to cover potential plasma states. The LTE results from present work are compared with existing data.

A near cathode non-LTE layer exists between LTE arc column and cathode surface. It is divided into a pre-sheath layer and a sheath layer. The energy flux for contact erosion depends on the physical processes inside the layers. Up to now, there has been no model that can correctly predict the erosion rate of the cathodic contact. A mathematical model that consists of the two-temperature (2T) pre-sheath and the collisionless space charge sheath is established in the present work in Chapter 3 to describe the physical processes inside the non-LTE layer. Copper vapour is the arcing gas because it has a much lower boiling temperature than tungsten when their mixture is used as the contact material in the real applications. A novel approach has been developed to bridge the solutions from the pre-sheath layer and the sheath layer, thus allowing a self-consistent determination of the near cathode layer potential drop for the non-refractory materials (copper). Our prediction of this overall potential drop (16.44 V) is reasonably in view of measurement results (15 V-17.5 V). Total mass evaporated from the cathode surface due to contact

erosion is predicted at three current levels (i.e. 22 kA, 27 kA and 32 kA). The predicted mass loss is only 30% of the measured mass loss because the latter includes the droplets of the cathode material that are spitted by melting and mechanical stress.

A computational study of nozzle ablation and its influences on the flow environment in a 145 kV/40 kA auto-expansion circuit breaker is carried out in Chapter 4. When the increase in nozzle diameter due to nozzle ablation is considered in the simulation, less subsequent nozzle ablation is normally obtained. The decreased ablated mass reduces the enthalpy and mass fluxes flowed into the expansion volume which results in a lower pressure rise. Results show that ablation leads to an excessive enlargement of the nozzle flat throat at high current and long arc duration, presenting as a limited factor that affects the lifetime of auto-expansion circuit breakers. The predicted specific ablation falls well within the experimental results obtained by ABB. Results obtained in the present work strongly suggest that, to achieve more realistic arc modelling, the dimensional variation of the nozzle due to ablation must be considered.

The influence of nozzle ablation on the interruption process of an auto-expansion circuit breaker is studied in Chapter 5. The turbulence model is first calibrated using results from two tests (similar cases but differing in arc duration). It is found that the turbulence parameter $c=0.32$ for Prandtl mixing length model is applicable to predict interruption performance of 145 kV/40 kA auto-expansion circuit breaker. The critical rate of rise of recovery voltage (RRRV), which represents the interruption capability of the circuit breaker, are predicted with results well matching the test results. The arc model is then used to study the deterioration of breaker's interruption capability by computationally repeating the same test duty on the breaker with the consideration of nozzle enlargement. For a typical case (Test 98), it has been shown that the reduction of approximately 20% in the predicted RRRV of the breaker is mainly caused by the dimensional variation of the main and auxiliary nozzles, especially the change of nozzle diameter from 19 mm (auxiliary nozzle) and 21 mm (main nozzle) to 21.4 mm/24 mm (auxiliary nozzle) and 23 mm/24.6 mm (main nozzle), giving an increase in the flow area of averagely 20% (auxiliary nozzle) and 14% (main nozzle).

Table of Contents

Acknowledgement	i
Abstract	ii
Table of Contents	iv
List of Figures	viii
List of Tables	xvii
List of Abbreviations	xx
List of Symbols	xxi
Chapter 1 Circuit Breakers and Their Intelligent Operations	1
1.1 Introduction to Power Networks and Role of Circuit Breakers	1
1.2 Intelligence in Circuit Breakers	2
1.3 Types of Circuit Breakers	6
1.4 Basics of Electric Arcs	13
1.4.1 Local thermal equilibrium (LTE) state of electric arcs	14
1.4.2 Radiation from arc plasma	16
1.5 Contacts and Nozzle(s)	16
1.5.1 Contacts	17
1.5.2 Nozzle(s)	18
1.6 Brief Review of Arc Models	20
1.7 The Objective and Organization of Thesis	21
Reference	23
Chapter 2 Thermodynamic Properties and Transport Coefficients of Pure Copper Plasma	28
2.1 Introduction	28
2.2 Determination of the species composition of pure copper plasma	29
2.2.1 Theory of chemical equilibrium	29
2.2.2 Calculation of chemical composition	33

2.3	Determination of thermophysical properties	36
2.3.1	Determination of thermodynamic properties	36
2.3.2	Determination of transport coefficients	37
2.3.3	Collision integral and cross section	48
2.3.4	Debye length	54
2.4	Calculation results	54
2.4.1	Internal partition function	54
2.4.2	Chemical composition of pure copper plasma	55
2.4.3	Thermophysical properties of pure copper plasma	58
2.5	Conclusion	66
	References	68
Chapter 3 A Cathode Layer Model for Arc-Contact Interaction in High Voltage Circuit Breakers		74
3.1	Description of the near cathode non-LTE layer	74
3.2	Ionization layer: pre-sheath	77
3.2.1	Mathematical model with respect to the pre-sheath layer	77
3.2.2	Boundary conditions for pre-sheath model	80
3.3	Space charge region: sheath	81
3.3.1	Mathematical model with respect to the sheath layer	81
3.3.2	Numerical solution for the sheath region	91
3.3.3	Energy transfer between the cathode and arc column	91
3.3.4	Overall solution for the non-LTE layer model	95
3.4	Determination of the mass loss from the cathode surface	96
3.4.1	Argon plasma with a tungsten cathode	96
3.4.2	SF ₆ plasma with a copper cathode	97
3.5	Conclusion	109
	References	111

Chapter 4	Nozzle Ablation and its Effects on the Interruption Process	117
4.1	Introduction	117
4.2	Simulation Geometry and Preconditions of the 145 kV/40 kA Auto-expansion Circuit Breaker	118
4.3	Mathematical Model for the Auto-expansion Circuit Breaker.....	119
4.3.1	Governing equations of the switching arc in LTE	119
4.3.2	Radiation and re-absorption.....	127
4.4	Numerical Prediction of Nozzle Ablation.....	132
4.4.1	Short line fault---L90.....	132
4.4.2	Associated experimental results of the mass loss from PTFE nozzle(s)	144
4.4.3	Variation of the nozzle flat throat dimension as a result of ablation ...	147
4.5	Gas Flow Environment Considering Dimensional Change due to the Nozzle Ablation.....	149
4.6	Conclusion.....	161
	References.....	163
Chapter 5	Prediction of the Critical Rate of Rise of Recovery Voltage Considering Nozzle Diameter Change due to PTFE Material Ablation	167
5.1	Introduction	167
5.2	Synthetic Testing Methods of High Voltage Circuit Breaker tests	168
5.3	Prediction of Nozzle Ablation with Different Test Duties.....	172
5.3.1	Terminal fault T30	172
5.3.2	Terminal fault T60	178
5.4	Critical RRRV Affected by Nozzle Ablation.....	195
5.4.1	Calibration of turbulence parameter in Prandtl mixing length model .	195
5.4.2	Critical rate of rise of recovery voltage	198
5.4.3	Comparative study of nozzle ablation and its effects	202
5.5	Conclusion.....	206

References.....	208
Chapter 6 Conclusions and Future Work	209
6.1 Contributions and Achievements in the Present Work	209
6.2 Future Work	210
6.2.1 Modified near cathode non-LTE layer model.....	210
6.2.2 Radiation model correlates to the nozzle ablation.....	211
6.2.3 Thermodynamic properties and transport coefficients of the mixture inside the arcing chamber	211
Appendix A.....	213
Appendix B.....	215

List of Figures

Figure 1.1 Relationship between the grid networks and the high voltage circuit breakers.	5
Figure 1.2 Overview of the usage of different circuit breakers [17].	6
Figure 1.3 Schematic diagram of air circuit breakers, (a) Plain air circuit breaker; (b) Axial blast air circuit breaker and (c) Cross blast air circuit breaker [22]....	8
Figure 1.4 Structure of the oil circuit breakers: (a) BOCB; (b) MOCB [23].....	9
Figure 1.5 Schematic diagram of the vacuum circuit breaker [26].....	10
Figure 1.6 Simplified schematic diagram of an puffer SF ₆ puffer circuit breaker, (a) closing position; (b) opening position [27].	11
Figure 1.7 Schematic diagram of a self-blast SF ₆ circuit breaker as an example. The labelled components are: 1. Fixed arcing contact; 2. Fixed main contact; 3. Nozzle; 4. Moving arcing contact; 5. Cylinder; 6. Control valve; 7. Compression chamber; 8. Expansion volume[28].	12
Figure 1.8 Diagram of circuit breaker arcing contacts erosion. Contact material is Cu/W. (a) 550 kV/63 kA circuit breaker; (b) 800 kV/63 kA circuit breaker [36]..	17
Figure 1.9 Diagram of ablation on different nozzle materials and test devices. (a) and (b) for ABB test device [39]; (c) and (d) for Pinggao Group product [36].	19
Figure 2.1 Internal partition function of Cu atoms and Cu ⁺ . Dotted lines: Reference. Solid lines: present work.....	55
Figure 2.2 Chemical compositions of pure copper plasma at (a) different pressure under LTE conditions (solid lines: P=0.1 MPa; dashed lines: P=1.0 MPa) and (b) different non-equilibrium degree at atmospheric pressure (solid lines: $\theta=1$; dashed lines: $\theta=4$). The solid and dashed lines with same color represent the same species.	56
Figure 2.3 Temperature dependence of electron number density at different (a) pressures under LTE condition and (b) non-equilibrium degrees at atmospheric pressure.....	57
Figure 2.4 Temperature dependence of electrons molar fraction at different (a) pressures under LTE conditions and (b) non-equilibrium degrees at atmospheric pressure.....	58

Figure 2.5 Temperature dependence of copper atoms molar fraction at different (a) pressures under LTE conditions and (b) non-equilibrium degrees at atmospheric pressure.....	58
Figure 2.6 Temperature dependence of density of copper plasma at different (a) pressures under LTE conditions and (b) non-equilibrium degrees at atmospheric pressure.....	59
Figure 2.7 Temperature dependence of electrical conductivity of pure copper plasma at different (a) pressures under LTE conditions and (b) non-equilibrium degrees at atmospheric pressure.....	60
Figure 2.8 Temperature dependence of viscosity of pure copper plasma at different (a) pressures under LTE conditions and (b) non-equilibrium degrees at atmospheric pressure.....	61
Figure 2.9 Temperature dependence of total thermal conductivity at different (a) pressures under LTE conditions and (b) non-equilibrium degrees at atmospheric pressure.....	62
Figure 2.10 Temperature dependence of electrons translational thermal conductivity at different (a) pressures under LTE conditions and (b) non-equilibrium degrees at atmospheric pressure.....	62
Figure 2.11 Calculated electron number density compared with the literature data [64].	63
Figure 2.12 Comparison of the (a) electrical conductivity, (b) viscosity and (c) thermal conductivity with the available literature data from the works of Cressault et al [64], [65], Hermette et al [66] and Kovitya [18]......	64
Figure 2.13 Computed electrical conductivity (a), viscosity (b) and thermal conductivity (c) as a function of temperature of the equilibrium copper plasma at atmospheric pressure with different definitions of the Debye length.	66
Figure 3.1 Schematic diagram of the non-LTE layer and the voltage distribution between the arcing contacts, where “1” is the sheath and “2” is the pre-sheath.	75
Figure 3.2 Schematic diagram of the structure of near cathode non-LTE layer; “a, e, +” represent the neutral atoms, electrons and positive ions respectively.....	76
Figure 3.3 Current density of the electrons emitted through thermionic emission as a function of cathode surface temperature.	84

Figure 3.4 Current density of electrons emitted through field emission as a function of the cathode surface electric field.....	86
Figure 3.5 Thermo-field emission as a function of surface temperature and electric field strength of copper cathode.	89
Figure 3.6 Calculation procedure of the non-LTE model.....	95
Figure 3.7 Spatial dependences of particles number densities (a), potential (b) and temperature (c) in the pre-sheath layer towards the sheath edge in comparison with the reference.	97
Figure 3.8 Spatial dependences of the number densities of particles in the pre-sheath layer towards the cathode surface.	98
Figure 3.9 Spatial dependence of potential in the pre-sheath layer.	99
Figure 3.10 Spatial dependence of the diffusion flux distributions of the electrons (a) and ions (b) while “ Γ ” represents the total diffusion flux and Γ_{Te} , Γ_{ne} , Γ_{na} , Γ_V represent the diffusion flux components driven by the variation of temperature, number density and potential respectively.	99
Figure 3.11 Spatial dependence of the temperature distributions for electrons and heavy particles from the arc side boundary of pre-sheath towards the sheath edge.	100
Figure 3.12 Spatial dependence of the (a) number density, (b) potential, (c) electron temperature and (d) heavy particle temperature distributions in the pre-sheath layer with and without the consideration of Debye-Hückel effect.	101
Figure 3.13 Surface electric field strength as a function of the total current density flowed to the cathode surface.....	102
Figure 3.14 Total current density flowed to the cathode surface as a function of the surface temperature at a given electric field strength.....	102
Figure 3.15 The energy flux for the cathode material vaporization at a given surface temperature (3,000K) with a constant total current density of 1.5×10^8 A/m ²	103
Figure 3.16 The energy flux for the cathode material vaporization at a given surface temperature (3,000K) with a constant total current density of 1.5×10^8 A/m ²	104
Figure 3.17 Total current density flowed to the cathode surface as a function of the surface temperature at a given electric field strength.....	107

Figure 3.18 Current curves captured from the model circuit breaker.....	108
Figure 4.1 Schematic diagram of the 145 kV/40 kA auto-expansion circuit breaker under investigation. Gases are free to enter or leave the computational domain. In case, the gas enters the domain is assumed to have a temperature of 300 K.	118
Figure 4.2 Diagram showing approximation of the round moving contact tip by blocks of different thickness. The blocks move in the simulation.	119
Figure 4.3 Thermodynamic properties and transport coefficients of the SF ₆ -PTFE mixture at 1.0 MPa with different PTFE concentration [28].	126
Figure 4.4 Thermodynamic properties and transport coefficients of the SF ₆ and copper mixture at 0.1 MPa and 1.0 MPa with different copper concentration: 1%, 10%, 30% and 50% [29], [30].....	127
Figure 4.5 Possible arc radial temperature profiles and the emission (0~R ₈₃) and re-absorption (R ₈₃ ~R _{5K}) regions. Black lines: (Solid) Monotonic temperature profile; (Dashed) Non-monotonic temperature profile; Red lines: Net radiation loss per unit and time.	128
Figure 4.6 Net emission coefficient of SF ₆ and copper mixture. Left: NEC as a function of temperature with different arc radii at atmospheric pressure. Right: NEC as a function of temperature and copper vapor concentration at 8atm. 1: 1%; 2: 5%; 3: 10%; 4: 50% [39].....	130
Figure 4.7 Net emission coefficient of SF ₆ plasma as a function of temperature with different arc radius and pressure [40].....	130
Figure 4.8 Net emission coefficient of SF ₆ and PTFE mixture as a function of temperature [41].	130
Figure 4.9 nozzle surface area diagram.	131
Figure 4.10 Travel curves of the solid contact and the current waveforms of Test 92, 93 and 98 respectively.....	132
Figure 4.11 Simplified geometry of 145kV auto-expansion circuit breaker. The red lines represent for the specified ablation surfaces.	133
Figure 4.12 Diagram of a simple nozzle with designed solid objects [44].....	133
Figure 4.13 Arc temperature distributions at several typical time instants during the arcing period (Test 92).	136
Figure 4.14 Concentration distributions of the produced PTFE vapour at typical time instants during the arcing period (Test 92).	137

Figure 4.15 Pressure distribution at several typical time instants during the arcing period (Test 92).	138
Figure 4.16 Positions of the solid contact tip in the arcing chamber corresponded to the current waveform of Test 92.	139
Figure 4.17 Predicted ablation energy and mass loss on the main and auxiliary nozzles of Test 92 with the original nozzle size.	140
Figure 4.18 Current and the predicted arc voltage between two contacts of Test 92.	140
Figure 4.19 Imposed transient recovery voltages of Test 92, 93 and 98.	141
Figure 4.20 Predicted ablation energy and mass loss on the main and auxiliary nozzles with the consideration of nozzle flat throat diameter variation resulted from Test 92.	142
Figure 4.21 Positions of the solid contact tip in the arcing chamber corresponded to the current of Test 98.	143
Figure 4.22 Temperature and PTFE concentration distributions approximately at the end of the high current phase of Test 98.	143
Figure 4.23 Predicted ablation energy and mass loss on the main and auxiliary nozzles with the consideration of nozzle flat throat diameter variation resulted from Test 93.	144
Figure 4.24 Predicted enthalpy and mass flow through the cross sections 1 (a) and 2 (b) in the hollow contact of Test 92 (Com.1). The six curves respectively represent (1): total enthalpy flow; (2): enthalpy flow carried PTFE vapor; (3): enthalpy flow carried by SF ₆ gas; (4): total mass flow; (5): mass flow carried by PTFE vapor; (6): mass flow carried by SF ₆ gas.	150
Figure 4.25 Predicted enthalpy and mass flow through the cross sections 3 (a), 4 (b) and 5 (c), each curve has the same meaning explained in Figure 4.24.	152
Figure 4.26 Predicted enthalpy and mass flow through cross sections 6 (a), 7 (b) and 8 (c) towards downstream, each curve has same meaning explained in Figure 4.24.	152
Figure 4.27 Predicted enthalpy and mass flow through cross sections 1 (a) and 2 (b) in hollow contact of Test 98 (Com.1), each curve has same meaning explained in Figure 4.24.	153
Figure 4.28 Predicted enthalpy and mass flow through the cross sections 3 (a), 4 (b) and 5 (c), each curve has the same meaning explained in Figure 4.24.	154

Figure 4.29 Pressure distribution at several typical time instants (Test 98: Com.1).	155
Figure 4.30 Temperature distributions at typical time instants with velocity vector (Test 98: Com.1). The arrow represents for the direction of the flow field.	157
Figure 4.31 Predicted enthalpy and mass flow through cross sections 6 (a), 7 (b) and 8 (c) towards the downstream, each curve has same meaning explained in Figure 4.24.	158
Figure 4.32 Predicted enthalpy and mass flow into (a) hollow contact, (b) expansion volume, (c) in front of main nozzle flat throat and (d) at the downstream respectively through cross sections 2 (a), 3 (b), 6 (c) and 8 (d) with considering the variations of nozzle flat throat diameter of Test 92.	159
Figure 4.33 Pressure distribution in the expansion volume at position A (in Figure 4.11) with considering nozzles flat throats radii variation after each computation.	159
Figure 4.34 Predicted enthalpy and mass flow through cross section 2 (a), 3 (b), 6 (c) and 8 (d) with considering nozzles flat throat diameter variation after each computation of Test 98.	160
Figure 4.35 Pressure distribution in the expansion volume at position A (in Figure 4.11) with considering nozzles flat throats radii variation after each computation.	161
Figure 5.1 Example of TRV waveform.	168
Figure 5.2 Examples of inherent test TRV with the two-parameter envelope (a) and four-parameter waveform (b) that satisfies the conditions to be met during the type test. t_d is a time delay in microseconds. [6].	170
Figure 5.3 Examples of inherent test TRV for short line fault that satisfies the conditions to be met during type test [6].	171
Figure 5.4 Specific ablation in the circuit breaker test device versus peak current density. Applied peak currents amounted from 4 to 64 kA and the arcing times are 5, 10 and 15 ms respectively [9].	172
Figure 5.5 Current waveforms and contact travel curves of T30 tests of 145 kV/40 kA auto-expansion circuit breaker.	173
Figure 5.6 Transient recovery voltages of T30 tests with different arc durations.	173
Figure 5.7 Predicted total enthalpy and mass flow in the hollow contact (a), towards the main nozzle downstream (b) and inside the expansion volume (c), (d) through cross sections 2 (a), 3 (b) and 6 (c) (d) respectively (Figure 4.11)	

with considering the diameter variation of nozzle flat throat. “S” represents for the short arc duration and “1, 2, 3” represent for the three computations.	176
Figure 5.8 Predicted total enthalpy and mass flow inside the expansion volume through cross section 3 (Figure 4.11) of medium (“M”) and long (“L”) arc duration cases with considering the diameter variation of nozzle flat throat.	177
Figure 5.9 Current waveforms and travel curves of T60 tests.	178
Figure 5.10 Transient recovery voltages of T60 tests with different arc durations. ..	178
Figure 5.11 Electrical energy input for different arc durations while “S, M, L” represent for the short, medium, long arc duration and “1,2,3” represent for the three computations with the consideration of nozzle flat throat diameter variation.	180
Figure 5.12 Three monitor positions for the pressures in expansion volume, middle of main nozzle flat throat and the downstream.	181
Figure 5.13 Pressure in the expansion volume (a), (c), (e) and at the middle of the main nozzle flat throat (b), (d), (f) with the consideration of nozzle flat throat diameter variation after each computation while “S, M, L” and “1, 2, 3” have the same meaning explained in Figure 5.11.	182
Figure 5.14 Mass loss rate and total mass loss from auxiliary nozzle flat throat after each computation with considering nozzle flat throat diameter variation of T60 long arc duration case and “L” and “1, 2, 3” have same meaning explained in Figure 5.11.	183
Figure 5.15 Temperature distribution in the arcing space when the solid contact arrives at four positions (Figure 5.12): (a) t=21.68ms; (b) t=23.88ms; (c) t=26.08ms; (d) t=27.05ms; The three curves respectively represent for the three computations of T60 long arc duration case: black-Com.1; red-Com.2; blue-Com.3.	184
Figure 5.16 Temperature distribution with the velocity vector at (a) t=21.68ms; (b) t=23.88ms of T60 long arc duration case (Com.1).	185
Figure 5.17 Temperature distribution within the arcing space at t=26.08 ms after the solid contact clears the main nozzle.	186
Figure 5.18 Radiation energy (a), ohmic heating (b) and the temperature distribution (c) in the radial direction at the middle of auxiliary nozzle flat throat at t=26.08 ms (T60-L-3); Each curve has same meaning explained in Figure 5.15. ..	187

Figure 5.19 Pressure distributions when the solid contact just clears the auxiliary nozzle flat throat of T60 long arc duration cases with considering the diameter variation of nozzle flat throat after each computation.	188
Figure 5.20 Pressure distribution within the arcing space after the solid contact leaves the main nozzle flat throat at $t=26.08$ ms.....	189
Figure 5.21 Positions of the solid contact in the arcing chamber corresponded to the current waveform for T60 long arc duration case.....	189
Figure 5.22 Predicted enthalpy flowed into the expansion volume through cross section 3 as shown in Figure 4.11 with considering the diameter variation of the nozzle flat throat after each computation (T60-L-1/2/3).....	191
Figure 5.23 Predicted mass flow rate outwards the main nozzle downstream and into the hollow contact respectively with considering the diameter variation of the nozzle flat throat after each computation (T60-L-1/2/3).....	191
Figure 5.24 Mass ablated rate and the total mass loss from auxiliary nozzle flat throat with considering the diameter variation of nozzles flat throats of Test 98.	192
Figure 5.25 Mass ablated rate and the total mass loss from main nozzle flat throat with considering the nozzles flat throats diameter variation for T60_1/2/3/4/5. The solid lines represent for the mass loss rate while the dashed lines represent for the total mass loss.....	194
Figure 5.26 Mass ablated rate and the total mass loss from auxiliary nozzle flat throat with considering the nozzles flat throats diameter variation for T60_1/2/3/4/5. The solid lines represent for the mass loss rate while the dashed lines represent for the total mass loss.	194
Figure 5.27 Post arc current calculated using different turbulence parameter c of Test 92 (Com.1).	195
Figure 5.28 Post arc current calculated using different turbulence parameter c for T60 short arc duration test (Com.1).....	196
Figure 5.29 Temperature distribution at the final current zero for Test 93 (a) with the consideration of nozzle flat throats diameter variation resulted from Test 92 (b).	197
Figure 5.30 Predicted post arc current with different c for Test 93 without (a) and with (b) the consideration of the nozzle flat throat diameter variation resulted from Test 92.....	197

Figure 5.31 Predicted post arc current with different RRRV of the short arc duration case Test 92 (Com.1).....	200
Figure 5.32 Pressure variation (a) in expansion volume and (b at the middle of main nozzle flat throat of the short arc duration cases;.....	202
Figure 5.33 Pressure variation inside the expansion volume (a) (c) and at the middle of main nozzle flat throat (b) (d) for T30 and T60 cases with different arc durations.....	203
Figure 5.34 Temperature distribution at the final current zero for Test 92 with the consideration of nozzle flat throats diameters variation.	204
Figure 5.35 Temperature distribution at the final current zero for Test 98 with the consideration of nozzle flat throats diameters variation.	205
Figure 5.36 Mass flow rate towards the main nozzle downstream (a) (c) and into the hollow contact (b) (e) before the final current zero through cross sections 7 and 2 respectively with different arc durations without the consideration of nozzles flat throats diameters variation.....	206

List of Tables

Table 1.1 Parameters need to be monitored during and after circuit breaker operation.	3
Table 1.2 Global warming potentials and lifetimes of different insulating gas species [11]–[16].	7
Table 2.1 The ionization energy of copper.	33
Table 2.2 Polarizability values of copper atom and copper cation [55], [56].	51
Table 3.1 Physical conditions in the sub-layers between cathode and arc column.	76
Table 3.2 Description of the boundary conditions at the arc plasma/pre-sheath interface.	80
Table 3.3 Comparison between the thermionic and non-thermionic cathodes.	83
Table 3.4 Prescribed parameters of the sheath region calculation.	91
Table 3.5 Current density within the cathode spot for various arc current levels.	105
Table 3.6 Mass loss of copper cathode in experimental measurement and estimation.	108
Table 3.7 Predicted mass loss from the cathode material due to erosion.	108
Table 4.1 Source terms and diffusion coefficients for above governing equations... ..	120
Table 4.2 Values of the five parameters in the k- ϵ model.	125
Table 4.3 Arc durations of the three tests in the first test round of L90.	133
Table 4.4 Experiment conditions on the test device and commercial circuit breaker [46], [47].	144
Table 4.5 Experimental result of the 145 kV/40 kA auto-expansion circuit breaker nozzle flat throat mass loss and changed flat throat radius after the first test round.	146
Table 4.6 Predicted mass loss and changed nozzle flat throat radius after the first test round (3 tests) with the consideration of radius variation resulted from each test.	146
Table 4.7 Predicted mass loss and changed nozzle flat throat radius after the first test round without the consideration of radius variation resulted from each test.	146
Table 4.8 Predicted PTFE mass loss and nozzle throat diameter variation after each test in the first test round.	147
Table 4.9 Predicted specific ablation for the three tests in the first test round.	147

Table 4.10 Predicted PTFE mass loss due to the nozzle ablation after each computation of Test 92 with the consideration of nozzle diameter variation.....	148
Table 4.11 Predicted PTFE mass loss due to the nozzle ablation after each computation of Test 93 with the consideration of nozzle diameter variation.....	148
Table 4.12 Predicted PTFE mass loss due to the nozzle ablation after each computation of Test 98 with the consideration of nozzle diameter variation.....	149
Table 5.1 Tested arc durations of different test duties for 145 kV/40 kA auto-expansion circuit breaker.....	171
Table 5.2 Typical parameters of T30 and T60 tests with different arc durations.....	171
Table 5.3 Predicted PTFE mass loss due to nozzle ablation after each valid breaking operation of rated operation sequence of T30 with considering the variation of nozzle flat throat diameter.	174
Table 5.4 Predicted PTFE mass loss due to nozzle ablation after each computation of T30 short arc duration case with considering the variation of nozzle flat throat diameter.	174
Table 5.5 Predicted PTFE mass loss due to nozzle ablation after each computation of T30 medium arc duration case with considering the variation of nozzle flat throat diameter.	175
Table 5.6 Predicted PTFE mass loss due to nozzle ablation after each computation of T30 long arc duration case with considering the variation of nozzle flat throat diameter.....	175
Table 5.7 Predicted PTFE mass loss due to nozzle ablation after each valid breaking operation of rated operation sequence of T60 with considering the variation of nozzle flat throat diameter.	179
Table 5.8 Predicted PTFE mass loss due to nozzle ablation after each computation of T60 short arc duration case with considering the variation of nozzle flat throat diameter.	179
Table 5.9 Predicted PTFE mass loss due to nozzle ablation after each computation of T60 medium arc duration case with considering nozzle flat throat diameter variation.....	179
Table 5.10 Predicted PTFE mass loss due to the nozzle ablation after each computation considering the variation of nozzle flat throat diameter of T60 long arc duration case.....	180

Table 5.11 Predicted PTFE mass loss due to the nozzle ablation with different nozzles dimensions of T60 long arc duration case.....	193
Table 5.12 Applicable RRRV values for different test duties introduced in the standards.	198
Table 5.13 Parameters used to define the TRV envelope for different test duties. ...	199
Table 5.14 Predicted critical RRRV values of Test 92 and 98 with the consideration of nozzle flat throat diameters variation.....	201
Table 5.15 Predicted critical RRRV values for the T60 test under different arc durations with the consideration of nozzle flat throat diameters variation.	201
Table 5.16 Predicted total mass loss from the flat throats of main and auxiliary nozzles for different test duties with different arc durations.....	201

List of Abbreviations

2T	Two-temperature
AC	Alternating current
AI	Artificial intelligence
ANSI	American National Standards Institute
BFC	Body fitted coordinate
BOCB	Bulk oil circuit breaker
CF ₃ I	Trifluoroiodomethane
CFD	Computational Fluid Dynamics
CO ₂	Carbon dioxide
CTE	Complete thermodynamic equilibrium
DC	Direct current
GWP	Global warming potential
HVDC	High voltage direct current
IEC	International Electrotechnical Commission
IEEE	Institute of Electrical and Electronics
L-J	Lennard-Jones
LCE	Local chemical equilibrium
LTE	Local thermodynamic equilibrium
MHD	Magneto-hydrodynamics
MOCB	Minimum oil circuit breaker
MoS ₂	Molybdenum disulfide
NEC	Net emission coefficient
NIST	National Institute of Standards and Technology
PTFE	Polytetrafluoroethylene
RRRV	Rate of rise of recovery voltage
SF ₆	Sulfur hexafluoride
SLF	Short line fault
T-F	Thermo-field
TRV	Transient recovery voltage

List of Symbols

A	Richardson constant
A_{eff}	Effective work function
b	Impact parameter
a_1, b_1	Fowler-Nordheim constants
B_e	Rigid rotator rotational spacing
B_v	Rigid rotational spacing
B_θ	Magnetic field strength
c	Turbulence parameter
C_d	Effective long-range London coefficient
c_m	Vapour mass concentration
C_{pi}	Specific heat at constant pressure of species i
\bar{c}_e	Electron mean velocity
dn_w	Number density of particles with velocities between v_w and $v_w + dv$
D	Tunnelling probability
D_e^T	Thermal diffusion coefficient of electrons
D_e	Anharmonic correction to rotational spacing
D_i^T	Thermal diffusion coefficient
D_{ii}^b	Self-diffusion coefficient of species i
D_{ij}^a	Ambipolar diffusion coefficient
D_{ij}^b	Binary diffusion coefficient
D_{ij}	Ordinary diffusion coefficient
D_l	Laminar diffusivity
D_t	Turbulence diffusivity
D_v	First anharmonic correction to rotational spacing
E	Electric field
$E(m)$	Complete elliptic integral
E_H	Ionization energy of hydrogen
E_1	First electronic excitation energy of neutral atoms
E_c	Electric field strength at cathode surface
E_{ieff}	Effective ionization energy

E_w	Ionization energy of species w
$E_{w,s}$	Energy of species w at excited state s
E_z	Axial component of electric field strength
f_r, f_z	Radial and axial components of Lorentz force
$f(v)$	Distribution function
F	Helmholtz's free energy
g_e	Statistical weight
g_{ij}	Relative velocity
g_j	Statistical weight of vibration
g_n	Statistical weight
$g_{w,s}$	Statistical weight of species w at excited state s
G	Gibbs free energy
h	Planck constant
h_e	Specific enthalpy of electrons
$h_{w,molecular}$	Specific enthalpy of molecular species
$h_{w,monatomic}$	Specific enthalpy of monatomic species
h_s	Specific enthalpy
H	Enthalpy
i, j, w	Specific species in the plasma
I_A, I_B, I_C	Principal moments of inertia
J	Quantum number of rotational energy level
J_{tot}	Total current density
J_{bd}	Current density of back diffusion electrons
J_e	Current density of electrons emitted from the cathode surface
J_{fe}	Current density of electrons emitted by field emission
J_i	Current density of ions in the sheath layer
J_{max}	Maximum quantum number of rotational energy level
j_{fe}	Number density flux of field emission electrons
j_i	Number density flux of ions
j_{bd}	Number density flux of back diffusion electrons
j_e	Number density flux of emitted electrons from cathode surface
J_r, J_z	Radial and axial components of the current density

J_{T-F}	Current density of electrons emitted by thermo-field emission
j_{T-F}	Number density flux of thermo-field emission electrons
J_{te}	Current density of electrons emitted by thermionic emission
k_B	Boltzmann constant
k	Turbulent kinetic energy per unit mass
$K(m)$	Complete elliptic integral
K_{eq}	Equilibrium constant for the overall reaction path
K_f	Forward rate coefficient of a reversible chemical reaction
K_t	Turbulence kinetic energy
K'_v	Monochromatic absorption coefficient
L_l	Orbital angular momentum quantum number
L_s	Turbulence scale
m	Mass of system
m_e	Electron mass
m_{ij}^*	Reduced mass
m_p	Mass of particle
m_{PTFE}	Total ablated mass
m_w	Mass of species w
\dot{m}	Mass flux
n	Quantum number of electronic energy level
$n_{Cu^+}, n_{Cu^{2+}},$ $n_{Cu^{3+}}, n_{Cu^{4+}}$	Number density of singly/doubly/triply/quadruply-charged copper ions
$n_{a,LTE}$	Equilibrium density of neutral species
$n_{c,SE}$	Number density of emitted electrons at the sheath edge
n_{Cu}	Number density of copper atoms
$n_{e,SE}$	Number density of electrons at the sheath edge
n_e	Number density of electrons
\dot{n}_e	Net ionization rate
n_{e1}	Number density of electrons emitted from the cathode surface
$n_{e2}(x)$	Number density of back diffusion electrons
n_i	Number density of species i
n_{i+1}	Number density of species $i+1$

$n_{p,SE}$	Number density of back diffusion electrons at the sheath edge
n_s	Number density of ions at the sheath edge
n_t	Total number density
n_w	Number density of species w
N_w	Number density per kilogram of species w
N_W	Number of electrons on cathode surface per time interval and area
$N(T_c, W, \phi_F)$	Fermi-Dirac distribution for free electrons in the cathode
$n_{w.s}$	Number density of species w at excited state s
p	Principal quantum number
$p(x)$	Electron momentum normal to the cathode surface
P	Pressure
P_0	Reference pressure
p_{max}	Maximum principal quantum number
P_{rt}	Prandtl number
p_{vap}	Metallic vapour pressure
q	Charge
q_0	Maximum volumetric energy source due to radiation reabsorption
q_a	Volumetric radiation source
$Q_{ablation}$	Total radiation
$q_{ablation}$	Radiation flux on the cell surface
q_{bd}	Energy flux brought by back-diffusion electrons
q_{con}	Thermal conduction by heavy particles
Q_{core}	Total radiation flux from the arc core
Q_i	Partition function of species i
Q_{i+1}	Partition function of species $i+1$
$Q_{ij}^l(\epsilon_r)$	Transport cross section
q_{ion}	Total energy flux carried by ions to heat up the cathode surface
$q_{kinetic}$	Kinetic energy of ions brings to the cathode
$q_{neutralize}$	Energy released at the cathode surface by neutralization
q_{not}	Energy flux carried by electrons by thermo-field emission
$q_{rad,c}$	Energy flux taken away by radiation from the cathode
q_{te}	Energy flux taken away by electrons by thermionic emission

q_{vap}	Energy flux taken away by vaporization of cathode material
Q_w	Partition function of species w
Q	Partition function
Q_e	Electronic partition function
Q_{int}	Internal partition function
Q_r	Rotational partition function
Q_t	Translational partition function
Q_v	Vibrational partition function
$\bar{Q}_{ij}^{(l,s)}(T_{ij}^*)$	Average collision integral (collision cross section)
r_{arc}	Arc radius
R_c	Radius of conducting column
Re	Reynolds number
r_e	Equilibrium distance
r_δ	Thermal radius of the arc column
S	Ablation surface cross section
S_l	Spin angular momentum quantum number
S_{C_t}, S_{C_l}	Schmidt number
S_{ij}^*	Mean rate of the strain tensor
S_ϕ	Source term
T	Temperature of particle
T_e	Temperature of electrons
T_h	Temperature of heavy particles
T^*	Inversion temperature
T_∞	Temperature near the nozzle wall
T_{arc}	Temperature of the arc column
t_{arc}	Arc duration
T_c	Cathode surface temperature
T_{es}	Temperature of electrons at the sheath edge
T_{ex}	Effective excitation temperature
$T_{h,SE}$	Temperature of heavy particles at the sheath edge
T_{ij}^*	Reduced temperature
T_{is}	Temperature of ions at the sheath edge

u	Velocity for directed motion
U	Internal energy
v_p	Speed of particle
v	Quantum number of vibrational energy level
V	Potential
V_c	Potential drop over the sheath layer
v_d	Dimensionless velocity
$V_E(x)$	Effective electron potential energy
v_{max}	Maximum quantum number of vibrational energy level
v_s	Velocity of ions at the sheath edge
v_{ts}	Velocity scale
\bar{v}	Mean velocity
\vec{V}	Velocity vector
W	Energy for electrons motion normal to the cathode surface
W_a	Effective constant potential energy in the cathode bulk
w_{max}^g	Total number of gaseous plasma species
w_{total}	Total number of considered species
x_i	Molar fraction of species i
Z	Charge number
Z^*	Generalized internal partition function
α_e	Nonrigid rotator correction to B_e
α_r	Reabsorption factor
α_{rec}	Three-body recombination coefficient
γ_e	Second anharmonic correction
Γ_{vap}	Flux density of atoms vaporization
Γ_ϕ	Diffusion coefficient
$\bar{\gamma}$	Euler constant
δ_{ij}	Kronecker delta
ϵ_0	Electric permittivity in vacuum
ϵ_{00}	Binding energy
ϵ_{el}	Electronic energy
ϵ_F	Fermi energy of the metal

ε_n	Electronic excitation energy of state n
ε_N	Net emission coefficient
ε_r	Kinetic energy
ε_{rot}	Rotational energy
ε_{vib}	Vibrational energy
ε_w	Reference energy of species w
θ_{rot}	Rotational constant
θ_T	Ratio between T_e and T_h
θ_δ	Thermal area of the arc
λ_D	Debye length
λ_{eff}	Effective thermal conductivity
λ_{int}	Internal thermal conductivity
λ_{reac}	Reactive thermal conductivity
λ_t	Turbulence enhanced thermal conductivity
λ_{tr}	Translational thermal conductivity
μ_0	Permeability of the arcing medium
μ_l	Laminar viscosity
μ_t	Turbulence eddy viscosity
μ_w^0	Chemical potential of species w in standard state
μ_w	Chemical potential of species w
v_e^{th}	Mean thermal velocity
σ_c	Symmetry number
τ_{ij}	Reynolds stress
ϕ_F	Material work function
$\Omega^{(l,s)*}$	Reduced collision integral
ω_e	Vibration spacing
$\omega_e x_e, \omega_e y_e,$ $\omega_e z_e$	Spectroscopically determined constants relating to each electronic state of the molecule
$\Omega_{ij}^{(l,s)}(T)$	Collision integral
ω_j	Vibration frequency
ΔE	Lowering of the ionization energy

Δh_l^* Changed enthalpy of l^{th} ionization reaction

ΔP Pressure correction term

Chapter 1

Circuit Breakers and Their Intelligent Operations

1.1 Introduction to Power Networks and Role of Circuit Breakers

A power network consists of electricity generation, transmission, distribution and loads. Alternating current (AC) transmission technology has been dominating the electricity market over 100 years since the first commercial power station was commissioned back in 1890 at Niagara Falls [1]. The highest AC transmission voltage reached 1,150 kV in the former Soviet Union at the beginning of the 1990s [2], [3]. In China, the first 1,000 kV AC transmission line was put in operation in 2009 over a distance of 640 km [4].

With the solid state electronics components for the high power applications such as the thyristors, transistors, diodes and sensors becoming commercially available, the high voltage direct current (HVDC) power transmission voltage experienced a revolutionary jump in the 1970s (from 100 kV to 400 kV) and it is reached 800 kV recently. HVDC transmission becomes economically advantageous when transmission distance is longer than the so-called “threshold distance” (approximately 700 km) with present available technologies [5]–[7]. Increasing interest and commercial exploration of the renewable power generations (solar and wind mainly) also lead to the development of distributed power generation and novel ways of the grid connection and control with a mixture of AC and DC networks.

Smart grid is regarded as the most promising solution to meet the future demand in the power generation, transmission and distribution at a global scale. It is an unprecedented opportunity to improve the electrical industry with higher efficiency, sustainability and availability by employing the innovative technologies on associated monitoring, control and communication. It is chiefly designed to achieve the bi-directional communications between the control system and the apparatuses, balance the electrical generation and consumption, advance the renewable energy integration and tighten the grid security. Whatever the topology of the smart grid is, the idea of being smart has to be realised by hardware components that are “intelligent” at the physical level and application level

as well. The important information on the state and functionality of various apparatuses in the smart grid needs to be made available to the grid by the use of monitoring devices such as power meter, sensor, operation monitor, fault detector and communication tools. In addition, an intelligent apparatus would be highly autonomous to act in response to the information it receives from the network. Given the sheer volume of the electricity demand and uninterruptable nature of power supply for modern society and industry, transition from present power grid to the smart grid will need to be gradual. Furthermore, the constituting equipment, e.g. HVDC converter station, circuit breaker, transformer and switching cabinet, should all possess sufficient level of intelligence to work in the smart grid.

1.2 Intelligence in Circuit Breakers

A network fault, if not cleared in time, will have lasting damaging effects on the power system. High voltage circuit breakers are typical fault clearance and system protection equipment. The clearing of a heavy current fault has three adverse effects on the breaker itself. Firstly, the nozzle, which is made of polytetrafluoroethylene (PTFE) to guide the high speed gas flow, is burnt by strong radiation from the arc, leading to a non-uniform ablation of the PTFE material and overall enlargement of the nozzle radius. This surface and size changes of the nozzle hole lead to a reduction in the interruption performance of circuit breaker. Secondly, strong heat flux from the arc will erode the arcing contacts, shorten the contact and deform its tip surface. It directly leads to the shortening of the electrical lifetime of the circuit breaker. Thirdly, the presence of high current arc results in the formation of powders and gas species, polluting the gaseous environment. Since the circuit breakers need to operate under various conditions such as normal load, no load and short circuit, they should be designed with ability to perform the bi-directional communications with the network system. They need to be able to check their “health” status and communicate to the network. They also need to receive information from the network on the network conditions, especially the operation status of the interconnected electrical apparatuses. Therefore, intelligent circuit breakers should be able to perform four fundamental operations: bi-directional communications, self-diagnosis, intelligent computing, and executing of different duties. The self-diagnosis ability is supported by changing the maintenance practice from service-time based to condition based, leading to reduced network disruption and cost savings.

Self-diagnosis is the ability of the intelligent circuit breakers to definitively characterise the functional fitness of all physical components that affect the operational performance of the breaker. The diagnostic process itself must not interfere with the switching duties of the breaker. This imposes restraints on the available time window that is required by the diagnosis process. The diagnostic methods also require the use of sensors to acquire data on the physical conditions of the operating components such as contact tip length and surface profile, gas composition and pressure, nozzle diameter and surface profile, environment temperature and driving mechanism travel profile. These basic data will be continuously updated, stored and processed by the computing unit based on artificial intelligence schemes to obtain the “health” status of whole circuit breaker. Application of online monitoring provides a continuous sampling of the data from the circuit breaker. Based on the standard C37.10.1 [8], some parameters need to be monitored during and after circuit breaker operation, as listed in Table 1.1.

Table 1.1 Parameters need to be monitored during and after circuit breaker operation.

Apparatus	Monitored Parameters	
Circuit Breaker	Environment	(1) Temperature (2) Pressure (3) Particle contamination (4) Gas composition and density (5) Gas species concentration
	Insulation	(1) Partial discharge (2) Arc voltage (3) Hardware component surface condition
	Dynamics	(1) Arc duration (2) Reaction time of operating components (e.g. opening/closing times of the contacts) (3) Contact velocity (4) Contact movement
	Consumption	(1) Contact tip length (2) Nozzle diameter
	Mechanics	(1) Energy accumulated by spring (2) Pressure of hydraulic fluid

The essential role of the circuit breaker is to break the circuit by interrupting the current passing through it. In HVAC circuit breakers, the arc is extinguished at a natural current zero of the a.c. current. However, the artificial current zero principles are used in HVDC circuit breakers since the d.c. current flows unidirectionally with no natural current zero. Arc extinction is realised by separating the contacts which are controlled by a driving mechanism. Despite the motion characteristics of those moving components, the circuit breaker needs to have the ability to perform a given switching duty from the grid system with minimum energy and least physical damage of the key components, which lies at the centre of the “intelligence” domain. The present work is closely related to this part of the intelligent circuit breakers and will be explained in following chapters.

At present, most of research on the intelligent operation of circuit breaker focuses on the development of microelectronic-based software and hardware systems that provide reliable in-service controlling and monitoring. Nevertheless, successful operation of the circuit breaker under complicated power system conditions remains difficult. The core question is that how to interrupt a current, especially a fault current, with optimised gas dynamics (e.g. flow, pressure and temperature field) and contact travel. It involves an in-depth understanding of the arcing process and its interaction with driving mechanism. A comprehensive relationship between the grid network system and circuit breaker is presented in Figure 1.1. To successfully complete an interruption duty, a circuit breaker needs to ensure two representative aspects. Firstly, the gas in the arcing space between the contacts changes from the conducting medium at high current to a poor conductor at the final current zero point of the AC current to quench the arc. Secondly, sufficient insulation needs to be restored at a shorter time scale ($\sim 100 \mu\text{s}$) after current zero. The first process during the interruption requires the circuit breaker to be able to carry the fault current through the arc without causing physical damage to hardware components or altering the gas environment. Besides that, strong arc cooling is required to reduce the arc temperature and arc column size, leading to an increased arc resistance.

The high current arc needs to be supported by the arcing contacts. The strong energy flux from the arc column to the contacts will cause erosion of the contacts. It removes the metal from the contact surface in vapour form and also causes a spitting of contact material in solid or liquid form. It not only shortens the contact length but also changes the surface conditions. In addition, strong radiation from the arc column causes ablation

of the nozzle (e.g. PTFE), leading to an enlargement of nozzle hole and changing nozzle surface conditions as well. Both contact erosion and nozzle ablation will influence the arc characteristics, and more importantly, the arc quenching capability of the designed arcing chamber. Therefore, a thorough understanding of these two areas is necessary to the design and implementation of the “intelligence” in circuit breakers.

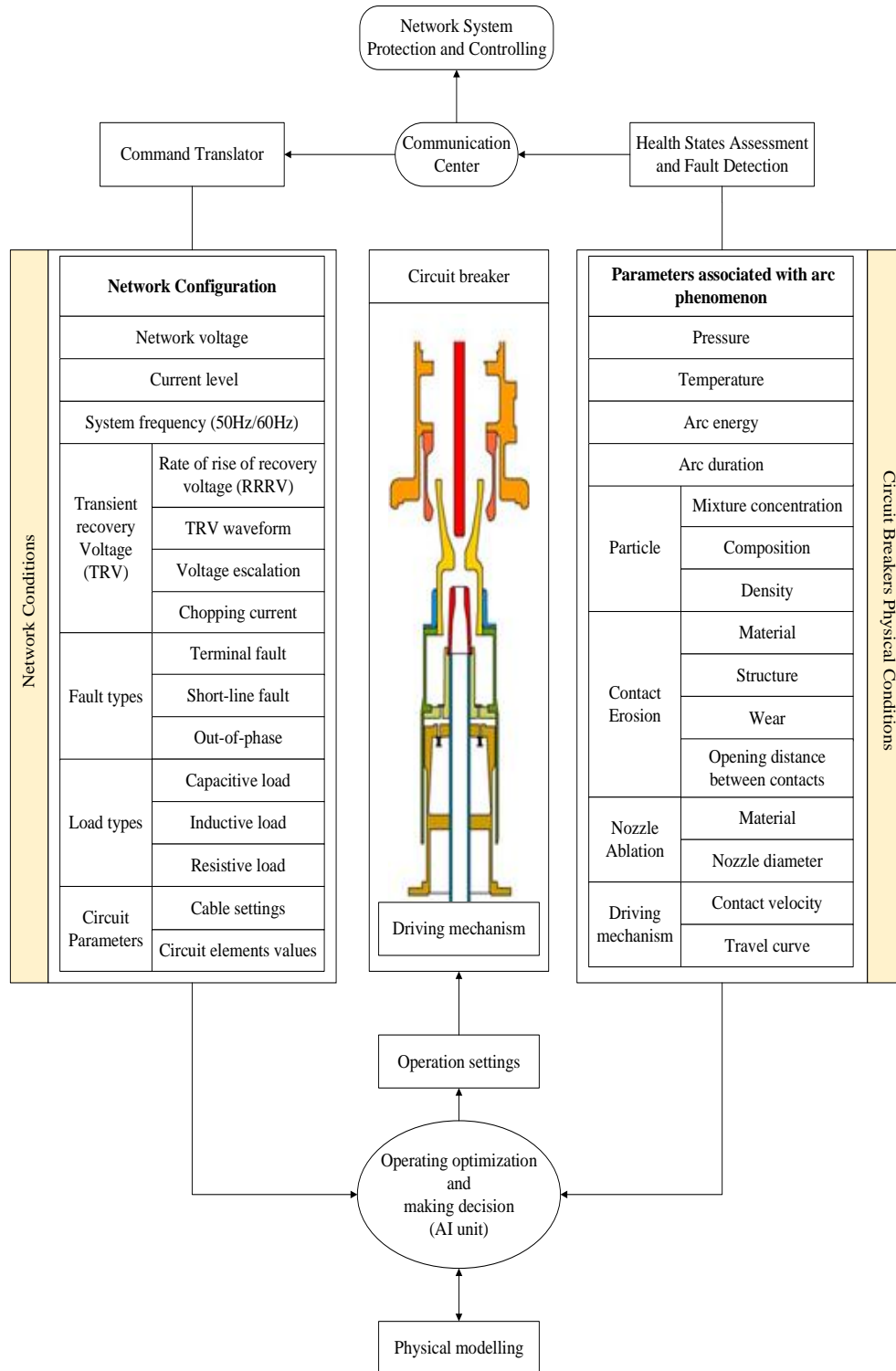


Figure 1.1 Relationship between the grid networks and the high voltage circuit breakers.

1.3 Types of Circuit Breakers

Based on the descriptions of voltage levels, the circuit breakers could be classified into low voltage (<1 kV), medium voltage (1~72.5 kV) and high voltage (>72.5 kV) which are being used in international standards: International Electrotechnical Commission (IEC) 62271-100 [9] and American National Standards Institute (ANSI) C37.06 [10]. In addition, the properties of the insulating medium are decisive important to ensure the effective interruptions of circuit breakers. From the insulating medium, circuit breakers could be categorised into the oil, air, SF₆ and vacuum types as presented in Figure 1.2.

For high voltage circuit breakers, SF₆ has been extensively used because of its higher dielectric strength and non-flammable characteristics since 1950. However, due to the stronger greenhouse effect of SF₆ which is evaluated by the Global Warming Potential (GWP), there is ongoing research to find environmentally friendly gases to replace SF₆, e.g. CO₂, air, CF₃I and g³ gas. The related GWPs of different gases are shown in Table 1.2 [11], [12]. The traditional gases such as air, CO₂ and N₂ have lower GWP, but the corresponded insulation strength is limited, approximately 40% or less in comparison with SF₆. CF₃I presents a better insulation strength with lower GWP. However, the high boiling temperature of CF₃I makes it impossible to use in the pure form. Therefore, it is normally mixed with N₂ or CO₂ for the research [13]. g³ is a developed mixture of 3MTM NovecTM 4710 fluid (Fluorinated nitrile) and CO₂. It has high dielectric strength and stability, low boiling temperature, and approximately 98% reduction of GWP in comparison with SF₆ [14]–[16]. Nevertheless, this replacement gas is relatively new in the high voltage applications and the development is still at the infancy stage so that more and more theoretical and experimental investigations are required especially for its insulation performance.

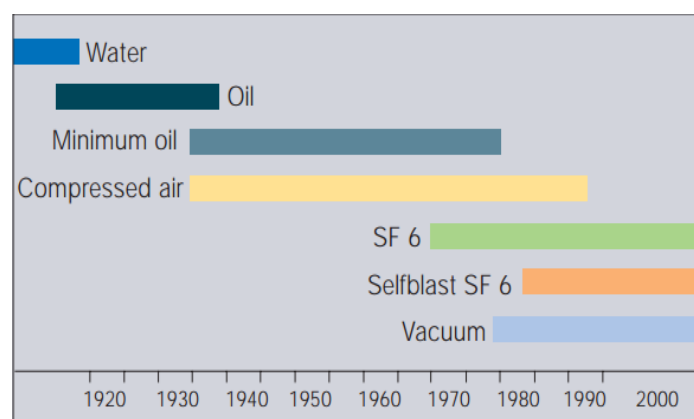


Figure 1.2 Overview of the usage of different circuit breakers [17].

Table 1.2 Global warming potentials and lifetimes of different insulating gas species [11]–[16].

Gas species	Life time (years)	GWP
CO ₂	Variable	1
SF ₆	3,200	23,900
CF ₃ I	0.005	1

A brief review of the circuit breakers with different insulating medium is described as following.

(1) Air circuit breaker

A circuit breaker that operates in the compressed air is known as an air circuit breaker. In an air circuit breaker, there are two pairs of contacts, referred as the arcing contacts for carrying the arc current and the main contacts for passing the normal current. Each set of the contacts is designed as a fixed one and a moving one. They are usually made of good conducting materials such as copper or coated by silver. During the operation of circuit breaker, the main contacts will firstly separate while the arcing contacts are still connected and there is no arc produced during this period. The arc is only initiated when the arcing contacts are separated and the gaseous medium is then breakdown and ionised.

As an easily obtained medium, air has good insulation property at normal temperatures but it is difficult to extinguish the arc since the air surrounding the arc would be heated up to high temperature. To improve the interruption performance of air circuit breaker, Slepian [18], [19] developed an approach by constructing a large number of airgaps in the chamber so that the arc could be blown into the gaps electromagnetically and the contacts could be kept cold by electromagnetic rotation of arc [20]. It is a fundamental breakthrough for improving the performance of high power air circuit breakers. From this innovation, a new approach was proposed by using the arc chutes which is normally made from refractory material [21], [22]. Arc chute is divided into small compartments using the splitters. Due to the convection of the gaseous medium, the arc is lengthened during the arc contacts motion. When the arc enters the arc chute, it would be split into the shorter arcs in series. There are two types of the air circuit breakers: plain air circuit breakers and air blast circuit breakers, as presented in Figure 1.3. The plain air circuit breaker (Figure 1.3 (a)) is preferable for low voltage applications.

The air blast circuit breaker is normally designed for comparative higher voltage ratings. The compressed air is chosen as the arc quenching medium and it is released to form high speed flow in the nozzle during the interruption. Depends on the gas flow direction in relation to the arc column, the air blast circuit breaker could be categorised into axial blast and cross blast, as presented in Figure 1.3 (b) and (c). In an axial blast air circuit breaker, the contacts are kept together by a spring. During the interruption, the air flow with high pressure is released into the arcing chamber and the spring is thus deformed to withdraw the moving contact from the fixed contact. In contrast, the cross blast air circuit breaker is designed with the fixed blast pipe in perpendicular to the movement direction of the moving contact. The air flows through the blast pipe and blows the arc column towards the splitters of the exhaust chamber for the final cooling [20]. The air circuit breaker is easy in construction, and maintenance by simply monitoring the air pressure.

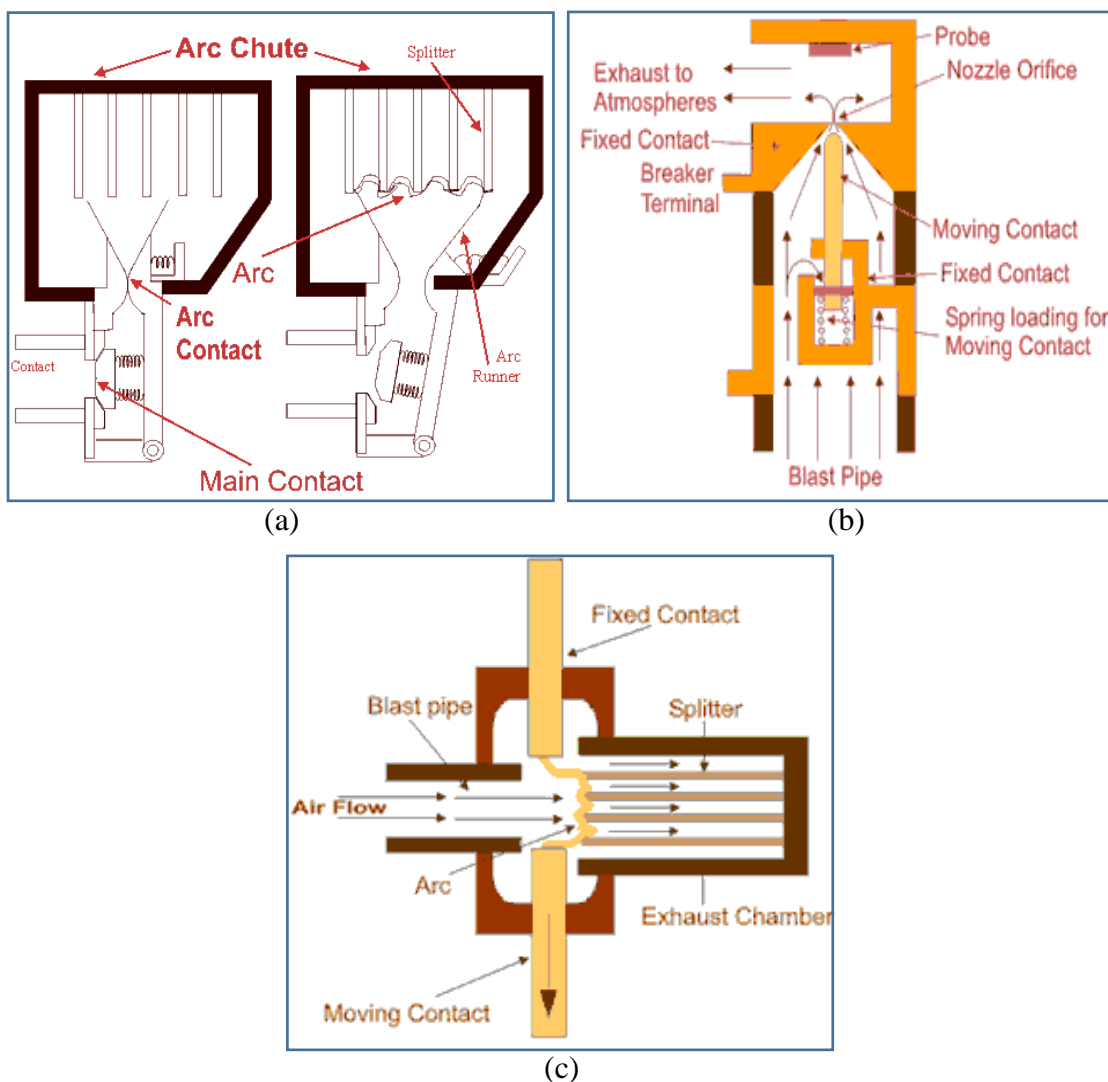


Figure 1.3 Schematic diagram of air circuit breakers, (a) Plain air circuit breaker; (b) Axial blast air circuit breaker and (c) Cross blast air circuit breaker [22].

(2) Oil circuit breaker

In an oil circuit breaker, the contacts are immersed into insulating oil such as the silicon oil and mineral oil with a better insulating property (dielectric strength of 10-15 MV/m) in comparison with air (3 MV/m). An arc is produced when the contacts separate and a large amount of heat is produced from the arc and exceeds the vaporization temperature of oil. The oil is then decomposed into mostly hydrogen gas to extinguish the arc. There are two types of the oil circuit breakers: bulk oil circuit breaker (BOCB) and minimum oil Circuit Breaker (MOCB), as illustrated in Figure 1.4 [23]. BOCB is named because of the larger quantity of oil that is used in the tank for arc extinction. Furthermore, the fixed and moving contacts are separated in the insulating oil. The arc formation results in a rapid production of hydrogen gas bubbles with high pressure. With the movement of moving contact, the arc is drawn and the arc resistance is increased correspondingly. The high pressure around the arc increases the gas de-ionisation which eventually leads to the arc quenching. Compared with bulk oil circuit breaker, the minimum oil circuit breaker requires less space for the installation with a reduced amount of oil. When the moving contact is drawn out from the fixed contact, they are submerged in the dielectric oil. The produced arc heats up the surrounding oil, leading to the oil decomposition and gas releasing, the produced high pressure gas is therefore driven into the arc extinguish device for cooling the arc. Nevertheless, oil is a kind of inflammable medium with risks of fire and the decomposed products are explosive. Moreover, the arcing products such as the carbonised particles contaminate the oil which leads to a decrease of the dielectric strength. In other words, MOCB is not suitable for frequent operations and it has to be cleaned after a certain number of interruptions.

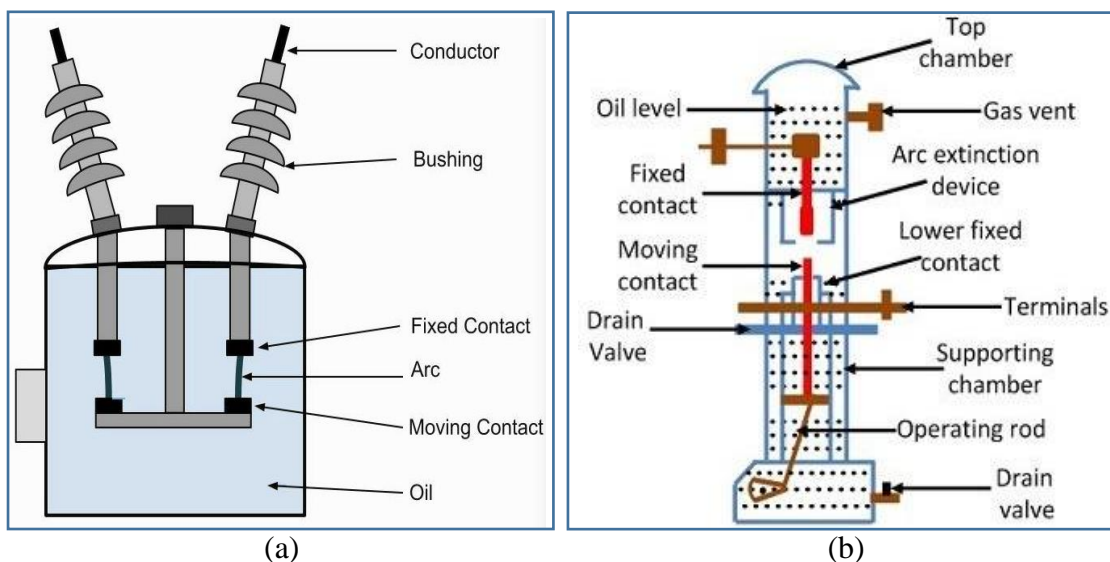


Figure 1.4 Structure of the oil circuit breakers: (a) BOCB; (b) MOCB [23].

(3) Vacuum circuit breaker

A vacuum circuit breaker is designed where the arc generates in vacuum condition. This kind of medium has excellent dielectric strength (10^{12} MV/m) [24]. Main components in the vacuum chamber of vacuum circuit breaker are vapour condensing shield, a pair of contacts and metallic bellows as shown in Figure 1.5. During the interruption process, the driving mechanism separates the contacts and a small amount of metallic vapour is produced from the contact surface. A molten metal bridge is then appeared between the contacts and an arc is formed as a result of metallic vapour ionization. The arc attached on the cathodic contact surface contains a number of cathode spots which move rapidly and the current carried by each spot is affected by the contact material (approximately 100 A for a copper cathode [25]). With the contact movement, the produced metallic vapour is condensed on the contact surface and when the current decreases towards its zero, the rate of vapour production becomes lower and the density of vapour is reduced as well. The condensation leads to a quick recovery of the dielectric strength to ensure the arc quenching. In the vacuum chamber, the vapour condensation shield is designed outside the contacts to protect the insulating enclosure from becoming conductive. The vacuum circuit breaker interruption capability highly depends on the contact material. The material should have high an electrical conductivity with low resistance for passing the current without overheating. Moreover, a high thermal conductivity is required as well to effectively dissipate the heat from the arc column.

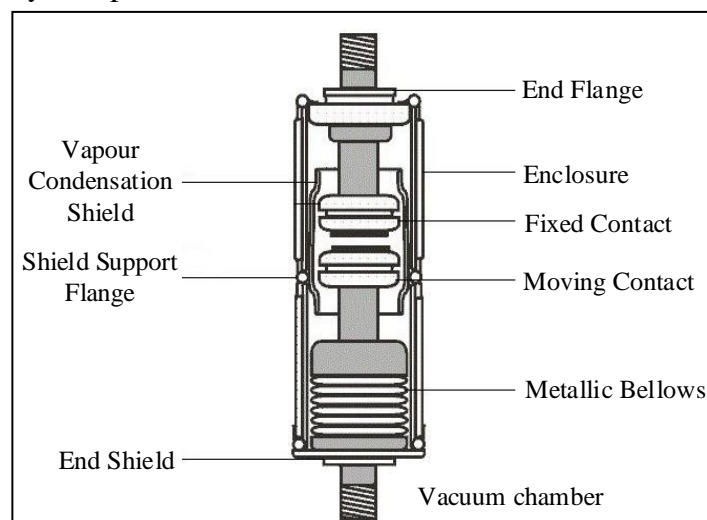


Figure 1.5 Schematic diagram of the vacuum circuit breaker [26].

(4) SF₆ circuit breaker

SF₆ is a chemically stable, non-flammable, non-corrosive, colourless and odourless gas. The peak thermal conductivity of SF₆, corresponding to the dissociation of the molecule,

is approximately around 2,000 K which is lower than air (6,000 K). It has an excellent insulating performance and high electron affinity [25]. SF₆ has been widely used as an interrupting medium in high voltage apparatuses since the beginning of the 1950s and the first SF₆ circuit breaker was commercially introduced in 1959. The better insulating, physical and chemical properties of SF₆ make the SF₆ circuit breakers performing much better than air and oil circuit breakers.

Two representative types of SF₆ circuit breaker have been extensively utilised, known as puffer type SF₆ circuit breaker and self-blast circuit breaker (auto-expansion circuit breaker). As illustrated in Figure 1.6, the puffer type SF₆ circuit breaker contains a fixed contact, a moving contact, a moving cylinder and a fixed piston. An arc is struck when the moving contact moves away from the fixed contact. Besides that, the volume of the puffer chamber becomes smaller with the movement of the moving cylinder while the fixed piston stays stationary, which results in a compression of the gas inside the puffer chamber. Before the fixed contact leaves the nozzle, the nozzle is clogged and effective cross section for the gas flow is smaller. With the movement of the moving contact, the arc is drawn and the compressed gas with higher pressure in the puffer chamber flows out through the nozzle. As a result of convection and turbulence cooling, the arc column becomes thinner and the arc is eventually extinguished at the current zero. It should be emphasised that the driving mechanism of puffer type SF₆ circuit breaker should be designed with sufficient energy to move the cylinder and separate the contacts.

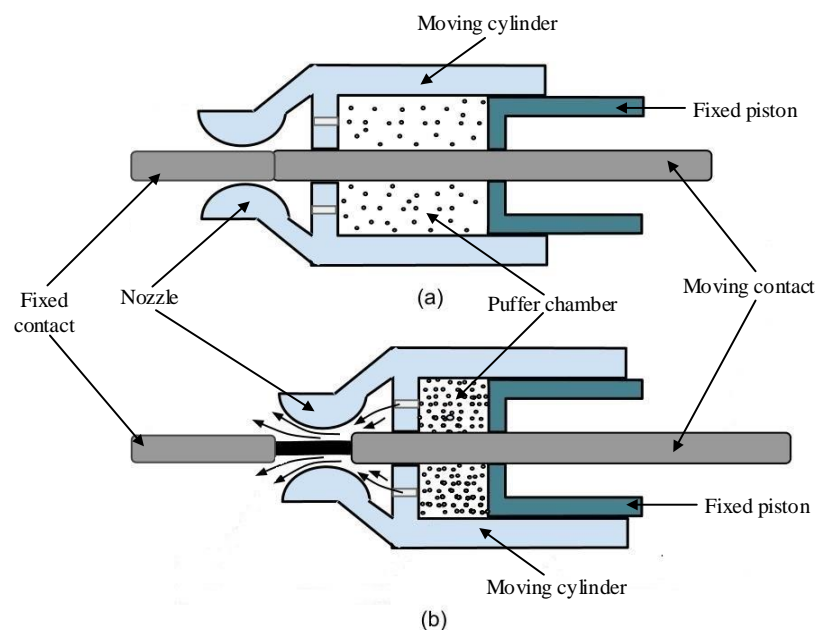


Figure 1.6 Simplified schematic diagram of an puffer SF₆ puffer circuit breaker, (a) closing position; (b) opening position [27].

Self-blast circuit breaker is designed based on the innovative interrupting principles to reduce the operation energy required from the driving mechanism. It is advantageous over the puffer type SF₆ circuit breaker. During the interruption process, energy from the arc need to be sufficiently utilised to develop an effective flow field environment in the arcing chamber for the arc quenching at the final current zero. There is an expansion volume (8) attached with a control valve (6) inside the arcing chamber as illustrated in Figure 1.7. When the moving arcing contact separates with the fixed contact, the arc is rapidly produced and lengthened. When interrupts a high current, sufficient arc energy produces a high pressure region between the arcing contacts and the high pressure gas is then driven into the expansion volume which results in a closure of the control valve. Because of the compression of the SF₆ gas inside the expansion volume and the thermal energy brought by the injected hot gas from arcing space, the pressure in the expansion volume becomes high. When the current approaches zero, the pressure in the arc region becomes lower which is because the decreased current drops the temperature of the arc column and the high pressure gas in the expansion volume is thus largely flowed out so that the arc is strongly blown and eventually extinguished. For self-blast circuit breaker, the nozzle is very important for guiding the gas flow and producing hot vapour to ensure the pressurisation in the expansion volume. Compared with puffer type circuit breaker, the physical phenomena and arc characteristics are more complicated. The investigation of the arc behaviour especially in the arcing space is significant for analysing the circuit breakers interruption capability.

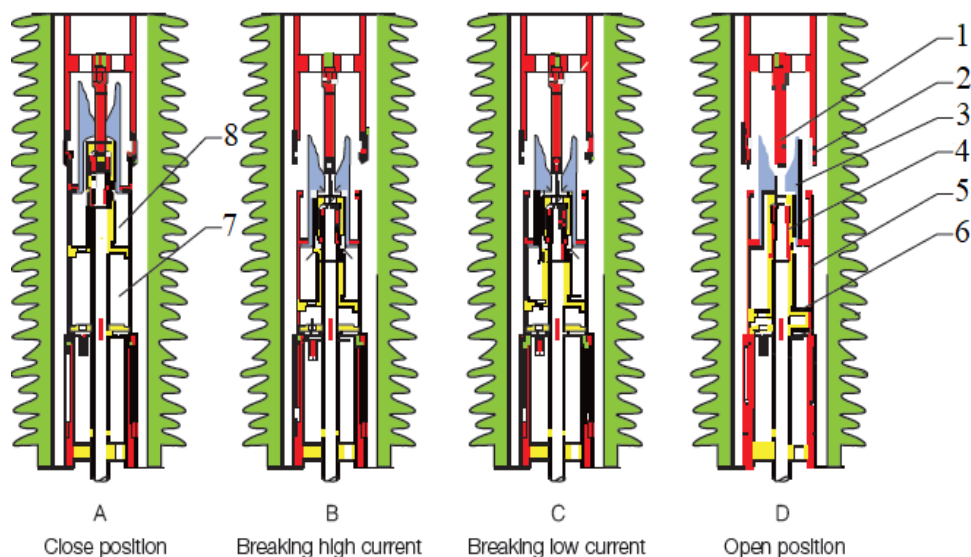


Figure 1.7 Schematic diagram of a self-blast SF₆ circuit breaker as an example. The labelled components are: 1. Fixed arcing contact; 2. Fixed main contact; 3. Nozzle; 4. Moving arcing contact; 5. Cylinder; 6. Control valve; 7. Compression chamber; 8. Expansion volume[28].

1.4 Basics of Electric Arcs

Arc is a key element associated with the operation performance of circuit breakers. The arc formed between the two arcing contacts is a phenomenon of electrical discharge. It is initiated as a result of breakdown of gas between the two arcing contacts. The electric arc in a gas-blast circuit breaker is normally a kind of thermal plasma which consists of neutral particles, electrons and ions. In an arc plasma, the ions and neutral particles are regarded as heavy particles since their masses are much heavier in comparison with the electrons. The arc is formed as a bright column because some of the heavy particles are in excited state and they could return to a less excited state or ground state by the photon emission [29]. For an arc plasma, quasi-neutrality is an important property that indicates the negative charges are balanced by the positive charges. During a current interruption, the circuit breaker could be treated as a good conductor (high electrical conductivity of the arc medium) when the arc plasma contains sufficient free charge carriers while the plasma medium should become a good insulator when the current approaches the final zero to withstand the applied voltage from power grid system. The physical properties of the arc plasma are correlated to the plasma chemical composition, arc temperature, pressure, etc. The arc could be simply classified into high pressure arc and vacuum arc [20]. High pressure arc defines the arc that exists at or above atmospheric pressure while vacuum arc is defined with pressures below 10^{-4} torr. For high pressure arcs, the arcing medium is composed of the filling gaseous medium (such as SF_6). However, a vacuum arc is produced due to the presence of metallic vapour produced from contact surface.

In reality, some important assumptions are required to analyse the complicated physical characteristics and dynamic behaviour of an arc plasma. Since a plasma contains a large number of particles (neutrals, ions and electrons), it is essential to know the distribution function of the existed particles so as to provide a macroscopic (large-scale) description of the plasma properties. Based on the plasma fluid theory, the plasma can be described by some macroscopic parameters such as density, temperature, and velocity which are functions of space and time only. In a thermal plasma, the collisions between particles are normally sufficiently rapid and frequent. At different temperatures, the interparticle collisions are dominated by different particles. At low temperatures, neutral particles which are largely presented in the arc plasma dominate the collisions. With temperature increases, neutral particles start to dissociate and ionise so that the numbers of charged

particles (positive and negative) become more and collisions between charged particles as a result of Coulomb interactions become dominant. Following the hydrodynamics of fluids and gases, it is reasonable to adopt the laws of equilibrium statistical mechanics to describe the plasma properties. Complete thermodynamic equilibrium (CTE) state is normally assumed to describe a uniform homogeneous plasma system which means all the related properties are functions of a temperature and the plasma satisfies the kinetic and chemical equilibrium. Nevertheless, the nonuniformity of the plasma results in the irreversible losses through conduction, convection and diffusion. Moreover, the Planck distribution is not suitable to describe the plasma radiation. With the consideration of this deviation from CTE conditions, it is more realistic to assume the plasma in the local thermal equilibrium (LTE) state where the particles have an identical temperature but the radiation is not required to be in equilibrium [31], [32]. Besides that, local chemical equilibrium (LCE) is assumed as well to simplify the calculation of the plasma chemical composition. Under LTE and LCE conditions, thermodynamic properties and transport coefficients of an arc plasma depend on the arc temperature and pressure only.

1.4.1 Local thermal equilibrium (LTE) state of electric arcs

The temperature of arc plasma is defined correlated to the thermal kinetic energy of per particle. In an LTE plasma, electrons collide with heavy particles and their temperatures are equilibrated rapidly as a result of frequent collision. This is the first requirement of an LTE plasma need to be satisfied: temperatures of electrons and heavy particles are identical. In addition, an LTE plasma also satisfies the following requirements [33] [34]:

(1) The speed distribution of particles follows the Maxwell-Boltzmann distribution:

Based on the theory of LTE plasma, the kinetic temperature of the plasma is determined using the particle average kinetic energy. The speed of a particle follows the Maxwell-Boltzmann distribution:

$$\frac{1}{2}m_p v_p^2 = \frac{3}{2}k_B T \quad (1.4.1)$$

where m_p is the particle mass; k_B is the Boltzmann constant; v_p is the particle speed and T is the temperature. The distribution function is determined by:

$$f(v_p) = 4\pi v_p^2 \left(\frac{m_p}{2\pi k_B T} \right)^{\frac{3}{2}} \cdot e^{-\frac{m_p v_p^2}{2k_B T}} \quad (1.4.2)$$

and the number density of particles dn_w with velocities between $v_{w,p}$ and $v_{w,p}+dv$ is:

$$dn_w = n_w f(v_{w,p}) dv_{w,p} = \left(\frac{m_p}{2\pi k_B T}\right)^{\frac{3}{2}} \cdot 4\pi n_w v_{w,p}^2 \cdot e^{-\frac{mv_{w,p}^2}{2k_B T}} dv_{w,p} \quad (1.4.3)$$

where n_w is the number density of the specific species w .

(2) Population density of excited states for all particles follows Boltzmann distribution: Boltzmann distribution describes the statistical distributions of particles over different states. Kinetic energy of particles is expressed in an exponential term in the Boltzmann distribution function:

$$\exp\left(-\frac{E_{w,s}}{k_B T}\right)$$

where $E_{w,s}$ is the energy of species w at excited state s . The expected number density of species w at state s could be determined by:

$$\frac{n_{w,s}}{n_w} = \frac{g_{w,s} \exp\left(-\frac{E_{w,s}}{k_B T}\right)}{Q_w} \quad (1.4.4)$$

where $n_{w,s}$ and $g_{w,s}$ are number density and corresponding statistical weight of species w at state s ; Q_w is the partition function of species w .

(3) Number densities of the particles can be determined using Saha equation:

Based on the thermophysical principles, the Boltzmann distribution could be applied to determine the number densities of particles existed in the plasma. For the gas with high temperatures, collisions between neutral particles become frequent. Electrons that orbit around the atomic nucleus will jump to higher energy levels after receiving energy. The neutral atoms will become ionised when the electrons are escaped. The Saha equation is used to determine the number densities of different particles in the LTE plasma:

$$\frac{n_{i+1} n_e}{n_i} = 2 \frac{Q_{i+1}}{Q_i} \left(\frac{2\pi m_e k_B T}{h^2}\right)^{\frac{3}{2}} \cdot \exp\left(-\frac{E_{i+1} - \Delta E_{(i)}}{k_B T}\right) \quad (1.4.5)$$

where n_e is the number density of electrons; n_i and n_{i+1} are the number densities of species i and $i+1$; Q_i and Q_{i+1} are the partition functions; m_e is the electron mass; h is the Planck constant; E_{i+1} is the ionization energy and ΔE is the lowering of ionization energy.

(4) The pressure of the particles in LTE plasma follows the Dalton's law:

Total pressure of gas mixture is the summation of partial pressures of individual species:

$$P = \sum_{w=1}^{w_{total}} k_B T n_w \quad (1.4.6)$$

where P is the total pressure in the system and w_{total} is total number of species.

(5) Electrical neutrality

$$n_e = \sum_{\substack{w=1 \\ w \neq e}}^{w_{total}-1} Z_w n_w \quad (1.4.7)$$

It describes the electrical neutrality of LTE plasma, where Z_w is the charge number of species w .

1.4.2 Radiation from arc plasma

The material properties of working medium in the arcing chamber are calculated based on the assumptions of LTE and LCE. Electrons and heavy particles have same kinetic temperature. Planck's law explains the electromagnetic radiation from a black body in the complete thermal equilibrium (CTE) state at a definite temperature. Such radiation implies a balance between the processes of emission and absorption. However, it is not applicable to describe the radiation of the arc plasma using Planck's law [35]. Therefore, radiation from the arc column should be calculated from basic theory. In thermal plasma, the radiation becomes more important as an energy transfer mechanism. Especially for the auto-expansion circuit breakers where the radiation becomes a dominant energy loss mechanism at the arc centre at high current. It is also the source of energy to ablate the nozzle material in particular in the auto-expansion circuit breakers to establish a high pressure zone in the expansion volume to develop the flow field conditions at the final current zero for arc quenching. Detailed descriptions are shown in following chapters.

1.5 Contacts and Nozzle(s)

Interactions between the arc column and solid materials lead to material consumption, and result in the change of circuit breakers interruption capability and gaseous medium insulation performance. Detailed knowledge on the dependence of the material change on the arcing process is essential for the realisation of "intelligence" in modern circuit breakers, which forms the main objective of the present work.

1.5.1 Contacts

The contacts in the arcing chamber of a circuit breaker play a significant role in current interruption. They are closed for most of the time as conductors to carry the load current. During the breaking operation, the main contacts are opened before the arcing contacts. There should be no erosion or deformation on the main contacts because the arc always initiated between the separated arcing contacts. To provide good electrical connections, the contacts especially the arcing contact set should be in reasonable conditions.

However, the arc between the arcing contacts has much higher temperature well above the vaporization point of the contact material, the stronger energy flux from the hot arc column to the contact surface leads to the vaporization or deformation of the contact tip. This is the so-called “contact erosion” which is a complicated process and affected by different factors such as contact material, arc current and arc duration. It is an avoidable result from current interruption. When the current is higher (>20 kA) and arc duration is longer (>10 ms), the erosion would be more and more serious, and eventually affects the operation performance of circuit breakers. Therefore, a thorough understanding of the contact erosion is required to analyse the physical process and its influences on arc behaviour. Real examples of the contact conditions after the current interruption from the experiments are presented in Figure 1.8. After the 16 interruptions of 63 kA current, it results in 4.6 mm (a) and 3.6 mm (b) length variations. The contact surface becomes unsmooth and even with serious cracks on the contact tip. The black residual is resulted from the material oxidation.

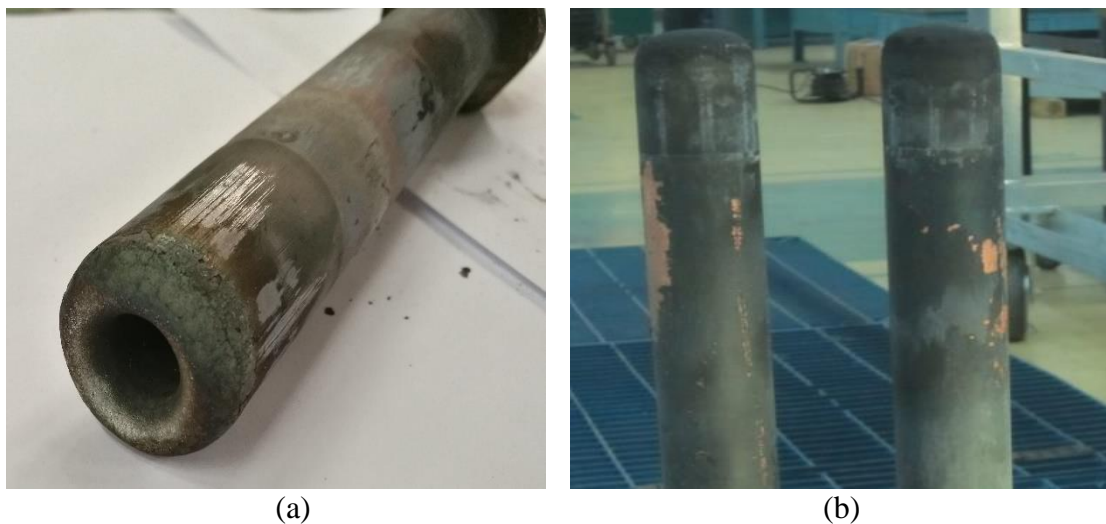


Figure 1.8 Diagram of circuit breaker arcing contacts erosion. Contact material is Cu/W. (a) 550 kV/63 kA circuit breaker; (b) 800 kV/63 kA circuit breaker [36].

Contact materials used in the circuit breakers are varied and they are normally classified into pure metals (e.g. Cu, Al and Ag), alloys (e.g. AgW and CuW), and the composite materials (e.g. Cu/C and Ag/C). The materials need to satisfy the common requirements such as low contact resistance, high mechanical strength and erosion-resistance. Copper is a kind of soft and malleable metal with excellent electrical conductivity and thermal conductivity. However, the melting and boiling temperatures of copper are lower (1,358 K and 2,835 K) in comparison with the refractory materials such as tungsten (3,695 K and 5,933 K). Normally in the high voltage circuit breaker, Cu/W alloy is preferable as the contact material which contains 80% tungsten and 20% copper. In comparison with pure copper, the Cu/W alloy has a higher boiling temperature and the copper vaporises before the tungsten melts.

Pure copper is a representative non-refractory material that evaporates more easily. To investigate the contact erosion phenomenon, pure copper is used as the contact material in the present study. In the experiments, it is observed that the arc roots move randomly and rapidly on pure copper contact, in the form of group of small size spots with large current density [37], [38]. Due to its lower melting temperature, the contact material is partly removed in the form of droplets. The arc would be able to cause severe damage and deformation on the contact surface and always leads to the formation of sharp micro protrusions where the local electric field would be enhanced. When the temperature around the contact is high enough, a significant portion of the material is eroded into vapour and injected into the arcing gas, changing its thermophysical properties as well as the arc behaviour.

1.5.2 Nozzle(s)

Nozzles are used in circuit breakers to perform two basic functions. Firstly, it is used to guide the arc and gas flow to ensure sufficient arc cooling. Secondly, in auto-expansion circuit breakers, it is used to generate hot vapour through ablation to create a “thermal puffer” that generates high speed gas flow when the current approaches zero to quench the arc. The nozzle has axisymmetric (apart from the holes in the auxiliary nozzle) and changing cross-sectional area to follow the converging-diverging structure. Similar to the arcing contacts, the inner geometry of the nozzle is an essential factor to affect the operation performance of SF₆ auto-expansion circuit breaker. It significantly influences

the pressure and velocity distributions within the arcing space of the contact gap. The mass is injected into the working medium by the ablation, changes the thermodynamic properties and transport coefficients of the gas mixture and the properties of arc. Nozzle ablation helps quenching the arc, but leads to the sacrifice of its mass. The enlargement and surface modification of the nozzle hole leads to the deterioration of the interruption performance, directly limiting the lifetime of circuit breaker. Therefore, it is necessary to mathematically predict the amount of ablated mass from the nozzle surface and its influences on the flow field environment within the arcing space for the arc quenching. Real examples of the nozzle surface conditions after the current interruption from the experiments are presented in Figure 1.9 where (a) and (b) present PTFE nozzle ablation of a test device (ABB [39]), (c) shows PTFE nozzle ablation of a 252 kV circuit breaker after L90 test (Pinggao [36]) and (d) shows MoS₂ nozzle ablation of a 550 kV circuit breaker after interrupt 63 kA current for 13 times.

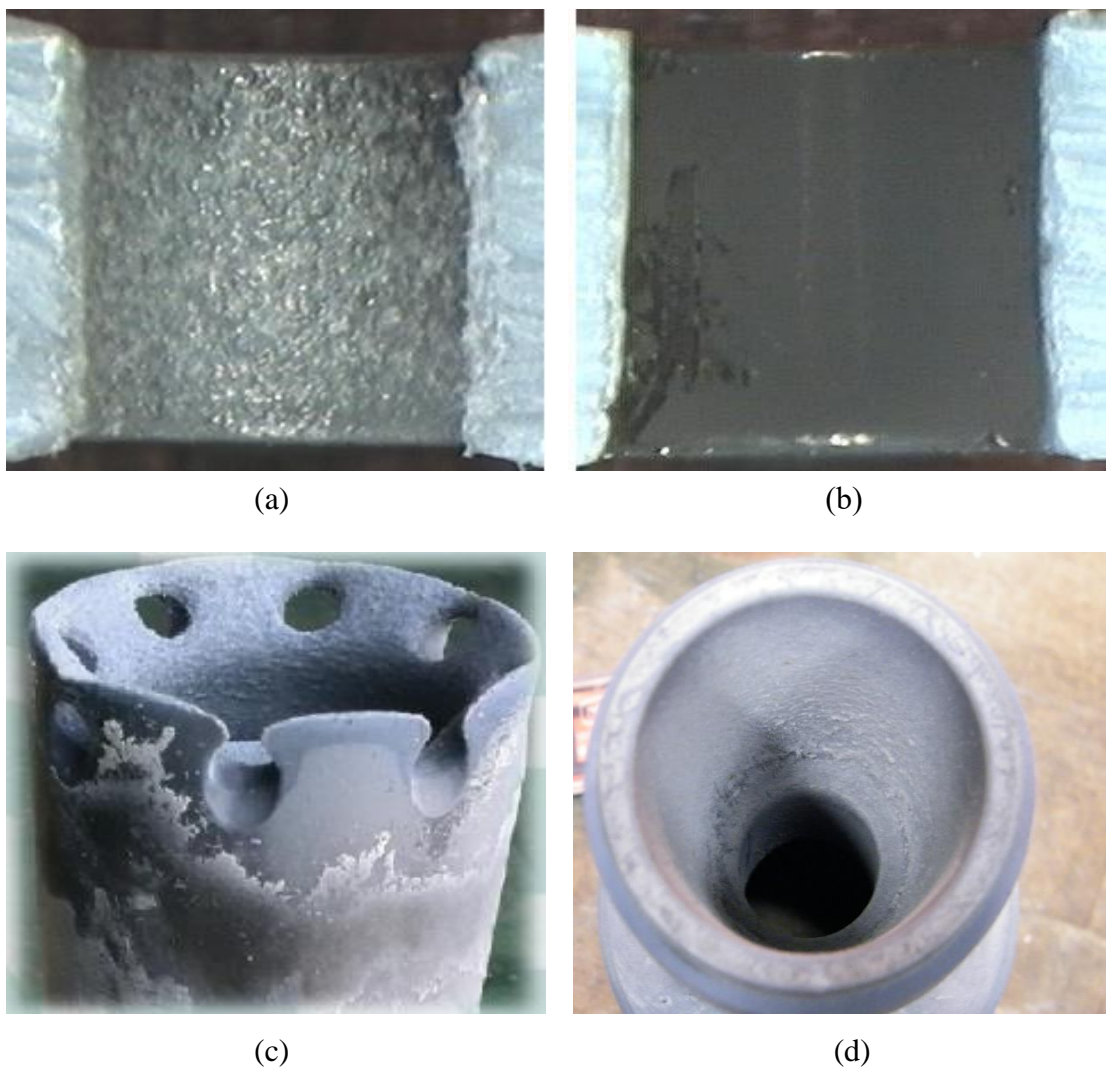


Figure 1.9 Diagram of ablation on different nozzle materials and test devices. (a) and (b) for ABB test device [39]; (c) and (d) for Pinggao Group product [36].

1.6 Brief Review of Arc Models

Over the past decades, researchers have investigated a variety of approaches to establish mathematical models for understanding arc behaviour. First mathematical model was introduced by Cassie in 1939 [40]. In 1946, Elenbaas introduced a model with an energy balance conservation equation to describe the arc characteristics. It is the earliest study to analyse the temperature distribution of a high pressure discharge arc. The arc plasma energy balance equation (Elenbaas-Heller equation) is expressed as [41]:

$$\frac{1}{r} \frac{d}{dr} \left(r \lambda(T) \frac{\partial T}{\partial r} \right) + \sigma(T) E^2 = 0 \quad (1.6.1)$$

The two associated energy terms are thermal conduction and ohmic heating. $\lambda(T)$ is the thermal conductivity, $\sigma(T)$ is the electrical conductivity and E is the electric field.

Following this attempt, integral arc modelling was developed to simplify the calculation. In 1975, Lowke and Ludwig proposed an integral arc model based on a conceptual view by neglecting many physical processes that have insignificant effects on arc behaviour, e.g. thermal conduction and turbulence cooling at the arc center [42]. In 1974, Chan *et al* developed an arc model and derived an energy balance integral equation for the arc core which is together with the external flow conservation equation [43]. In 1980, Fang proposed the scaling laws for the high current phase [44] and a current zero model [45] based on the method described by Chan.

In 1980s, to simplify the calculation of the complicated mechanisms in the switching arcs, the differential method was developed and different arc models were created for various arc conditions [46]–[51]. Following the proposed differential methods, Fang *et al* contributed considerable effort on numerical arc modelling with the consideration of different mechanisms in the arc plasma. In 1987, an approximate radiation model was derived [52] to reasonably estimate the radiation emission and re-absorption conditions in the N₂ arc. Since 1999, the research of arc characteristics in an auto-expansion circuit breaker with considering all the significant processes, e.g. radiation, turbulence cooling, and interaction between arc and contact/nozzle was performed by Yan and Zhang [53]–[55]. These models according to the differential method are still adopted by the current research.

In addition, the application of Computational Fluid Dynamics (CFD) simulation on the physical processes in circuit breakers gained great advantages on the investigations of arc behaviour with advanced computing technologies. The commercial CFD packages such as PHOENICS (used in present work) and Fluent are widely used for this purpose.

1.7 The Objective and Organization of Thesis

Quantitative predictions of contact erosion and nozzle ablation especially the geometry change as a result of material mass loss provide baseline data for the development of intelligent circuit breakers. The present work is concerned with the “intelligence” at the physical layer. The main objectives of the present work are:

- (1) To develop a model that is able to predict the mass loss from the contact due to the vaporization. As already explained, the total mass loss from contacts is higher than that from vaporization because some of the contact material is lost in solid particles or liquid droplets. The percentage of the mass loss in vapour will be assessed.
- (2) To use an arc model to investigate the effects of nozzle ablation on the interruption performance of the auto-expansion circuit breaker. The work involves different test duties to gain a complete picture of the influences of nozzle ablation.

The thesis is organised into 6 chapters. This chapter gives a brief review of background knowledge associated with the present work. Calculations of thermodynamic properties and transport coefficients of pure copper plasma under equilibrium and non-equilibrium conditions are described in Chapter 2. The chemical composition of pure copper plasma is firstly calculated using the Saha ionization equation coupled with Dalton’s law and the principle of electrical quasi-neutrality of the plasma. Chapman-Enskog method with higher order approximations is then applied to determine the thermophysical properties of pure copper plasma under LTE and non-LTE conditions. The computation results of LTE pure copper plasma are compared with available literature data. The influences of different pressures and non-equilibrium degrees on the plasma physical properties are discussed.

In Chapter 3, a 1-D near cathode non-LTE layer model is built to analyse the physical processes of contact erosion. This model consists of two sub-models: pre-sheath model and sheath model. The solutions for these two sub-models are patched according to the

Bohm criterion and a total potential drop in this non-LTE layer is obtained. The current transfer process in the sheath layer and the energy exchange on the cathode surface are considered as well. From the determination of vaporization energy, the mass loss from the cathode surface and the variation of the cathode length as a result of cathode erosion are predicted.

Chapter 4 presents a comparative study of the nozzle ablation and its influences on the flow field conditions in a 145 kV/40 kA auto-expansion circuit breaker when interrupts the type test duty L90 with the consideration of three different arc durations and three computations of each arc duration case are performed in sequence with considering the variation of the nozzle flat throat diameter resulted from each prior computation. In the calculation, the ablated mass loss from the nozzle surface and the changed diameter of the nozzle flat throat are predicted. The influenced flow conditions at different positions (e.g. expansion volume, hollow contact, arcing space, main nozzle downstream and exit) within the arcing chamber due to the nozzle ablation are analysed as well. Besides that, the pressure variation inside the expansion volume which is directly associated with the enlarged nozzle holes under different arc durations are also discussed.

The work described in Chapter 5 focuses on another two type test duties (T30 and T60). Nozzle ablation as a consequence of different interrupted current levels is investigated. The predictions of the critical RRRV of a 145 kV/40 kA auto-expansion circuit breaker under different test duties (L90 and T60) are carried out. In the calculation, to accurately predict the turbulence cooling effect especially during current zero phase, a turbulence parameter c introduced in the Prandtl mixing length model is calibrated with test results. In addition, the interruption capability of the circuit breaker (variation of critical RRRV) affected by the enlarged nozzle holes due to nozzle ablation is discussed as well.

Finally, Chapter 6 summarises the findings and draws reasonable conclusions from the work. The existed problems and suggestions for the future work are also discussed.

Reference

- [1] M. Guarnieri, “The Beginning of Electric Energy Transmission: Part Two [Historical],” *IEEE Ind. Electron. Mag.*, vol. 7, no. 2, pp. 52–59, Jun. 2013.
- [2] M. Candas and O. S. Meric, “The Application of Ultra High Voltage in the World,” *J. Power Energy Eng.*, vol. 3, no. 4, pp. 453–457, 2015.
- [3] R. Lings, “Overview of transmission lines above 700 kV,” in *Proceedings of the Inaugural IEEE PES 2005 Conference and Exposition in Africa*, 2005, no. July, pp. 33–43.
- [4] Z. Liu, *Ultra-High Voltage AC/DC Grids*, 1st ed. China Electric Power Press, 2014.
- [5] D. Tiku, “dc Power Transmission: Mercury-Arc to Thyristor HVdc Valves [History],” *IEEE Power Energy Mag.*, vol. 12, no. 2, pp. 76–96, Mar. 2014.
- [6] M. Ardelean and P. Minnebo, “HVDC Submarine Power Cables in the World,” 2015.
- [7] D. Povh, D. Retzmann, and E. Teltsch, “Use of HVDC for Power Transmission Improvements,” in *CONFERENCE AND EXHIBITION*, 2004.
- [8] IEEE-SA Standards Board, “IEEE Guide for the Selection of Monitoring for Circuit Breakers.” IEEE, 2000.
- [9] IEC, “IEC 62271-100: 2008 High-Voltage Switchgear and Controlgear-Part 100: Alternating current circuit breakers.” p. 695, 21-Apr-2008.
- [10] IEEE Standards, “IEEE Std C37.06-2009 - IEEE Standard for AC High-Voltage Circuit Breakers Rated on a Symmetrical Current Basis - Preferred Ratings and Related Required Capabilities for Voltages Above 1000 V.” pp. 1–46, 2009.
- [11] J. T. Houghton, L. G. Meiro Filho, B. A. Callender, N. Harris, A. Katternberg, and K. Maskell, *Climate Change 1995: The Science of Climate Change*. Cambridge University Press, 1996.
- [12] J. T. Houghton *et al.*, “IPCC Third Assessment Report: Climate Change 2001. The Scientific Basis Contribution of Working Group I to the Third Assessment Report of the Intergovernmental Panel on Climate Change (IPCC).,” vol. 57, no. August, p. 944, 2001.
- [13] H. Katagiri, H. Kasuya, H. Mizoguchi, and S. Yanabu, “Investigation of the performance of CF₃I Gas as a Possible Substitute for SF₆,” *IEEE Trans. Dielectr. Electr. Insul.*, vol. 15, no. 5, pp. 1424–1429, Oct. 2008.

- [14] Y. Kieffel, “Characteristics of g 3 - an alternative to SF₆,” in *2016 IEEE International Conference on Dielectrics (ICD)*, 2016, pp. 880–884.
- [15] Y. Kieffel, F. Biquez, P. Ponchon, and T. Irwin, “SF₆ alternative development for high voltage Switchgears,” in *2015 IEEE Power & Energy Society General Meeting*, 2015, pp. 1–5.
- [16] M. Hyrenbach and S. Zache, “Alternative insulation gas for medium-voltage switchgear,” in *2016 Petroleum and Chemical Industry Conference Europe (PCIC Europe)*, 2016, pp. 1–9.
- [17] F. Pinnekamp, “The circuit breaker: A showcase of industrial product development,” Zürich, 2007.
- [18] J. Slepian, “Theory of the Deion Circuit-Breaker,” *Trans. Am. Inst. Electr. Eng.*, vol. 48, no. 2, pp. 523–527, Apr. 1929.
- [19] J. Slepian, “Flames from electric arcs,” *J. A.I.E.E.*, vol. 48, no. 9, pp. 661–664, Sep. 1929.
- [20] C. H. F.- C.H. Flurschein, *Power Circuit Breaker Theory and Design*. The Institution of Engineering and Technology, Michael Faraday House, Six Hills Way, Stevenage SG1 2AY, UK: IET, 1982.
- [21] E. W. Boehne and L. J. Linde, “‘Magne-Blast’ air circuit breaker for 5,000-volt service,” *Electr. Eng.*, vol. 59, no. 4, pp. 202–212, Apr. 1940.
- [22] electrical4u, “Air Circuit Breaker Air Blast Circuit Breaker | Electrical4u,” 2016. [Online]. Available: <https://www.electrical4u.com/air-circuit-breaker-air-blast-circuit-breaker/>. [Accessed: 14-Oct-2016].
- [23] Circuit globe, “Bulk Oil and Minimum Oil Circuit Breaker.” [Online]. Available: <http://circuitglobe.com/bulk-oil-and-minimum-oil-circuit-breaker.html>. [Accessed: 13-Dec-2016].
- [24] W. M. Haynes, *CRC handbook of chemistry and physics*, 91st ed. CRC Press, 2009.
- [25] R. D. Garzon, *HIGH VOLTAGE CIRCUIT BREAKERS: Design and Applications*, Second. New York, NY: Marcel Decker, 2002.
- [26] Electrical Edition, “Vacuum Circuit Breakers (VCB) Construction, Operation | Electrical Edition - Online Electrical Engineering Magazine.” [Online]. Available: <http://www.electricaledition.com/2015/12/vacuum-circuit-breakers-vcb-construction-advantages.html>. [Accessed: 15-Dec-2016].
- [27] “Electrical Systems: SF₆ Circuit Breaker Working Principle.” [Online].

- Available: <http://www.skm-eleksys.com/2012/02/sf6-circuit-breaker-working.html>. [Accessed: 22-Dec-2016].
- [28] “High Voltage Product - LW36.” [Online]. Available: <http://www.multi-link.com.my/lw36.html>. [Accessed: 01-Oct-2016].
- [29] M. I. Boulos, P. Fauchais, and E. Pfender, *Thermal Plasmas*. Boston, MA: Springer US, 1994.
- [30] M. F. Hoyaux, *Arc Physics*, vol. 8. Berlin, Heidelberg: Springer Berlin Heidelberg, 1968.
- [31] R. J. Goldston and P. H. Rutherford, *Introduction to Plasma Physics*. 1995.
- [32] A. Fridman and L. A. Kennedy, *Plasma Physics and Engineering*. Taylor & Francis, 2004.
- [33] M. N. Hirsh and H. J. (Hendrik J. Oskam, *Gaseous electronics*. Academic Press, 1978.
- [34] M. I. Boulos, P. Fauchais, and E. Pfender, *Thermal Plasmas: Fundamentals and Applications (Volume 1)*. Boston, MA: Springer US, 1994.
- [35] M. Hotinceanu, Z. Borsos, and O. Dinu, “Aspects of Thermodynamic Equilibrium in Plasma,” *Bul. Univ. Pet. – Gaze din Ploiești*, vol. 62, no. 2, pp. 97–102, 2010.
- [36] Pinggao Group, “Private Communication,” 2015.
- [37] R. N. Szente, M. G. Drouet, and R. J. Munz, “Current distribution of an electric arc at the surface of plasma torch electrodes,” *J. Appl. Phys.*, vol. 69, no. 3, p. 1263, 1991.
- [38] A. Anders, S. Anders, B. Jüttner, H. Pursch, W. Bötticher, and H. Lück, “Vacuum arc cathode spot parameters from high-resolution luminosity measurements,” *J. Appl. Phys.*, vol. 71, no. 10, p. 4763, 1992.
- [39] M. Seeger, J. Tepper, T. Christen, and J. Abrahamson, “Experimental study on PTFE ablation in high voltage circuit-breakers,” *J. Phys. D. Appl. Phys.*, vol. 39, no. 23, pp. 5016–5024, Dec. 2006.
- [40] A. M. Cassie, “Arc rupture and circuit severity: a new theory,” in *Internationale des Grands Reseaux Electriques a Haute Tension (CIGRE)*, 1939, p. 17.
- [41] H. K. Kuiken, “Asymptotic treatment of the Elenbaas–Heller equation,” *Appl. Phys. Lett.*, vol. 58, no. 17, pp. 1833–1835, Apr. 1991.
- [42] J. J. Lowke and H. C. Ludwig, “A simple model for high-current arcs stabilized by forced convection,” *J. Appl. Phys.*, vol. 46, no. 8, pp. 3352–3360, Aug. 1975.

- [43] S. K. Chan, M. D. Cowley, and M. T. C. Fang, "Integral methods of analysing electric arcs. III. Shape-factor correlation for low radiation and laminar flow," *J. Phys. D. Appl. Phys.*, vol. 9, no. 7, pp. 1085–1099, May 1976.
- [44] M. T. C. Fang, S. Ramakrishnan, and H. K. Messerle, "Scaling Laws for Gas-Blast Circuit-Breaker Arcs during the High Current Phase," *IEEE Trans. Plasma Sci.*, vol. 8, no. 4, pp. 357–362, Dec. 1980.
- [45] M. T. C. Fang and D. Brannen, "A Current-Zero Arc Model Based on Forced Convection," *IEEE Trans. Plasma Sci.*, vol. 7, no. 4, pp. 217–229, 1979.
- [46] R. W. Liebermann and J. J. Lowke, "Radiation emission coefficients for sulfur hexafluoride arc plasmas," *J. Quant. Spectrosc. Radiat. Transf.*, vol. 16, no. 3, pp. 253–264, Mar. 1976.
- [47] W. Hermann and K. Ragaller, "Theoretical description of the current interruption in hv gas blast breakers," *IEEE Trans. Power Appar. Syst.*, vol. 96, no. 5, pp. 1546–1555, Sep. 1977.
- [48] K. Ragaller, W. Egli, and K. P. Brand, "Dielectric recovery of an axially blown SF₆-Arc after current zero: part II-theoretical investigations," *IEEE Trans. Plasma Sci.*, vol. 10, no. 3, pp. 154–162, Sep. 1982.
- [49] E. Schade and K. Ragaller, "Dielectric recovery of an axially blown SF₆-Arc after current zero: part I-experimental investigations," *IEEE Trans. Plasma Sci.*, vol. 10, no. 3, pp. 141–153, Sep. 1982.
- [50] R. R. Mitchell, D. T. Tuma, and J. F. Osterle, "Transient Two-Dimensional Calculations of Properties of Forced Convection-Stabilized Electric Arcs," *IEEE Trans. Plasma Sci.*, vol. 13, no. 4, pp. 207–220, 1985.
- [51] J. J. Lowke and H. E. Lee, "A numerical study of a two dimensional circuit breaker arc during current interruption," in *8th International Conference on Gas Discharges and Their Applications*, 1985, pp. 54–56.
- [52] J. F. Zhang, M. T. C. Fang, and D. B. Newland, "Theoretical investigation of a 2 kA DC nitrogen arc in a supersonic nozzle," *J. Phys. D. Appl. Phys.*, vol. 20, no. 3, pp. 368–379, Mar. 1987.
- [53] J. D. Yan, M. T. C. Fang, and W. Hall, "The development of PC based CAD tools for auto-expansion circuit breaker design," *IEEE Trans. Power Deliv.*, vol. 14, no. 1, pp. 176–181, 1999.
- [54] J.L. Zhang, J.D. Yan, A. B. Murphy, W. Hall, and M. T. C. Fang, "Computational investigation of arc behavior in an auto-expansion circuit

breaker contaminated by ablated nozzle vapor,” *IEEE Trans. Plasma Sci.*, vol. 30, no. 2, pp. 706–719, Apr. 2002.

- [55] J. L. Zhang, J. D. Yan, and M. T. C. Fang, “Electrode Evaporation and Its Effects on Thermal Arc Behavior,” *IEEE Trans. Plasma Sci.*, vol. 32, no. 3, pp. 1352–1361, Jun. 2004.

Chapter 2

Thermodynamic Properties and Transport Coefficients of Pure Copper Plasma

2.1 Introduction

The development of smart grid especially for intelligent apparatuses is still at its earlier stage, attracting much concerns and interests from industrial applications and academic research. As an important apparatus in the grid system, the operation performance of high voltage circuit breakers becomes to a critical issue which would be influenced by different aspects such as driving mechanism, solid structure design and arc behaviour. With the development of “intelligent circuit breaker”, the knowledge on the interactions between the arc plasma and hardware components, e.g. contacts and nozzle(s), becomes essential in configuring the operational characteristics (e.g. relative travel of contacts and cylinder/piston, and valve operation) of high voltage circuit breakers in respond to the particular type of the network fault.

Numerical modelling of the thermal arc plasma as a fundamental knowledge has gained a significant progress to systematically predict the high intensity arc characteristics and its influence on the high voltage circuit breakers interruptions. Accurate prediction of thermodynamic properties and transport coefficients of the working medium inside the arcing chamber is significant for the numerical modelling of the switching arc physical properties. Contact erosion and nozzle ablation have been the subjects of considerable interests for a long time when studies the arc behaviour in circuit breakers because the produced vapour injects into the arcing chamber and brings extra mass, momentum and energy into the arcing space. It changes the chemical composition and thermophysical properties of the gaseous medium. Unfortunately, the transport coefficients are difficult to calculate because of the large uncertainties of intermolecular potentials that are used to quantitatively determine the collision cross sections between the existed particles.

To simplify the calculation, the arc plasma is assumed in LCE and LTE states. However, the assumption of LTE is no longer valid when steep temperature gradient exists. When

the arc plasma interacts with cold contacts, or when the cold gas flow rushed into the arcing space at the moment of the AC current passing its final zero, the temperature of electrons may differ with heavy particles and it leads to a deviation of the equilibrium state of the plasma. For instance, when a hot arc column interacts with a cold cathode, a thin non-LTE layer is presented in front of the cathode. Such layer is characterized by the steep gradient, e.g. temperature, potential and number density of particles, which is resulted from insufficient collisions between electrons and heavy particles [1].

In the present work, to approximate the erosion on copper contact when interrupts high currents, the non-LTE layer is assumed to be filled with pure copper vapour produced from the contact surface because of severe arcing. A mathematical model is built with the consideration of this non-LTE layer to systematically analyse the contact erosion. To set up the model accurately, the two-temperature model with the assumption of LCE is applied for the determination of thermodynamic properties and transport coefficients of the non-equilibrium arc plasma in front of the cold contact.

2.2 Determination of the species composition of pure copper plasma

2.2.1 Theory of chemical equilibrium

Theoretically, particles number densities are crucial in determining the thermodynamic properties and transport coefficients of the arc plasma. Based on the statistical theory, the chemical equilibrium is mainly described by the minimization or maximization of a defined “thermodynamic potential”, e.g. internal energy U , Helmholtz’s free energy F , Gibbs’ free energy G , and Enthalpy H [2]. In the present work, chemical composition is determined with independent variables pressure P and temperature T by applying the minimization of Gibbs’ free energy G . The Gibbs free energy of the system is given by:

$$G = \sum_{w=1}^{w_{total}} n_w \mu_w \quad (2.2.1)$$

where w_{total} is the total number of considered species; n_w and u_w are number density and chemical potential of species “w”. The chemical potential can be determined by [3]:

$$\mu_w = \mu_w^0 + RT \ln \left(\frac{P}{P_0} \right) + RT \ln \left(\frac{n_w}{\sum_{w=1}^{w_{max}^g} n_w} \right) \quad (2.2.2)$$

where μ_w^0 is the chemical potential in standard state; P_0 is the reference pressure; R is the gas constant ($8.314 \text{ J}/(\text{mol} \cdot \text{K})$) and w_{max}^g is the total number of gaseous plasma species.

The thermodynamic properties and transport coefficients could be determined if the chemical compositions of the system are known. To determine the Gibbs free energy of the system, the chemical potentials associated with number densities are calculated by determining the partition function which is defined to describe statistical properties of thermodynamic equilibrium system. It is expressed as [4]:

$$Q = Q_{int}Q_t = Q_eQ_vQ_rQ_t \quad (2.2.3)$$

where Q_{int} , Q_e , Q_v , Q_r and Q_t represent the internal, electronic, vibrational, rotational and translational contributions to the partition function.

(1) Translation partition function

$$Q_t = \left(\frac{2\pi m k_B T}{h^2} \right)^{\frac{3}{2}} \quad (2.2.4)$$

where h is the Planck constant ($6.63 \times 10^{-34} \text{ J} \cdot \text{s}$).

(2) Electronic partition function

$$Q_e = \sum_e^{\varepsilon_n < E_{ieff}} g_e \exp\left(-\frac{\varepsilon_n}{k_B T_e}\right) \quad (2.2.5)$$

where ε_n is the electronic excitation energy of state n ; E_{ieff} is the effective ionization energy; g_e is the statistical weight; T_e is the temperature of electrons which equals to the heavy particles temperature T_h in LTE conditions. It should be mentioned that the excited levels of the monatomic particles are mostly populated by electrons collisions so that the species electronic partition function for the non-LTE cases is expressed as a function of T_e only. In addition, the internal partition function of the monatomic species only considers the electronic contribution [5], [6]. However, a critical problem is posed about how many excitation energy levels need to be included in the calculation. From literature review, an infinite number of the bound states exist below the ionization limit for a hypothetical isolated atom [7]. Therefore, the excited energy levels considered in the calculation should be cutoff based on the reliable criterions.

In the calculation, the electronic partition function of monatomic species is determined by two summations. In the first summation, tabulated values of the electronic energies and corresponded statistical weights are taken from the NIST website [8]. In the second summation, the energy terms of configurations characterized by high values of principal quantum number follows the hydrogenic approximation and the statistical weights are determined from the corresponded isoelectronic sequences. In reality, the ground state is considered as the only contributor in low temperatures when calculates the electronic partition function because the smaller exponential terms could be neglected. Otherwise, all the energy levels up to the cutoff should be included by treating the quantum number of levels “missing” in higher electrons orbital as “hydrogenic” [9]–[11]. In 1964, Griem introduced a formula to predict the contributions of the “missing” levels on electronic partition function [9]:

$$Q_{Z-1}(T_e) \approx \sum_{p=1}^{p'} g_{Z-1}(p) \exp \left[-\frac{E_{Z-1}(p)}{k_B T_e} \right] + (2S_1 + 1)(2L_1 + 1) \cdot \sum_{p'+1}^{p_{max}} 2p^2 \exp \left[-\frac{E_{Z-1}(\infty) - \Delta E_{Z-1}(\infty)}{k_B T_e} \right] \quad (2.2.6)$$

where p , S_1 and L_1 represent the principle, spin angular momentum and orbital angular momentum quantum numbers; Z is the species charge and maximum principal quantum number for species with charge $Z-1$ is given by:

$$p_{max} \leq \left(\frac{Z^2 E_H}{\Delta E_{Z-1}(\infty)} \right)^{\frac{1}{2}} \quad (2.2.7)$$

Rewrites Eq. (2.2.6),

$$Q_{Z-1}(T_e) \approx \sum_{p=1}^{p'} g_{Z-1}(p) \exp \left[-\frac{E_{Z-1}(p)}{k_B T_e} \right] + \frac{2}{3} (2S_1 + 1)(2L_1 + 1) \cdot \left(\frac{Z^2 E_H}{\Delta E_{Z-1}(\infty)} \right)^{\frac{3}{2}} \exp \left[-\frac{E_{Z-1}(\infty) - \Delta E_{Z-1}(\infty)}{k_B T_e} \right] \quad (2.2.8)$$

where E_H is the ionization energy of hydrogen (13.6 eV) and $\Delta E_{Z-1}(\infty)$ is the lowering of ionization energy.

For diatomic species, vibrational and rotational contributions to the internal partition function are also included. K.S.Drellishak proposed the Morse Potential Minimization

Method to determine the internal partition functions for the diatomic species expressed as [12],

$$Q_{int} = \frac{1}{\sigma_c} \sum_n g_n \exp\left(-\frac{\varepsilon_{el}}{k_B T_e}\right) \sum_n^{v_{max}} \exp\left(-\frac{\varepsilon_{vib}(n,v)}{k_B T_h}\right) \sum_J^{J_{max}} (2J + 1) \exp\left(-\frac{\varepsilon_{rot}(n,J,v)}{k_B T_h}\right) \quad (2.2.9)$$

where σ_c is a symmetry number that equals 1 for heteronuclear and 2 for homonuclear molecules; ε_{el} , ε_{vib} , ε_{rot} are the energies corresponded to the electronic, vibrational and rotational states; g_n is the statistical weight of n^{th} energy level; n, v, J are respectively the quantum number of electronic, vibrational and rotational energy levels; v_{max} and J_{max} are the maximum quantum numbers of the vibrational and rotational energy levels. Vibrational energy of v^{th} vibrational state and rotational energy of J^{th} rotational state are then determined by [12]–[15]:

$$\frac{\varepsilon_{vib}(n, v)}{hc} = \omega_e \left(v + \frac{1}{2}\right) - \omega_e x_e \left(v + \frac{1}{2}\right)^2 + \omega_e y_e \left(v + \frac{1}{2}\right)^3 + \omega_e z_e \left(v + \frac{1}{2}\right)^4 \quad (2.2.10)$$

$$\frac{\varepsilon_{rot}(n, v, J)}{hc} = B_v J(J + 1) - D_v [J(J + 1)]^2 + H_v [J(J + 1)]^3 \quad (2.2.11)$$

where $\omega_e x_e$, $\omega_e y_e$ and $\omega_e z_e$ are the spectroscopically determined constants relating to each electronic state of the molecule, which are the first, second and third anharmonic corrections to the vibrational spacing; ω_e is the harmonic oscillator vibrational spacing; B_v is the rigid rotator rotational spacing; D_v and H_v are the first and second anharmonic corrections to the rotational spacing. These parameters could be determined by [12]:

$$B_v = B_e - \alpha_e \left(v + \frac{1}{2}\right) \quad (2.2.12)$$

$$D_v = D_e - \beta_e \left(v + \frac{1}{2}\right) \quad (2.2.13)$$

$$B_e = \frac{h^2}{8\pi^2 \mu r_e^2 c} \quad (2.2.14)$$

$$D_e = \frac{4B_e^3}{\omega_e^2} \quad (2.2.15)$$

where B_e is the rigid rotator rotational spacing; α_e is the nonrigid rotator correction to B_e ; D_e is the anharmonic correction to the rotational spacing; β_e is the first anharmonic

correction; μ is the reduced molecular mass; γ_e is the second anharmonic correction and r_e is the equilibrium internuclear distance (Bond length: pm).

In comparison with the monatomic and diatomic molecules, the calculation of internal partition function of polyatomic species is more complicated. With the consideration of the harmonic oscillator approximation, determination of this internal partition function could be simplified with the form:

$$Q_{int} = \sum_n g_n \exp\left(-\frac{\varepsilon_{el}}{kT_e}\right) \prod_j \left[\frac{\exp\left(-\frac{\omega_j}{2kT_h}\right)}{1 - \exp\left(-\frac{\omega_j}{kT_h}\right)} \right]^{g_j} \left(\frac{T_h}{\theta_{rot}}\right)^{3/2} \quad (2.2.16)$$

where Q_{int} is the internal partition function; ω_j is the fundamental vibration frequency; g_j is the statistical weight of vibration and θ_{rot} is the rotational constant.

$$\left(\frac{T_h}{\theta_{rot}}\right)^{3/2} = \frac{\pi^{1/2}}{\sigma_c h^3} (I_A I_B I_C)^{1/2} (8kT_h)^{3/2} \quad (2.2.17)$$

where I_A , I_B and I_C are the three principal moments of inertia. In the calculation, all the numerical values of associated variables are tabulated in the JANAF tables [16].

2.2.2 Calculation of chemical composition

To determine the chemical composition of the pure copper plasma, it is assumed that only the gaseous species are considered: e, Cu, Cu⁺, Cu²⁺, Cu³⁺ and Cu⁴⁺. The ionization energy of the copper atom is listed in Table 2.1 [8]. For the pure copper plasma with the considered temperature and pressure range from 300K to 30,000K and 0.1MPa to 1MPa, the following independent ionization reactions are considered:

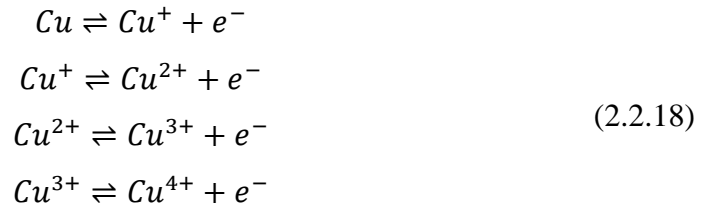


Table 2.1 The ionization energy of copper.

Copper	1 st	2 nd	3 rd	4 th	5 th	6 th
Ionization Energy (eV)	7.726	20.292	36.845	57.377	79.805	102.606

The chemical composition could be determined by solving a set of equations, i.e. Saha equation and a pressure equation following the Dalton's law with assuming the plasma satisfies the electrical neutrality.

For the equilibrium plasma, the Saha equations are written as:

$$\frac{n_e n_{Cu^+}}{n_{Cu}} = 2 \left(\frac{Q_{Cu^+}(T)}{Q_{Cu}(T)} \right) \left(\frac{2\pi m_e k_B T}{h^2} \right)^{\frac{3}{2}} \exp\left(-\frac{E_{i,Cu} - \Delta E_{(0)}}{kT}\right) \quad (2.2.19)$$

$$\frac{n_e n_{Cu^{2+}}}{n_{Cu^+}} = 2 \left(\frac{Q_{Cu^{2+}}(T)}{Q_{Cu^+}(T)} \right) \left(\frac{2\pi m_e k_B T}{h^2} \right)^{\frac{3}{2}} \exp\left(-\frac{E_{i,Cu^+} - \Delta E_{(1)}}{kT}\right) \quad (2.2.20)$$

$$\frac{n_e n_{Cu^{3+}}}{n_{Cu^{2+}}} = 2 \left(\frac{Q_{Cu^{3+}}(T)}{Q_{Cu^{2+}}(T)} \right) \left(\frac{2\pi m_e k_B T}{h^2} \right)^{\frac{3}{2}} \exp\left(-\frac{E_{i,Cu^{2+}} - \Delta E_{(2)}}{kT}\right) \quad (2.2.21)$$

$$\frac{n_e n_{Cu^{4+}}}{n_{Cu^{3+}}} = 2 \left(\frac{Q_{Cu^{4+}}(T)}{Q_{Cu^{3+}}(T)} \right) \left(\frac{2\pi m_e k_B T}{h^2} \right)^{\frac{3}{2}} \exp\left(-\frac{E_{i,Cu^{3+}} - \Delta E_{(3)}}{kT}\right) \quad (2.2.22)$$

where n and Q with subscripts e , Cu , Cu^+ , Cu^{2+} , Cu^{3+} and Cu^{4+} are respectively number densities and internal partition functions of electrons, copper atoms, singly-charged, doubly-charged, triply-charged and quadruply-charged copper ions. m_e is the electron mass (9.11×10^{-31} kg); E_i is the corresponded ionization energy of different particles and ΔE is the lowering of ionization energy which is obtained by Gleizes et al [17].

$$\Delta E_{(Z)} = (Z + 1) \frac{1}{4\pi\epsilon_0} \frac{e^2}{\lambda_D} \quad (2.2.23)$$

where Z is the charge number and ϵ_0 is the electric permittivity in vacuum that equal to 8.85×10^{-12} F/m. λ_D is the Debye length which is explained in following contents.

Nevertheless, a two-temperature (2T) model need to be adopted for the non-equilibrium copper plasma since the electrons and heavy particles are regarded as two fluids with different temperatures (T_e and T_h) when the plasma is deviated from the LTE state. The form of 2T Saha equations that adopted in the present study is obtained following the method of Van de Sanden *et al.* [17]:

$$n_e \frac{n_{Cu^+}}{n_{Cu}} = 2 \left(\frac{Q_{Cu^+}(T_e)}{Q_{Cu}(T_e)} \right) \left(\frac{2\pi m_e k_B T_e}{h^2} \right)^{\frac{3}{2}} \exp\left(-\frac{E_{i,Cu} - \Delta E_{(0)}}{kT_{ex}}\right) \quad (2.2.24)$$

$$n_e \frac{n_{Cu^{2+}}}{n_{Cu^+}} = 2 \left(\frac{Q_{Cu^{2+}}(T_e)}{Q_{Cu^+}(T_e)} \right) \left(\frac{2\pi m_e k_B T_e}{h^2} \right)^{\frac{3}{2}} \exp\left(-\frac{E_{i,Cu^+} - \Delta E_{(1)}}{kT_{ex}}\right) \quad (2.2.25)$$

$$n_e \frac{n_{Cu^{3+}}}{n_{Cu^{2+}}} = 2 \left(\frac{Q_{Cu^{3+}}(T_e)}{Q_{Cu^{2+}}(T_e)} \right) \left(\frac{2\pi m_e k_B T_e}{h^2} \right)^{\frac{3}{2}} \exp\left(-\frac{E_{i,Cu^{2+}} - \Delta E_{(2)}}{kT_{ex}}\right) \quad (2.2.26)$$

$$n_e \frac{n_{Cu^{4+}}}{n_{Cu^{3+}}} = 2 \left(\frac{Q_{Cu^{4+}}(T_e)}{Q_{Cu^{3+}}(T_e)} \right) \left(\frac{2\pi m_e k_B T_e}{h^2} \right)^{\frac{3}{2}} \exp\left(-\frac{E_{i,Cu^{3+}} - \Delta E_{(3)}}{kT_{ex}}\right) \quad (2.2.27)$$

where T_{ex} is an effective excitation temperature depends on the elastic collisions. Based on the work of Van de Sanden *et al*, this excitation temperature T_{ex} for atomic ionization reaction is assumed to be T_e [17]. In the calculation, the temperature ratio between T_e and T_h that describes the non-equilibrium degree is defined as θ_T .

Dalton's law is applied to describe the system total pressure which equals to the sum of partial pressure of each species and the total pressure of LTE and non-LTE plasmas are respectively determined by:

$$P = \sum_{w=1}^{w_{total}} n_w k_B T \quad (2.2.28)$$

$$P = k_B T_e n_e + \sum_{\substack{w=1 \\ w \neq e}}^{w_{total}-1} k_B T_h n_w \quad (2.2.29)$$

where n_w is the number density of species “w”; summation term in Eq.(2.2.29) is the total pressure of heavy particles. With considering the effects of electrostatic interaction between charged particles, the pressure correction term (Debye-Hückel correction) ΔP should be considered as well [18], [19], with forms:

$$P + \Delta P = P + \frac{k_B T}{24\pi\lambda_D^3} = \sum_{w=1}^{w_{total}} n_w k_B T \quad (2.2.30)$$

$$P + \Delta P = P + \frac{\sum_{w=1}^{w_{total}-1} Z_w^2 n_w}{24\pi\epsilon_0\lambda_D} = \sum_{\substack{w=1 \\ w \neq e}}^{w_{total}-1} k_B T_h n_w + k_B T_e n_e \quad (2.2.31)$$

where Z_w is the charge number of species “w”. In addition, the plasma is assumed to be the quasi-neutrality and the number density of electron equals to the sum of ions number densities weighted by their corresponded charges.

$$n_e = \sum_w^{w_{total}-1} Z_w n_w \quad (2.2.32)$$

$$n_e = 1n_{Cu^+} + 2n_{Cu^{2+}} + 3n_{Cu^{3+}} + 4n_{Cu^{4+}} \quad (2.2.33)$$

2.3 Determination of thermophysical properties

2.3.1 Determination of thermodynamic properties

The thermodynamic properties are computed if the chemical composition of the plasma is determined. Representative properties are introduced below.

(1) Mass density

$$\rho = \sum_{w=1}^{w_{total}} m_w n_w \quad (2.3.1)$$

where m_w and n_w are the mass (kg) and number density (m^{-3}) of species “w”.

(2) Specific enthalpy

The enthalpy is calculated based on the law of statistical thermodynamics [20]–[22]:

$$H = k_B T \sum_{w=1}^{w_{total}} N_w \left(\frac{d \ln Q_w}{d \ln T} \right)_{P, N_w} + \sum_{w=1}^{w_{total}} N_w \varepsilon_w \quad (2.3.2)$$

where N_w is the number density per kilogram of species w; ε_w is a reference energy of species “w” that defined in JANAF tables [23] and Q_w is the partition function.

$$N_w = \frac{n_w}{\rho} \quad (2.3.3)$$

$$Q_w = Q_{int,w} \frac{N_w k_B T}{P} \left(\frac{2\pi m_w k_B T}{h^2} \right)^{\frac{3}{2}} \quad (2.3.4)$$

where $Q_{int,w}$ is the internal partition function of species “w”; The specific enthalpy that commonly used in the calculation is expressed as $h_s = H/m$ (J/Kg) and m is the mass of the system. For non-LTE plasma, the reactional, translational and internal contributions to the specific enthalpy as a result of electrons excitation are considered [24]. Specific enthalpies of the electrons, monatomic and molecular species are given by [3]:

$$h_e = \frac{5}{2} \frac{k_B}{\rho} n_e T_e \quad (2.3.5)$$

$$h_{w,monatomic} = \frac{5}{2} \frac{k_B}{\rho} n_w T_h + \frac{1}{\rho} n_w E_w + \frac{k_B}{\rho} n_w \left(T_e^2 \frac{\partial \ln Q_w^{el}}{\partial T_e} \right) \quad (2.3.6)$$

$$h_{w,molecular} = \frac{5}{2} \frac{k_B}{\rho} n_w T_h + \frac{1}{\rho} n_w E_w + \frac{k_B}{\rho} n_w \left(T_e^2 \frac{\partial \ln Q_w^{el}}{\partial T_e} + T_h^2 \frac{\partial \ln(Q_w^{rot} Q_w^{vib})}{\partial T_h} \right) \quad (2.3.7)$$

2.3.2 Determination of transport coefficients

The transport coefficients are determined using the classical Chapman-Enskog method [25]. Relevant formulas are derived from the Boltzmann nonlinear integro-differential equation with assuming the velocity distribution of the particles following the Maxwell-Boltzmann distribution in the thermodynamic equilibrium system. These equations are resolved using the perturbation techniques described by Chapman and Enskog [20] and they are expressed with the consideration of Sonine Polynomial approximations. Based on this method, the transport coefficients are derived as a function of particles number densities and collision cross-sections between interacted particles which are calculated by intermolecular potentials. The collision cross section, that describes the interactions between two colliding particles, could be indirectly calculated by the defined collision integral which is associated with appropriate values of l and s [26]:

$$\Omega_{ij}^{(l,s)}(T) = \sqrt{\frac{k_B T}{2\pi m_{ij}^*}} \int_0^\infty e^{-\gamma^2} \gamma^{2s+3} Q_{ij}^l(\varepsilon_r) d\gamma \quad (2.3.8)$$

where γ is defined correlated to the relative velocity g_{ij} ; m_{ij}^* is the reduced mass of two colliding species; ε_r is the kinetic energy. They are calculated by:

$$\gamma^2 = \frac{m_{ij}^* (g_{ij}^*)^2}{2kT_{ij}^*} \quad (2.3.9)$$

$$m_{ij}^* = \frac{m_i m_j}{m_i + m_j} \quad (2.3.10)$$

$$\varepsilon_r = \frac{1}{2} m_{ij}^* g_{ij}^2 \quad (2.3.11)$$

and $Q_{ij}^l(\varepsilon_r)$ is the transport cross section (\AA^2), determined by:

$$\begin{aligned} Q^l(\varepsilon_r) &= 2\pi \int_0^\pi \sigma(\varepsilon_r, \chi) (1 - \cos^l \chi) \sin \chi d\chi \\ &= 2\pi \int_0^\infty (1 - \cos^l \chi) b db \end{aligned} \quad (2.3.12)$$

where b is the impact parameter and χ is the deflection angle of molecules in the centre of gravity coordinate system.

$$\chi = \pi - 2b \int_0^\infty \frac{dr}{r^2 \sqrt{1 - \frac{2\varphi(r)}{m_{ij}^* g_{ij}^2} - \frac{b^2}{r^2}}} \quad (2.3.13)$$

The indices l and s are determined according to the approximation orders used in the calculation (l :1-2 and s :1-5 in the present work). The transport coefficients is calculated by considering the binary collisions between particles so that the corresponded collision cross sections (also recognised as the ‘‘average collision integrals’’) could be determined using the following relationships with the known collision integrals [26]:

$$\begin{aligned}\bar{Q}_{ij}^{(l,s)}(T_{ij}^*) &= \frac{4(l+1)}{(s+1)! [2l+1 - (-1)^l]} \int_0^\infty e^{-\gamma^2} \gamma^{2s+3} Q_{ij}^l(\varepsilon_r) d\gamma \\ &= \frac{4(l+1)\Omega_{ij}^{(l,s)}(T_{ij}^*)}{(s+1)! [2l+1 - (-1)^l] \sqrt{\frac{k_B T_{ij}^*}{2\pi m_{ij}}}}\end{aligned}\quad (2.3.14)$$

and for the 2T plasma in non-LTE state, the reduced temperature T_{ij}^* is used to compute the associated collision integrals and cross sections, expressed as:

$$T_{ij}^* = \frac{m_i T_j + m_j T_i}{m_i + m_j} \quad (2.3.15)$$

2.3.2.1 Diffusion coefficients

In the calculation, the ordinary diffusion coefficient, thermal diffusion coefficient and binary diffusion coefficient involving particles i and j are determined by [20], [27]:

$$D_{ij}(\xi) = \frac{\rho n_i}{2nm_j} \sqrt{\frac{2k_B T}{m_i}} C_{i0}^{(j,i)}(\xi) \quad (2.3.16)$$

$$D_i^T(\xi) = \frac{n_i m_i}{2} \sqrt{\frac{2k_B T}{m_i}} a_{i0}(\xi) \quad (2.3.17)$$

$$D_{ij}^b = \frac{3}{16n} \sqrt{\frac{2\pi k_B T}{m_{ij}^*}} \frac{1}{\bar{Q}_{ij}^{(1,1)}} \quad (2.3.18)$$

where n is the total number density and ξ is the number of terms in Sonine expansions.

The values of $C_{i0}^{(j,i)}(\xi)$ and $a_{i0}(\xi)$ are determined from [28]:

$$\sum_{j=1}^v \sum_{p=0}^M q_{ij}^{mp} a_{jp} = -\frac{15\pi^2 n_i}{2} \delta_{m1} \quad (2.3.19)$$

$$\sum_{j=1}^v \sum_{p=0}^M q_{ij}^{mp} C_{jp}^{hk} = 3\pi^2 (\delta_{ik} - \delta_{ih}) \delta_{m0} \quad (2.3.20)$$

where “ i ” ranges from 1 to w and m ranges from 1 to M ; M is the number of terms used in the Sonine expansions; q_{ij}^{mp} is the coefficients related to the set of collision integrals.

To ensure a higher accuracy, ordinary and thermal diffusion coefficients are determined with the second approximation, expressed as [28]:

$$[D_{ij}]_2 = \frac{3\rho n_i}{2nm_j} \sqrt{\frac{2\pi k_B T}{m_i}} \frac{1}{|q_1|} \quad (2.3.21)$$

$$[D_i^T]_2 = \frac{15n_i}{4} \sqrt{2\pi m_i k_B T} \frac{1}{|q_2|} \quad (2.3.22)$$

where q_1 and q_2 are two determinants expressed using a set of collision integrals from q_{ij}^{mp} ,

$$|q_1| = \begin{vmatrix} q_{hk}^{00} & q_{hk}^{01} & \delta_{hj} - \delta_{hi} \\ q_{hk}^{10} & q_{hk}^{11} & 0 \\ \delta_{ki} & 0 & 0 \end{vmatrix} \quad (2.3.23)$$

$$|q_2| = \begin{vmatrix} q_{hk}^{00} & q_{hk}^{01} & 0 \\ q_{hk}^{10} & q_{hk}^{11} & n_h \\ \delta_{ki} & 0 & 0 \end{vmatrix} \quad (2.3.24)$$

Nevertheless, calculation of the diffusion coefficients of the non-equilibrium plasma is complicated. For a two-temperature (2T) non-thermal plasma, the electrons and heavy particles are regarded as two separated fluids. The electrons with smaller mass move faster than the heavy particles. Due to the insufficient collisions between electrons and heavy particles, the corresponded temperature of electrons would be relatively higher than heavy particles. The binary diffusion coefficient of the 2T plasma is thus calculated using the expression derived by Ramshaw [29], [30]:

$$D_{ij}^b = \frac{3k_B^2 T_i T_j}{16P m_{ij}^* T_{ij}^* \Omega_{ij}^{(1,1)}} \quad (2.3.25)$$

and the ordinary coefficient is obtained based on the work from Hirschfelder *et al.*, [20]:

$$D_{ij} = \frac{F^{ji} - F^{ii}}{m_j |F|} \quad (2.3.26)$$

$$F_{ij} = \frac{1}{\rho} \left(\frac{n_i}{D_{ij}^b} + \sum_{l \neq i} \frac{n_l m_j}{m_i D_{il}^b} \right) (1 - \delta_{ij}) \quad (2.3.27)$$

where F^{ji} is the cofactor of F_{ij} which is defined in terms of D_{ij}^b , written as:

$$F_{ij} = \frac{1}{\rho} \left[\frac{n_i}{D_{ij}^b} + \sum_{l \neq i} \frac{n_l m_j}{m_i D_{il}^b} \right] (1 - \delta_{ij}) \quad (2.3.28)$$

where δ_{ij} is the Dirac delta function:

$$\delta_{ij} = \begin{cases} 1 & i = j \\ 0 & i \neq j \end{cases} \quad (2.3.29)$$

The ambipolar diffusion is calculated by means of ordinary diffusion coefficient [31]:

$$D_{ij}^a = D_{ij} + \frac{\alpha_i}{\beta} \sum_s Z_s D_{sj} \quad (2.3.30)$$

$$\alpha_i = \sum_j \frac{m_j n_j Z_j D_{ij}}{T_j} \quad (2.3.31)$$

$$\beta = - \sum_i Z_i \sum_j \frac{m_j n_j Z_j D_{ij}}{T_j} \quad (2.3.32)$$

where Z_j is the charge number of species “ j ”.

The thermal diffusion coefficient of electrons is defined with the third approximation [20], [32]:

$$D_e^T = \frac{15n_e^2 \sqrt{2\pi m_e k_B T_e}}{4} \begin{vmatrix} q^{01} & q^{02} \\ q^{21} & q^{22} \end{vmatrix} \left(\begin{vmatrix} q^{00} & q^{01} & q^{02} \\ q^{10} & q^{11} & q^{12} \\ q^{20} & q^{21} & q^{22} \end{vmatrix} \right)^{-1} \quad (2.3.33)$$

where elements q^{mp} in the determinants are calculated from the collision cross sections $\bar{Q}_{ij}^{(l,s)}$ of interactions between the particles [33]. In the present work, “1” represents the electrons ($i=1$) and “2, 3, 4, 5, 6” represent the heavy particles Cu, Cu⁺, Cu²⁺, Cu³⁺ and Cu⁴⁺ respectively ($j=2, 3, 4, 5, 6$). The maximum number of “ l ” is 2 and “ s ” is 5 for the third approximation.

$$q^{00} = 8 \sum_j n_1 n_j \bar{Q}_{1j}^{(1,1)} \quad (2.3.34)$$

$$q^{10} = q^{01} = 8 \sum_j n_1 n_j \left[\frac{5}{2} \bar{Q}_{1j}^{(1,1)} - 3 \bar{Q}_{1j}^{(1,2)} \right] \quad (2.3.35)$$

$$q^{11} = 8\sqrt{2} n_1^2 \bar{Q}_{11}^{(2,2)} + 8 \sum_j n_1 n_j \left[\frac{25}{4} \bar{Q}_{1j}^{(1,1)} - 15 \bar{Q}_{1j}^{(1,2)} + 12 \bar{Q}_{1j}^{(1,3)} \right] \quad (2.3.36)$$

$$q^{20} = q^{02} = 8 \sum_j n_1 n_j \left[\frac{35}{8} \bar{Q}_{1j}^{(1,1)} - \frac{21}{2} \bar{Q}_{1j}^{(1,2)} + 6 \bar{Q}_{1j}^{(1,3)} \right] \quad (2.3.37)$$

$$q^{21} = q^{12} = 8\sqrt{2}n_1^2 \left[\frac{7}{4} \bar{Q}_{11}^{(2,2)} - 2 \bar{Q}_{11}^{(2,3)} \right] + 8 \sum_j n_1 n_j \left[\frac{175}{16} \bar{Q}_{1j}^{(1,1)} - \frac{315}{8} \bar{Q}_{1j}^{(1,2)} + 57 \bar{Q}_{1j}^{(1,3)} - 30 \bar{Q}_{1j}^{(1,4)} \right] \quad (2.3.38)$$

$$q^{22} = 8\sqrt{2}n_1^2 \left[\frac{77}{16} \bar{Q}_{11}^{(2,2)} - 7 \bar{Q}_{11}^{(2,3)} + 5 \bar{Q}_{11}^{(2,4)} \right] + 8 \sum_j n_1 n_j \left[\frac{1225}{64} \bar{Q}_{1j}^{(1,1)} - \frac{735}{8} \bar{Q}_{1j}^{(1,2)} + \frac{399}{2} \bar{Q}_{1j}^{(1,3)} - 210 \bar{Q}_{1j}^{(1,4)} + 90 \bar{Q}_{1j}^{(1,5)} \right] \quad (2.3.39)$$

The thermal diffusion coefficient of the heavy particles is given by [28]:

$$D_i^T = \frac{15n_i \sqrt{2\pi m_i k_B T_h}}{4} \left(\begin{vmatrix} q_{ij}^{00} & q_{ij}^{01} \\ q_{ij}^{10} & q_{ij}^{11} \end{vmatrix} \right)^{-1} \begin{vmatrix} q_{ij}^{00} & q_{ij}^{01} & 0 \\ q_{ij}^{10} & q_{ij}^{11} & n_i \\ \delta_{ij} & 0 & 0 \end{vmatrix} \quad (2.3.40)$$

where the elements q_{ij}^{mp} in the determinants are calculated from collision cross sections $\bar{Q}_{ij}^{(l,s)}$.

$$q_{ij}^{00} = 8 \sum_{l=1}^v \frac{n_l m_l^{\frac{1}{2}}}{(m_i + m_l)^{\frac{1}{2}}} \bar{Q}_{il}^{(1,1)} \left[n_i \left(\frac{m_l}{m_j} \right)^{\frac{1}{2}} (\delta_{ij} - \delta_{jl}) - n_j \frac{(m_l m_j)^{\frac{1}{2}}}{m_i} (1 - \delta_{il}) \right] \quad (2.3.41)$$

$$q_{ij}^{01} = 8n_i \left(\frac{m_i}{m_j} \right)^{\frac{3}{2}} \sum_{l=1}^v \frac{n_l m_l^{\frac{3}{2}}}{(m_i + m_l)^{\frac{3}{2}}} \left[\frac{5}{2} \bar{Q}_{il}^{(1,1)} - 3 \bar{Q}_{il}^{(1,2)} \right] (\delta_{ij} - \delta_{jl}) \quad (2.3.42)$$

$$q_{ij}^{10} = \left(\frac{m_j}{m_i} \right) q_{ij}^{01} \quad (2.3.43)$$

$$q_{ij}^{11} = 8n_i \left(\frac{m_i}{m_j} \right)^{\frac{3}{2}} \sum_{l=1}^v \frac{n_l m_l^{\frac{1}{2}}}{(m_i + m_l)^{\frac{5}{2}}} \left\{ (\delta_{ij} - \delta_{jl}) \left[\frac{5}{4} (6m_j^2 + 5m_l^2) \bar{Q}_{il}^{(1,1)} - 15m_l^2 \bar{Q}_{il}^{(1,2)} + 12m_l^2 \bar{Q}_{il}^{(1,3)} \right] + (\delta_{ij} + \delta_{jl}) 4m_j m_l \bar{Q}_{il}^{(2,2)} \right\} \quad (2.3.44)$$

2.3.2.2 Thermal conductivity

The thermal conductivity is a summation of three components, i.e. translational (λ_{tr}), internal (λ_{int}) and reactive (λ_{reac}) thermal conductivities, expressed as:

$$\lambda = \lambda_{tr} + \lambda_{int} + \lambda_{reac} \quad (2.3.45)$$

For the LTE plasma, it could be calculated using the expression giving below [20]:

$$\lambda = \lambda' - \frac{k_B}{2n} \sum_{i,j} \frac{n_i n_j}{D_{ij}(1)} \left[\frac{D_i^T}{n_i m_i} - \frac{D_j^T}{n_j m_j} \right]^2 \quad (2.3.46)$$

and

$$\lambda'(\xi) = -\frac{5}{4} \sum_j n_j \sqrt{\frac{2k_B T}{m_j}} a_{j1}(\xi) \quad (2.3.47)$$

where $a_{j1}(\xi)$ is calculated using Eq.(2.3.19).

For the non-equilibrium plasma, contributions of electrons and heavy particles on the thermal conductivity should be both considered.

$$\lambda = \lambda_{tre} + \lambda_{trh} + \lambda_{int} + \lambda_{reac} \quad (2.3.48)$$

$$\lambda_{reac} = \lambda_{reac,e} + \theta_T \lambda_{reac,h} \quad (2.3.49)$$

where λ_{tre} and $\lambda_{reac,e}$ are the translational and reactive components of electrons; λ_{trh} and $\lambda_{reac,h}$ represent the corresponded components of heavy particles, and λ_{int} is the internal thermal conductivity of heavy particles;

The translational thermal conductivities of electrons and heavy particles are calculated with third and second approximations respectively [26]:

$$\lambda_{tre} = \frac{75n_e^2 k_B}{8} \sqrt{\frac{2\pi k_B T_e}{m_e}} \left(q^{11} - \frac{(q^{12})^2}{q^{22}} \right)^{-1} \quad (2.3.50)$$

$$\lambda_{trh} = -\frac{75k_B}{8} \frac{\sqrt{2\pi k_B T_h}}{|q|} \begin{vmatrix} q_{ij}^{00} & q_{ij}^{01} & 0 \\ q_{ij}^{10} & q_{ij}^{11} & n_i \\ 0 & \frac{n_j}{\sqrt{m_j}} & 0 \end{vmatrix} \quad (2.3.51)$$

According to the Hirschfelder-Eucken approximation, the internal thermal conductivity is resulted from the internal degrees of freedom of molecules, which means only heavy

particles contribute to the determination of the internal thermal conductivity [34], [35], which is calculated by:

$$\lambda_{int} = \sum_{i \neq e}^v x_i D_{ii}^b k_B (C_{pi}/R - 2.5) \left(\sum_{j \neq e}^v \frac{x_j D_{ii}^b}{x_i D_{ij}^b} \right)^{-1} \quad (2.3.52)$$

where $x_i = n_i / \sum_{i=1}^v n_i$; D_{ii}^b and C_{pi} represent molar fraction, self-diffusion coefficient and specific heat at constant pressure of species “ i ”.

The reactive thermal conductivity is related to the energy transport process as a result of particles diffusion [36], [37]. For the monatomic species, the energy transport (heat transfer) is determined by the ionization reactions. A total of 4 reactions with 6 particle species are involved in the present work. The changed enthalpy of l^{th} ionization reaction is:

$$\Delta h_l^* = \sum v_{ik} h_{products} - \sum v_{ik} h_{reactants} \quad (2.3.53)$$

where v_{ik} is the stoichiometric coefficient and h is the enthalpy. The enthalpy variation for pure copper plasma could be expressed as:

$$\Delta h_1^* = h_1^* + h_3^* - h_2^* \quad (2.3.54)$$

$$\Delta h_2^* = h_1^* + h_4^* - h_3^* \quad (2.3.55)$$

$$\Delta h_3^* = h_1^* + h_5^* - h_4^* \quad (2.3.56)$$

$$\Delta h_4^* = h_1^* + h_6^* - h_5^* \quad (2.3.57)$$

where h_i^* denotes the enthalpy of species i^{th} and the subscripts 1~6 have same meaning explained before.

$$h_1^* = \frac{5}{2} \frac{k_B}{\rho} k_B T_e \quad (2.3.58)$$

$$h_{i=2,3,4,5,6}^* = \frac{5}{2} \frac{k_B}{\rho} k_B T_h + \frac{1}{\rho} n_i E_i + \frac{k_B}{\rho} n_i T_e^2 \frac{\partial \ln Q_a^{int}}{\partial T_e} \quad (2.3.59)$$

Reactive thermal conductivities of electrons and heavy particles are determined using the method developed by Chen and Li [37] which is an extension of method proposed by Brokaw and Butlers [38], [39]:

$$\lambda_{re} = \sum_{r=1}^w \Delta h_r^* \frac{n}{\rho k_B T_h} \left(\sum_{j=1}^v m_j D_{rj}^a \frac{\partial p_j}{\partial T_e} + \frac{T_h}{T_e} m_e D_{re}^a \frac{\partial p_e}{\partial T_e} \right) \quad (2.3.60)$$

$$\lambda_{rh} = \sum_{r=1}^w \Delta h_r^* \frac{n}{\rho k_B T_h} \left(\sum_{j=1}^v m_j D_{rj}^a \frac{\partial p_j}{\partial T_h} + \frac{T_h}{T_e} m_e D_{re}^a \frac{\partial p_e}{\partial T_h} \right) \quad (2.3.61)$$

where w is the number of reactions.

The terms $\frac{\partial p_j}{\partial T_e}$, $\frac{\partial p_j}{\partial T_h}$, $\frac{\partial p_e}{\partial T_e}$, $\frac{\partial p_e}{\partial T_h}$ could be determined by the differential of partial pressure equations and Saha equations with respect to the independent variables T_e and T_h . The partial derivatives of partial pressures is derived based on Dalton's law Eq. (2.3.31):

$$\sum_{i=2}^v \frac{\partial p_i}{\partial T_e} + \frac{\partial p_e}{\partial T_e} = 0 \quad (2.3.62)$$

$$\sum_{i=2}^v \frac{\partial p_i}{\partial T_h} + \frac{\partial p_e}{\partial T_h} = 0 \quad (2.3.63)$$

The Saha equations associated with partial pressures are rewritten as:

$$\frac{p_e p_3}{p_2} = k_B T_e \left(2 \left(\frac{Q_{Cu^+}(T_e)}{Q_{Cu}(T_e)} \right) \left(\frac{2\pi m_e k_B T_e}{h^2} \right)^{\frac{3}{2}} \exp \left(-\frac{E_{i,Cu} - \Delta E_{(0)}}{k T_e} \right) \right) \quad (2.3.64)$$

$$\frac{p_e p_4}{p_3} = k_B T_e \left(2 \left(\frac{Q_{Cu^{2+}}(T_e)}{Q_{Cu^+}(T_e)} \right) \left(\frac{2\pi m_e k_B T_e}{h^3} \right)^{\frac{3}{2}} \exp \left(-\frac{E_{i,Cu^{2+}} - \Delta E_{(1)}}{k T_e} \right) \right) \quad (2.3.65)$$

$$\frac{p_e p_5}{p_4} = k_B T_e \left(2 \left(\frac{Q_{Cu^{3+}}(T_e)}{Q_{Cu^{2+}}(T_e)} \right) \left(\frac{2\pi m_e k_B T_e}{h^3} \right)^{\frac{3}{2}} \exp \left(-\frac{E_{i,Cu^{3+}} - \Delta E_{(2)}}{k T_e} \right) \right) \quad (2.3.66)$$

$$\frac{p_e p_6}{p_5} = k_B T_e \left(2 \left(\frac{Q_{Cu^{4+}}(T_e)}{Q_{Cu^{3+}}(T_e)} \right) \left(\frac{2\pi m_e k_B T_e}{h^3} \right)^{\frac{3}{2}} \exp \left(-\frac{E_{i,Cu^{4+}} - \Delta E_{(3)}}{k T_e} \right) \right) \quad (2.3.67)$$

where p_e , p_2 , p_3 , p_4 , p_5 and p_6 represent the partial pressure of each species. By taking the logarithms of these formulas (derived in Appendix A.1), two sets of linear equations for electrons and heavy particles are obtained:

$$AX_1 = B_1 \frac{\partial p_e}{\partial T_e} + B_2 \quad (2.3.68)$$

$$AX_2 = B_1 \frac{\partial p_e}{\partial T_h} \quad (2.3.69)$$

where

$$A = \begin{bmatrix} 1 & 1 & 1 & 1 & 1 \\ \frac{1}{p_2} & -\frac{1}{p_3} & 0 & 0 & 0 \\ 0 & \frac{1}{p_3} & -\frac{1}{p_4} & 0 & 0 \\ 0 & 0 & \frac{1}{p_4} & -\frac{1}{p_5} & 0 \\ 0 & 0 & 0 & \frac{1}{p_5} & -\frac{1}{p_6} \end{bmatrix} \quad (2.3.70)$$

$$X_1 = \left[\frac{\partial p_2}{\partial T_e} \quad \frac{\partial p_3}{\partial T_e} \quad \frac{\partial p_4}{\partial T_e} \quad \frac{\partial p_5}{\partial T_e} \quad \frac{\partial p_6}{\partial T_e} \right]^T \quad (2.3.71)$$

$$X_2 = \left[\frac{\partial p_2}{\partial T_h} \quad \frac{\partial p_3}{\partial T_h} \quad \frac{\partial p_4}{\partial T_h} \quad \frac{\partial p_5}{\partial T_h} \quad \frac{\partial p_6}{\partial T_h} \right]^T \quad (2.3.72)$$

$$B_1 = \left[-1 \quad \frac{1}{p_e} \quad \frac{1}{p_e} \quad \frac{1}{p_e} \quad \frac{1}{p_e} \right]^T \quad (2.3.73)$$

$$B_2 = [0 \quad -C_1 \quad -C_2 \quad -C_3 \quad -C_4]^T \quad (2.3.74)$$

and X_1 and X_2 are solved according to Cramer's rule.

The terms $\frac{\partial p_e}{\partial T_e}$ and $\frac{\partial p_e}{\partial T_h}$ are obtained from the partial pressure of electrons ($p_e = n_e k_B T_e$):

$$\frac{\partial p_e}{\partial T_e} = k_B T_e \frac{\partial n_e}{\partial T_e} + n_e k_B \quad (2.3.75)$$

$$\frac{\partial p_e}{\partial T_h} = k_B T_e \frac{\partial n_e}{\partial T_h} \quad (2.3.76)$$

$$n = n_e + n_{Cu} + n_{Cu^+} + n_{Cu^{2+}} + n_{Cu^{3+}} + n_{Cu^{4+}} \quad (2.3.77)$$

In Eq. (2.3.75) and (2.3.76), terms $\frac{\partial n_e}{\partial T_e}$ and $\frac{\partial n_e}{\partial T_h}$ are obtained by the partial differentiation equations of Eq.(2.2.33) and Eq.(2.3.77) with respect to T_e and T_h , given by:

$$\frac{\partial n_e}{\partial T_e} - \frac{\partial n_{Cu^+}}{\partial T_e} - 2 \frac{\partial n_{Cu^{2+}}}{\partial T_e} - 3 \frac{\partial n_{Cu^{3+}}}{\partial T_e} - 4 \frac{\partial n_{Cu^{4+}}}{\partial T_e} = 0 \quad (2.3.78)$$

$$\frac{\partial n_e}{\partial T_h} - \frac{\partial n_{Cu^+}}{\partial T_h} - 2 \frac{\partial n_{Cu^{2+}}}{\partial T_h} - 3 \frac{\partial n_{Cu^{3+}}}{\partial T_h} - 4 \frac{\partial n_{Cu^{4+}}}{\partial T_h} = 0 \quad (2.3.79)$$

$$\frac{\partial n_e}{\partial T_e} + \frac{\partial n_{Cu^+}}{\partial T_e} + \frac{\partial n_{Cu^{2+}}}{\partial T_e} + \frac{\partial n_{Cu^{3+}}}{\partial T_e} + \frac{\partial n_{Cu^{4+}}}{\partial T_e} = \frac{\partial n}{\partial T_e} \quad (2.3.80)$$

$$\frac{\partial n_e}{\partial T_h} + \frac{\partial n_{Cu^+}}{\partial T_h} + \frac{\partial n_{Cu^{2+}}}{\partial T_h} + \frac{\partial n_{Cu^{3+}}}{\partial T_h} + \frac{\partial n_{Cu^{4+}}}{\partial T_h} = \frac{\partial n}{\partial T_h} \quad (2.3.81)$$

$$\frac{\partial n}{\partial T_e} = -(\theta_T - 1) \frac{\partial n_e}{\partial T_e} - \frac{n_e}{T_h} \quad (2.3.82)$$

$$\frac{\partial n}{\partial T_h} = n \left(\frac{n_e}{n} - 1 \right) \frac{1}{T_h} - (\theta_T - 1) \frac{\partial n_e}{\partial T_e} \quad (2.3.83)$$

and taking the logarithms of these formulas as described in Appendix A.2, two sets of linear equations for electrons and heavy particles are obtained:

$$FY_1 = B_3 \quad (2.3.84)$$

$$FY_2 = B_4 \quad (2.3.85)$$

where

$$F = \begin{bmatrix} 1 & 1 & 1 & 1 & 1 & \theta_T \\ 0 & -1 & -2 & -3 & -4 & 1 \\ -\frac{1}{n_{Cu}} & \frac{1}{n_{Cu^+}} & 0 & 0 & 0 & \frac{1}{n_e} \\ 0 & -\frac{1}{n_{Cu^+}} & \frac{1}{n_{Cu^{2+}}} & 0 & 0 & \frac{1}{n_e} \\ 0 & 0 & -\frac{1}{n_{Cu^{2+}}} & \frac{1}{n_{Cu^{3+}}} & 0 & \frac{1}{n_e} \\ 0 & 0 & 0 & -\frac{1}{n_{Cu^{3+}}} & \frac{1}{n_{Cu^{4+}}} & \frac{1}{n_e} \end{bmatrix} \quad (2.3.86)$$

$$Y_1 = \left[\frac{\partial n_{Cu}}{\partial T_e} \quad \frac{\partial n_{Cu^+}}{\partial T_e} \quad \frac{\partial n_{Cu^{2+}}}{\partial T_e} \quad \frac{\partial n_{Cu^{3+}}}{\partial T_e} \quad \frac{\partial n_{Cu^{4+}}}{\partial T_e} \quad \frac{\partial n_e}{\partial T_e} \right]^T \quad (2.3.87)$$

$$Y_2 = \left[\frac{\partial n_{Cu}}{\partial T_h} \quad \frac{\partial n_{Cu^+}}{\partial T_h} \quad \frac{\partial n_{Cu^{2+}}}{\partial T_h} \quad \frac{\partial n_{Cu^{3+}}}{\partial T_h} \quad \frac{\partial n_{Cu^{4+}}}{\partial T_h} \quad \frac{\partial n_e}{\partial T_h} \right]^T \quad (2.3.88)$$

$$B_3 = \left[-\frac{n_e}{T_h} \quad 0 \quad D_1 \quad D_2 \quad D_3 \quad D_4 \right]^T \quad (2.3.89)$$

$$B_4 = \left[\frac{n \left(\frac{n_e}{n} - 1 \right)}{T_h} \quad 0 \quad 0 \quad 0 \quad 0 \quad 0 \right]^T \quad (2.3.90)$$

All the associated terms to determine the reactive thermal conductivity for pure copper plasma in this work are derived. The expressions for C and D are presented in Appendix A.1 and 2.

2.3.2.3 Electrical conductivity

For the LTE plasma, the electrical conductivity that represents the plasma conducting strength is given by:

$$\sigma = \frac{e^2 n}{\rho k_B T} \sum_{j \neq e, j=2}^v (n_j m_j Z_j D_{1j} - Z_j \sum_{i=1}^v n_i m_i Z_i D_{ji}) \quad (2.3.91)$$

and when neglecting the influences of ions, it could be simplified as:

$$\sigma \approx \frac{e^2 n}{\rho k_B T} \sum_{j \neq e, j=2}^v n_j m_j Z_j D_{1j} \quad (2.3.92)$$

For the non-equilibrium plasma, electrical conductivity only considers the contribution of electrons, which is computed using the third approximation and given by:

$$\sigma = \frac{3e^2 n_e^2}{2k_B T_e} \sqrt{\frac{2\pi k_B T_e}{m_e}} \begin{vmatrix} q^{11} & q^{12} \\ q^{21} & q^{22} \end{vmatrix} \left(\begin{vmatrix} q^{00} & q^{01} & q^{02} \\ q^{10} & q^{11} & q^{12} \\ q^{20} & q^{21} & q^{22} \end{vmatrix} \right)^{-1} \quad (2.3.93)$$

2.3.2.4 Viscosity

For the equilibrium plasma, the viscosity is calculated using the second approximation [28]:

$$\eta = \frac{1}{2} k_B T \sum_{i=1}^v n_i b_{i0} \quad (2.3.94)$$

where the coefficient b_{i0} is determined from:

$$\sum_{j=1}^v \sum_{p=0}^1 \tilde{q}_{ij}^{mp} b_{jp} = 5n_i \sqrt{\frac{2\pi m_i}{k_B T}} \delta_{m0} \quad (2.3.95)$$

while for the non-equilibrium plasma, the determination of the viscosity only considers the effects of heavy particles because of its heavier mass and it could be calculated by:

$$\eta(\xi) = \eta_e + \eta_h \cong \eta_h \quad (2.3.96)$$

$$\eta_h = \frac{k_B T_h}{2} \sum_{j=2, j \neq e} b'_{j0}(\xi) \quad (2.3.97)$$

where the coefficient b'_{j0} is given by:

$$\sum_{j, j \neq e} \sum_{m'=0}^{\xi-1} \tilde{q}_{ij}^{mm'} b'_{jm'}(\xi) = -5n_i \delta_{m0} \quad (2.3.98)$$

$$\eta = -\frac{5(2\pi k_B T_h)^{\frac{1}{2}}}{2|\tilde{q}|} \begin{vmatrix} \tilde{q}_{ij}^{00} & \tilde{q}_{ij}^{01} & n_i m_i^{\frac{1}{2}} \\ \tilde{q}_{ij}^{10} & \tilde{q}_{ij}^{11} & 0 \\ n_j & 0 & 0 \end{vmatrix} \quad (2.3.99)$$

and elements of \tilde{q}_{ij}^{mp} in the determinants are determined from collision cross sections $\bar{Q}_{ij}^{(l,s)}$ [28]:

$$\tilde{q}_{ij}^{00} = 8n_i \left(\frac{m_i}{m_j}\right) \sum_l \frac{n_l m_i^{\frac{1}{2}}}{(m_i + m_l)^{\frac{3}{2}}} \left[\frac{10}{3} \bar{Q}_{il}^{(1,1)} (\delta_{ij} - \delta_{jl}) m_j \right. \\ \left. + 2m_l \bar{Q}_{il}^{(2,2)} (\delta_{ij} + \delta_{jl}) \right] \quad (2.3.100)$$

$$\tilde{q}_{ij}^{01} = 8n_i \left(\frac{m_i}{m_j}\right)^2 \sum_l \frac{n_l m_i^{\frac{3}{2}}}{(m_i + m_l)^{\frac{5}{2}}} \left[(\delta_{ij} - \delta_{jl}) m_j \left(\frac{35}{3} \bar{Q}_{il}^{(1,1)} - 14 \bar{Q}_{il}^{(1,2)} \right) \right. \\ \left. + m_l (\delta_{ij} + \delta_{jl}) (7 \bar{Q}_{il}^{(2,2)} - 8 \bar{Q}_{il}^{(2,3)}) \right] \quad (2.3.101)$$

$$\tilde{q}_{ij}^{10} = \left(\frac{m_j}{m_i}\right) \tilde{q}_{ij}^{01} \quad (2.3.102)$$

$$\tilde{q}_{ij}^{11} = 8n_i \left(\frac{m_i}{m_j}\right)^2 \sum_l \frac{n_l m_i^{\frac{1}{2}}}{(m_i + m_l)^{\frac{7}{2}}} \left\{ (\delta_{ij} \right. \\ \left. - \delta_{jl}) m_j \left[\frac{1}{6} (140m_j^2 + 245m_l^2) \bar{Q}_{il}^{(1,1)} \right. \right. \\ \left. \left. - m_l^2 (98 \bar{Q}_{il}^{(1,2)} - 64 \bar{Q}_{il}^{(1,3)} - 24 \bar{Q}_{il}^{(3,3)}) \right] \right. \\ \left. + (\delta_{ij} + \delta_{jl}) m_l \left[\frac{1}{6} (154m_j^2 + 147m_l^2) \bar{Q}_{il}^{(2,2)} \right. \right. \\ \left. \left. - m_l^2 (56 \bar{Q}_{il}^{(2,3)} - 40 \bar{Q}_{il}^{(2,4)}) \right] \right\} \quad (2.3.103)$$

The computation could be simplified with using the first approximations with deleting the \tilde{q}_{ij}^{mp} elements with m or p=1.

$$\eta = -\frac{5(2\pi k_B T_h)^{\frac{1}{2}}}{2} \begin{vmatrix} \tilde{q}_{ij}^{00} & n_i m_i^{\frac{1}{2}} \\ n_j & 0 \end{vmatrix} (|\tilde{q}_{ij}^{00}|)^{-1} \quad (2.3.104)$$

2.3.3 Collision integral and cross section

The collision integrals and collision cross sections between the particles are sensitively changed by the used potentials. The involved interactions in the present work contains electrons-atoms, atoms-atoms, atoms-charged particles and charged particles.

2.3.3.1 Electron-copper atom interaction

In 1974, Williams and Trajmar [40], [41] firstly provided an empirical measurement on collision cross section between electrons and copper atoms. In 1992, Krenek performed an extrapolation of this experimental result to calculate the transport coefficients [42]. Sakuta and Takashima substituted this cross section using a constant value (10^{-18} m^2) [43] in their work while $2 \times 10^{-18} \text{ m}^2$ estimated by Maecker was used by Shayler and Fang [44] [45]. In 1995, a comparative study of the collision cross section with different approximations was carried out by Chervy *et al* and the results indicate that the constant value of 10^{-18} m^2 and $2 \times 10^{-18} \text{ m}^2$ give results of the electrical conductivity close to that obtained using the method introduced by Scheiner *et al* [46].

2.3.3.2 Charged particles interaction

Screened coulomb potential is recommended by Debye and Hückel [47] to determine the collision integrals and cross sections of the interactions between charged particles with the consideration of Debye shielding effect, expressed as [48]:

$$\varphi(r) = \frac{1}{4\pi\epsilon_0} \frac{q}{r} \exp\left(-\frac{r}{\lambda_D}\right) \quad (2.3.105)$$

where q is the charge ($q = Z_i Z_j e^2$) and r is distance between two colliding particles.

Based on the derivation by Liboff [49], the transport cross sections are given as:

$$Q^{(1)} = \frac{(\alpha_N \lambda_D)^2}{2} \left[\ln\left(\frac{2}{\alpha_N}\right) - \frac{1}{2} - \bar{\gamma} + \ln 2 \right] \quad (2.3.106)$$

$$Q^{(2)} = (\alpha_N \lambda_D)^2 \left[\ln\left(\frac{2}{\alpha_N}\right) - 1 - \bar{\gamma} + \ln 2 \right] \quad (2.3.107)$$

where $\bar{\gamma}$ is the Euler constant ($\bar{\gamma} = 0.5772$);

α_N is a non-dimensional parameter:

$$\alpha_N = \frac{\Delta}{\lambda_D v_d^2} \quad (2.3.108)$$

where v_d is the dimensionless velocity and Δ is the particle diameter [50]:

$$\Delta = \beta \left(\frac{1}{4\pi\epsilon_0} \cdot \frac{Z_i Z_j e^2}{k_B T_{ij}^*} \right) \quad (2.3.109)$$

where β is set to an estimated value of 1.03.

The collision integrals computed using the screened coulomb potential are given by:

$$\Omega_{ij}^{(1,s)} = \left(\frac{2\pi k_B T_{ij}^*}{m_{ij}^*} \right)^{\frac{1}{2}} \cdot (s-1)! b_0^2 \cdot \beta^2 \left[\ln \Lambda - \frac{1}{2} - 2\bar{\gamma} + \Psi(s) \right] \quad (2.3.110)$$

$$\Omega_{ij}^{(2,s)} = 2 \left(\frac{2\pi k_B T_{ij}^*}{m_{ij}^*} \right)^{\frac{1}{2}} \cdot (s-1)! b_0^2 \cdot \beta^2 [\ln \Lambda - 1 - 2\bar{\gamma} + \Psi(s)] \quad (2.3.111)$$

where

$$\Psi(s)|_{s \neq 1} = \sum_{n=1}^{s-1} \frac{1}{n}; \quad \Psi(1) = 0 \quad (2.3.112)$$

$$\Lambda = \frac{2\lambda_D}{\beta b_0} \quad (2.3.113)$$

$$b_0 = \frac{Z_i Z_j e^2}{8\pi \epsilon_0 k_B T_{ij}^*} \quad (2.3.114)$$

2.3.3.3 Copper atoms interaction

From the investigations, the Lennard-Jones potential has been widely used to determine the collision cross section of the interaction between neutral particles, expressed as [51]:

$$\varphi(r) = 4\varepsilon \left[\left(\frac{\sigma_r}{r} \right)^{12} - \left(\frac{\sigma_r}{r} \right)^6 \right] \quad (2.3.115)$$

where ε and σ_r are the depth of the potential well and finite distance at which the inter-particle potential is zero; r is the interatomic distance between neutral particles. In the present work, the new interaction potential (phenomenological potential) proposed by Capitelli *et al* as an improvement of L-J potential [52]–[54] is adopted:

$$\varphi = \varepsilon_{00} \left[\frac{m_\beta}{n(x) - m_\beta} \left(\frac{1}{x} \right)^{n(x)} - \frac{n(x)}{n(x) - m_\beta} \left(\frac{1}{x} \right)^{m_\beta} \right] \quad (2.3.116)$$

$$x = \frac{r}{r_e} \quad (2.3.117)$$

$$n(x) = \beta + 4\chi^2 \quad (2.3.118)$$

$$\beta = 6 + \frac{5}{s_i + s_j} \quad (2.3.119)$$

where r_e is the equilibrium distance; ε_{00} is the binding energy (eV); m_β has the value of 6 for the interactions between neutral particles and β is a parameter range from 6 to 10; “ i ” and “ j ” are the colliding species; s_i and s_j are the cubic roots of the polarizability, as shown in Table 2.2.

Table 2.2 Polarizability values of copper atom and copper cation [55], [56].

Species	Polarizability (\AA^3)
Cu	7.4
Cu ⁺	0.204

For the interactions between neutral particles, the phenomenological method introduces the parameters ε_{00} (eV) and r_e (\AA) in terms of the polarizability α (\AA^3) of the colliding particles, with forms [54]:

$$\varepsilon_{00} = 0.72 \frac{C_d}{r_e^6} \quad (2.3.120)$$

$$r_e = 1.767 \frac{\alpha_i^{\frac{1}{3}} + \alpha_j^{\frac{1}{3}}}{(\alpha_i \alpha_j)^{0.095}} \quad (2.3.121)$$

where C_d (eV \AA^6) is an effective long-range London coefficient:

$$C_d = 15.7 \frac{\alpha_i \alpha_j}{(\sqrt{\alpha_i/N_i} + \sqrt{\alpha_j/N_j})} \quad (2.3.122)$$

and N is the effective number of electrons that contribute to the polarization of neutral species. The corresponded reduced collision integrals of interactions between neutral particles are determined by:

$$\Omega^{(l,s)\star} = \frac{4(l+1)}{(s+1)! [2l+1 - (-1)^l] \pi \sigma^2} \int_0^\infty e^{-\gamma^2} \gamma^{2s+3} Q^l(\gamma) d\gamma \quad (2.3.123)$$

with a logarithmic form:

$$\begin{aligned} \ln \Omega_{ij}^{(l,s)\star} = & [a_1(\beta) + a_2(\beta) \ln T^\star] \frac{e^{\frac{\ln T^\star - a_3(\beta)}{a_4(\beta)}}}{e^{\frac{a_3(\beta) - \ln T^\star}{a_4(\beta)}} + e^{\frac{\ln T^\star - a_3(\beta)}{a_4(\beta)}}} \\ & + a_5(\beta) \frac{e^{\frac{\ln T^\star - a_6(\beta)}{a_7(\beta)}}}{e^{\frac{a_6(\beta) - \ln T^\star}{a_7(\beta)}} + e^{\frac{\ln T^\star - a_6(\beta)}{a_7(\beta)}}} \end{aligned} \quad (2.3.124)$$

where

$$T^\star = \frac{k_B T_h}{\varepsilon_{00}} \quad (2.3.125)$$

and the parameters a_i are polynomial functions of β :

$$a_i(\beta) = \sum_{j=0}^2 c_j \beta^j \quad (2.3.126)$$

where parameters c_j are tabulated in [53]. It should be mentioned that reduced collision integral is a dimensionless variable and therefore $\pi\sigma_0^2$ is multiplied to determine the dimensional collision integral, which is calculated with:

$$\sigma_0 = x_0 r_e \quad (2.3.127)$$

where x_0 is determined as a function of β :

$$x_0 = \xi_1 \beta^{\xi_2} \quad (2.3.128)$$

and the parameters ξ have the value $\xi_1 = 0.8002$ and $\xi_2 = 0.049256$.

2.3.3.4 Copper atoms and copper cations interaction

To describe the interactions between neutral atoms and ions, both the resonant charge-exchange inelastic process and the pure elastic process should be considered. The total collision integral is determined based on an empirical mixing rule [57]:

$$\Omega_{ij}^{(l,s)} = \sqrt{(\Omega_{ij,in}^{(l,s)})^2 + (\Omega_{ij,el}^{(l,s)})^2} \quad (2.3.129)$$

where the subscripts *in* and *el* denote the collision integral derived from inelastic and elastic processes respectively.

(1) Cu-Cu⁺ interaction

Phenomenological potential is also used to calculate the elastic collision cross sections of the interactions between neutral particles and ions [54] with introducing a parameter ρ_i which characterises a relative role of dispersion and induction attraction components in proximity to the equilibrium distance [58]:

$$r_e = 1.767 \frac{\alpha_i^{\frac{1}{3}} + \alpha_n^{\frac{1}{3}}}{(\alpha_i \alpha_n [1 + \frac{1}{\rho_i}])^{0.095}} \quad (2.3.130)$$

$$\varepsilon_{00} = 5.2 \frac{Z^2 \alpha_n}{r_e^4} (1 + \rho_i) \quad (2.3.131)$$

$$\rho_i = \frac{\alpha_i}{Z^2 [1 + (\frac{2\alpha_i}{\alpha_n})^{\frac{2}{3}}] \sqrt{\alpha_n}} \quad (2.3.132)$$

where α_n and α_i are the polarizabilities of the neutral and ionic particles with values given in Table 2.2. Parameter m sets to 4 and coefficients a_i are determined using Eq. ((2.3.126). Parameters ξ for the interactions between the neutral particles and ions have the value $\xi_1 = 0.7564$ and $\xi_2 = 0.064605$;

To calculate the inelastic collision integral terms of interactions between neutral atoms and singly-charged ions, the transport cross section $Q_{ij}^l(\varepsilon_r)$ can be estimated by:

$$Q_{ij}^l(\varepsilon_r) = 2Q_{ex} \quad (2.3.133)$$

where Q_{ex} is the charge-exchange cross section, calculated by:

$$Q_{ex} = \frac{1}{2} [A - B \ln(g)]^2 \quad (2.3.134)$$

with the parameters $A=2.278$ nm and $B=0.08797$ nm [59].

(2) Cu-Cu²⁺/Cu³⁺/Cu⁴⁺ interactions

Through the literature review, there is no available experimental or theoretical values for the polarizability of multiple-charged copper ions. Hence, a polarization potential model is recommended even though the potential is only an approximation. It has less influences on the calculation of transport coefficients due to the lower number density of considered multiple-charged particles. The corresponded reduced collision integrals are given by [52]:

$$\sigma^2 \Omega_{ij}^{(l,s)\star} = \frac{4(l+1)}{(s+1)! [2l+1 - (-1)^l]} A^{(l)}(\delta) \sqrt{\frac{d \cdot \delta}{k_B T}} \Gamma(s+2 - \frac{2}{\delta}) \quad (2.3.135)$$

and

$$d = -\frac{Z^2 e^2 \alpha_{pol}}{8\pi \varepsilon_0 r^4} \quad (2.3.136)$$

where Γ is the Gamma function; α_{pol} is the polarizability of neutral atoms and $A^{(l)}(\delta)$ is the temperature-free coefficient correlated to the transport cross section [60]:

$$A^{(1)}(4) = 0.5523; A^{(2)}(4) = 0.3846; A^{(3)}(4) = 0.6377 \quad (2.3.137)$$

and it leads to several simple relations:

$$\begin{aligned} \sigma^2 \Omega_{ij}^{(1,1)\star} &= 425.4Z \left(\frac{\alpha_n}{r_{ij}^*}\right)^{\frac{1}{2}}; \sigma^2 \Omega_{ij}^{(1,2)\star} = 0.8333 \sigma^2 \Omega_{ij}^{(1,1)\star} \\ \sigma^2 \Omega_{ij}^{(1,3)\star} &= 0.7292 \sigma^2 \Omega_{ij}^{(1,1)\star}; \sigma^2 \Omega_{ij}^{(1,4)\star} = 0.656 \sigma^2 \Omega_{ij}^{(1,1)\star} \\ \sigma^2 \Omega_{ij}^{(1,5)\star} &= 0.602 \sigma^2 \Omega_{ij}^{(1,1)\star}; \sigma^2 \Omega_{ij}^{(2,2)\star} = 0.870 \sigma^2 \Omega_{ij}^{(1,1)\star} \\ \sigma^2 \Omega_{ij}^{(2,3)\star} &= 0.761 \sigma^2 \Omega_{ij}^{(1,1)\star}; \sigma^2 \Omega_{ij}^{(2,4)\star} = 0.685 \sigma^2 \Omega_{ij}^{(1,1)\star} \end{aligned} \quad (2.3.138)$$

In addition, due to the similarities of interactions between copper atoms and multiple-charged positive ions which was justified by Devoto [33] and Abdelhakim *et al* [61], the collision integrals are assumed equal to that of interactions between copper atoms.

2.3.4 Debye length

From previous introduction, the consideration of Debye shielding has significant effects when determines the transport coefficients especially for the computation of Coulomb collision integrals of the interactions between charged particles. But it is still debatable for whether the ions shielding effects should be considered or not. Without considering the ions effects, the Debye length is calculated by [27]:

$$\frac{1}{\lambda_D^2} = \frac{4\pi e^2 n_e}{k_B T} \quad (2.3.139)$$

With considering the shielding effects contributed by the electrons and ions in non-LTE plasma, the Debye length is determined by [48]:

$$\frac{1}{\lambda_D^2} = \frac{e^2}{\varepsilon_0 k_B} \left[\frac{n_e}{T_e} + \sum_{i \neq e}^v \frac{Z_i^2 n_i}{T_h} \right] \quad (2.3.140)$$

Besides that, S. Ghorui and A. K. Das [50] proposed a modified definition of the Debye length to avoid the effect of computed negative collision cross sections which is adopted in the present work. It considers the incorporating contributions of electrons and ions but assuming they have identical temperatures to avoid the divergence of the associated collision integrals, expressed as:

$$\frac{1}{\lambda_q^2} = \frac{e^2}{\varepsilon_0 k_B T_e} \left[n_e + \sum_{\substack{i=1 \\ i \neq e}}^v z_i^2 n_i \right] \quad (2.3.141)$$

2.4 Calculation results

2.4.1 Internal partition function

The internal partition functions of copper atoms and Cu^+ are illustrated in Figure 2.1. The calculation results demonstrate a good agreement in comparison with the literature data for the temperature range from 2,000K to 10,000K at atmospheric pressure [62].

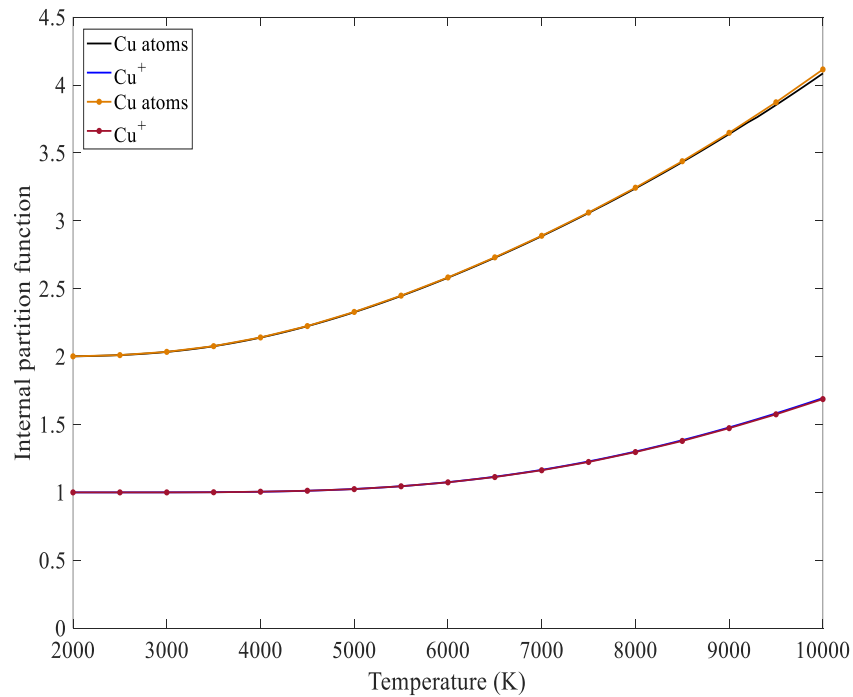


Figure 2.1 Internal partition function of Cu atoms and Cu⁺. Dotted lines: Reference. Solid lines: present work.

2.4.2 Chemical composition of pure copper plasma

Variation of chemical composition of pure copper plasma under equilibrium and non-equilibrium conditions are demonstrated in Figure 2.2. At low temperatures, the plasma composition is dominated by the copper atoms. When the temperature increases, the copper atoms start to ionize and singly-charged positive ions (Cu⁺) are predominantly produced from 1,500 K due to the relatively lower ionization energy for copper (7.726 eV). Further temperature increase results in an ionization of Cu⁺ with the formation of multiply-charged positive ions approximately from 6,300 K. In Figure 2.2 (a), it is observed that the number densities of e, Cu, Cu⁺ and Cu²⁺ become comparatively higher at a given electron temperature when the pressure increases (e.g. $P=1.0$ MPa), based on $nk_B T=P$. Nevertheless, the ionization reaction is confined by the increased pressure and thus the ionizations of the multiply-charged positive ions (Cu³⁺ and Cu⁴⁺) are shifted to slightly higher electron temperatures. As a consequence of the continuous ionization of copper atoms, its number density illustrates a noticeable decreasing approximately from 10,000 K while the number density variation of electrons becomes less with increased temperature. In addition, the increased non-equilibrium degrees have similar effects on the number density variation of the particles (Figure 2.2 (b)) in comparison with that affected by the changed pressure (Figure 2.2 (a)).

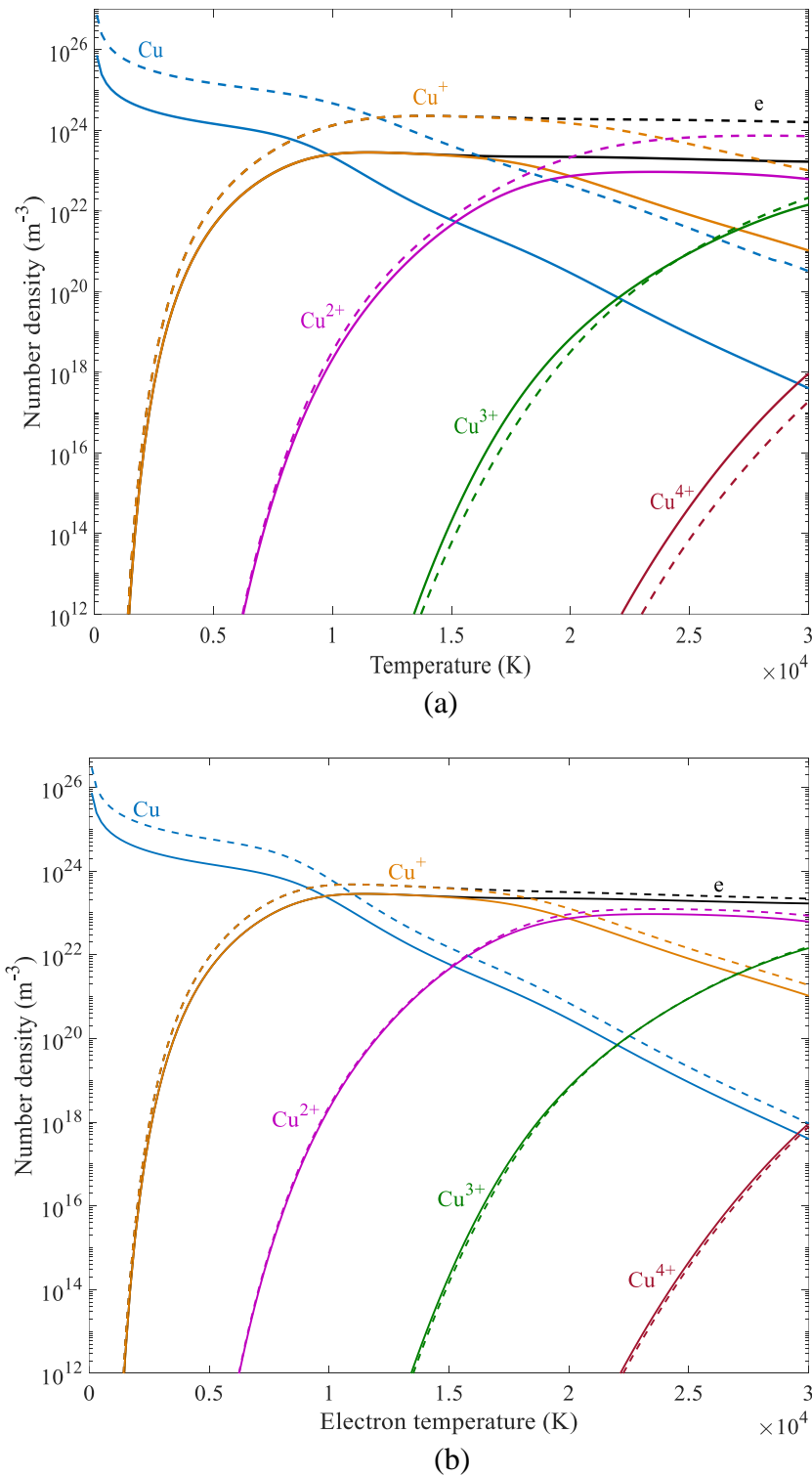


Figure 2.2 Chemical compositions of pure copper plasma at (a) different pressure under LTE conditions (solid lines: $P=0.1$ MPa; dashed lines: $P=1.0$ MPa) and (b) different non-equilibrium degree at atmospheric pressure (solid lines: $\theta=1$; dashed lines: $\theta=4$). The solid and dashed lines with same color represent the same species.

The electron number density at different pressures and non-equilibrium degrees are presented in Figure 2.3. It is found that the electron number density of LTE pure copper plasma at atmospheric pressure illustrates a substantial increase when the temperature

roughly below 11,000 K (Figure 2.3 (a)). The temperature where the number density reached its maximum has a shift with the increased pressure. Furthermore, the number density of electrons has a reducing trend beyond a certain temperature and the variation becomes noticeable at high pressures. It could be explained based on the Le Chatelier's principle which describes that if a system at equilibrium states is subjected to a variation, e.g. pressure or temperature, it would readapt to counterbalance the variation [63]. For non-equilibrium pure copper plasma (Figure 2.3 (b)), the variation of electron number density presents similar profiles. It becomes higher with the increased non-equilibrium degree. For a mixture contains monatomic species only, the chemical composition that determined by the modified Saha equation highly depends on the electron temperature T_e for the non-LTE plasma. The electron number density is grown when T_e rises up to 11,000 K and furtherly decreased as T_e increases.

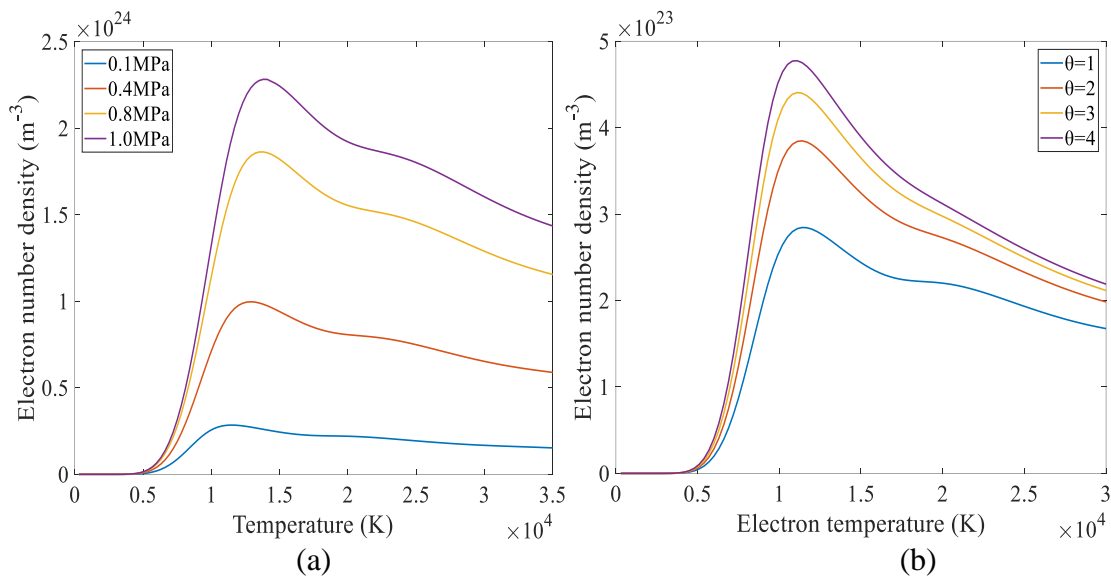


Figure 2.3 Temperature dependence of electron number density at different (a) pressures under LTE condition and (b) non-equilibrium degrees at atmospheric pressure.

The temperature dependence of the molar fractions of electrons and copper atoms at different pressures and non-equilibrium degrees are presented in Figure 2.4 and 2.5. As a result of continuous ionization of copper atoms, the molar fraction of electrons rapidly grows around 5,000 K. The variation becomes gradually roughly from 12,000 K which is affected by the decreased electron number density as shown in Figure 2.3. However, the electrons molar fraction is reduced when the pressure or non-equilibrium degree increases, corresponding to the growing of the copper atoms molar fraction as a result of ionization suppression.

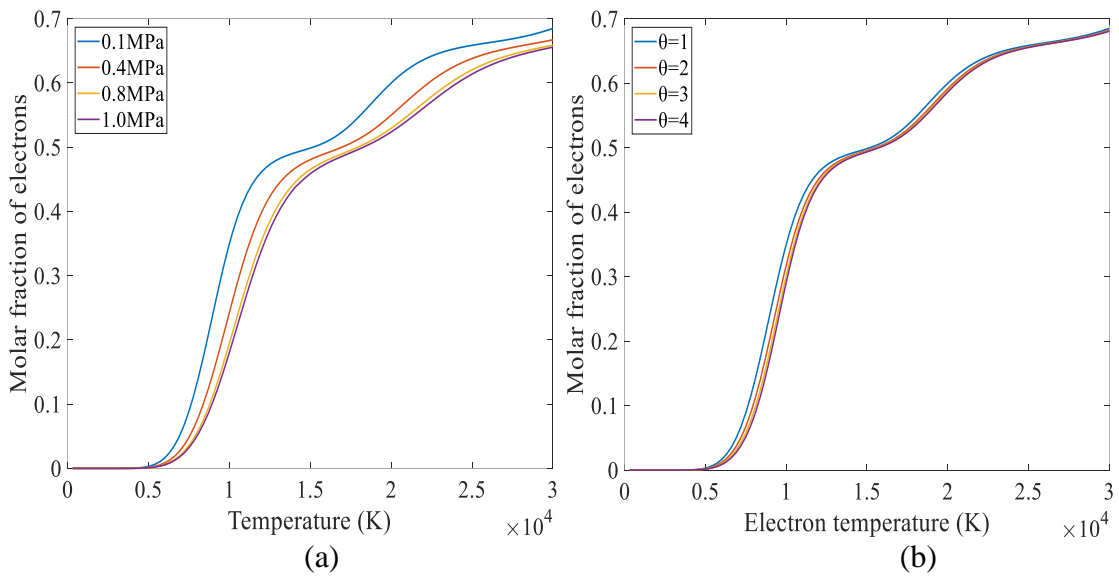


Figure 2.4 Temperature dependence of electrons molar fraction at different (a) pressures under LTE conditions and (b) non-equilibrium degrees at atmospheric pressure.

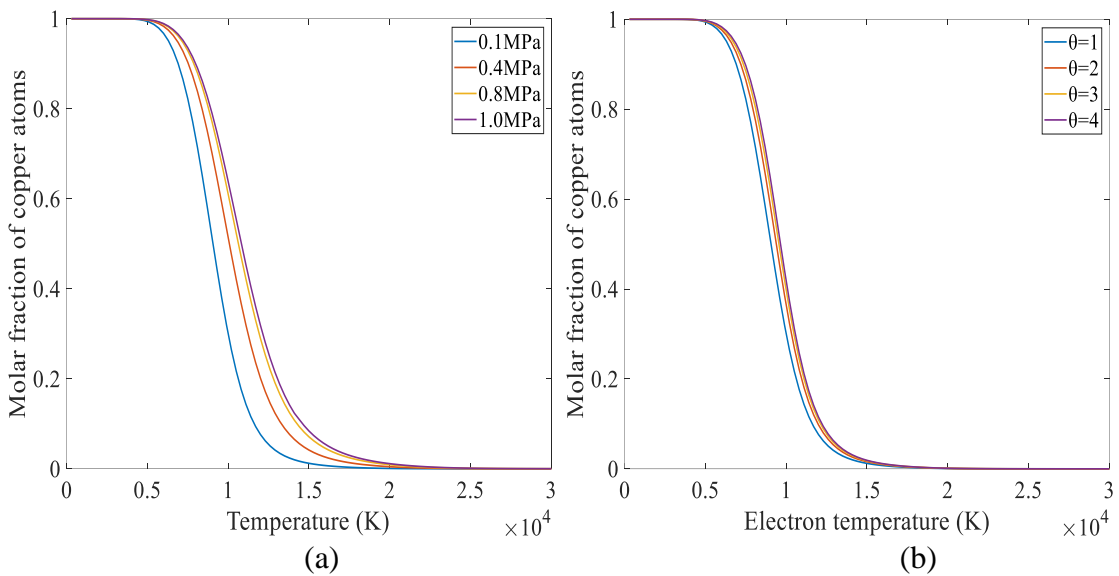


Figure 2.5 Temperature dependence of copper atoms molar fraction at different (a) pressures under LTE conditions and (b) non-equilibrium degrees at atmospheric pressure.

2.4.3 Thermophysical properties of pure copper plasma

(1) Density

The variation of plasma mass density under equilibrium and non-equilibrium conditions are shown in Figure 2.6. The ionization reactions cause the mass density decrease with the temperature increases while the increasing pressure or non-equilibrium degree leads to a comparative rise of the mass density over the whole temperature range due to the ionization suppression.

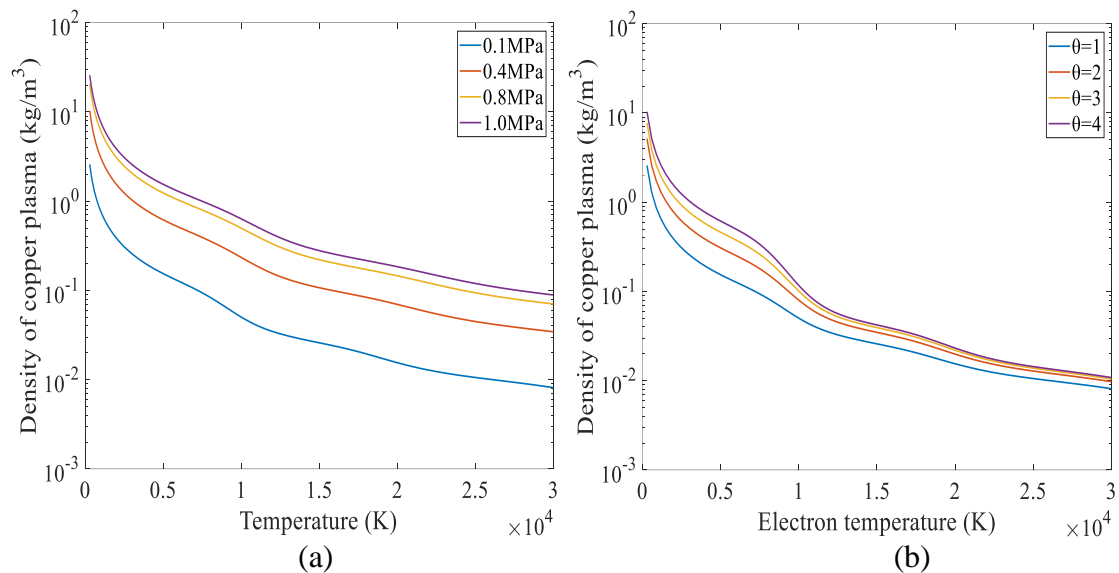


Figure 2.6 Temperature dependence of density of copper plasma at different (a) pressures under LTE conditions and (b) non-equilibrium degrees at atmospheric pressure.

(2) Electrical conductivity

As shown in Figure 2.7, the electrical conductivity is continuously increased with the temperature. In reality, collisions between electrons and other particles has a dominant effect on the electrical conductivity behaviour. For the equilibrium copper plasma, the increasing pressure results in a decrease of electrical conductivity when the temperature roughly below 10,000 K, but contrarily it significantly increases when the temperature becomes high ($>10,000$ K), as presented in Figure 2.7 (a). It is affected by the collisions of particles with electrons. Collisions between electrons and copper atoms are largely occurred at low temperatures due to the high mobilities of electrons. With the increased pressure, the ionization reactions are restricted and results in a lowering of electrical conductivity. Nevertheless, the ionization of copper atoms becomes sufficient when the temperature is increased, and the positive ions provide a predominant contribution on the collisions with electrons, which has a negative effect on the electrical conductivity because of the corresponded larger Coulomb collision integrals. The further increasing of electrical conductivity with the pressure is resulted from the restraint of the ionization reactions that lowers the number density of the positive ions and the Coulomb collision integrals of the interactions between the charged particles become smaller. For the non-equilibrium plasma, the variation of electrical conductivity presents a relatively weaker dependence on the non-equilibrium degree which is resulted from the small variation of electrons molar fraction as shown in Figure 2.7 (b).

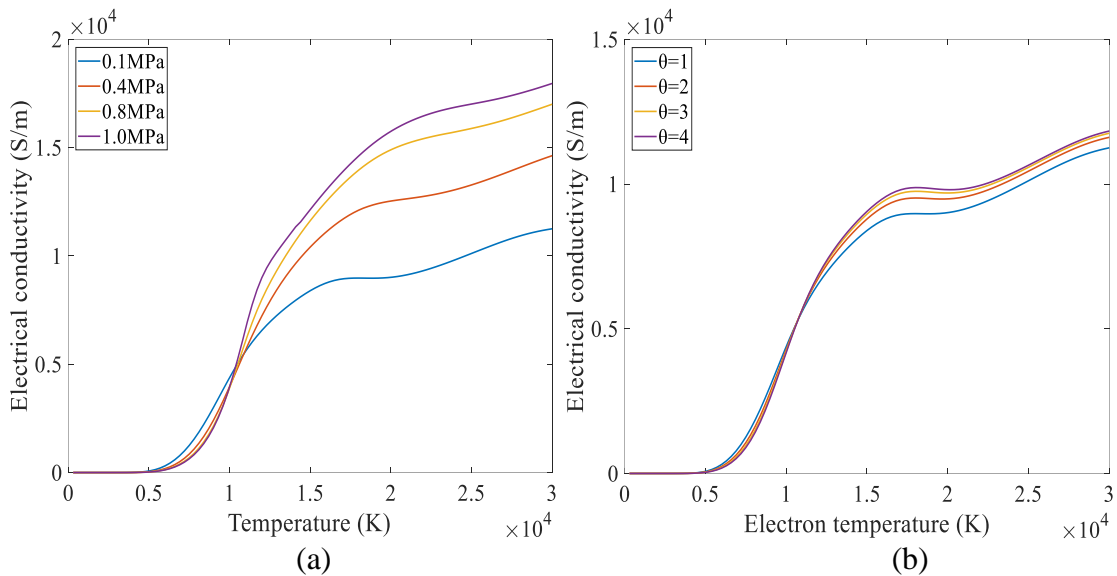


Figure 2.7 Temperature dependence of electrical conductivity of pure copper plasma at different (a) pressures under LTE conditions and (b) non-equilibrium degrees at atmospheric pressure.

(3) Viscosity

Based on the theory of fluid dynamics, the viscosity is a quantity to describe the fluid resistance that opposes the deformation from shear and tensile stresses. Following the Chapman-Enskog method, the determination of the viscosity using first approximation is greatly affected by the heavy particles. As shown in Figure 2.8 (a) for the equilibrium plasma, the viscosity is initially increased which is due to the dominant interactions between copper atoms. With the temperature increases, the charged particles are largely produced and start to dominate the collisions and results in the larger collision integrals (Coulomb interaction), leading to a substantial decrease of the viscosity. The maximum viscosity represents a change of the elastic collisions in the plasma. At low temperatures, the neutral particles dominate the collisions in plasma, However, at high temperatures, as a result of copper atoms continuous ionization, the number density of copper atoms become less and the charged particles are dominantly existed in the plasma. When the temperature is approximately higher than 6,500 K, the Coulomb interactions between charged particles become less important due to the increased pressure and the viscosity becomes larger. The rising pressure also leads to a shift of the corresponded temperature where the viscosity reaches its maximum. For the non-equilibrium plasma as presented in Figure 2.8 (b), the changed non-equilibrium degree has a significant effect on the viscosity when temperature below 15,000 K. The increasing θ_T results in a decreased peak of the viscosity and a slight shift of the corresponded electron temperature as a

result of heavy particles temperature reduction. When the temperature increases above 20,000K, the variation of viscosity becomes insignificant.

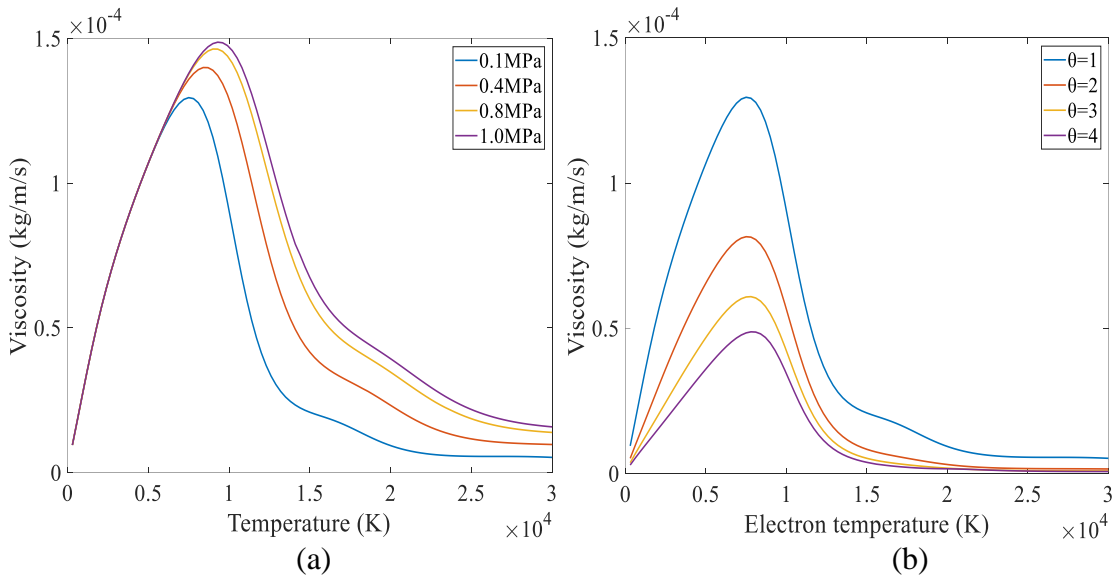


Figure 2.8 Temperature dependence of viscosity of pure copper plasma at different (a) pressures under LTE conditions and (b) non-equilibrium degrees at atmospheric pressure.

(4) Thermal conductivity

Figure 2.9 shows the temperature dependence of total thermal conductivity at different pressures and non-equilibrium degrees. The thermal conductivity is decisive significant to determine the heat transfer capacity of the plasma. At low temperatures between 300 K to 7,500 K when the copper atoms are largely existed in plasma, thermal conductivity is predominantly determined by the translational component of heavy particles. When the temperature increases to about 10,900 K, the thermal conductivity grows to its first peak which is determined by the ionization of copper atoms and interactions between heavy particles as shown in Figure 2.9 (a). The further growth of thermal conductivity when the temperature rises above 14,000 K is dominated by the translational component of electrons as shown in Figure 2.10 (a). The overall calculation of thermal conductivity indicates that the heavy particles contribution becomes insignificant in comparison with the electrons effects. Moreover, the increased pressure causes a slight reduction of the total thermal conductivity at low temperatures and the copper atoms ionization shifts to a higher temperature as well. Furtherly when the temperature rises above a certain value, the stronger collisions between charged particles results in the larger computed collision integrals and the thermal conductivity is comparatively increased when pressure grows. Variation of thermal conductivity resulted from the increased non-equilibrium degree

presents similar profiles (Figure 2.9 (b)) which indicates that the increasing θ_T has a positive effect on the determination of thermal conductivity.

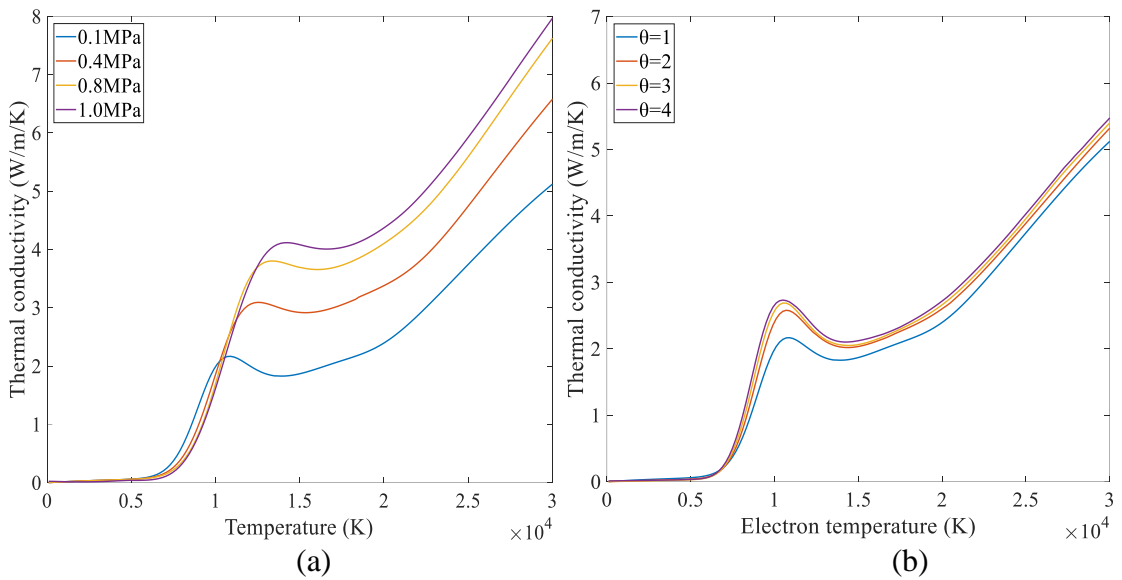


Figure 2.9 Temperature dependence of total thermal conductivity at different (a) pressures under LTE conditions and (b) non-equilibrium degrees at atmospheric pressure.

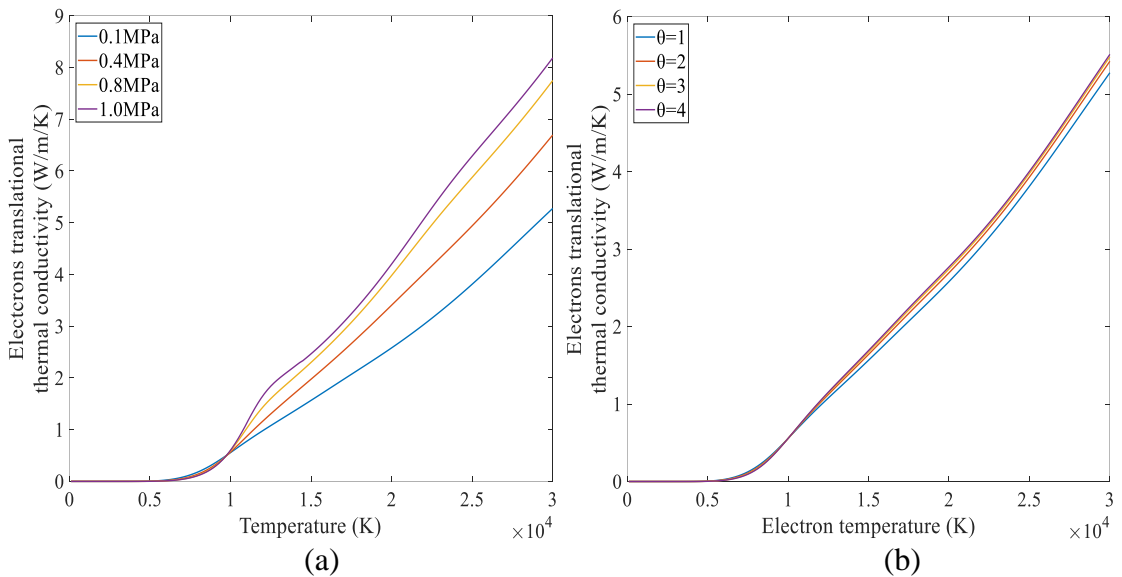


Figure 2.10 Temperature dependence of electrons translational thermal conductivity at different (a) pressures under LTE conditions and (b) non-equilibrium degrees at atmospheric pressure.

(5) Comparison with available literature data

Figure 2.11 demonstrates a comparison of the computed electron number density with literature data and a good agreement is observed especially for high temperatures. The discrepancy is probably attributed to the considered species in the present work which Cu_2 and Cu^- are neglected due to their inconsequential contribution to number density.

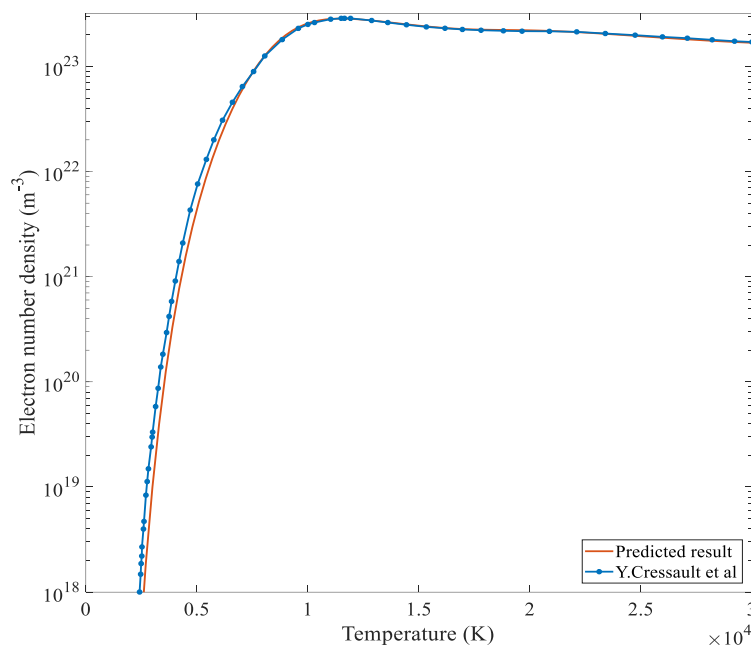


Figure 2.11 Calculated electron number density compared with the literature data [64].

The computed transport coefficients of pure copper plasma under equilibrium condition at the atmospheric pressure are compared with the available literature data, as presented in Figure 2.12. From the comparison, a general agreement could be observed although some discrepancies are presented by different authors. A possible reason might be the species considered in the calculation which leads to a different chemical composition of the plasma. Besides that, the uncertainties in the determination of collision integrals and cross sections using different intermolecular potentials has a significant influence on the computation of transport coefficients. As shown in Figure 2.12 (a), the difference of electrical conductivity is possibly attributed by the collision cross section of the interactions between copper atoms and electrons which is the dominating collisions in pure copper plasma at comparatively lower temperatures (approximately below 10,000 K). The calculated viscosity presents a better agreement with the result of Cressault *et al* at higher temperatures (roughly >9,000K) while a large deviation is found especially at low temperatures (Figure 2.12 (b)) which is probably due to different intermolecular potentials to compute the collision cross sections between neutral particles. Lennard-Jones like phenomenological potential is adopted in present work while Cressault *et al* calculated the corresponded collision cross sections using a polynomial function given by Chervy *et al* [22]. For thermal conductivity as demonstrated in Figure 2.12 (c), the higher maximum value is resulted from the collision cross sections of the interactions between copper atoms and positive ions.

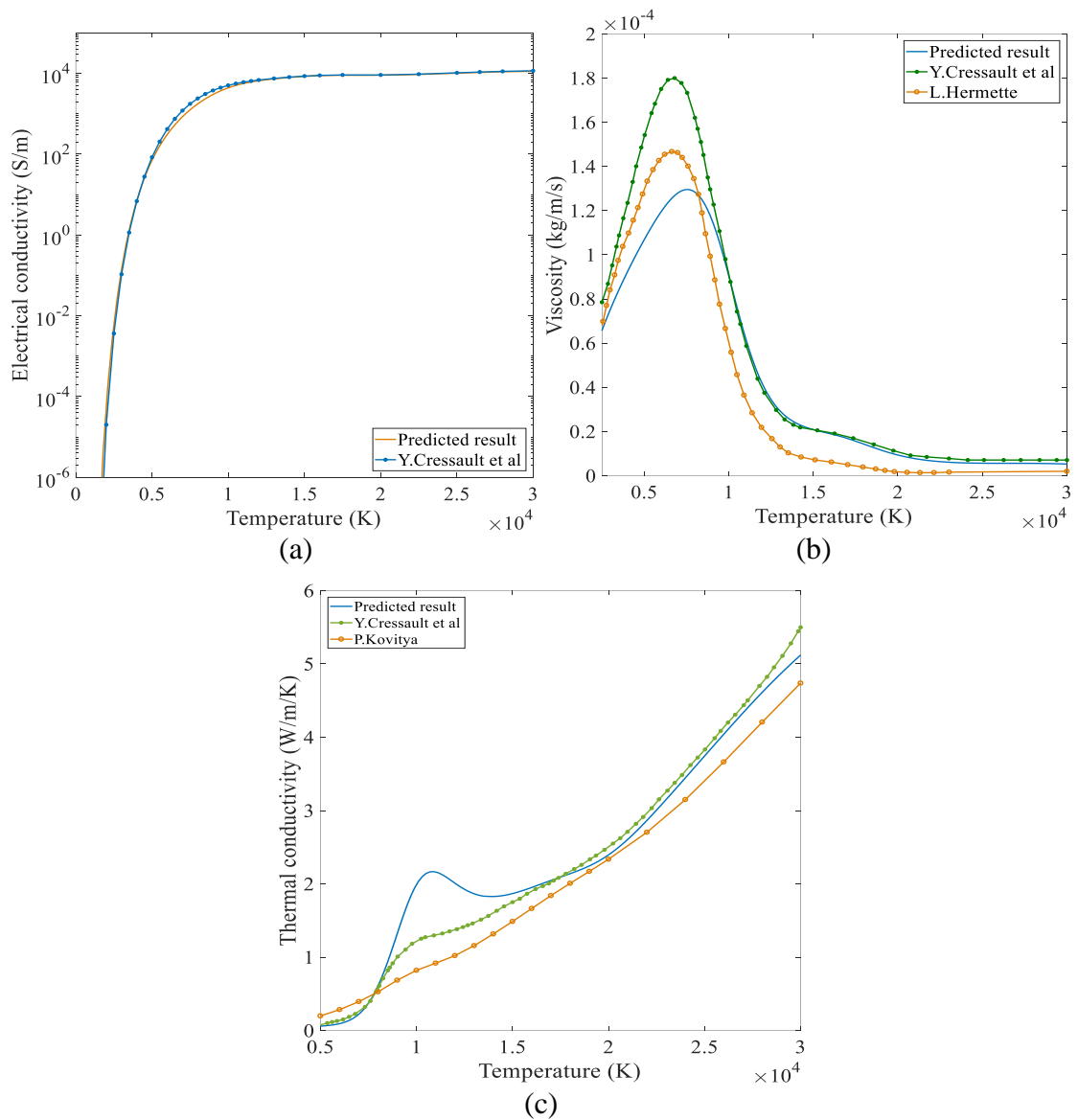
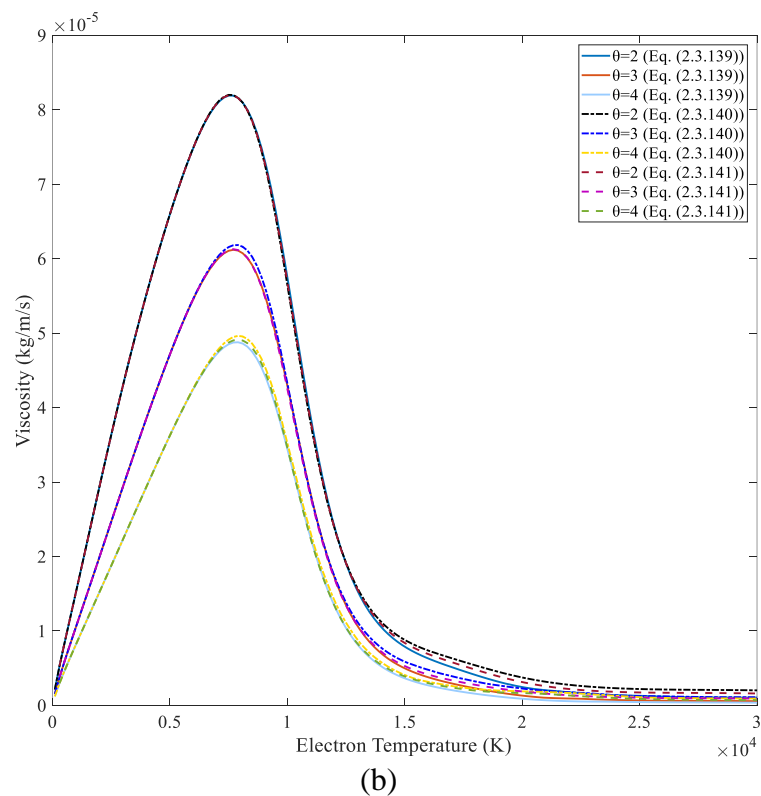
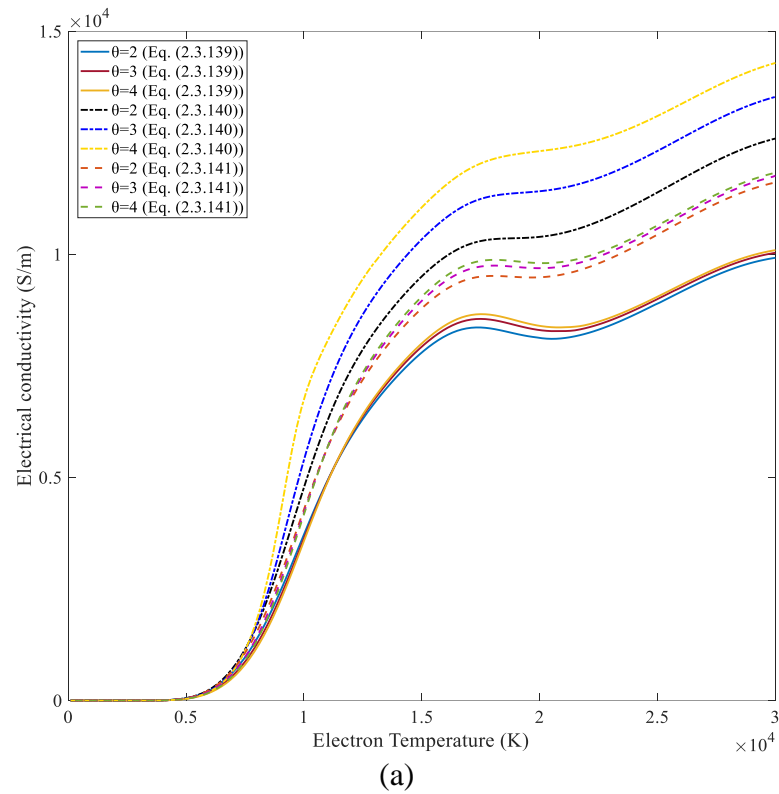


Figure 2.12 Comparison of the (a) electrical conductivity, (b) viscosity and (c) thermal conductivity with the available literature data from the works of Cressault et al [64], [65], Hermette et al [66] and Kovitya [18].

Despite these conceivable reasons, the different definitions of Debye length also result in the variations of computed transport coefficients as illustrated in Figure 2.13. It is observed that the consideration of both electrons and ions shielding effects leads to a relatively smaller Debye radius. It reduces the collision cross sections between charged particles (Coulomb interactions) and transport coefficients become larger especially at high temperatures. Furthermore, the changed Debye length also results in the variations of computed chemical composition which is due to the decreased term “ $\Delta E_{(l)}$ ”.

Based on the definition of the Debye length proposed by S. Ghorui and A. K. Das [50], the calculated transport coefficients are lower than that obtained using (Eq.(2.3.140)),

which is due to the larger Debye radius when assumes the electrons and heavy particles have identical temperatures. In addition, the variation of Debye radius has small effects on the viscosity which is because the viscosity highly depends on the collisions between neutral atoms at low temperatures.



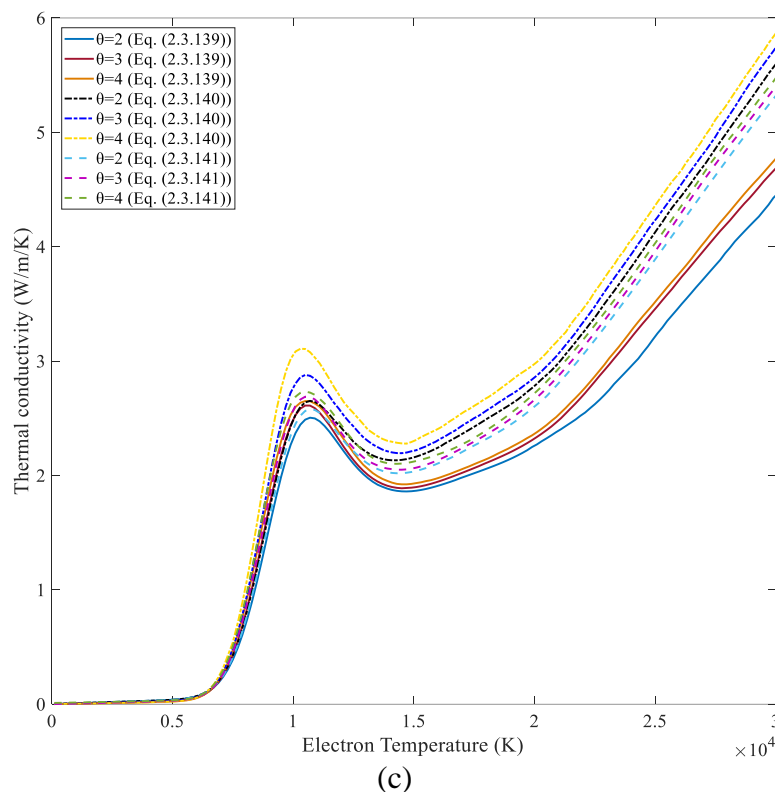


Figure 2.13 Computed electrical conductivity (a), viscosity (b) and thermal conductivity (c) as a function of temperature of the equilibrium copper plasma at atmospheric pressure with different definitions of the Debye length.

2.5 Conclusion

This chapter presents a detailed calculation of thermodynamic properties and transport coefficients of pure copper plasma in LTE and non-LTE states with temperature range from 300 K to 30,000 K at different pressures (i.e. 0.1 MPa, 0.4 MPa, 0.8 MPa, 1.0 MPa) and non-equilibrium degrees ($\theta=1$ to 4) using MATLAB. The principal purpose of this work is to reasonably predict the physical properties of pure copper plasma under LTE and non-LTE conditions. In the calculation, the plasma chemical composition is obtained by solving Saha equations using Newton-Raphson iterative method.

For pure copper plasma that only contains monatomic species, electronic contributions to the associated partition function are determined considering all the observed energy levels of the species from NIST website. The absent higher energy levels are included in the calculation by assuming the species has “hydrogenic” structures and a reasonable cutoff criterion is applied to determine the contributions of these “missing energy levels” on electronic partition function. The partition functions of species Cu and Cu⁺ obtained

from the present work show excellent agreements compared with the available literature data.

The thermodynamic properties and transport coefficients of the pure copper plasma are determined using Chapman-Enskog method with the calculated chemical composition. Following this method, the transport coefficients (e.g. viscosity, electrical conductivity and thermal conductivity) are expressed in the forms of collision cross sections between different particles interactions (e.g. e-e, e-Cu, Cu-Cu, etc). The cross sections involved in different interactions are computed with intermolecular potentials. Additionally, the Debye shielding effect is considered during the calculation although it is remained as a debated issue of whether the contributions of ions shielding effect need to be considered or not. It is found that the consideration of ions shielding effects leads to larger transport coefficients. In the calculation, the results obtained for pure copper plasma where LTE holds ($T_e=T_h$) show general agreements with published data.

The results in this study indicate that the thermophysical properties of plasma especially the transport coefficients are sensitively affected by the collision cross sections between different particles. The calculated results are vital for modelling the physical processes when the arc plasma interacts with cold contact, which will be described in following contents.

References

- [1] K. C. Hsu and E. Pfender, “Analysis of the cathode region of a free-burning high intensity argon arc,” *J. Appl. Phys.*, vol. 54, no. 7, p. 3818, 1983.
- [2] D. Godin and J. Y. Trépanier, “A robust and efficient method for the computation of equilibrium composition in gaseous mixtures,” *Plasma Chemistry and Plasma Processing*, vol. 24, no. 3, pp. 447–473, 2004.
- [3] W. Wang, “INVESTIGATION OF THE DYNAMIC CHARACTERISTICS AND DECAYING BEHAVIOUR OF SF₆ ARCS IN SWITCHING APPLICATIONS,” 2013.
- [4] J. Aubreton, M. F. Elchinger, and P. André, “Influence of Partition Function and Interaction Potential on Transport Properties of Thermal Plasmas,” *Plasma Chem. Plasma Process.*, vol. 33, no. 1, pp. 367–399, 2012.
- [5] L. a Milone and D. C. Merlo, “PARTITION FUNCTIONS OF THE LIGHT ELEMENTS (H TO NA), A REVISION LUIS A. MILONE and DAVID C. MERLO *,” no. 5000, pp. 173–189, 1998.
- [6] M. Capitelli, G. Colonna, and A. D’Angola, *Fundamental Aspects of Plasma Chemical Physics*, vol. 66. New York, NY: Springer New York, 2012.
- [7] S. Gordon and B. J. McBride, “Thermodynamic Data to 20 000 K for Monatomic Gases,” 1999.
- [8] NIST, “NIST: Atomic Spectra Database - Energy Levels Form.” [Online]. Available: http://physics.nist.gov/PhysRefData/ASD/levels_form.html. [Accessed: 10-Jan-2017].
- [9] J. Cooper, “Plasma spectroscopy,” vol. 35, pp. 34–130, 1966.
- [10] D. Bruno, M. Capitelli, C. Catalfamo, and A. Laricchiuta, “Cutoff criteria of electronic partition functions and transport properties of atomic hydrogen thermal plasmas,” *Phys. Plasmas*, vol. 15, no. 11, p. 112306, Nov. 2008.
- [11] J. Bacri and S. Raffanel, “Calculation of some thermodynamic properties of air plasmas: Internal partition functions, plasma composition, and thermodynamic functions,” *Plasma Chem. Plasma Process.*, vol. 7, no. 1, pp. 53–87, Mar. 1987.
- [12] K. S. Drellishak, D. P. Aeschliman, and A. B. Cambel, “Partition Functions and Thermodynamic Properties of Nitrogen and Oxygen Plasmas,” *Phys. Fluids*, vol. 8, no. 9, p. 1590, 1965.
- [13] G. Herzberg, *Molecular Spectra and Molecular Structure. I. Spectra of*

- Diatomic Molecules*, 2nd ed. New York, NY, NY: Van Nostrand Reinhold, 1950.
- [14] K. P. Huber and G. Herzberg, *Molecular Spectra and Molecular Structure. IV. Constants of Diatomic Molecules*. Boston, MA: Springer US, 1979.
- [15] S. N. Suchard and J. E. Melzer, *Spectroscopic data. Volume 2, Homonuclear diatomic molecules*. 1975.
- [16] M. Chase, "NIST-JANAF Thermochemical Tables, 4th Edition," *J. Phys. Chem. Ref. Data, Monogr. 9*, p. 1952, 1998.
- [17] A. Gleizes, B. Chervy, and J. J. Gonzalez, "Calculation of a two-temperature plasma composition: bases and application to SF 6," *J. Phys. D. Appl. Phys.*, vol. 32, no. 16, pp. 2060–2067, Aug. 1999.
- [18] P. Kovitya, "Physical Properties of High-Pressure Plasmas of Hydrogen and Copper in the Temperature Range 5000–60 000 K," *IEEE Trans. Plasma Sci.*, vol. 13, no. 6, pp. 587–594, 1985.
- [19] M. I. Boulos, P. Fauchais, and E. Pfender, *Thermal Plasmas: Fundamentals and Applications (Volume 1)*. Boston, MA: Springer US, 1994.
- [20] J. O. Hirschfelder and Charles F. Curtiss, *Molecular Theory of Gases and Liquids*. 1954.
- [21] Y. Cressault and A. Gleizes, "Thermodynamic properties and transport coefficients in Ar–H₂–Cu plasmas," *J. Phys. D. Appl. Phys.*, vol. 37, no. 4, pp. 560–572, 2004.
- [22] B. Chervy, A. Gleizes, and M. Razafinimanana, "Thermodynamic properties and transport coefficients in SF₆ , -Cu mixtures at temperatures of 300-30 000 K and pressures of 0.1-1MPa," *J. Phys. D Appl. Phys.*, vol. 27, pp. 1193–1206, 1994.
- [23] M.W.Chase, C.A.Daives, J.R.Downey, D.J.Frurip, R.A.McDonald, and A.N.Syverud, "JANAF THERMOCHEMICAL TABLES Third Edition," *Anal. Chem.*, vol. 62, no. 10, p. 588A–588A, May 1990.
- [24] W. Z. Wang, M. Z. Rong, J. D. Yan, A. B. Murphy, and J. W. Spencer, "Thermophysical properties of nitrogen plasmas under thermal equilibrium and non-equilibrium conditions," *Phys. Plasmas*, vol. 18, no. 11, p. 113502, 2011.
- [25] M. Akbi and A. Lefort, "Work function measurements of contact materials for industrial use," *J. Phys. D. Appl. Phys.*, vol. 31, pp. 1301–1308, 1999.
- [26] S. Ghorui, J. V. R. Heberlein, and E. Pfender, "Thermodynamic and Transport Properties of Two-Temperature Nitrogen-Oxygen Plasma," *Plasma Chem.*

- Plasma Process.*, vol. 28, no. 4, pp. 553–582, Aug. 2008.
- [27] R. S. Devoto, “Transport coefficients of ionized argon,” *Phys. Fluids*, vol. 16, no. 5, p. 616, 1973.
- [28] R. S. Devoto, “Transport Properties of Ionized Monatomic Gases,” *Phys. Fluids*, vol. 9, p. 1230, 1966.
- [29] J. D. Ramshaw, “Simple Approximation For Thermal Diffusion In Gas Mixtures,” *J. Non-Equilibrium Thermodyn.*, vol. 21, no. 1, pp. 233–238, 1996.
- [30] J. D. Ramshaw, “Hydrodynamic Theory of Multicomponent Diffusion and Thermal Diffusion in Multitemperature Gas Mixtures,” *J. Non-Equilibrium Thermodyn.*, vol. 18, no. 2, pp. 121–134, 1993.
- [31] J. D. Ramshaw and C. H. Chang, “Ambipolar diffusion in two-temperature multicomponent plasmas,” *Plasma Chem. Plasma Process.*, vol. 13, no. 3, pp. 489–498, Sep. 1993.
- [32] W. F. Ahtye, *A critical evaluation of methods for calculating transport coefficients of partially and fully ionized gases* /. Washington, D.C. :, 1965.
- [33] R. S. Devoto, “Simplified Expressions for the Transport Properties of Ionized Monatomic Gases,” *Phys. Fluids*, vol. 10, no. 10, p. 2105, 1967.
- [34] J. O. Hirschfelder, “Heat Transfer in Chemically Reacting Mixtures. I,” *J. Chem. Phys.*, vol. 26, no. 2, pp. 274–281, Feb. 1957.
- [35] J. O. Hirschfelder, “Heat Conductivity in Polyatomic or Electronically Excited Gases. II,” *J. Chem. Phys.*, vol. 26, no. 2, pp. 282–285, Feb. 1957.
- [36] W. Wang, M. Rong, J. D. Yan, and Y. Wu, “The Reactive Thermal Conductivity of Thermal Equilibrium and Nonequilibrium Plasmas : Application to Nitrogen,” *IEEE Trans. Plasma Sci.*, vol. 40, no. 4, pp. 980–989, 2012.
- [37] X. Chen and H. P. Li, “The reactive thermal conductivity for a two-temperature plasma,” *Int. J. Heat Mass Transf.*, vol. 46, pp. 1443–1454, 2003.
- [38] J. N. Butler and R. S. Brokaw, “Thermal Conductivity of Gas Mixtures in Chemical Equilibrium,” *J. Chem. Phys.*, vol. 26, no. 6, pp. 1636–1643, Jun. 1957.
- [39] R. S. Brokaw, “Thermal Conductivity of Gas Mixtures in Chemical Equilibrium. II,” *J. Chem. Phys.*, vol. 32, no. 4, pp. 1005–1006, Apr. 1960.
- [40] W. Williams and S. Trajmar, “Elastic and Inelastic Electron Scattering at 20 and 60 eV from Atomic Cu,” *Phys. Rev. Lett.*, vol. 33, no. 4, pp. 187–190, Jul. 1974.
- [41] S. Trajmar, W. Williams, and S. K. Srivastava, “Electron-impact cross sections for Cu atoms,” *J. Phys. B At. Mol. Phys.*, vol. 10, no. 16, pp. 3323–3333, Nov.

- 1977.
- [42] P. KRENEK, “Thermophysical properties of the reacting mixture SF₆ and Cu in the range 3,000 to 50 000 K and 0.1 to 2 MPa,” *Acta Techn.*, vol. 37, pp. 399–410, 1992.
- [43] T. Sakuta and T. Takashima, “Multi-mixing effects of nozzle and electrode materials on transport and thermodynamic properties of SF₆ under current interrupting condition,” in *Proc. 10th Int. Conf. Gas Discharges their Application*, 1992, vol. 1, pp. 110–113.
- [44] P. J. Shayler and M. T. C. Fang, “The transport and thermodynamic properties of a copper-nitrogen mixture,” *J. Phys. D. Appl. Phys.*, vol. 10, no. 12, pp. 1659–1669, 2001.
- [45] H. Maecker, “Über den Querschnitt des Fluoratoms gegenüber Elektronenstoß,” *Ann. Phys.*, vol. 453, no. 5–8, pp. 441–446, 1956.
- [46] B. Chervy, O. Dupont, a Gleizes, and P. Krenek, “The influence of the cross section of the electron-copper atom collision on the electrical conductivity of Ar-Cu and SF₆-Cu plasmas,” *J. Phys. D ...*, vol. 28, pp. 2060–2066, 1995.
- [47] E. Hückel and P. Debye, “Zur Theorie der Elektrolyte. I. Gefrierpunktserniedrigung und verwandte Erscheinungen,” *Phys. Z.*, vol. 24, no. 9, pp. 185–206, 1923.
- [48] F. Chen, *Introduction to Plasma Physics and Controlled Fusion*. Cham: Springer International Publishing, 2016.
- [49] R. L. Liboff, “Transport Coefficients Determined Using the Shielded Coulomb Potential,” *Phys. Fluids*, vol. 2, no. 1, p. 40, 1959.
- [50] S. Ghorui and A. K. Das, “Collision integrals for charged-charged interaction in two-temperature non-equilibrium plasma,” *Phys. Plasmas*, vol. 20, no. 9, p. 93504, Sep. 2013.
- [51] P. André *et al.*, “Transport coefficients in thermal plasma. Applications to Mars and Titan atmospheres,” *Eur. Phys. J. D*, vol. 57, no. 2, pp. 227–234, Apr. 2010.
- [52] D. Bruno *et al.*, “Transport properties of high-temperature Jupiter atmosphere components,” *Phys. Plasmas*, vol. 17, no. 11, p. 112315, Nov. 2010.
- [53] D. Bruno *et al.*, “Transport Properties of High-Temperature Mars-Atmosphere Components,” NASA Astrophysics Data System, 2008.
- [54] a. Laricchiuta *et al.*, “Classical transport collision integrals for a Lennard-Jones like phenomenological model potential,” *Chem. Phys. Lett.*, vol. 445, no. 4–6,

- pp. 133–139, 2007.
- [55] M. B. Knickelbein, “Electric dipole polarizabilities of copper clusters,” *J. Chem. Phys.*, vol. 120, no. 22, pp. 10450–10454, Jun. 2004.
- [56] P. J. · A. Toro–Labbe, “Polarizability of neutral copper clusters,” *J. Mol. Model.*, vol. 20, no. 9, 2014.
- [57] A. B. Murphy and C. J. Arundell, “Transport Coefficients of Argon , Nitrogen , Oxygen , Argon-Nitrogen , and Argon-Oxygen Plasmas,” vol. 14, no. 4, 1994.
- [58] D. Cappelletti, G. Liuti, and F. Pirani, “Generalization to ion—neutral systems of the polarizability correlations for interaction potential parameters,” *Chem. Phys. Lett.*, vol. 183, no. 3–4, pp. 297–303, Aug. 1991.
- [59] A. Yang *et al.*, “Thermodynamic Properties and Transport Coefficients of CO₂–Cu Thermal Plasmas,” *Plasma Chem. Plasma Process.*, vol. 36, no. 4, pp. 1141–1160, Jul. 2016.
- [60] T. Kihara, M. H. Taylor, and J. O. Hirschfelder, “Transport Properties for Gases Assuming Inverse Power Intermolecular Potentials,” *Phys. Fluids*, vol. 3, no. 5, p. 715, 1960.
- [61] H. Abdelhakim, J. P. Dinguirard, and S. Vacquie, “The influence of copper vapour on the transport coefficients in a nitrogen arc plasma,” *J. Phys. D ...*, vol. 13, p. 1427, 1980.
- [62] S. W. Bowen, “Properties of Copper: Calculation of the Partition FUNCTION, Species Concentration, and Spectral-Line Intensities.” 1964.
- [63] “Le Châtelier’s Principle - Chemwiki.” [Online]. Available: http://chemwiki.ucdavis.edu/Physical_Chemistry/Equilibria/Le_Châtelier’s_Principle. [Accessed: 01-Nov-2015].
- [64] Y. Cressault, R. Hannachi, P. Teulet, a Gleizes, J.-P. Gonnet, and J.-Y. Battandier, “Influence of metallic vapours on the properties of air thermal plasmas,” *Plasma Sources Sci. Technol.*, vol. 17, no. 3, p. 35016, 2008.
- [65] Y. Cressault, A. B. Murphy, P. Teulet, A. Gleizes, and M. Schnick, “Thermal plasma properties for Ar–Cu, Ar–Fe and Ar–Al mixtures used in welding plasmas processes: II. Transport coefficients at atmospheric pressure,” *J. Phys. D. Appl. Phys.*, vol. 46, no. 41, p. 415207, Oct. 2013.
- [66] L. HERMETTE, Y. Cressault, A. Gleizes, P. TEULET, and K. BOUSOLTANE, “Thermodynamic properties and transport coefficients in SF₆ High Voltage Circuit Breakers Arc Plasma: Influence of vapours (PTFE, Cu) and validity of

mixing rules.,” 2014, no. June 2015, pp. 1–2.

Chapter 3

A Cathode Layer Model for Arc-Contact Interaction in High Voltage Circuit Breakers

3.1 Description of the near cathode non-LTE layer

Contacts play an essential role in the current interruption process of high voltage circuit breakers. Insufficient lifetime of contact resulting from severe damage and deformation during the interruption is one of the representative limiting factors. Recently, advanced sensing technologies enable real-time online monitoring on the conditions of contacts. Nevertheless, the sensors need to be physically present in the arcing chamber of a circuit breaker, which may impose insulation risks in addition to the potential deterioration of sensor performance in the hostile environment. Furthermore, there are many difficulties and limitations in carrying out relevant experiments especially under high voltage and current conditions. It means that the estimation of contact conditions through numerical modelling, supported and verified by test results, is expected to be an alternative method to thoroughly analyse the contact properties during the interruption process.

Vaporization of contact material is an unavoidable result when the arc plasma interacts with contacts, since arc especially at high current generates strong energy flux towards the contact tip. There have been some investigations concerning the contact erosion by modelling and experiments [1]–[11]. Existing models are either for the low current with idealised contact surface condition or the energy flux flowed from the arc is determined by considering an LTE arc column.

The objective of the work in this chapter is to build a model to consider the interaction between the arc column and the contact tip with the consideration of a non-LTE layer formed in front of the contact. It is aimed for a more accurate method to evaluate the erosion of contacts in the interruption process so that the lifetime of the contacts can be predicted with reasonable accuracy. As is recognised from previous study, the plasma is deviated from LTE states within the non-LTE layer due to insufficient collisions and energy transfer between electrons and heavy particles (neutral atoms and ions). It means

that the heavy particles inside this thin layer are treated differently from electrons. This thin non-LTE layer, where the physical characteristics is complicated, consists of two different sub-layers (pre-sheath and sheath). Approaching the cathodic contact (referred as “cathode”) from the arc column where LTE holds, gas temperature (heavy particles temperature) decreases continuously towards the cathode surface temperature because cathode is much colder than the arc column. Nevertheless, electrons are free to have a higher temperature than heavy particles. This gives rise to the so-called pre-sheath layer where the plasma is electrically quasi-neutral but the electrons are hotter than the heavy particles under the action of electric field within the sheath layer. The existed ions move towards the cathode surface while the electrons move towards the LTE arc column. The repelling and depletion of electrons that emitted from the cathode surface leads to the formation of this sheath layer immediately by the cathode surface where positive space charge appear and collisions between particles are negligible. The strong electric field induced by the space charge in sheath layer makes the electrons ejected from cathode surface easily by decreasing the potential barrier. The emitted electrons are accelerated in the sheath layer towards the pre-sheath layer where collision between the particles is the dominant mechanism to generate new electrons to maintain the plasma conductivity and sustain the discharge current. The energy flux from arc column to cathode surface is a key parameter in the study of the arc-contact interaction. To determine the energy transfer between the arc column and contact, the work is started with a comprehensive analysis of the physical processes occurred in the non-LTE layer. A schematic diagram of this near cathode non-LTE layer is shown in Figure 3.1 with $x=0$ being the cathode surface.

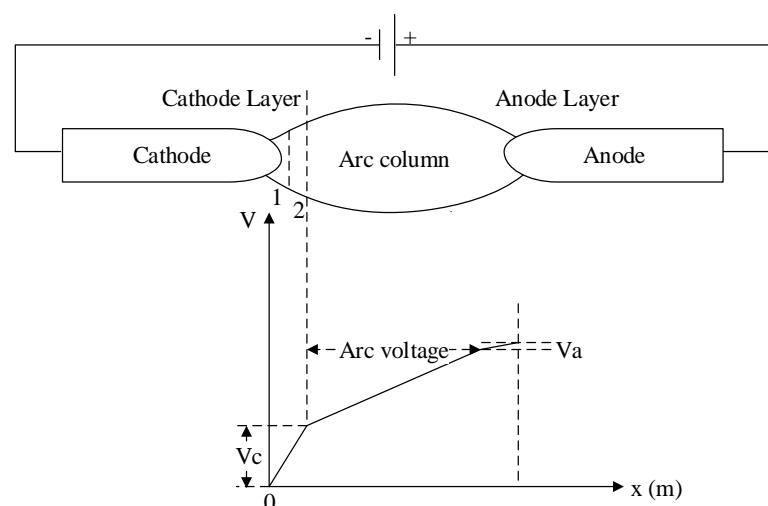


Figure 3.1 Schematic diagram of the non-LTE layer and the voltage distribution between the arcing contacts, where “1” is the sheath and “2” is the pre-sheath.

The space-charge sheath layer (collisionless layer) that adjacent to the cathode surface has a typical thickness of several Debye length while pre-sheath layer (ionization layer) is thicker. The physical properties of the two sub-layers are presented in Figure 3.2 and the physical conditions in different sub-layers (sheath, pre-sheath and LTE arc column) are explained in Table 3.1. T_e and T_h are temperatures of electrons and heavy particles.

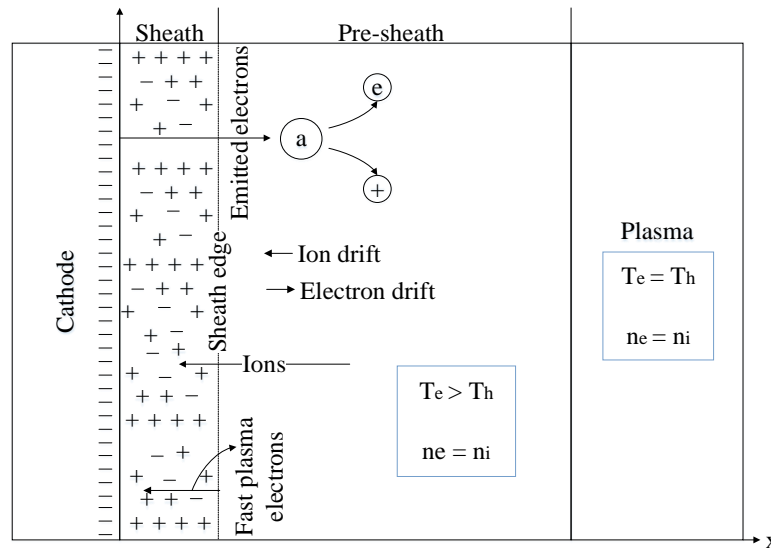


Figure 3.2 Schematic diagram of the structure of near cathode non-LTE layer; “a, e, +” represent the neutral atoms, electrons and positive ions respectively.

Table 3.1 Physical conditions in the sub-layers between cathode and arc column.

	Thermal equilibrium	Ionization equilibrium	Quasi neutrality
Sheath	-	Collisionless	$n_e \neq n_i$
Pre-sheath	$T_e > T_h$	$\dot{n}_e \neq 0$	$n_e = n_i$
Arc column	$T_e = T_h$	$\dot{n}_e = 0$	$n_e = n_i$

The contact material in the present work is pure copper which is a kind of non-refractory material that vaporization can be caused by arc heating easily due to its lower melting and vaporization temperatures. In addition, the present model assumes severe contact erosion at high current conditions and thus the near cathode non-LTE layer with a very small thickness contains only pure copper vapour. It should be emphasised that energy exchange between the arc column and anode is different from that between the arc and cathode. The electrons are attracted to the anode surface with a lower potential drop in comparison with the cathode. Anode erosion is much lower than that of the cathode. In the present work, the anode is not included in the mathematical model.

3.2 Ionization layer: pre-sheath

The quasi-neutral pre-sheath adjacent to the sheath layer is a collision dominated layer where the electrons with sufficient kinetic energy collide with heavy particles to ionise the neutral particles. While the temperature of the heavy particles reduces to the cathode surface temperature ($\sim 2,860\text{K}$ for copper cathode) when they move from the arc column towards the cathode surface, sufficient electrons have to be present in pre-sheath layer to conduct the current. These electrons are either supplied from the cathode surface or generated by ionization through electron impact in the pre-sheath layer.

3.2.1 Mathematical model with respect to the pre-sheath layer

The particles within the pre-sheath layer includes electrons, ions and neutral atoms. The equations in the pre-sheath model that describe the physical conditions inside the pre-sheath layer are derived with considering a 2T non-LTE arc plasma [12].

(1) Continuity equations for electrons and ions

$$\nabla \cdot \Gamma_e = \nabla \cdot (n_e u_e) = \dot{n}_e \quad (3.2.1)$$

$$\nabla \cdot \Gamma_i = \nabla \cdot (n_i u_i) = \dot{n}_e \quad (3.2.2)$$

where Γ is the flux; u is the velocity for directed motion and n is the number density. Subscripts “ i ” and “ e ” designate ions and electrons. The number density of ions equals to the electrons ($n_e = n_i$) and the net ionization rate is given by:

$$\dot{n}_e = \alpha_{rec} n_e^3 \left(\frac{n_a}{n_{a,LTE}} - 1 \right) \quad (3.2.3)$$

$$n_a = \frac{P - k_B n_e (T_e + T_h)}{k_B T_h} \quad (3.2.4)$$

where n_a is the number density of neutral species in the pre-sheath layer; α_{rec} (m^6/s) is the three-body recombination coefficient; P is the total pressure in the system;

Recombination is an energy releasing process in a plasma system. For the plasma with monatomic species only, recombination would occur through two mechanisms: radiative recombination and three-body collisional recombination [13]. Radiative combination is dominant when collisions are insufficient in the plasma, which occurs when the positive ions capture free electrons to its bound orbit with releasing photons. In a denser plasma, as a result of frequent collisions, the three-body recombination involving electrons and ions/atoms becomes dominant. The three-body recombination coefficient is determined

as the ratio between a forward rate coefficient K_f of a reversible chemical reaction and an equilibrium constant for the overall reaction path K_{eq} . The forward rate coefficient is calculated by [14],

$$K_{fe} = S_1 \sqrt{\frac{32}{\pi} \left(\frac{m_a + m_e}{m_a m_e} \right)} (k_B T_e)^{\frac{3}{2}} \left(\frac{E_1}{2k_B T_e} + 1 \right) \exp\left(-\frac{E_1}{k_B T_e}\right) \quad (3.2.5)$$

where K_{fe} is the coefficient of electron-catalysed reaction; m_a and m_e ($9.11 \times 10^{-31} \text{kg}$) are the masses of neutral atoms and electrons; S_1 is the first excitation cross-section; k_B is the Boltzmann constant ($1.38 \times 10^{-23} \text{J/K}$) and E_1 (eV) is the first electronic excitation energy of neutral atoms. The equilibrium constant is given by:

$$K_{eq} = \frac{2Q_i}{Q_a} \left(\frac{2\pi m_e k_B T_e}{h^2} \right)^{3/2} \exp\left(-\frac{E_i}{k_B T_e}\right) \quad (3.2.6)$$

where E_1/k_B is defined as a characteristic temperature for the excitation to the first excited state and E_i/k_B is a characteristic temperature for the first ionization of neutral atoms. Thus, the three-body recombination coefficient $\alpha_{rec,ei}$ is calculated by:

$$\alpha_{rec,ei} = \frac{K_{fe}}{K_{eq}} \quad (3.2.7)$$

The equilibrium density of the neutral species $n_{a,LTE}$ in Eq. (3.2.3) is calculated using generalized Saha equation for arc plasma in LTE states:

$$n_e \left(\frac{n_i}{n_{a,LTE}} \right) = 2 \left(\frac{Q_i(T_e)}{Q_a(T_e)} \right) \left(\frac{2\pi m_e k_B T_e}{h^2} \right)^{\frac{3}{2}} \exp\left(-\frac{E_{a,Cu} - \Delta E_{(0)}}{k_B T_e}\right) \quad (3.2.8)$$

The determination of particles number density has been detailedly explained in Chapter 2. The work in this chapter only considers the singly-charged copper ions Cu^+ based on a numerical computation of the non-LTE layer with considering the effects of multiply-charged ions by Almeida *et al* [15] who drew a conclusion that total ion current in non-LTE layer is mostly contributed by the singly-charged ions. Therefore, in the pre-sheath layer, fluxes of electrons and ions are determined following modified Chapman-Enskog method [16]–[19],

$$\begin{aligned} \Gamma_e = n_e u_e = & - \left(\frac{D_e^T}{m_e T_e} + \frac{m_e n_t n_e D_{ee}}{\rho T_e} \right) \nabla T_e - \frac{m_e n_t}{\rho} D_{ee} \nabla n_e \\ & + \frac{m_e n_t n_e D_{ee}}{\rho k_B T_e} e \nabla V \end{aligned} \quad (3.2.9)$$

$$\Gamma_i = n_i u_i = -\frac{n_a m_a D_{ia}}{\rho} \nabla n_e + \frac{n_e m_i D_{ia}}{\rho} \nabla n_a - \frac{n_t^2 n_e m_i D_{ia} e}{P \rho} \nabla V \quad (3.2.10)$$

where V is the potential; $P = \sum_{\xi=e,i,a} n_{\xi} k_B T_{\xi}$ is the total pressure of the system; $\rho = \sum_{\xi=e,i,a} n_{\xi} m_{\xi}$ is the overall mass density; $n_t = \sum_{\xi=e,i,a} n_{\xi}$ is the total number density; D_e^T is the thermal diffusion coefficient of electrons; D_{ia} is ordinary diffusion coefficient of ions-neutral atoms; D_{ee} is the electron self-diffusion coefficient, expressed as:

$$D_{ee} = \frac{\rho k_B T_e}{m_e n_t n_e e^2} \sigma \quad (3.2.11)$$

where σ is the electrical conductivity (S/m).

(2) Energy conservation equation of electrons

The electrons within the non-LTE layer acquire sufficient energy from the electric field in the space charge sheath layer when emitted from the cathode surface and move into the pre-sheath layer. During the collisions, the electrons pass part of their energy to the ions. Furthermore, the number density of neutral particles is expected to be lower in the majority of pre-sheath layer in comparison with charged particles due to the relatively lower ionization energy of copper atoms. In pre-sheath layer, the energy conservation equation of the electrons is expressed as:

$$e\Gamma_e \cdot \nabla V = -\nabla \cdot (\lambda_{tre} \nabla T_e) + \frac{5}{2} k_B \alpha \Gamma_e \cdot \nabla T_e + \left(\frac{5}{2} k_B T_e \alpha + E_i \right) n_e + W_{eh} \quad (3.2.12)$$

$$\alpha = 1 + \frac{2\rho D_e^T}{5n_e n_t m_e m_a D_{ee}} \quad (3.2.13)$$

$$W_{eh} = n_e \frac{3}{2} k_B \frac{2m_e}{m_a} (T_e - T_h) (n_a Q_{ea} + n_e Q_{ei}) v_e^{th} \quad (3.2.14)$$

where λ_{tre} is the electron translational thermal conductivity; v_e^{th} is the electrons mean thermal velocity; Q_{ea} and Q_{ei} are collision cross-sections of electron-atom interactions and electron-ion interactions. The corresponding energy terms are thermal conduction, enthalpy flux transport by electron diffusion, energy loss by inelastic collisions and loss by elastic collisions with the heavy particles. Assuming that the velocity of the particles follows the Maxwell distribution [20] and the average kinetic energy of each particle is $3k_B T/2$, the mean velocity is thus given by:

$$\bar{v} = \left(\frac{8k_B T}{\pi m} \right)^{\frac{1}{2}} \quad (3.2.15)$$

(3) Energy conservation equation of heavy particles

The energy balance of heavy particles is expressed as:

$$-e\Gamma_i \cdot \nabla V + W_{eh} = -\nabla \cdot (\lambda_{trh} \nabla T_h) \quad (3.2.16)$$

where λ_{trh} is the translational thermal conductivity of heavy particles.

3.2.2 Boundary conditions for pre-sheath model

The solution of the pre-sheath model is determined by the boundary conditions imposed on the arc plasma side where the LTE conditions are valid. It means that the developed near cathode non-LTE layer model need to be coupled to the magneto-hydrodynamics (MHD) model for the arc column to obtain the boundary conditions of the pre-sheath that adjacent to the LTE arc. In the calculation, since the thickness of the non-LTE layer is much smaller compared with the radius of the cathode, a one-dimensional analysis is therefore applied. The related boundary conditions are specified in Table 3.2.

Table 3.2 Description of the boundary conditions at the arc plasma/pre-sheath interface.

Boundary Conditions	
Temperature at plasma side	$T_e = T_h = 15000K$
Number density of electrons	$n_e = n_i = 2.45 \times 10^{23} m^{-3}$
Electric potential (V)	$V = 15 V$
Gradient of temperature	$\frac{dT_e}{dx} = \frac{dT_h}{dx} = -5.8 \times 10^7 K/m$
Gradient of electron number density	$\frac{dn_e}{dx} = \frac{dn_i}{dx} = -3.9 \times 10^{24} m^{-4}$

The potential of 15 V at the arc plasma side is arbitrarily given as a reference value and the electric field strength dV/dx at the arc plasma side need to be adjusted reasonably to make the temperature of heavy particles equal to the cathode surface temperature. The equations of the pre-sheath model are closed with the assumption of a constant thermal pressure (0.1 MPa in the present work) and these equations governed in the pre-sheath layer are numerically solved using the iteration algorithms from the boundary at the arc plasma side towards the so-called “sheath edge” which is the interface between the pre-sheath layer and sheath layer. The applicable method to solve the high-order nonlinear differential equations with many unknown variables in the present work is the Runge-Kutta-Gill integration method. The ordinary and second-order differential forms of the conservation equations of the pre-sheath model are derived in Appendix B.

3.3 Space charge region: sheath

3.3.1 Mathematical model with respect to the sheath layer

3.3.1.1 Potential distribution in the sheath region

The very thin space charge sheath layer is located adjacent to the cathode surface with a considerable shorter length compared with the pre-sheath layer. It is usually assumed to be collisionless. The potential drop in sheath layer is decisive important to determine the distribution of particles. The potential distribution over the sheath layer is obtained by Poisson's Equation:

$$-\varepsilon_0 \frac{d^2V}{dx^2} = e(n_i(x) - n_{e1}(x) - n_{e2}(x)) \quad (3.3.1)$$

where V is the potential (V); e is the elementary charge (1.60×10^{-19} C) and ε_0 is the permittivity of free space (8.85×10^{-12} F/m); $n_i(x)$ is the number density of ions move towards the cathode surface ($1/m^3$); $n_{e1}(x)$ is the number density of electrons emitted from the cathode surface ($1/m^3$); $n_{e2}(x)$ is the number density of fast electrons moving towards the cathode surface through back diffusion ($1/m^3$); x is the direction normal to the cathode surface oriented from the surface towards the arc column. This equation requires the boundary conditions at cathode surface ($x = 0$) and sheath edge ($x = L_s$).

3.3.1.2 Ions density distribution

The ion flux is conserved over the whole sheath layer since there is no ionization and recombination happened. It means that the number density flux of the ions towards the cathode surface equals to the flux at sheath edge. The conserved number density flux of ions entering from the sheath edge is given by:

$$j_i = n_s v_s = n_i(x) v_i(x) \quad (3.3.2)$$

where j_i is the number density flux of ions; n_s and v_s are respectively the ions number density and velocity at the sheath edge while $n_i(x)$ and $v_i(x)$ represent number density and velocity distributions of the ions over the sheath layer. Once the ions move into the sheath layer, they are accelerated by the potential drop $V_c - V(x)$ to a velocity:

$$v_i(x) = \sqrt{v_s^2 + \frac{2e[V_c - V(x)]}{m_i}} \quad (3.3.3)$$

where V_c is the potential drop over the sheath layer and $V(x)$ is the potential distribution. The ions are accelerated towards the cathode surface by the sheath potential drop and the corresponded number density is decreased to maintain a constant ion flux. Based on the Bohm criterion, the ions velocity at the sheath edge v_s is assumed to be the Bohm velocity [21],

$$v_s = \sqrt{\frac{k_B(T_{es} + T_{is})}{m_i}} \quad (3.3.4)$$

where T_{es} and T_{is} are the temperatures of the electrons and ions at the sheath edge (K). The ions density distribution over the sheath layer is thus determined following current conservation,

$$n_i(x) = n_{e,SE} \sqrt{\frac{k_B(T_{es} + T_{is})}{2e[V_c - V(x)] + k_B(T_{es} + T_{is})}} \quad (3.3.5)$$

where $n_{e,SE}$ is the number density of electrons at the sheath edge that equals to the ions number density ($n_{i,SE}$) and it would be solved as a part of the solutions in the pre-sheath layer as well as the temperatures of the electrons and heavy particles T_{es} and T_{is} . They are taken as the boundary conditions for the sheath model.

3.3.1.3 Density of electrons emitted from the cathode surface

As the predominant mechanism to remove the thermal energy, electrons emission from the cathode surface is sensitively affected by the cathode material properties. Generally, the cathode that could withstand high pressure arcs is classified in terms of thermionic (hot) cathode and non-thermionic (cold) cathode, which depends on two representative parameters: cathode surface temperature and induced surface electric field. Thermionic cathode normally uses refractory material with boiling temperature higher than 3000K [22] (e.g. tungsten, carbon) in comparison with non-thermionic cathode (e.g. copper). The electrons emitted from thermionic cathode is principally determined by the cathode surface temperature while the induced electric field has a negligible impact. In contrast, the electrons that largely extracted from non-thermionic cathode surface is determined by the induced electric field while the cathode surface temperature is comparative lower. These two cathode types differ in their capability to sustain electrons emission from the surface without significant material melting and vaporization. A comparison between the thermionic and non-thermionic cathodes are listed in Table 3.3.

Table 3.3 Comparison between the thermionic and non-thermionic cathodes.

Cathode types \ Parameters	Thermionic	Non-thermionic
Surface temperature	Generally, > 3000 K	Generally, < 3000 K if field emission dominates
Estimated current density	$\approx 10^7 - 10^8 \text{ A/m}^2$	> 10^{10} A/m^2 or as high as 10^{11} A/m^2 or 10^{12} A/m^2
Arc attachment	Fix or move slow	Move rapidly and randomly

(1) Thermionic emission

The electrons are principally emitted from the cathode surface by thermionic emission when the cathode is heated to a sufficient high temperature. The corresponding current density is calculated by the Richardson-Dushman equation [23]:

$$J_{te} = \frac{4\pi m_e k_B^2 e}{h^3} T_c^2 \cdot \exp\left(-\frac{\phi_F}{k_B T_c}\right) \quad (3.3.6)$$

where ϕ_F is the material work function (4.4 eV for copper) and T_c is the cathode surface temperature. The theoretical value of the Richardson constant is:

$$A = \frac{4\pi m_e k_B^2 e}{h^3}$$

normally, this constant should be multiplied with a correction factor which depends on the material and A is approximately $120 \text{ Acm}^{-2}\text{K}^{-2}$ for pure copper [24].

The thermionic emission is used to define the process of free electrons emitted from the cathode surface by external thermal energy. The material work function represents the required minimum energy for electrons escaping from cathode surface by overcoming the attractive force. The thermionic emission current density illustrates an exponentially dependence on the cathode surface temperature only. As presented in Figure 3.3, only a smaller number of electrons are emitted from the cathode surface at low temperatures and it is increased substantially from 3,000 K for the tungsten cathode (2.63 eV for the tungsten) while it is still less for the copper cathode.

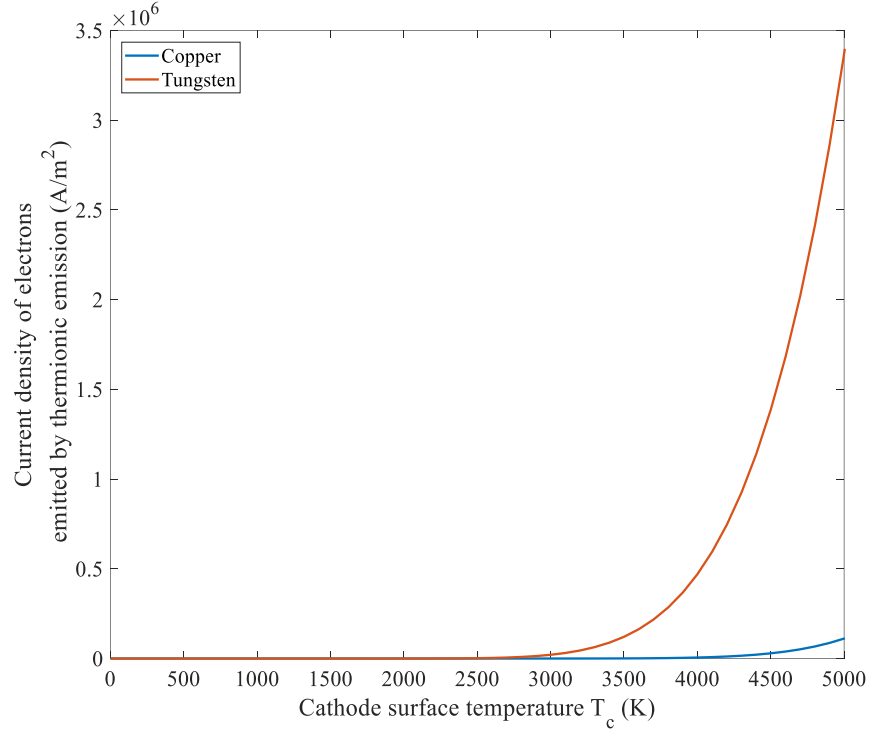


Figure 3.3 Current density of the electrons emitted through thermionic emission as a function of cathode surface temperature.

As a result of electrons emission, the cathode surface is constantly biased negative. The emitted electrons are repelled from the cathode surface towards the pre-sheath layer and the ions in the pre-sheath layer are attracted and bombarded towards the cathode surface. An electric field is induced at the cathode surface due to this negatively charged cathode surface. With considering the effects of this induced electric field, the surface potential barrier for electrons escaping from the cathode surface is decreased which reduces the required energy for electrons escaping from the cathode surface and the current density of electrons emitted by this field-enhanced thermionic emission is given as [25], [26]:

$$J_{te} = \frac{4\pi m_e k_B^2 e}{h^3} T_c^2 \cdot \exp\left(-\frac{A_{eff}}{k_B T_c}\right) \quad (3.3.7)$$

$$A_{eff} = \phi_F - \sqrt{\frac{e^3 E_c}{4\pi \epsilon_0}} \quad (3.3.8)$$

where E_c is the electric field strength at cathode surface and A_{eff} is the effective work function (eV) with the consideration of the Schottky correction term.

(2) Field emission

When the induced electric field becomes very high, the electrons could be emitted from the cathode surface by tunnelling. Based on the descriptions of the quantum-mechanical

effect of tunnelling [27], the current density of electrons emitted by field emission could be determined using the Fowler-Nordheim formula [28], [29]:

$$J_{fe} = \frac{e^2}{2\pi h} \cdot \frac{1}{(\phi_F + \varepsilon_F)} \cdot \sqrt{\frac{\varepsilon_F}{\phi_F}} \cdot \exp\left(-\frac{8\pi\sqrt{2m}\phi_F^{3/2}}{3ehE}\right) \quad (3.3.9)$$

where ε_F is the Fermi energy of the metal [30], [31] and E is the external electric field. This formula could be simplified as [32]:

$$J_{fe} = \frac{e^3}{8\pi h t^2(y)} \cdot \frac{E_c^2}{\phi_F} \cdot \exp\left(-\frac{8\pi\sqrt{2m_e}\phi_F^{3/2}}{3ehE_c} v(y)\right) \quad (3.3.10)$$

where the Nordheim parameter y (dimensionless) is calculated by:

$$y = \frac{\sqrt{e^3 E_c / 4\pi \varepsilon_0}}{\phi_F} \approx 3.794687 \times 10^{-5} \frac{\sqrt{E_c}}{\phi_F} \text{ eV} \cdot V^{-\frac{1}{2}} \cdot m^{\frac{1}{2}} \quad (3.3.11)$$

and the correction factors $t(y)$ and $v(y)$ are expressed as:

$$v(y) = \sqrt{1+y} \cdot [E(m) - yK(m)] \quad (3.3.12)$$

$$t(y) = (1+y)^{-\frac{1}{2}} \{(1+y)E(m) - yK(m)\} \quad (3.3.13)$$

where $K(m)$ and $E(m)$ are complete elliptic integrals [33] and m is calculated with y :

$$m = k^2 = \frac{1-y}{1+y} \quad (3.3.14)$$

A simplified approximation for $v(y)$ is given as:

$$v(y) = 1 - y^2 + qy^2 \ln y^2 \quad (3.3.15)$$

and $t(y)$ is given in terms of v and $\frac{dv}{dy}$ by [34], [35]:

$$t(y) = v(y) - \frac{2}{3} y \frac{dv}{dy} \quad (3.3.16)$$

where q is an adjustable constant and according to the least squares minimization of the absolute and relative errors, Forbes and Deane [35] found $q=1/6$ is close to the optimum value. With the known $v(y)$, $t(y)$ could be simply calculated by:

$$t(y) \approx 1 + \frac{1}{9} (y^2 - y^2 \ln y) \quad (3.3.17)$$

There are two defined Fowler-Nordheim constants a_1 and b_1 with forms:

$$a_1 \equiv \frac{e^3}{8\pi h} \approx 1.541434 \times 10^{-6} \text{ A} \cdot \text{eV} \cdot V^{-2} \quad (3.3.18)$$

$$b_1 \equiv \frac{8\pi\sqrt{2m_e}}{3eh} \approx 6.83089 \times 10^9 \text{ eV}^{-\frac{3}{2}} \cdot \text{V} \cdot \text{m}^{-1} \quad (3.3.19)$$

and the corresponded current density could be rewritten as a function of E_c . Figure 3.4 shows the variation of field emission current density with respect to the induced surface electric field.

$$J_{fe} = \frac{a}{t^2(y)} \cdot \frac{E_c^2}{\phi_F} \cdot \exp\left(-\frac{b\phi_F^{\frac{3}{2}}}{E_c} v(y)\right) \quad (3.3.20)$$

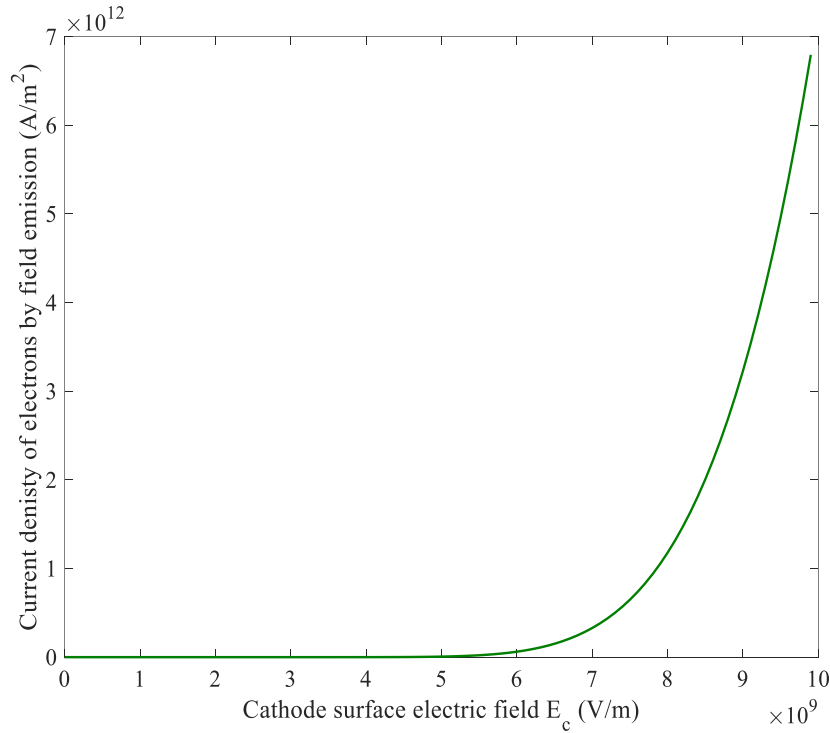


Figure 3.4 Current density of electrons emitted through field emission as a function of the cathode surface electric field.

(3) Thermo-field emission

In practical conditions for the arc-cathode interaction when the surface temperature and the induced electric field are both higher, the electrons would be emitted as a combined result of thermionic and field emissions. This is known as “Thermo-field emission” (T-F emission). The current density of thermo-field emission is determined by Murphy and Good [36], [37],

$$J_{T-F}(T_c, E_c, \phi_F) = e \int_{-W_a}^{+\infty} N(T_c, W, \phi_F) D(E_c, W) dW \quad (3.3.21)$$

where W describes the energy for the electrons motion normal to the cathode surface,

$$W = \frac{p^2(x)}{2m} + V_E(x) \quad (3.3.22)$$

where x is the coordinate normal to the surface; $p(x)$ is electron momentum normal to the surface and $V_E(x)$ is the effective electron potential energy,

$$V_E(x) = \begin{cases} -e^2(4x)^{-1} - eE_c x & x > 0 \text{ outside the emitter} \\ -W_a & x < 0 \text{ inside the emitter} \end{cases} \quad (3.3.23)$$

The terms $-e^2(4x)^{-1}$ and $-eE_c x$ represent the contributions from the image force and the electric field induced at cathode surface E_c ; $-W_a$ is the effective constant potential energy in the cathode bulk and the actual value is not important in the calculation which can be set as $-\infty$ since it is much lower than the Fermi energy (7.0 eV for copper) [38]; N is the Fermi-Dirac distribution for free electrons in the cathode, determined by:

$$N(T_c, W, \phi_F) = \frac{4\pi m_e k_B T_c}{h^3} \ln \left[1 + \exp \left(-\frac{W + \phi_F}{k_B T_c} \right) \right] \quad (3.3.24)$$

and $D(E_c, W)$ is the tunnelling probability:

$$D(E_c, W) = \begin{cases} 1 & W > W_l \\ \frac{1}{1 + \exp \left[\frac{a \cdot v(y)}{y^{\frac{3}{2}}} \right]} & W < W_l \end{cases} \quad (3.3.25)$$

with

$$W_l = -\sqrt{\frac{e^3 E_c}{8\pi \epsilon_0}} \quad (3.3.26)$$

$$a = \frac{4\sqrt{2}}{3(4\pi \epsilon_0)^{\frac{3}{4}}} \left[\frac{(2\pi)^4 m_e^2 e^5}{h^4 E_c} \right]^{\frac{1}{4}} \quad (3.3.27)$$

$$y = \frac{\sqrt{2} W_l}{W} \quad (3.3.28)$$

$$v(y) = \begin{cases} \sqrt{1+y} \left[E \left(\left(\frac{1-y}{1+y} \right)^{\frac{1}{2}} \right) - y K \left(\left(\frac{1-y}{1+y} \right)^{\frac{1}{2}} \right) \right] & y < 1 \\ \sqrt{\frac{y}{2}} \left[2E \left(\left(\frac{y-1}{2y} \right)^{\frac{1}{2}} \right) - (y+1) K \left(\left(\frac{y-1}{2y} \right)^{\frac{1}{2}} \right) \right] & y > 1 \end{cases} \quad (3.3.29)$$

The complete elliptic integrals of the first kind $K(k)$ and second kind $E(k)$ as a function of elliptic modulus k are respectively calculated:

$$K(k) = \int_0^{\frac{\pi}{2}} \frac{1}{\sqrt{1 - k^2 \sin^2 \theta}} d\theta \quad (3.3.30)$$

$$E(k) = \int_0^{\frac{\pi}{2}} \sqrt{1 - k^2 \sin^2 \theta} d\theta \quad (3.3.31)$$

substituting them into Eq.(3.3.29),

$$\begin{aligned} & J_{T-F}(T_c, E_c, \phi_F) \\ &= \frac{4\pi m_e k_B T_c e}{h^3} \left\{ \int_{-\infty}^{W_l} \frac{\ln \left[1 + \exp \left(-\frac{W + \phi_F}{k_B T_c} \right) \right]}{1 + \exp \frac{av(y)}{y^{\frac{3}{2}}}} dW \right. \\ & \quad \left. + \int_{W_l}^{+\infty} \ln \left[1 + \exp \left(-\frac{W + \phi_F}{k_B T_c} \right) \right] dW \right\} \end{aligned} \quad (3.3.32)$$

A simplified formula with a good approximation of the thermo-field emission current density could be used in the present work. It is reasonable for the induced electric field range from 1.1×10^8 V/m to 1.2×10^{10} V/m with the cathode surface temperature from 300 K to 10,000 K. Hantzsche [39] derived this formula as a harmonic combination of thermionic and field emission formula using Padé approximant in the framework based on the Murphy-Good theory, with form:

$$J_{T-F} = K \left(A_1 T_c^2 + B_1 E_c^{\frac{9}{8}} \right) \exp \left[- (C_1 T_c^2 + D_1 E_c^2)^{-\frac{1}{2}} \right] \quad (3.3.33)$$

where K is a correction factor that mainly depends on the cathode surface temperature and surface electric field strength,

$$K = \frac{8.1 \times 10^3 T_c^3 + 3.5 \times 10^{-5} E_c^2}{9.1 \times 10^3 T_c^3 - 53 \times E_c T_c + 7.5 \times 10^{-5} E_c^2} \quad (3.3.34)$$

and the constants A, B, C and D are listed below for copper with work function 4.4 eV [40]:

$$\begin{aligned} A_1 &= 1.74 \times 10^6 \text{ Am}^{-2} \text{ K}^{-2} \\ B_1 &= 1.14 \times 10^4 \text{ AV}^{-9/8} \text{ m}^{-7/8} \\ C_1 &= 3.83 \times 10^{-10} \text{ K}^{-2} \\ D_1 &= 2.52 \times 10^{-22} \text{ V}^{-2} \text{ m}^2 \end{aligned} \quad (3.3.35)$$

The thermo-field emission current density as a function of surface temperature (T_c) and induced electric field strength (E_c) is presented in Figure 3.5.

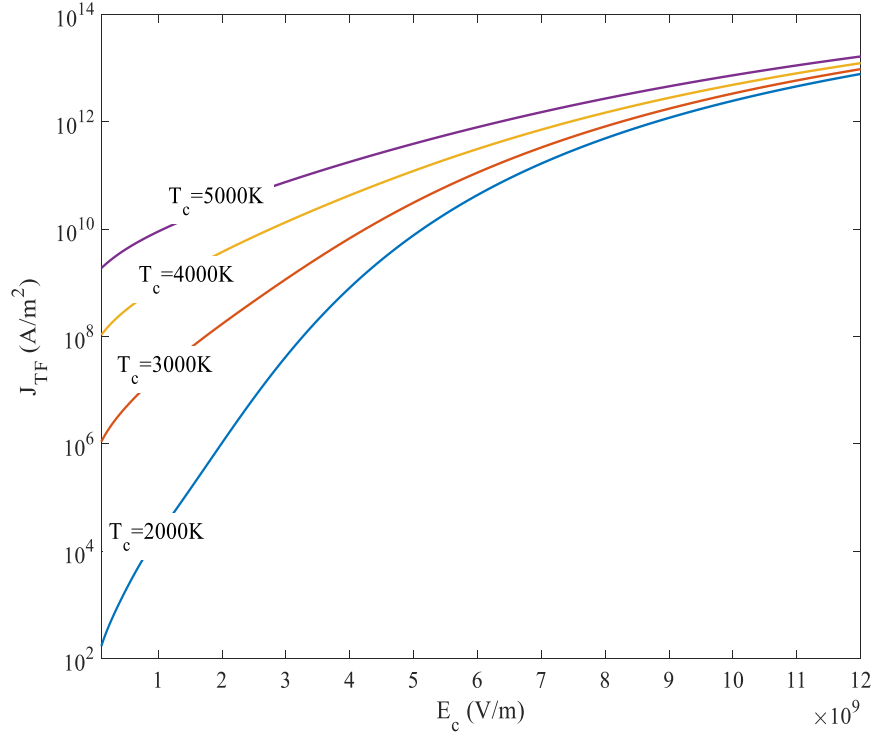


Figure 3.5 Thermo-field emission as a function of surface temperature and electric field strength of copper cathode.

(4) Number density of electrons emitted from the cathode surface

The velocity distribution of the emitted electrons is determined from the derivative of Maxwell-Boltzmann distribution [41]. The mean kinetic energy of emitted electrons is $2k_B T_c$. The electrons are accelerated by the cathode sheath potential drop towards the pre-sheath layer and the electrical potential energy of these electrons in the sheath layer is determined by $e\phi(x)$. The energy balance equation of emitted electrons in the sheath layer is,

$$\frac{1}{2} m_e v_e^2(x) + [-eV(x)] = 2k_B T_c \quad (3.3.36)$$

where $v_e(x)$ is the velocity of the electrons in the sheath layer:

$$v_e(x) = \sqrt{\frac{4k_B T_c + 2eV(x)}{m_e}} \quad (3.3.37)$$

and the number density of electrons emitted from the cathode surface is thus calculated by:

$$n_{e1}(x) = \frac{J_e}{e \cdot v_e(x)} \quad (3.3.38)$$

and the number density of emitted electrons arrives at the sheath edge becomes:

$$n_{c,SE} = \frac{J_e}{e \sqrt{\frac{4k_B T_c + 2eV_c}{m_e}}} \quad (3.3.39)$$

3.3.1.4 Density of the back-diffusion electrons

From previous explanation that the cathode surface becomes negative as a consequence of electrons emission, the emitted electrons are accelerated towards the pre-sheath layer. However, a smaller portion of electrons in the pre-sheath overcome the sheath potential drop and eventually reach the cathode surface. The number density of these electrons that back diffused to the cathode surface from the plasma is determined by:

$$n_{e2}(x) = n_{p,SE} \exp\left\{\frac{e[V(x) - V_c]}{k_B T_{es}}\right\} \quad (3.3.40)$$

and the number density flux of back diffusion electrons is determined by:

$$j_{bd} = \frac{1}{4} n_{p,SE} \bar{c}_e \exp\left[-\frac{eV_c}{k_B T_{es}}\right] \quad (3.3.41)$$

where $n_{p,SE}$ is the number density of back diffusion electrons at the sheath edge and \bar{c}_e is the electron mean velocity.

$$n_{p,SE} = n_{e,SE} - n_{c,SE} \quad (3.3.42)$$

$$\bar{c}_e = \sqrt{\frac{8k_B T_e}{\pi m_e}} \quad (3.3.43)$$

Up to here, the net electric current density flowed in the space charge sheath layer could be treated as a summation of three terms:

$$\begin{aligned} J_{tot} &= J_i + J_e - J_{bd} \\ J_i &= e j_i \\ J_{bd} &= e j_{bd} \\ J_e &= e j_e \end{aligned} \quad (3.3.44)$$

where J_i , J_{bd} and J_e represent the current densities of ions, back-diffusion electrons and emitted electrons while j_i , j_{bd} and j_e are the corresponded number density fluxes.

3.3.2 Numerical solution for the sheath region

To solve the equations of the sheath model, reasonable boundary conditions should be specified. At the sheath edge, boundary conditions are taken from the overall solutions of the pre-sheath model and the potential at the sheath edge φ_{SE} is assumed to be zero. Other prescribed parameters in the calculation are listed in Table 3.4:

Table 3.4 Prescribed parameters of the sheath region calculation.

Boundary Conditions	
Total current density (J)	$1.5 \times 10^8 \text{ A/m}^2$
Temperature at cathode surface	$T_c = 3000 \text{ K}$
Cathode sheath initial voltage drop (Set to the experimentally determined value [42])	15 V

The boundary condition at the sheath edge is one of the most important factors to obtain an overall solution of the established near cathode non-LTE layer model. In the present work, Bohm criterion is adopted to describe the sheath edge where continuum approach becomes invalid in the sheath layer.

3.3.3 Energy transfer between the cathode and arc column

To determine the mass loss from the cathode surface, the energy transfer at the interface between the cathode bulk and non-LTE arc column need to be specified. The predicted thermal conduction flowed inside the cathode bulk and radiation from the arc column, which only contribute small portions of total flux, are not considered in present study. The associated energy flux terms transferred at cathode surface are described as below.

(1) Ions bombardment heating effect

The ions inside the sheath layer is produced from the ionization in the pre-sheath. They are accelerated by the cathode sheath potential drop and the current carried by the ions over the sheath layer keeps constant. In addition, the ions not collide with other particles and it means that the ions temperature in the sheath layer equals to that at the sheath edge. With assuming positive ions are immediately neutralized at the cathode surface, the kinetic energy of ions brings to the cathode is:

$$q_{kinetic} = eV_c \quad (3.3.45)$$

and the energy released at the cathode surface by the neutralization is:

$$q_{neutralize} = E_i - A_{eff} \quad (3.3.46)$$

where E_i is the ionization energy (eV) of the plasma gas.

With the consideration of enthalpy effects, the total energy flux carried by ions to heat up the cathode surface is determined by:

$$q_{ion} = j_i \left[eV_c + E_i - A_{eff} + \frac{5}{2} k_B T_{h,SE} \right] \quad (3.3.47)$$

where $T_{h,SE}$ is the temperature of heavy particles at the sheath edge.

(2) Thermal conduction by heavy particles

The thermal conduction from the arc plasma to the cathode is simply calculated by [43]:

$$q_{con} = \lambda_{eff} \nabla T = \frac{\lambda_{eff} (T_{arc} - T_c)}{\delta} \quad (3.3.48)$$

where λ_{eff} is the effective thermal conductivity at the arc-cathode interface that taken as the harmonic mean of thermal conductivities of the arc plasma and cathode material; δ is the length of cathodic non-LTE layer and T_{arc} is the temperature of the arc column.

(3) Heating effects by the back-diffusion electrons

The energy liberated by back diffusion electrons when they reach the cathode surface is determined by the flux:

$$q_{bd} = j_e (A_{eff} + \frac{5}{2} k_B T_{es}) \quad (3.3.49)$$

(4) Cooling effects by electrons emitted from the cathode surface

The electrons emission has important effect on the energy balance condition at cathode surface. As mentioned before, the electrons are confined in the cathode by the potential barrier. If electrons overcome this barrier and emit by thermionic emission, the energy flux taken away by these emitted electrons is determined by:

$$q_{te} = j_{te} (A_{eff} + \frac{5}{2} k_B T_c) \quad (3.3.50)$$

With the considerations of quantum tunnelling effect when the induced surface electric field becomes strong, the energy would be transferred as a consequence of “Nottingham effect”. It could not be simply treated as cooling or heating process [44] which is judged by a defined inversion temperature [45], [46], [47].

The average energy of an emitted electron is determined by the “Nottingham potential” [1], [38], [48]:

$$\varepsilon = \frac{e}{j(T_c, E_c, \phi)} \int_{-\infty}^{+\infty} W P_W(W, T_c, E_c, \phi) dW + \phi \quad (3.3.51)$$

where $P_W(W, T_c, E_c, \phi) dW$ is the energy distribution for electrons.

$$W = \frac{p^2(x)}{2m_e} + V(x) \quad (3.3.52)$$

$$P_W(W, T_c, E_c, \phi) = \int_{-\infty}^W N_W(W, T_c, \phi) D_W(W, E_c) dW \quad (3.3.53)$$

where N_W is the number of electrons on the cathode surface per time interval and area; D_W is the tunnelling probability [38]. The supply function N_W could be determined by assuming the emitted electrons from the cathode follow Fermi-Dirac distribution. With the Fowler-Nordheim approximation, the average energy is calculated analytically by:

$$\varepsilon_{FN} = -\pi k_B T \cot\left(\frac{\pi T}{2 T^*}\right) \quad (3.3.54)$$

where T^* is the so-called inversion temperature. The cathode is heated by the electrons if cathode surface temperature is below this value and it is cooled otherwise. The energy carried by electrons, as a result of Nottingham effect, is proportional to the flux $j\varepsilon$,

$$q_{not} = j_{T-F} \varepsilon_{FN} \quad (3.3.55)$$

and the inversion temperature could be calculated using a fitting formula in the range of $E \in [2 \times 10^8, 10^{10}] V/m$ and $\phi \in [2, 5] eV$,

$$T^* = \omega_1 \frac{E^{\omega_2}}{\phi^{\omega_3}} \left\{ 1 + \frac{\omega_4}{\phi^{\omega_5}} \left[1 + \tanh\left(\omega_6 \frac{E^{\omega_7}}{\phi^{\omega_8}} - \omega_9\right) \right] \right\} \quad (3.3.56)$$

where the optimized values of ω_i are:

$$\begin{aligned} \omega_1 &= 7.1130 \times 10^{-7}; \omega_2 = 0.98604; \\ \omega_3 &= 0.47483; \omega_4 = 1.0296; \\ \omega_5 &= 0.91905; \omega_6 = 4.8022; \\ \omega_7 &= 8.8832 \times 10^{-2}; \omega_8 = 0.15358; \\ \omega_9 &= 30.371; \end{aligned} \quad (3.3.57)$$

The average energy of an emitted electron can be obtained by a fitting formula as well:

$$\varepsilon_N = \begin{cases} -a_2 a_{T^*} \frac{2}{\pi} T \cot\left(\frac{\pi T}{2 T^*}\right) & T \leq T^* \\ a_2 a_{T^*} (T - T^*) (1 - \vartheta) + (a_\infty T + b_2) \vartheta & T > T^* \end{cases} \quad (3.3.58)$$

with

$$a_{T^*} := \frac{d}{dT} \varepsilon_N |_{T=T^*} = \frac{\pi^2 k_B}{2} \quad (3.3.59)$$

$$a_\infty := \frac{d}{dT} \varepsilon_N |_{T \rightarrow \infty} = 2k_B \quad (3.3.60)$$

$$\vartheta = \frac{p^s}{1 + p^s} \quad (3.3.61)$$

$$p = c_2 \left(\frac{T}{T^*} - 1 \right) \quad (3.3.62)$$

where the optimized values are specified as:

$$a_2 = 1 - 1.03104 \times 10^{-2} \frac{E^{0.193326}}{\phi^{0.821433}} \quad (3.3.63)$$

$$b_2 = \phi - 1.99435 \times 10^{-5} E^{0.533739} \quad (3.3.64)$$

$$c_2 = \frac{0.687365}{\phi^{0.0525966}} \quad (3.3.65)$$

$$s = 3.48481 \quad (3.3.66)$$

(5) Radiation cooling from the cathode

The radiative loss is calculated by means of the principle of black-body radiation.

$$q_{rad,c} = \varepsilon \sigma T_c^4 \quad (3.3.67)$$

where ε is the emissivity of cathode material (0.07 for copper [49]) and σ is the Stefan-Boltzmann constant ($5.67 \times 10^{-8} \text{ Wm}^{-2} \text{ K}^{-4}$).

(6) Cathode material vaporization

When the cathode surface temperature continuously increased and exceeds the material melting and vaporization points, the extra energy would change the material from solid to liquid and finally to vapour. The vaporization flux is obtained by:

$$q_{vap} = q_{con} + q_{ion} + q_{bd} - q_{not} - q_{rad,c} \quad (3.3.68)$$

and the rate of the material vaporization is calculated by:

$$\dot{m} = \frac{q_{vap}}{h_v} \quad (3.3.69)$$

where h_v is the energy required for vaporization (5204 J/kg for copper).

3.3.4 Overall solution for the non-LTE layer model

Numerical calculation of the near cathode non-LTE model is performed from the LTE arc plasma side towards the cathode surface by patching the solutions of pre-sheath and sheath models. The calculation procedure is presented in Figure 3.6.

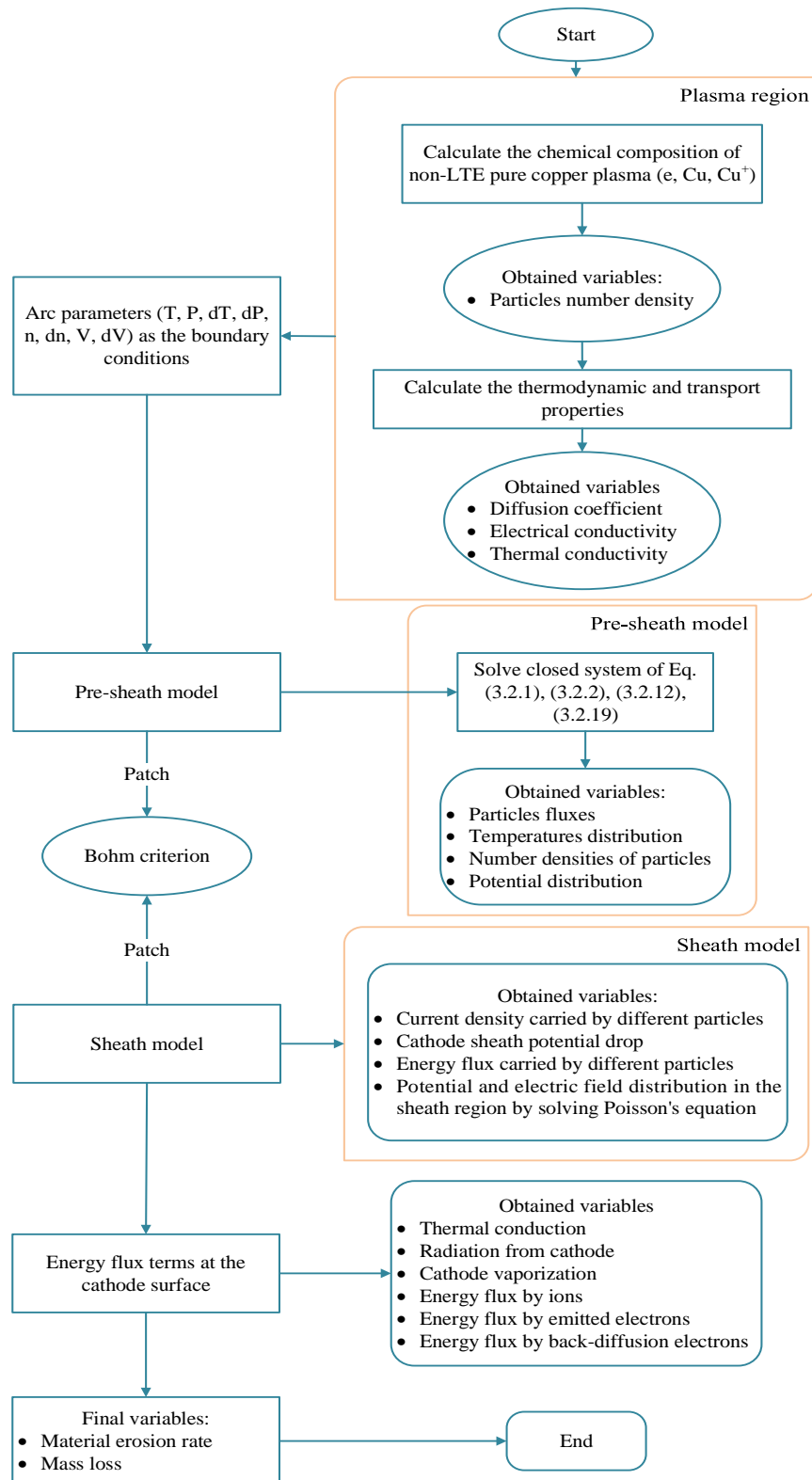


Figure 3.6 Calculation procedure of the non-LTE model.

3.4 Determination of the mass loss from the cathode surface

In the model, the total current density and pressure are prescribed with constant values. The established pre-sheath model in this chapter is compared with the works of Hsu *et al* [50] and Rethfeld *et al* [12] by calculating the case of argon plasma interacts with a tungsten cathode.

3.4.1 Argon plasma with a tungsten cathode

In the pre-sheath model, the second-order differential equations (3.2.1), (3.2.2), (3.2.12) and (3.2.16) are numerically solved with a set of conditions at the pre-sheath boundary of arc plasma side: $T_e=T_h=21,000$ K; $\partial T/\partial x=-4.0\times 10^7$ K/m; $n_e=n_i=1.727\times 10^{23}$ m⁻³; $\partial n/\partial x=1.692\times 10^{24}$ m⁻⁴; $V=8.5$ V; $\partial V/\partial x=-1.45\times 10^4$ V/m. The total current density is set to $J_{tot}=1.2\times 10^8$ A/m² at atmospheric pressure. From the models described by Hsu and Rethfeld, the Potapov method is used to determine the number densities of particles while the method of Van de Sanden *et al* is adopted in the present work which has been described in Chapter 2. The generalized Saha equation for the two-temperature plasma ionization following the method of Potapov is given by [51]:

$$n_e \left(\frac{n_i}{n_a} \right)^{\frac{1}{\theta}} = 2 \left(\frac{Z_i^*}{Z_a^*} \right)^{\frac{1}{\theta}} \left(\frac{2\pi m_e k_B T_e}{h^2} \right)^{\frac{3}{2}} \exp \left(-\frac{E_{i,Cu} - \Delta E_{(0)}}{k_B T_{ex}} \right) \quad (3.4.1)$$

where Z_i^* and Z_a^* are the generalized internal partition function of monatomic species and determined by:

$$Z_w^* = [Z_w^e(T_e)]^\theta = [Z_w^{int}(T_e)]^\theta \quad (3.4.2)$$

where w is the species contained in the plasma.

As shown in Figure 3.7, the results indicate that the thickness of pre-sheath is slightly larger in comparison with that of Hsu's (0.09 mm) [50]. In the calculation, the electrons and heavy particles have the identical temperatures at the outer pre-sheath boundary of the plasma side. The thicker pre-sheath layer results in a higher potential drop (6.8 V). Despite the difference of computed thermophysical properties, the discrepancy of the calculation results is possibly due to the boundary condition at the sheath edge as well. Based on his description, the continuum approach used for the pre-sheath model is valid until the variation of electron number density over the one electron mean free path reaches the same order of magnitude as electron number itself. This criterion is of more

qualitative nature compared with Bohm criterion. Moreover, the method of Potapov to calculate the chemical composition of the gaseous medium always cause more intense change of species concentration and lead to a much more drastic change of the plasma thermophysical properties [52] while the method of Van de Sanden *et al* provides more realistic calculation which is preferred in the present work based on a comparison [51].

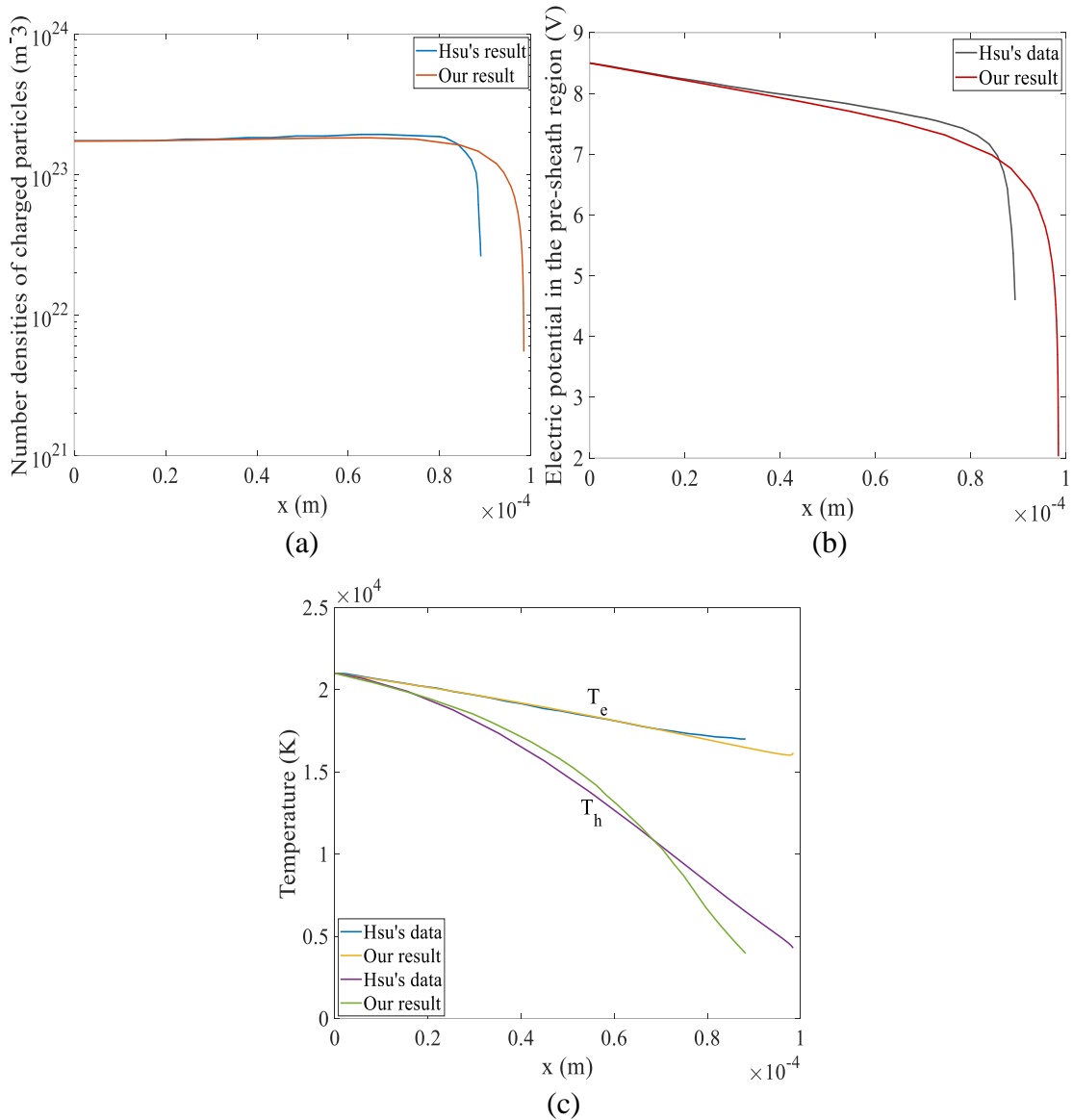


Figure 3.7 Spatial dependences of particles number densities (a), potential (b) and temperature (c) in the pre-sheath layer towards the sheath edge in comparison with the reference.

3.4.2 SF₆ plasma with a copper cathode

3.4.2.1 Pre-sheath layer

With assuming a severe contact erosion occurred, the non-LTE layer with much smaller thickness contains only pure copper vapour which contains three species: e , Cu and Cu^+ .

Figure 3.8 presents the spatial distributions of the particle number densities in the pre-sheath layer from the boundary ($x=0$) at the arc plasma side towards the sheath edge. It is observed that the charged particles number density is decreased towards the sheath edge which is due to the collisions in the pre-sheath layer. However, the ionization rate is substantially increased towards the cathode surface because large amount of metallic vapour is produced from the cathode surface. It leads to a considerable increase of the neutral particles number density although it is expected to be lower in the majority of the pre-sheath due to the lower ionization energy of copper atoms.

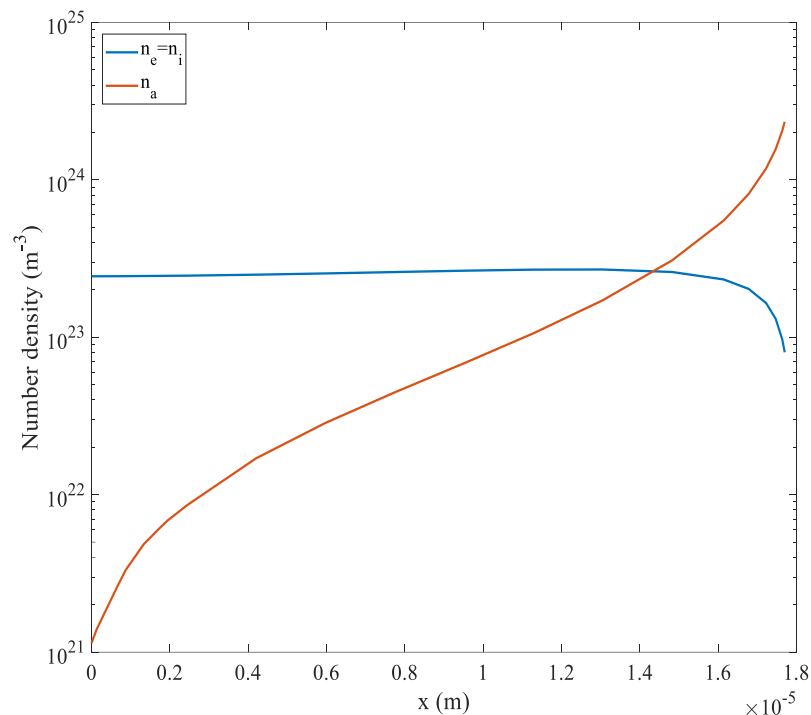


Figure 3.8 Spatial dependences of the number densities of particles in the pre-sheath layer towards the cathode surface.

From the calculation, there is an approximately 3.6 V potential drop over the pre-sheath layer from the arc plasma side towards the sheath edge, as shown in Figure 3.9. Actually, the initial potential value of 15 V at the arc side boundary of the pre-sheath is arbitrarily given as a reference value and it could be adjusted to the real value from the magneto-hydrodynamics model for the calculation of LTE arc plasma. In addition, the diffusion fluxes of electrons and ions and the corresponded terms described in Eq. (3.2.9) and (3.2.10) are demonstrated in Figure 3.10. The negative sign represents the flux diffusion direction which is opposite to the defined positive direction from the cathode surface to the arc plasma. The results indicate that the diffusion fluxes of electrons and ions are dominantly driven by the potential drop over the pre-sheath layer.

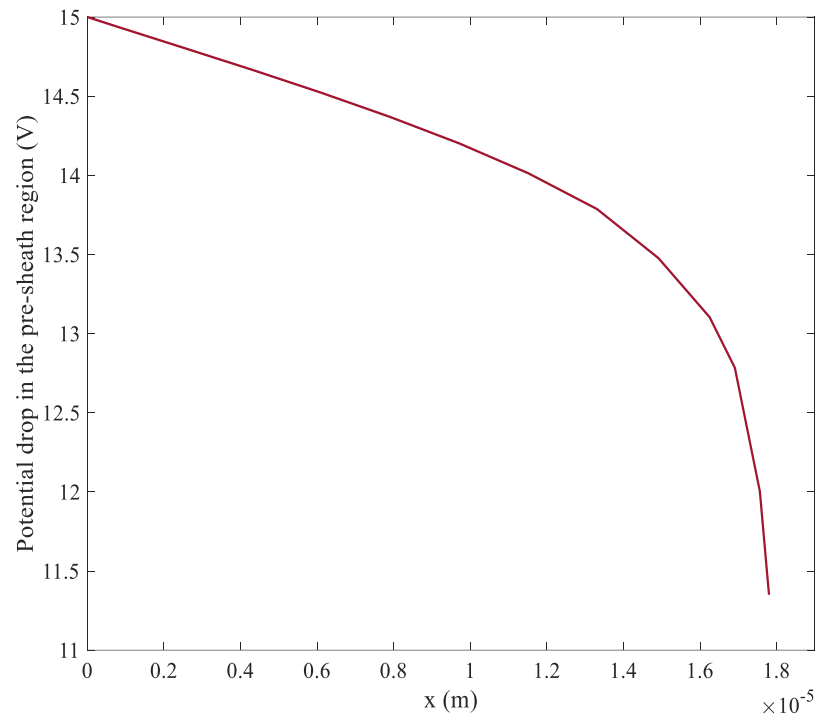


Figure 3.9 Spatial dependence of potential in the pre-sheath layer.

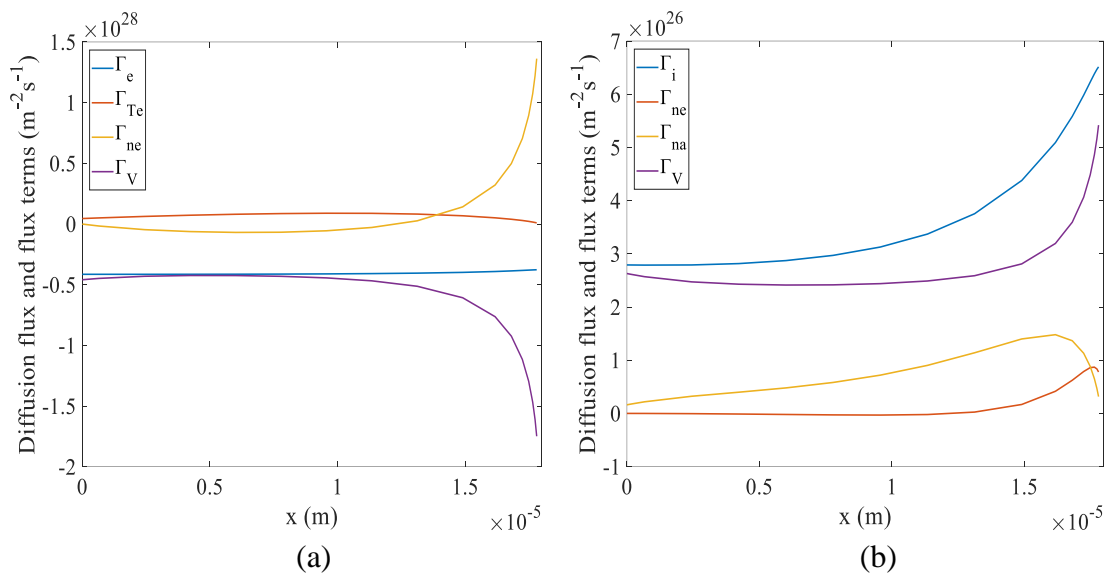


Figure 3.10 Spatial dependence of the diffusion flux distributions of the electrons (a) and ions (b) while “ Γ ” represents the total diffusion flux and Γ_{Te} , Γ_{ne} , Γ_{na} , Γ_V represent the diffusion flux components driven by the variation of temperature, number density and potential respectively.

Figure 3.11 presents the spatial distribution of the charged particles temperatures. It is observed that the temperature of heavy particles is reduced significantly in comparison with the electrons. Over the pre-sheath layer, the electrons temperature differs from the heavy particles due to the non-equilibrium environment. Since the electrons are lighter than the heavy particles and they are emitted from the cathode surface with much higher

velocity, the temperature equilibration process during the collisions becomes faster and easier for electrons. Moreover, the heavy particles temperature continuously decreases to the cathode surface temperature (3,000 K in the present work) from the arc column.

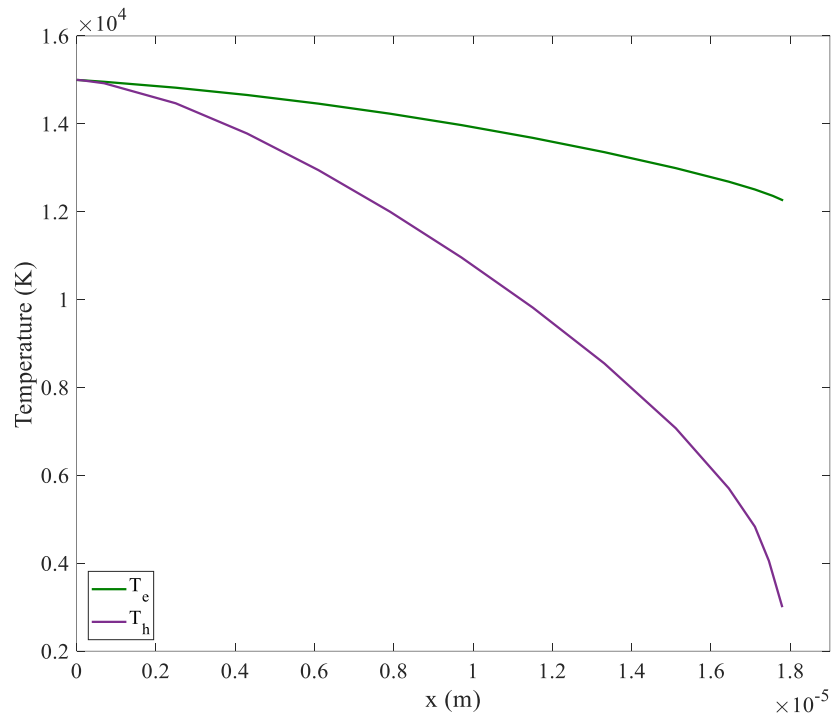
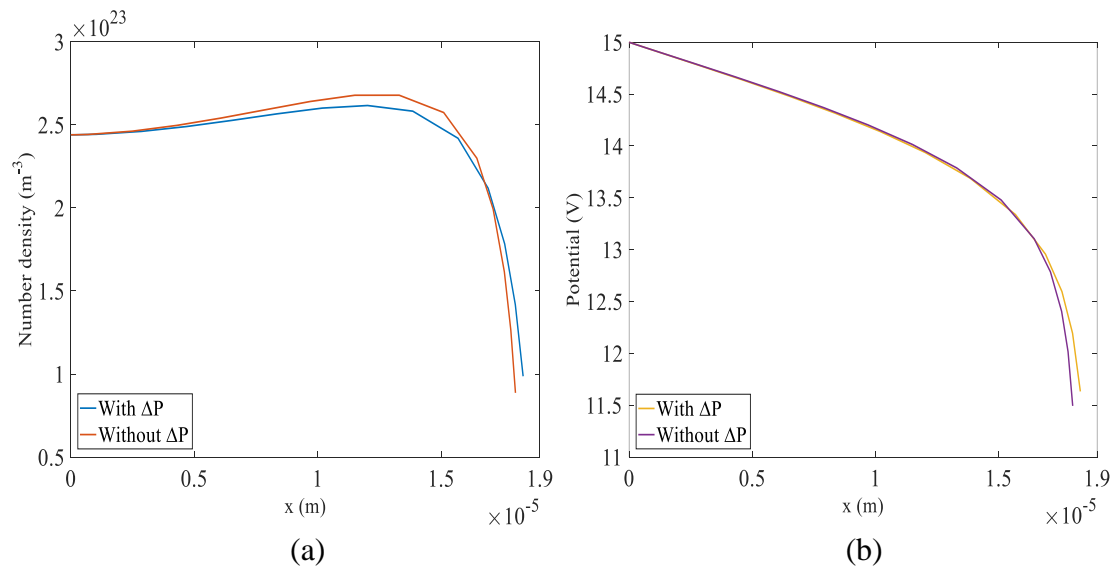


Figure 3.11 Spatial dependence of the temperature distributions for electrons and heavy particles from the arc side boundary of pre-sheath towards the sheath edge.

3.4.2.2 Considerations of the pressure correction due to Coulomb interactions

The Debye-Hückel effect caused by the Coulomb interaction between charged particles is also considered in the calculation. Computations with and without the consideration of Debye-Hückel effects are illustrated in Figure 3.12.



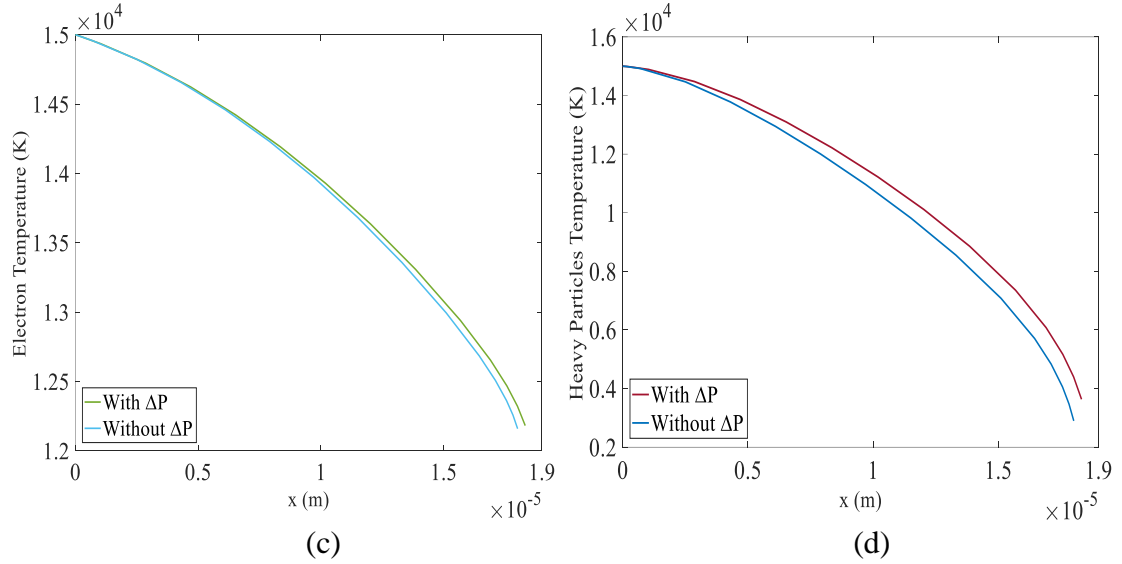


Figure 3.12 Spatial dependence of the (a) number density, (b) potential, (c) electron temperature and (d) heavy particle temperature distributions in the pre-sheath layer with and without the consideration of Debye-Hückel effect.

Following Debye-Hückel theory, when calculates the chemical composition of a non-LTE plasma, an internally consistent system of corrections is normally applied for the determination of chemical potential, Saha equation, partition function and equations of states. From the calculation, it is found that Debye approximation dose not contribute much to the system kinetic pressure and the physical properties of the non-LTE plasma in the pre-sheath layer.

3.4.2.3 Sheath layer

Two representative factors need to be considered when analyses the physical conditions in the sheath layer: current transfer and cathode sheath potential drop. The total current density derived in the sheath model is expressed with potential distribution V , induced cathode surface electric field E_c and sheath potential drop V_c . From the literature review, V_c is normally assumed (15 V) based on the experiments and empirical experiences [42]. In the present work, given that the numbers of plasma back diffusion electrons reaching the cathode surface is lower in comparison with other particles and the electrons located on the pre-sheath side of the sheath edge are moving towards the arc column at a rate of $n_{e}u_e$ as appearing in Eq. (3.2.1), energy of electrons associated with this flux should be supplied by the electrons emitted from cathode surface and accelerated across the sheath layer. It governs a relationship between the overall potential drop in the cathode sheath and the related parameters at the sheath edge. On solving the equations described

for the sheath layer, a potential drop of 12.84V is obtained. The results indicate that the induced surface electric field strength is sensitive to the total current density, as shown in Figure 3.13 and the relationship between the total current density and cathode surface temperature at a given electric field strength is shown in Figure 3.14.

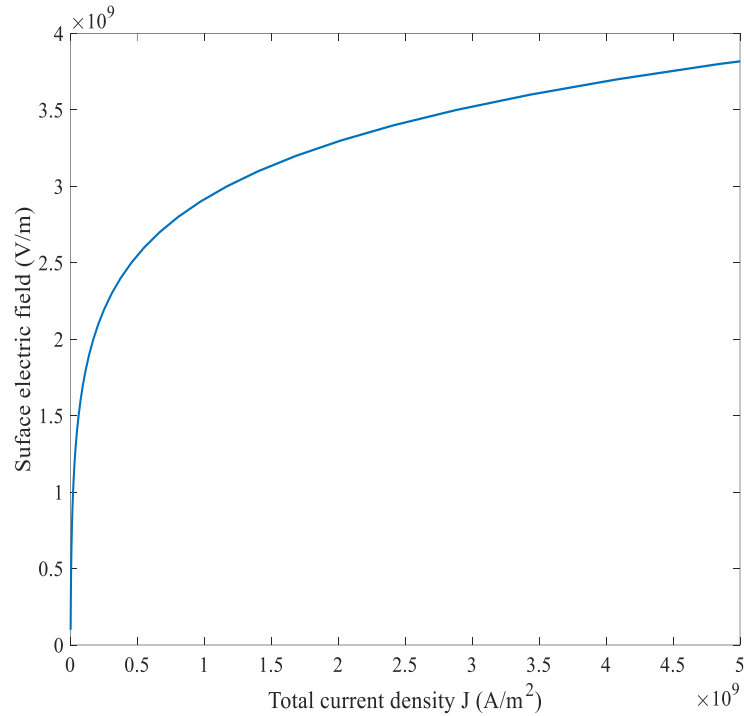


Figure 3.13 Surface electric field strength as a function of the total current density flowed to the cathode surface.

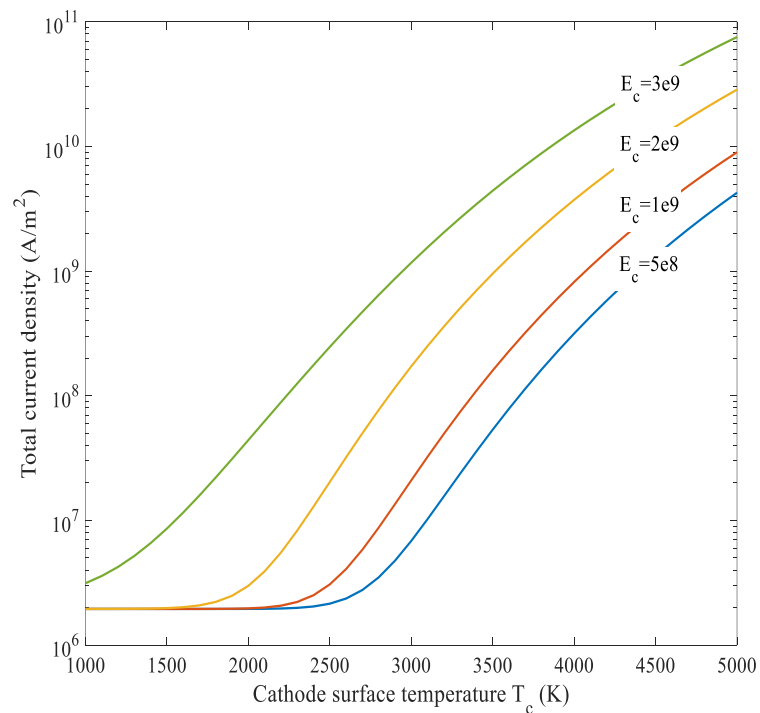


Figure 3.14 Total current density flowed to the cathode surface as a function of the surface temperature at a given electric field strength.

In the present study, the total current density flowed to cathode surface is prescribed as a given parameter ($1.5 \times 10^8 \text{ A/m}^2$). In reality, actual total current density during the arc-cathode interaction is uncertain due to the dynamic characteristics of the arc column. An approximate value is thus used by assuming the cathode surface is fully covered by the arc column. It is noted that total current density is significantly increased when the surface temperature becomes higher which is due to the increased number of emitted electrons by thermo-field emission.

3.4.2.4 Energy transfer at the cathode surface

Figure 3.15 and 3.16 present the associated energy flux terms (net heat flux of positive ions q_{ion} , back diffusion electrons q_e , heavy particles thermal conduction q_{cond} , electrons emission q_{not} and radiation from cathode surface $q_{rad,c}$) transferred on cathode surface with prescribed total current density and cathode surface temperature. It is found that the electrons emission plays a dominant role for removing the thermal energy from the cathode surface when the induced electric field becomes very high. However, it results in a decrease of the energy flux carried by the material vaporization. Moreover, the cathode surface cooling is mostly balanced by the ions bombardment effect on cathode surface and the thermal conduction of heavy particles. In addition, because of the much smaller amount of the electrons reaches at the cathode surface, the heating flux carried by the back-diffusion electrons only takes a smaller proportion of the net energy flux on the cathode surface.

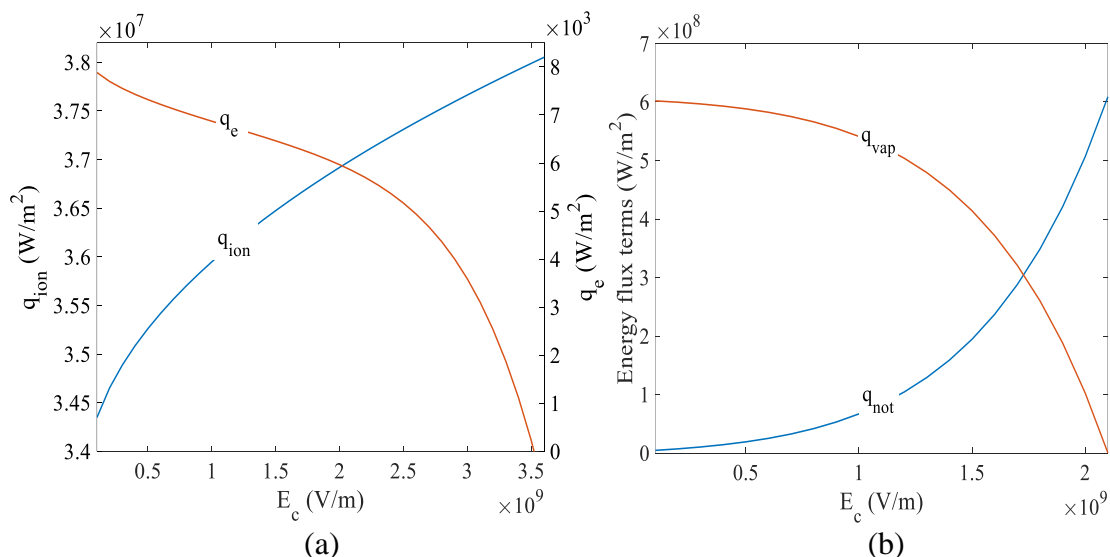


Figure 3.15 The energy flux for the cathode material vaporization at a given surface temperature (3,000K) with a constant total current density of $1.5 \times 10^8 \text{ A/m}^2$.

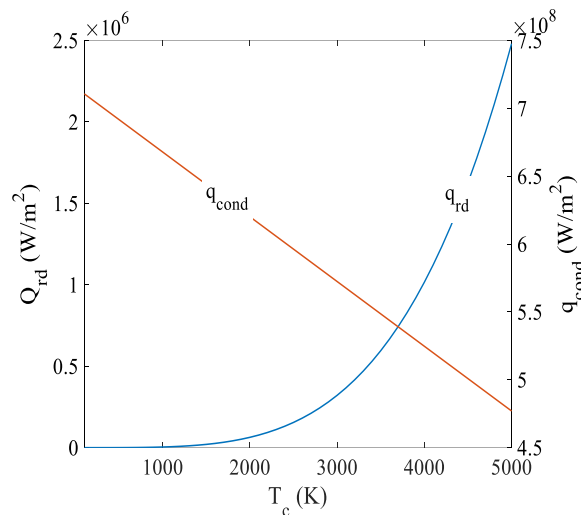


Figure 3.16 The energy flux for the cathode material vaporization at a given surface temperature (3,000K) with a constant total current density of 1.5×10^8 A/m².

3.4.2.5 Comparative study of the localized parameters within the sheath layer

(1) Arc attachment on the cathode surface

In recent years, there has been considerable effort in developing the mathematic models to investigate the attachment modes of the high intensity discharge (HID) arc interacted with cathode bulk [53]–[55]. It highly depends on the mechanism of electrons emission from the cathode surface and the physical properties of the used cathode materials [56]. There are two attachment modes: spot mode and diffuse mode [57]–[59] and physical properties of these two attachment modes have been explained according to theoretical investigations and experiment observations [2], [55], [60], [61]. The arc attached on the cathode surface with a lower current density but larger attachment area is defined as the diffuse mode. However, the arc attached on the cathode surface with smaller area than the cathode diameter but higher current density is defined as the spot mode. In reality, the spot mode is normally occurred when the arc attached on a non-thermionic cathode both in vacuum and in gas [62]. A number of cathode spots with higher current densities are attached on the cathode surface and the plasma in front of the cathode is formed by the ionisation of metallic vapour produced from the cathode erosion. However, when the arc attached on a thermionic cathode, the arc is formed by ionization of surrounding gaseous medium. This difference influences the proportion of ions moved into the space charge sheath layer. For the thermionic cathode, the number of ions inside the sheath layer are determined by the ambient gas pressure of surrounding gaseous medium while the metallic vapour limits the pressure when the arc attached on non-thermionic cathode (metallic vapour pressure), which may be higher than the ambient gas pressure.

(2) Current density within the cathode spots

Optical observation of the luminous phenomenon shows that cathode spot diameter is about 100 μm with current density smaller than 10^9 A/m^2 . Nevertheless, an even higher current density ($>10^{12} \text{ A/m}^2$) is estimated when observes the erosion traces left on the cathode surface after a current interruption process [15]–[19]. A wide range of current density estimation is presented in Table 3.5.

Table 3.5 Current density within the cathode spot for various arc current levels.

Contact Material	Current Level (kA)	Current density (10^9 A/m^2)	Ref
Copper cathode	20	50	[63]
	16	8-800	
	5	12-1200	
	3	0.25	
	0.05-2	0.2-0.7	
Copper anode	6-18	0.6-1.2	[64]
	0.01	>0.5	

(3) Metallic vapour pressure in front of the cathode

For high pressure arc interacts with non-thermionic cathode, a self-sustaining operation regime would become possible if there is a sufficient electron flux emitted from cathode surface. Within the sheath layer, the electrons emission is significantly affected by the ions flux. Large amount of ions bombard on cathode surface would induce high surface electric field, resulting in the high current density of emitted electrons. However, the ions flux is sensitively affected by the localized vapour pressure in the non-LTE layer.

The non-LTE layer in front of the cathode is treated as a two-scale problem of the quasi-neutral pre-sheath and collisionless sheath, which is limited to the case of a small Debye length ($\lambda_D \rightarrow 0$) and a suitable condition at the sheath edge is proposed following the Bohm criterion. However, from the calculation, a discontinuity of the electric field is occurred at the sheath edge which is due to the patching of solutions of the pre-sheath and sheath models. From the work of Riemann [21], another transition layer is required between sheath and pre-sheath layers, which is known as “Knudsen layer”, also called the vaporization layer. It is defined to smoothly match the solutions of sheath and pre-sheath models to avoid the singularity induced from patching method. With assuming

ions from the pre-sheath layer are bombarded and recombined on the cathode surface, which leads to a decrease of the ions number density, the velocity of ions at the sheath edge need to be larger, which is accelerated in the Knudsen layer. Based on the model proposed by Schmitz and Riemann [65], the Knudsen layer is assumed to be adjacent between the sheath and pre-sheath layers with a typical scale of ion mean free path which is much smaller than the pre-sheath length. It could be treated as a quasi-neutral layer without ionization and recombination occurred. The presence of Knudsen layer leads to an extension of pre-sheath and results in a slightly larger velocity of the ions at the sheath edge,

$$u_{is} = \sqrt{\frac{k_B T_e}{m_i}} \left(0.9107 + 0.2363 \frac{T_h}{T_e} \right) \quad (3.4.3)$$

where c_1 and c_2 are two coefficients [66], [67], and the current density ions in the sheath layer is thus calculated by:

$$J_i = en_{is} \sqrt{\frac{k_B T_e}{m_i}} \left(0.9107 + 0.2363 \frac{T_h}{T_e} \right) \quad (3.4.4)$$

In addition, with the consideration of the Knudsen layer, the vaporization flux could be simply determined as a function of cathode surface temperature only [68],

$$\Gamma_{vap} = \frac{p_{vap}(T_c)}{\sqrt{2\pi m_a k_B T_c}} \quad (3.4.5)$$

where Γ_{vap} is the flux density of atoms vaporization ($\text{m}^{-2}\text{s}^{-1}$); $p_{vap}(T_c)$ is the localized vapour pressure,

$$\log(p_{vap}) = \frac{A_2}{T_c} + B_2 + C_2 \log(T_c) + D_2 T_c \quad (3.4.6)$$

where A_2 , B_2 , C_2 and D_2 are constants obtained from the pressure curve. For the copper cathode, this pressure is calculated by [69], [70]:

$$p_{vap} = 133.3 T_c^{-1.27} \cdot 10^{\left(13.39 - \frac{17656}{T_c}\right)} \quad (3.4.7)$$

Based on Kogan and Makaschew [71], the maximum vapour density is given by [25]:

$$\Gamma_{vap,max} = \frac{p(T_c)}{4 \sqrt{\frac{m_a k_B T_c}{3}}} \quad (3.4.8)$$

and the vaporization flux is thus determined by [72]:

$$q_{vap} = \Gamma_{vap} \cdot \eta \quad (3.4.9)$$

where η is the condensation energy of the cathode material atoms (3.43 eV) and m_a is the mass of copper atoms. As presented in Figure 3.17, the vapour pressure increases with the cathode surface temperature exponentially.

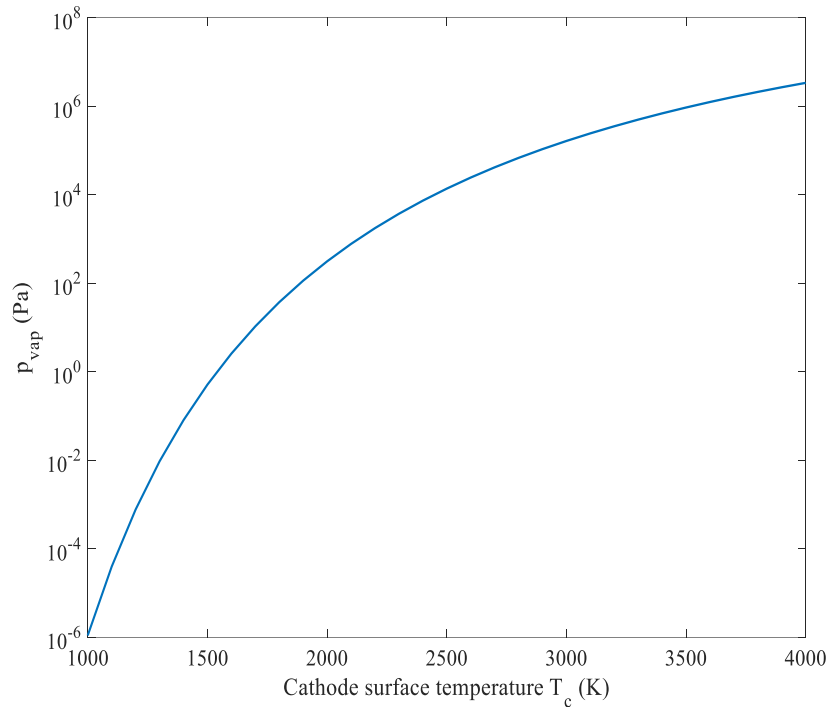


Figure 3.17 Total current density flowed to the cathode surface as a function of the surface temperature at a given electric field strength.

3.4.2.6 Erosion rate and mass loss

The estimated material mass loss due to the contact erosion is presented in Table 3.6 and compared with experiment results. The associated experiments are performed with different interrupted current levels (Figure 3.18) on an air circuit breaker at atmospheric pressure. The tested arc duration is 10 ms and the arc column is not confined with a nozzle. The mass loss predicted in this work has the same order of magnitude of the mass vaporized from a negative contact in the test circuit breaker. The results indicate that the cathode material erosion rate increases with the total current, 0.036 g/s at 22 kA, 0.045 g/s at 27 kA and 0.053 g/s at 32 kA with an estimated current density of 1.5×10^8 A/m². The predicted cathode mass loss considering the effects of Knudsen layer in comparison with the estimated results from present model is shown in Table 3.7. It is found that when an atmospheric pressure arc interacts the with cathode, the presence of Knudsen layer has an insignificant effect on the sheath formation which is due to the

smaller difference between the Bohm velocity and the new velocity of ions accelerated in the Knudsen layer.

Table 3.6 Mass loss of copper cathode in experimental measurement and estimation.

Material loss Current (kA)	Measurement (g)	Prediction	
		Mass loss (g)	Length variation due to erosion (mm)
22	0.29	0.11	0.048
27	0.42	0.13	0.057
32	0.44	0.16	0.071

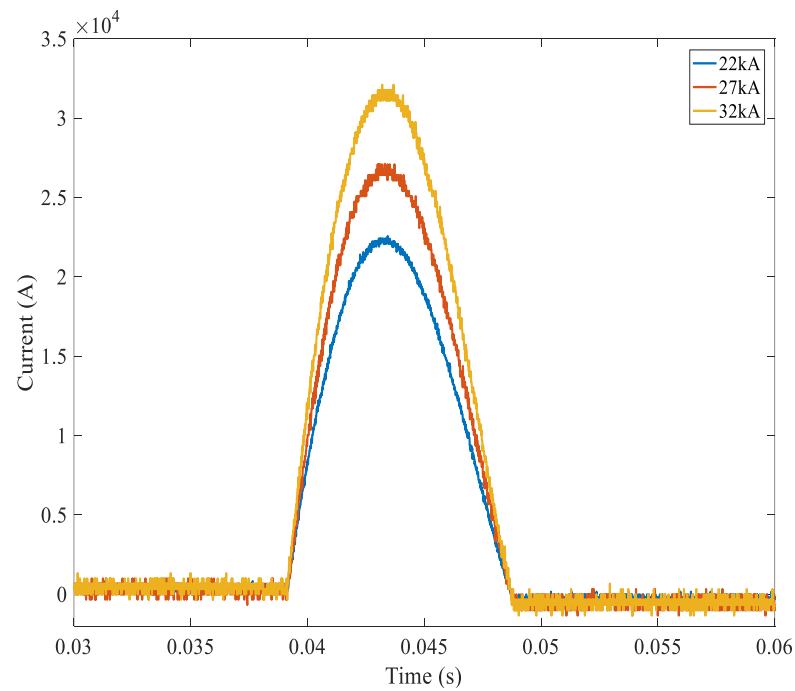


Figure 3.18 Current curves captured from the model circuit breaker.

Table 3.7 Predicted mass loss from the cathode material due to erosion.

Mass loss (g) Current (kA)	Prediction		
	$q_{vap}=q_{in}-q_{out}$	$q_{vap}=\Gamma_{vap} \cdot \eta$	$q_{vap, max}$
22	0.11	0.10	0.11
27	0.13	0.12	0.13
32	0.16	0.14	0.15

3.5 Conclusion

This Chapter established a mathematical model correlated to the near cathode layer in front of cathode. The potential drop over the non-LTE layer could be calculated instead of the empirical assumptions used in previous models. A value of 16.44V potential drop across the near cathode non-LTE layer is obtained from present work although there is a discontinuity of the electric field at the sheath edge which is a direct consequence of the assumptions of electrical quasi-neutrality in the pre-sheath layer and collisionless in the sheath layer. Finally, the transferred energy flux terms at the cathode surface are obtained to determine the total mass loss of the cathode material.

The present model poses some limitations:

- (1) The estimated total current density is a necessary parameter in the absence of actual size of arc column. However, it is difficult to accurately determine because of the dynamic characterises when the hot arc column interacts with the cathode surface.
- (2) The temperature distribution on the cathode surface is unknown which a reasonable value is assumed.

In the further work, two limitations listed above could be solved by:

- (1) Simulate the whole arcing region coupled with the near cathode non-LTE layer model to calculate the total current density.
- (2) Obtain the temperature distribution from the overall solution of the arc column and non-LTE layer model by coupling with the conjugate heat transfer model.

In this work, the final prediction of cathode material total mass loss is smaller than the measurements which is possible because:

- The heat conduction into the cathode bulk is not considered in the present work and 3,000K is taken as the cathode surface temperature.
- The boundary conditions from the arc plasma side of the pre-sheath layer are not obtained by the coupled simulation.
- The metallic particles detached from the cathode surface is also not included, which could significantly influence the total mass loss in reality. This is because they are spitted from the cathode at the temperature lower than its vaporization temperature, thus needs less energy in heating them up. This will increase the total mass loss.

Following the present work, it could be concluded that a reasonable estimation of the hardware conditions through the computer modelling, supported and verified by the test results, is expected to be an alternative solution for acquiring the knowledge of the arc-contact interaction. Moreover, numerical modelling of the arc plasma and its interaction with the contacts is fundamental to the contacts optimum design. In the future, to make the model more practical, the reliable data from the real circuit breakers arcing tests under various conditions are required.

References

- [1] S. Coulombe, “A Model of the Electric Arc Attachment on Non-Refractory (Cold) Cathodes,” McGill University, 1997.
- [2] P. Solana, P. Kapadia, and J. Dowden, “A mathematical analysis of heating effects and electrode erosion in conical electrical arc cathodes,” *J. Phys. D. Appl. Phys.*, vol. 31, no. 24, pp. 3446–3456, Dec. 1998.
- [3] A. Marotta, L. I. Sharakhovsky, and A. M. Essiptchouk, “A Simple Cold-Electrode Erosion Model for Non-stationary Arc Spots: I. Application to Electric Arc Heaters,” *Jpn. J. Appl. Phys.*, vol. 42, no. Part 1, No. 8, pp. 5290–5294, Aug. 2003.
- [4] a Marotta and L. I. Sharakhovsky, “A theoretical and experimental investigation of copper electrode erosion in electric arc heaters: I. The thermophysical model,” *J. Phys. D. Appl. Phys.*, vol. 29, no. 9, pp. 2395–2403, Sep. 1996.
- [5] L. I. Sharakhovsky, A. Marotta, and V. N. Borisjuk, “A theoretical and experimental investigation of copper electrode erosion in electric arc heaters: II. The experimental determination of arc spot parameters,” *J. Phys. D. Appl. Phys.*, vol. 30, no. 14, pp. 2018–2025, Jul. 1997.
- [6] X. Zhou and J. Heberlein, “An experimental investigation of factors affecting arc-cathode erosion,” *J. Phys. D. Appl. Phys.*, vol. 31, no. 19, pp. 2577–2590, Oct. 1998.
- [7] K. HORI, M. OHTSUKA, and M. HARA, “Arc erosion characteristics of Cu-W contact at load current range in sf6 gas,” *Electr. Eng. Japan*, vol. 118, no. 1, pp. 41–50, 1997.
- [8] C. W. Kimblin, “Cathode spot erosion and ionization phenomena in the transition from vacuum to atmospheric pressure arcs,” *J. Appl. Phys.*, vol. 45, no. 12, p. 5235, 1974.
- [9] R. J. Munz and M. Habelrih, “Cathode erosion on copper electrodes in steam, hydrogen, and oxygen plasmas,” *Plasma Chem. Plasma Process.*, vol. 12, no. 2, pp. 203–218, Jun. 1992.
- [10] J. L. Zhang, J. D. Yan, and M. T. C. Fang, “Electrode Evaporation and Its Effects on Thermal Arc Behavior,” *IEEE Trans. Plasma Sci.*, vol. 32, no. 3, pp. 1352–1361, Jun. 2004.
- [11] J. Tepper, M. Seeger, T. Votteler, V. Behrens, and T. Honig, “Investigation on

- Erosion of Cu/W Contacts in High-Voltage Circuit Breakers,” *IEEE Trans. Components Packag. Technol.*, vol. 29, no. 3, pp. 658–665, Sep. 2006.
- [12] B. Rethfeld, J. Wendelstorf, T. Klein, and G. Simon, “A self-consistent model for the cathode fall region of an electric arc,” *J. Phys. D. Appl. Phys.*, vol. 29, no. 1, pp. 121–128, 1999.
- [13] T. G. OWANO, C. H. KRUGER, and R. A. BEDDINI, “Electron-ion three-body recombination coefficient of argon,” *AIAA J.*, vol. 31, no. 1, pp. 75–82, Jan. 1993.
- [14] M. I. Hoffert, “Quasi-One-Dimensional, Nonequilibrium Gas Dynamics of Partially Ionized Two-Temperature Argon,” *Phys. Fluids*, vol. 10, no. 8, p. 1769, 1967.
- [15] R. M. S. Almeida, M. S. Benilov, and G. V Naidis, “Simulation of the layer of non-equilibrium ionization in a high-pressure argon plasma with multiply-charged ions,” *J. Phys. D. Appl. Phys.*, vol. 33, no. 8, pp. 960–967, Apr. 2000.
- [16] K. Kumar, “The Chapman-Enskog solution of the Boltzmann equation: a reformulation in terms of irreducible tensors and matrices,” *Aust. J. Phys.*, vol. 20, p. 205, 1967.
- [17] J. O. Hirschfelder and Charles F. Curtiss, *Molecular Theory of Gases and Liquids*. 1954.
- [18] R. S. Devoto, “Simplified Expressions for the Transport Properties of Ionized Monatomic Gases,” *Phys. Fluids*, vol. 10, no. 10, p. 2105, 1967.
- [19] A. L. Garcia and B. J. Alder, “Generation of the Chapman-Enskog Distribution,” *J. Comput. Phys.*, vol. 140, no. 1, pp. 66–70, 1998.
- [20] M. I. Boulos, P. Fauchais, and E. Pfender, *Thermal Plasmas: Fundamentals and Applications (Volume 1)*. Boston, MA: Springer US, 1994.
- [21] K.-U. Riemann, “The Bohm criterion and sheath formation,” *J. Phys. D. Appl. Phys.*, vol. 24, no. 4, pp. 493–518, Apr. 1991.
- [22] A. E. Guile, “Arc-electrode phenomena,” *Proc. Inst. Electr. Eng.*, vol. 118, no. 9R, p. 1131, 1971.
- [23] T. Gyergyek, B. Jurčič-Zlobec, M. Čerček, and J. Kovačič, “Sheath structure in front of an electron emitting electrode immersed in a two-electron temperature plasma: a fluid model and numerical solutions of the Poisson equation,” *Plasma Sources Sci. Technol.*, vol. 18, no. 3, p. 35001, Aug. 2009.
- [24] “Miscellaneous Electrical Materials,” p. 50.
- [25] X. Zhou and J. Heberlein, “Analysis of the arc-cathode interaction of free-

- burning arcs,” *Plasma Sources Sci. Technol.*, vol. 3, pp. 564–574, 1994.
- [26] A. J. Shirvan, “Modelling of Electric Arc Welding: arc-electrode coupling,” 2013.
- [27] A. Fridman and L. A. Kennedy, *Plasma Physics and Engineering*. Taylor & Francis, 2004.
- [28] R. H. Fowler and L. Nordheim, “Electron Emission in Intense Electric Fields,” *Proc. R. Soc. A Math. Phys. Eng. Sci.*, vol. 119, no. 781, pp. 173–181, May 1928.
- [29] R. G. Forbes, “Field emission: New theory for the derivation of emission area from a Fowler–Nordheim plot,” *J. Vac. Sci. Technol. B Microelectron. Nanom. Struct.*, vol. 17, no. 2, p. 526, 1999.
- [30] “Fermi Energies, Fermi Temperatures, and Fermi Velocities.” [Online]. Available: <http://hyperphysics.phy-astr.gsu.edu/hbase/tables/fermi.html>.
- [31] R. Eisberg and R. Resnick, *Quantum Physics of Atoms, Molecules, Solids, Nuclei, and Particles, 2nd Edition*, 2nd ed. 1985.
- [32] R. G. Forbes, “Use of a spreadsheet for Fowler–Nordheim equation calculations,” *J. Vac. Sci. Technol. B Microelectron. Nanom. Struct.*, vol. 17, no. 2, p. 534, 1999.
- [33] P. F. Byrd and M. D. Friedman, *Handbook of Elliptic Integrals for Engineers and Scientists*, 2nd ed. Berlin, Heidelberg: Springer Berlin Heidelberg, 1971.
- [34] R. G. Forbes, “Simple good approximations for the special elliptic functions in standard Fowler-Nordheim tunneling theory for a Schottky-Nordheim barrier,” *Appl. Phys. Lett.*, vol. 89, no. 11, p. 113122, 2006.
- [35] R. G. Forbes and J. H. B. Deane, “Reformulation of the standard theory of Fowler–Nordheim tunnelling and cold field electron emission,” *Proc. R. Soc. A Math. Phys. Eng. Sci.*, vol. 463, no. 2087, pp. 2907–2927, Nov. 2007.
- [36] E. L. Murphy and R. H. Good, “Thermionic Emission, Field Emission, and the Transition Region,” *Phys. Rev.*, vol. 102, no. 6, pp. 1464–1473, Jun. 1956.
- [37] M. S. Benilov and L. G. Benilova, “Field to thermo-field to thermionic electron emission: A practical guide to evaluation and electron emission from arc cathodes,” *J. Appl. Phys.*, vol. 114, no. 6, p. 63307, Aug. 2013.
- [38] J. Paulini, T. Klein, and G. Simon, “Thermo-field emission and the Nottingham effect,” *J. Phys. D. Appl. Phys.*, vol. 26, no. 8, pp. 1310–1315, Aug. 1993.
- [39] E. Hantzsche, “The Thermo-Field Emission of Electrons in Arc Discharges,” *Beiträge aus der Plasmaphys.*, vol. 22, no. 4, pp. 325–346, 1982.

- [40] J. Mitterauer and P. Till, “Computer Simulation of the Dynamics of Plasma-Surface Interactions in Vacuum Arc Cathode Spots,” *IEEE Trans. Plasma Sci.*, vol. 15, no. 5, pp. 488–501, 1987.
- [41] D. H. Dowell, “Electron Emission and Cathode Emittance.” pp. 1–24, 2008.
- [42] K. I. G, “Laws governing the cathode drop and the threshold currents in an arc discharge on pure metals,” *Sov. Phys.-Tech. Phys.*, vol. 9, p. 1146, 1965.
- [43] J. Hu and H. L. Tsai, “Heat and mass transfer in gas metal arc welding. Part I: The arc,” *Int. J. Heat Mass Transf.*, vol. 50, no. 5–6, pp. 833–846, Mar. 2007.
- [44] A. Anders, *Cathodic Arcs: From Fractal Spots to Energetic Condensation*. New York, NY: Springer New York, 2008.
- [45] W. B. Nottingham, “Remarks on Energy Losses Attending Thermionic Emission of Electrons from Metals,” *Phys. Rev.*, vol. 59, no. 11, pp. 906–907, Jun. 1941.
- [46] G. M. Fleming and J. E. Henderson, “The Energy Losses Attending Field Current and Thermionic Emission of Electrons from Metals,” *Phys. Rev.*, vol. 58, no. 10, pp. 887–894, Nov. 1940.
- [47] F. M. Charbonnier, R. W. Strayer, L. W. Swanson, and E. E. Martin, “Nottingham Effect in Field and T-F Emission: Heating and Cooling Domains, and Inversion Temperature,” *Phys. Rev. Lett.*, vol. 13, no. 13, pp. 397–401, Sep. 1964.
- [48] L. W. Swanson, L. C. Crouser, and F. M. Charbonnier, “Energy Exchanges Attending Field Electron Emission,” *Phys. Rev.*, vol. 151, no. 1, pp. 327–340, Nov. 1966.
- [49] “Table of Emissivity of Various Surfaces.” [Online]. Available: http://www-eng.lbl.gov/~dw/projects/DW4229_LHC_detector_analysis/calculations/emissivity2.pdf.
- [50] K. C. Hsu and E. Pfender, “Analysis of the cathode region of a free-burning high intensity argon arc,” *J. Appl. Phys.*, vol. 54, no. 7, p. 3818, 1983.
- [51] A. Gleizes, B. Chervy, and J. J. Gonzalez, “Calculation of a two-temperature plasma composition: bases and application to SF 6,” *J. Phys. D. Appl. Phys.*, vol. 32, no. 16, pp. 2060–2067, Aug. 1999.
- [52] W. Wang, M. Rong, and J. W. Spencer, “Nonuniqueness of two-temperature Guldberg-Waage and Saha equations: Influence on thermophysical properties of SF 6 plasmas,” *Phys. Plasmas*, vol. 20, no. 11, p. 113504, Nov. 2013.
- [53] M. S. Benilov and M. D. Cunha, “Heating of refractory cathodes by high-

- pressure arc plasmas: I,” *J. Phys. D. Appl. Phys.*, vol. 35, no. 14, pp. 1736–1750, Jul. 2003.
- [54] M. S. Benilov and M. D. Cunha, “Heating of refractory cathodes by high-pressure arc plasmas: II,” *J. Phys. D. Appl. Phys.*, vol. 36, no. 6, pp. 603–614, Mar. 2003.
- [55] L. Dabringhausen, O. Langenscheidt, S. Lichtenberg, M. Redwitz, and J. Mentel, “Different modes of arc attachment at HID cathodes: simulation and comparison with measurements,” *J. Phys. D. Appl. Phys.*, vol. 38, no. 17, pp. 3128–3142, Sep. 2005.
- [56] A. Fridman and Y. I. Cho, *Advances in heat transfer. Volume 40, Transport phenomena in plasma*, 1st ed. Elsevier, 2007.
- [57] N. K. Mitrofanov and S. M. Shkol’nik, “Two forms of attachment of an atmospheric-pressure direct-current arc in argon to a thermionic cathode,” *Tech. Phys.*, vol. 52, no. 6, pp. 711–720, Jun. 2007.
- [58] S. Lichtenberg, D. Nandelstädt, L. Dabringhausen, M. Redwitz, J. Luhmann, and J. Mentel, “Observation of different modes of cathodic arc attachment to HID electrodes in a model lamp,” *J. Phys. D. Appl. Phys.*, vol. 35, no. 14, pp. 1648–1656, Jul. 2002.
- [59] M. S. Benilov, “Non-linear surface heating and modes of current transfer to thermionic cathodes,” *Czechoslov. J. Phys.*, vol. 48, no. S2, pp. 263–268, Feb. 1998.
- [60] B. Jüttner, “Cathode spots of electric arcs,” *J. Phys. D. Appl. Phys.*, vol. 34, no. 17, pp. R103–R123, Sep. 2001.
- [61] R. Bötticher and W. Bötticher, “Numerical modelling of arc attachment to cathodes of high-intensity discharge lamps,” *J. Phys. D. Appl. Phys.*, vol. 33, no. 4, pp. 367–374, Feb. 2000.
- [62] B. Jüttner, “Properties of Arc Cathode Spots,” *Le J. Phys. IV*, vol. 7, no. C4, pp. C4-31-C4-45, Oct. 1997.
- [63] V. I. Rakhovskii, “Experimental Study of the Dynamics of Cathode Spots Development,” *IEEE Trans. Plasma Sci.*, vol. 4, no. 2, pp. 81–102, 1976.
- [64] J. D. Cobine and E. E. Burger, “Analysis of Electrode Phenomena in the High-Current Arc,” *J. Appl. Phys.*, vol. 26, no. 7, p. 895, 1955.
- [65] H. Schmitz and K.-U. Riemann, “Consistent analysis of the boundary layer of a Saha plasma,” *J. Phys. D. Appl. Phys.*, vol. 34, no. 8, pp. 1193–1202, Apr. 2001.

- [66] H. Schmitz and K.-U. Riemann, “Analysis of the cathodic region of atmospheric pressure discharges,” *J. Phys. D. Appl. Phys.*, vol. 35, no. 14, pp. 1727–1735, Jul. 2002.
- [67] S. Lichtenberg, L. Dabringhausen, O. Langenscheidt, and J. Mentel, “The plasma boundary layer of HID-cathodes: modelling and numerical results,” *J. Phys. D. Appl. Phys.*, vol. 38, no. 17, pp. 3112–3127, Sep. 2005.
- [68] R. E. Honig and D. A. Kramer, “Vapor Pressure Data for the Solid and Liquid Elements,” *RCA Rev*, vol. 30, pp. 285–305, 1969.
- [69] T. Nielsen, A. Kaddani, and M. Benilov, “Model for arc cathode region in a wide pressure range,” *J. Phys. D Appl. ...*, vol. 34, no. 2001, pp. 2016–2021, 2001.
- [70] A. Kaddani, “Modelisation 2D et 3D des arcs ´ electriques ´ dans l’argon a pression atmosph ´ erique avec la prise en ´ compte du couplage thermique et electrique arc- ´ electrodes ´ et de l’influence des vapeurs metalliques,” Pierre et Marie Curie University, 1995.
- [71] M. N. Kogan and N. K. Makashev, “Role of the Knudsen layer in the theory of heterogeneous reactions and in flows with surface reactions,” *Fluid Dyn.*, vol. 6, no. 6, pp. 913–920, 1974.
- [72] S. Coulombe and J.-L. Meunier, “Arc-cold cathode interactions: parametric dependence on local pressure,” *Plasma Sources Sci. Technol.*, vol. 6, no. 4, pp. 508–517, Nov. 1997.

Chapter 4

Nozzle Ablation and its Effects on the Interruption Process

4.1 Introduction

An auto-expansion circuit breaker utilises the ablated PTFE vapour from the nozzle(s) at high current to establish the required flow conditions at the final current zero for arc quenching. Nozzle ablation is affected by a number of factors, such as current level, arc duration and the travel characteristics of the moving contacts that controls the arc length.

Nozzle ablation results in the deformation of the nozzle surface and the enlargement of the nozzle hole. Due to the uncontrollable deformation and damage, the nozzle surface becomes rough as a result of ablation by strong arc radiation as well. All of these make changes to the flow field and affect the interruption process. When nozzle ablation takes place, the produced PTFE vapour is inevitably injected into working medium, bringing mass, momentum and energy into the flow field, especially within the arcing space. The vapour then mixes with SF₆ gas and changes the chemical composition, thermodynamic properties and transport coefficients of the arcing gaseous mixture. The arc column is assumed in LTE and LCE states which could be described by three variables: pressure, temperature and vapour concentration. Besides that, the thermodynamic properties and transport coefficients of SF₆-PTFE mixture are determined using a modified model of that described in Chapter 2 and given in section 4.3.1.4 in this chapter.

Despite that there has been a significant amount of work on gas blast circuit breakers, including both puffer and auto-expansion types, there has been little work on the effects of nozzle ablation on the flow field that is critical in interruption process. This chapter presents a comparative study of the nozzle ablation with different arc durations and its influences on the flow environment inside the arcing chamber. Nozzle ablation can be separately studied because it is caused by the arc radiation from the LTE column while contact erosion is only controlled by the energy into the contact tip which is influenced by the non-LTE contact layer. Nozzle ablation is hardly affected by this non-LTE layer since the thickness of the non-LTE layer is much smaller in comparison with the length between the separated contacts.

4.2 Simulation Geometry and Preconditions of the 145 kV/40 kA Auto-expansion Circuit Breaker

The current interruption process of a 145 kV/40 kA auto-expansion circuit breaker is studied under different discharge conditions, e.g. interrupting current level, arc duration, and contact travel curve. Different from existing work on circuit breaker arc simulation, the diameter changes of nozzles (main nozzle and auxiliary nozzle) has been considered. Cases with short, medium and long arc durations are studied. PHOENICS 3.6.1 is used for its capability to handle the moving objects and flexibility in controlling the solution process.

The schematic diagram of the 145 kV/40 kA auto-expansion circuit breaker is presented in Figure 4.1. The power frequency is 60 Hz and the filling gas is SF₆ with an absolute pressure of 0.6 MPa at 300 K. Figure 4.1 also describes the computational domain. The pressure at the two ends is set to a fixed value of 0.6 MPa. The pressure at the exit is also set to 0.6 MPa. In the arcing chamber of this circuit breaker, the flat throat of main nozzle has a length of 22.4 mm and a radius of 10.5 mm. The auxiliary nozzle flat throat has a length same as the radius of 9.5 mm.

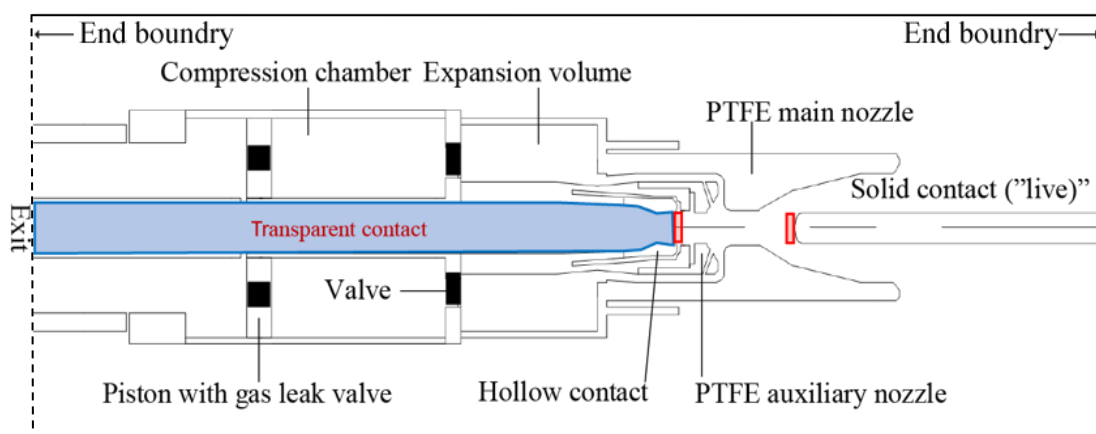


Figure 4.1 Schematic diagram of the 145 kV/40 kA auto-expansion circuit breaker under investigation. Gases are free to enter or leave the computational domain. In case, the gas enters the domain is assumed to have a temperature of 300 K.

Body fitted coordinate (BFC) system is used to define the structured grids of the model. Nevertheless, due to the limitation of this version of PHOENICS which could not model the movement of a round tipped contact accurately, curved tip is replaced by superposed rectangular blocks as shown in Figure 4.2. The number of blocks should ensure that the curved tip is adequately represented. In the model, the solid contact and the piston are

moving while the nozzle and hollow contact including the cylinder stays stationary. It is the opposite in reality. This is done to simplify the modelling process because objects with irregular shape are difficult to move in structured grid. It however does not affect the results since the puffer action to generate high pressure depends only on the relative motion of the piston and the cylinder. In addition, the gas speed in the arcing chamber is much higher than the speed of the moving contact or piston.

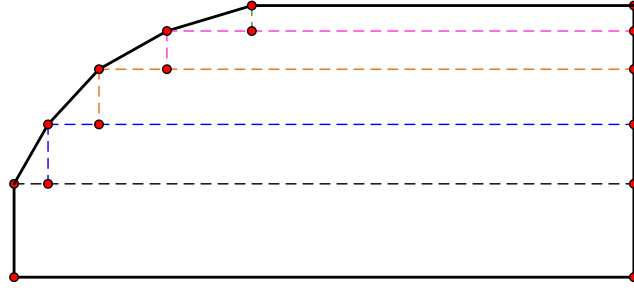


Figure 4.2 Diagram showing approximation of the round moving contact tip by blocks of different thickness. The blocks move in the simulation.

4.3 Mathematical Model for the Auto-expansion Circuit Breaker

4.3.1 Governing equations of the switching arc in LTE

Theories of hydrodynamics and electromagnetics are considered to analyse the dynamic behaviour of the arc. An arc is produced by the breakdown of the gas in the contact gap (SF_6 in the present work) and the flow in the arcing chamber is assumed to be turbulent [1], [2]. The behaviour of the arc is described by the modified time-averaged Navier-Stokes equations (conservation equations of mass, momentum and energy) and mass concentration of PTFE vapour in the presence of nozzle ablation. Since the arc pressure is well above atmospheric, the gaseous mixture of SF_6 and PTFE vapour is assumed to be in LTE and LCE. Moreover, the arcing chamber is rotationally symmetric. A general form for these conservation equations can be written as:

$$\frac{\partial(\rho\phi)}{\partial t} + \nabla \cdot (\rho\phi\vec{V}) - \nabla \cdot (\Gamma_\phi\nabla\phi) = S_\phi \quad (4.3.1)$$

and in a 2D cylindrical polar coordinate system as:

$$\frac{\partial(\rho\phi)}{\partial t} + \frac{1}{r} \frac{\partial}{\partial r} (r\rho v\phi - r\Gamma_\phi \frac{\partial\phi}{\partial r}) + \frac{\partial}{\partial z} (\rho w\phi - \Gamma_\phi \frac{\partial\phi}{\partial z}) = S_\phi \quad (4.3.2)$$

where ϕ is the dependent variable; ρ is the gas density; \vec{V} is the velocity vector contains radial (v) and axial (w) velocity components; Γ_ϕ is the diffusion coefficient and S_ϕ is the source term for different conservation equations given in Table 4.1 [3].

Table 4.1 Source terms and diffusion coefficients for above governing equations.

Equation	ϕ	Γ_ϕ	S_ϕ
Mass	1	0	0
Z-momentum	w	$\mu_l + \mu_t$	$-\frac{\partial P}{\partial z} + J_r B_\theta + \text{viscous terms}$
R-momentum	v	$\mu_l + \mu_t$	$-\frac{\partial P}{\partial r} - J_z B_\theta + \text{viscous terms}$
Enthalpy	h	$\frac{\lambda_l + \lambda_t}{c_p}$	$\sigma E^2 - q + \frac{dP}{dt} + \text{viscous dissipation}$
Copper/PTFE mass concentration	c_m	$\rho(D_l + D_t)$	0
Current continuity	φ	σ	0

where μ is the dynamic viscosity; P is the pressure; J_r and J_z are the radial and axial components of the current density; θ is the azimuthal direction of the cylindrical polar coordinates system; λ is the thermal conductivity; σ is the electrical conductivity; c_p is the specific heat at constant pressure; E is the electric field strength; the subscripts of l and t represent the laminar and turbulent parts of the diffusion coefficients respectively; the term σE^2 denotes the ohmic heating and q represents the net radiation loss per unit volume and time; D is the diffusivity and c_m is the vapour mass concentration which is calculated by:

$$c_{m,Cu} = \frac{x_{Cu} M_{Cu}}{x_{Cu} M_{Cu} + x_{SF_6} M_{SF_6}} \quad (4.3.3)$$

$$c_{m,PTFE} = \frac{x_{PTFE} M_{PTFE}}{x_{PTFE} M_{PTFE} + x M_{SF_6}} \quad (4.3.4)$$

where x is the molar fraction and M is the molar mass of the vapour.

4.3.1.1 Ohmic heating

The ohmic heating is a process of converting electric energy into thermal energy of the arcing medium and the gas is heated up to a high temperature by the ohmic heating. To determine the ohmic heating σE^2 , electrical conductivity σ is determined as a function of temperature and pressure, which has already been explained in Chapter 2. There are

two representative models in determining the electric field: slender arc model and non-slender arc model. The former one is defined especially for the long arc with low current where the variation of radial electric field component is negligible and axial component of the electric field is then calculated by:

$$E_z = \frac{I}{\int_0^{R_c} \sigma \cdot 2\pi r dr} \quad (4.3.5)$$

where R_c is the radius of the conducting column which is normally taken as the radial distance from the axis to the point of $T=3,000$ K. It is derived following the Ohm's law with the relationship between the current density J and electric field strength E :

$$J = \sigma E = \frac{I}{\int_0^{R_c} 2\pi r dr} \quad (4.3.6)$$

Moreover, the electrical conductivity of arcing medium is very small at low temperature (e.g. $T < 3,000$ K). In the present work, R_c is set to the radius of the nozzle flat throat [3].

The radial current density component could not be neglected at high current level since the radial dimension of the arc column changes significantly, especially at the arc roots. Under this condition, the electric field and current density are determined using the non-slender arc model by numerically solving the current continuity equation which is given by:

$$\frac{\partial \rho}{\partial t} + \nabla \cdot (\sigma \nabla \varphi) = 0 \quad (4.3.7)$$

Following the international standards which describe the test duties on the high voltage circuit breakers, the operation power frequency is normally at 50 Hz or 60 Hz [4]. On the basis of low-frequency approximation, $\frac{\partial \rho}{\partial t}$ is smaller and it could be omitted, and the electric field is thus obtained directly by:

$$\nabla \cdot (\sigma \nabla \varphi) = 0 \quad (4.3.8)$$

The radial and axial components of the current density are calculated from the electrical potential distribution ($E = -\nabla \varphi$) [5]:

$$J_r = -\sigma \frac{\partial \varphi}{\partial r} \quad (4.3.9)$$

$$J_z = -\sigma \frac{\partial \varphi}{\partial z} \quad (4.3.10)$$

The boundary conditions to solve the current continuity equation is defined according to the long-range nature of the electric field. In other words, the computational domain for solving current continuity equation should be sufficiently large so the uncertainties in the boundary conditions do not affect the solution in the domain of interest. In the calculation, the boundary is extended until the potential distribution in the nozzle does not change anymore when the domain is further enlarged.

4.3.1.2 Lorentz force

In the 2D cylindrical coordinates system, the arc column is rotationally symmetric and the Lorentz force is calculated as a function of the axial and radial current densities and the magnetic field in azimuthal direction induced by current. The azimuthal magnetic field is calculated by [5]:

$$\frac{1}{r} \frac{\partial}{\partial r} (r B_\theta) = \mu_0 J_z \quad (4.3.11)$$

and the magnetic flux density is determined by:

$$\nabla \times \vec{B} = \mu_0 \vec{J} \quad (4.3.12)$$

where μ_0 is the permeability of arcing medium ($\mu_0 = 4\pi \times 10^{-7} \text{ H/m}$) that is assumed to be homogenous. The magnetic field could be obtained following the Biot-Savart Law and Ampère's circuital law:

$$B_\theta = \frac{\mu_0 I}{2\pi r} = \frac{\mu_0 \int_0^r J_z 2\pi \xi d\xi}{2\pi r} \quad (4.3.13)$$

and the Lorentz force term as the volumetric force in the momentum equation is given by:

$$f_r = -J_z B_\theta \quad (4.3.14)$$

$$f_z = J_r B_\theta \quad (4.3.15)$$

4.3.1.3 Turbulence energy transport

Whether a flow is laminar or turbulent flow depends on the relative largeness of flow inertia and flow friction due to the viscosity. Some turbulence models have been studied [6]–[10] when applied to the arc modelling for high voltage circuit breakers [11]–[17].

In 1973, Niemeyer and Ragaller [18], [19] pointed out that the transition from a hydrodynamically unstable shear layer at the arc boundary to a turbulent layer appears at the downstream of the nozzle throat. The presence of turbulence leads to an enhancement of the energy and momentum transfer [20]. It is a dominant mechanism to remove the arc thermal energy in particular in the final current zero phase. After current zero, there is a residual plasma with a small current flow between the arcing contacts. During this period, the energy is effectively removed by the convection and turbulent cooling, and eventually results in a successful thermal recovery. In the theory of fluid dynamics, the turbulence is described by the Reynolds number which is defined as the ratio of inertial force over viscous force, with the form [21]:

$$Re = \frac{VL}{\nu} \quad (4.3.16)$$

where V is mean velocity of the gas; L is a characteristic length and ν is the kinematic viscosity. To obtain the Reynolds stresses in the momentum equations, the concept of turbulence eddy viscosity is introduced according to Boussinesq approximation [22]. It describes a proportional relationship between Reynolds stress tensor and mean rate of strain tensor [23]:

$$\tau_{ij} = 2\mu_t S_{ij}^* - \frac{2}{3}\mu_t \frac{\partial(U_v)_k}{\partial x_k} \delta_{ij} - \frac{2}{3}\rho K_t \delta_{ij} \quad (4.3.17)$$

where τ_{ij} is the Reynolds stress; μ_t is the turbulence eddy viscosity; ρ is the density; K_t is the turbulence kinetic energy; δ_{ij} is the Kronecker delta; U_v is the velocity and S_{ij}^* is the mean rate of the strain tensor, defined by:

$$S_{ij}^* = \frac{1}{2} \left(\frac{\partial u_i}{\partial x_j} + \frac{\partial u_j}{\partial x_i} \right) \quad (4.3.18)$$

and the turbulence viscosity is determined with a length scale and velocity scales due to the dimensional effect [24].

$$\mu_t = C\rho L_s v_{ts} \quad (4.3.19)$$

where C is a constant; L_s and v_{ts} are the turbulence length scale and velocity scale.

In SF₆ switching arc modelling, Prandtl mixing length model is the simplest model and the turbulence viscosity is calculated by [5]:

$$\mu_t = \rho L_s^2 \left[2 \left(\frac{v}{r} \right)^2 + \left(\frac{\partial w}{\partial r} + \frac{\partial v}{\partial z} \right)^2 \right] \quad (4.3.20)$$

and the length scale is assumed to be proportional to the local thermal radius of the arc column [17],

$$L_s = cr_\delta \quad (4.3.21)$$

where c is the turbulence parameter and r_δ is the thermal radius of the arc, defined as,

$$r_\delta = \sqrt{\frac{\theta_\delta}{\pi}} \quad (4.3.22)$$

and θ_δ is the thermal area of the arc that given by:

$$\theta_\delta = \int_0^\infty \left(1 - \frac{T_\infty}{T}\right) 2\pi r dr \quad (4.3.23)$$

where T_∞ is the temperature near the nozzle wall where the radial temperature gradient is negligible and the gas temperature is low. However, compared with the simple nozzle arcs, the complicated geometry of a circuit breaker and flow field conditions makes it less easily to determine the arc radius. Therefore, based on empirical experience, the arc radius is defined as the radial distance from the axis to the 5,000 K isotherm for the high current phase and to 3,000 K isotherm for the current zero and post arc phases [3]. In the calculation, the turbulence parameter c should be calibrated in accordance with at least one set of experiment results. Because of the influences of the arc radius on the turbulence parameter, the value of c used for the high and low current conditions should be adjusted accordingly. It is higher at low current because of stronger turbulent cooling effect. A linear relationship of turbulence parameter c with current is expressed as [25]:

$$T_p = T_{p_{HI}} + \frac{|I| - 1.5 \times 10^4}{0 - 1.5 \times 10^4} (T_{p_{I0}} - T_{p_{HI}}) \quad (4.3.24)$$

where T_p is the name of the turbulence parameter used in the program; $T_{p_{I0}}$ and $T_{p_{HI}}$ ($T_{p_{HI}}=0.05$ in the present work) are the turbulence parameters in the current zero phase and high current phase respectively; I is the arcing current. The turbulence parameter used in the post arc phase is also equal to $T_{p_{I0}}$.

Additionally, the turbulence viscosity obtained from the more sophisticated turbulence model ‘‘K-Epsilon model’’ is determined by [17]:

$$\mu_t = \rho C \frac{k^2}{\varepsilon} \quad (4.3.25)$$

where k is the turbulent kinetic energy per unit mass and ε is the dissipation rate. There are five constants in the k- ε model as listed in Table 4.2. Based on a comparative study

[17], the Prandtl mixing length model has computational advantages compared with the two-parameter k - ε model. Moreover, only turbulence parameter c requires adjustment for the Prandtl mixing length model.

Table 4.2 Values of the five parameters in the k - ε model.

Constant parameters	Values
σ_k	1.0
σ_ε	1.3
C	0.09
C_{1e}	1.44
C_{2e}	1.92

Closure of Eq. (4.3.1) needs a knowledge of turbulence enhanced thermal conductivity which is related to the turbulence viscosity and the turbulence Prandtl number P_{rt} . P_{rt} is a dimensionless quantity that represents the ratio of the diffusion of momentum over energy, in the form of [26]:

$$P_{rt} = \frac{\mu_t}{\lambda_t/c_p} \quad (4.3.26)$$

where λ_t is the turbulence enhanced thermal conductivity and c_p is the specific heat at constant pressure. The value of P_{rt} could be assumed to be unity for switching arcs.

In addition, the turbulence and laminar diffusivities are determined with the turbulence and laminar viscosities, given by [27]:

$$D_t = \frac{\mu_t}{\rho S_{C_t}} \quad (4.3.27)$$

$$D_l = \frac{\mu_l}{\rho S_{C_l}} \quad (4.3.28)$$

where S_{C_t} and S_{C_l} are Schmidt number around unity.

4.3.1.4 Material properties of the gaseous mixture

The thermodynamic properties and transport coefficients of gas mixture are tabulated using the data available from publications, as shown in Figure 4.3 and 4.4. Furthermore,

an interpolation method is used to calculate the thermodynamic properties and transport coefficients at arbitrary temperature based on the tabulated values during the iteration calculation.

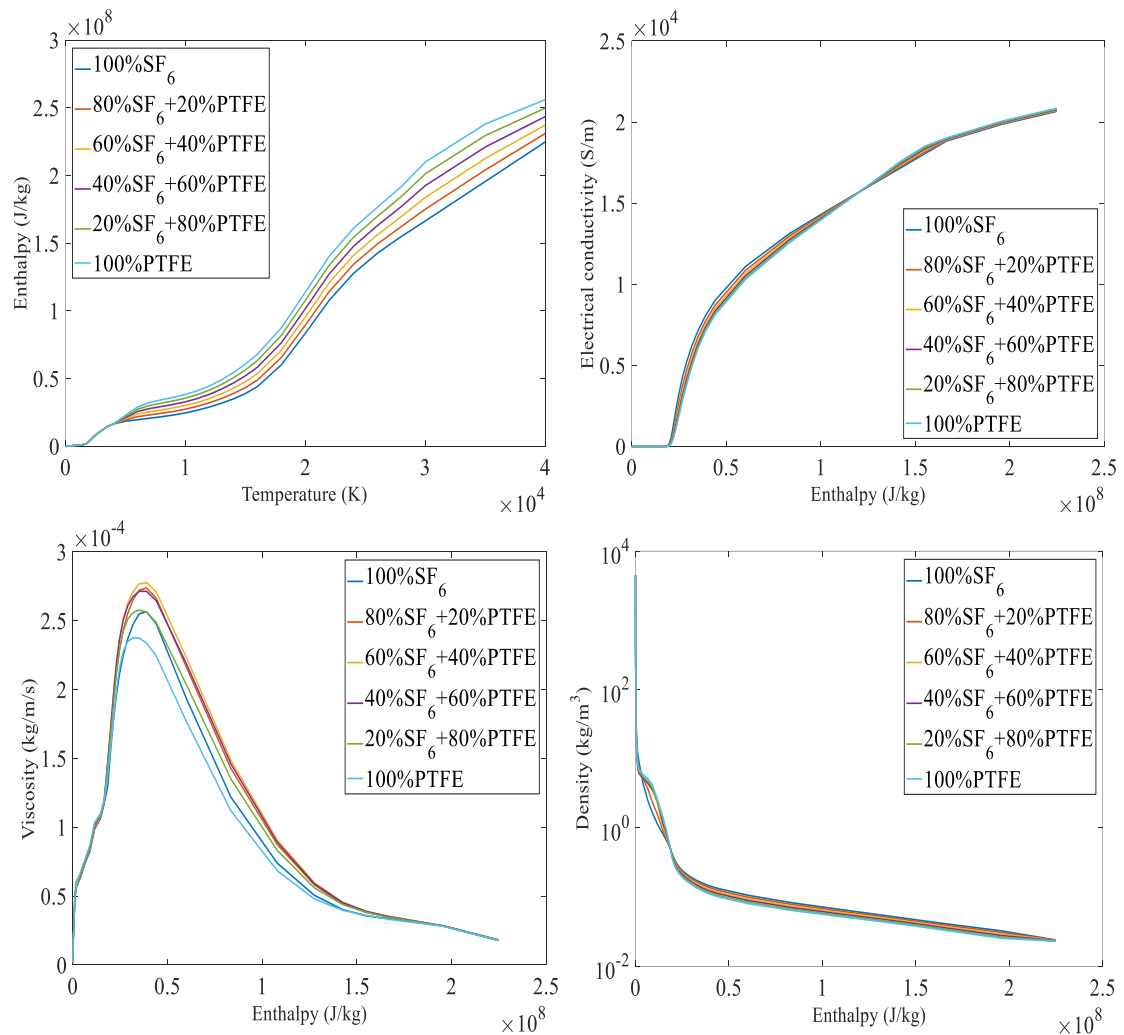
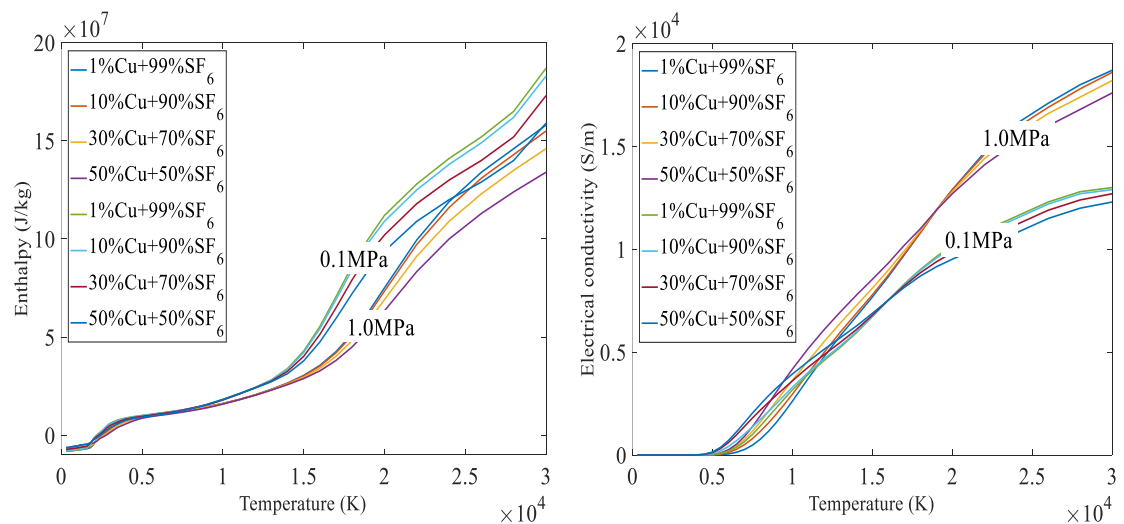


Figure 4.3 Thermodynamic properties and transport coefficients of the SF_6 -PTFE mixture at 1.0 MPa with different PTFE concentration [28].



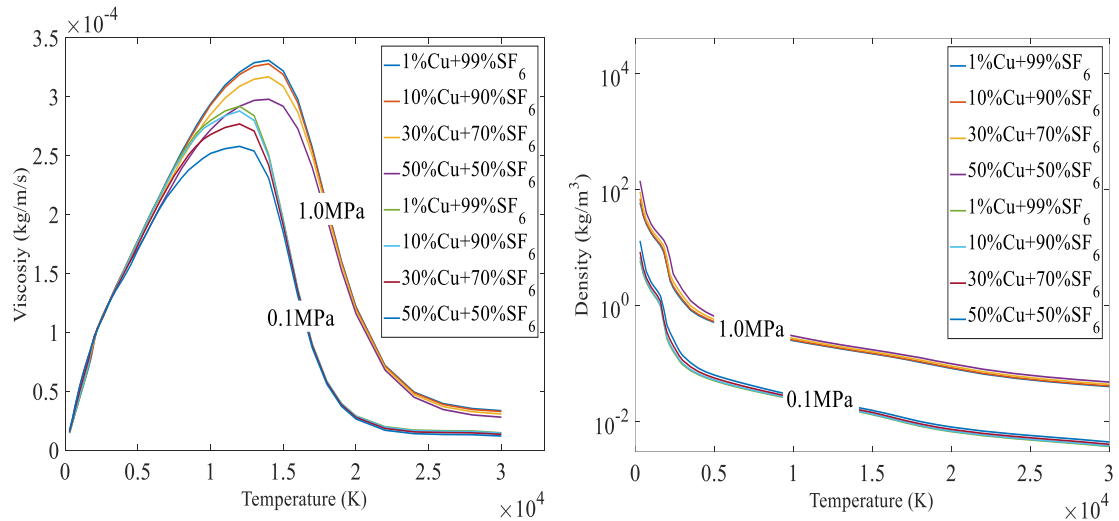


Figure 4.4 Thermodynamic properties and transport coefficients of the SF₆ and copper mixture at 0.1 MPa and 1.0 MPa with different copper concentration: 1%, 10%, 30% and 50% [29], [30].

4.3.2 Radiation and re-absorption

The radiation is the fastest mechanism of energy exchange since it travels at the speed of light. Radiation transport is a complicated process involving tens of thousands of the spectral lines whose absorption coefficient is the function of temperature and pressure. To accurately calculate the mass loss from nozzle due to ablation, a reasonable radiation model should be used. A number of the models are available, such as P1 model [31], method of partial characteristics [32] and a semi-empirical model introduced by Zhang *et al.* [33] based on the work in [34]. This semi-empirical model has been successfully used to SF₆ arcs [35]. It defines an arc core region which starts from the axis and ends at the point of αT_{max} where α is suggested to be 0.83. It is the defined radiation emission region where the radiation energy is calculated by the net emission coefficient (NEC) which is expressed as a function of pressure, temperature and cylindrical column radius. The cylindrical column radius is defined as the radial distance from the axis to the 4,000 K (puffer)/5,000 K (auto-expansion) isotherm. A significant proportion of the radiation core is re-absorbed in arc region from $0.83T_{max}$ to the 4,000 K/5,000 K isotherm. The radial arc temperature profile in a nozzle is normally monoatomic. However, for auto-expansion circuit breaker where the temperature near the nozzle surface can be higher than 4,000 K and the flow field makes the radial temperature profile non-monotonic. A definition to produce stable arc column radius is needed. For the high current phase that ends at 15 kA before the final current zero, the emission radius is defined as the distance from the axis to $0.83T_{max}$ and for the current zero phase from 15 kA to final current zero,

the emission radius is defined as the average of emission radii ending at $0.83T_{max}$ and 5,000 K respectively [2], [3]. Two typical temperature profiles and their corresponding radiative fluxes are plotted in Figure 4.5. The distribution of the volumetric source in re-absorption region is given by:

$$q_a(r_{arc}) = q_0 \left[1.1 - \left(\frac{R_{T_x} + R_{0.83T_{max}} - 2r_{arc}}{R_{T_x} - R_{0.83T_{max}}} \right)^2 \right] \quad (4.3.29)$$

where r_{arc} is the arc radius; q_a is the volumetric radiation source; q_0 is the maximum volumetric energy source due to the radiation re-absorption, expressed as:

$$q_0 = \frac{\alpha_r Q_{core}}{\int_{R_{0.83T_{max}}}^{R_{T_x}} \left[1.1 - \left(\frac{R_{T_x} + R_{0.83T_{max}} - 2r_{arc}}{R_{T_x} - R_{0.83T_{max}}} \right)^2 \right] 2\pi r_{arc} dr_{arc}} \quad (4.3.30)$$

where Q_{core} is the total radiation flux from the arc core and α_r is the percentage of the reabsorbed radiation flux.

The expression defined by Eq. (4.3.29) is derived with the empirical experience. For a normal nozzle flow where the arc is surrounded by a layer of cold SF₆, 80% of radiation is re-absorbed at the core edge which is higher than that in the auto-expansion circuit breaker (assumed to be 50% [36]).

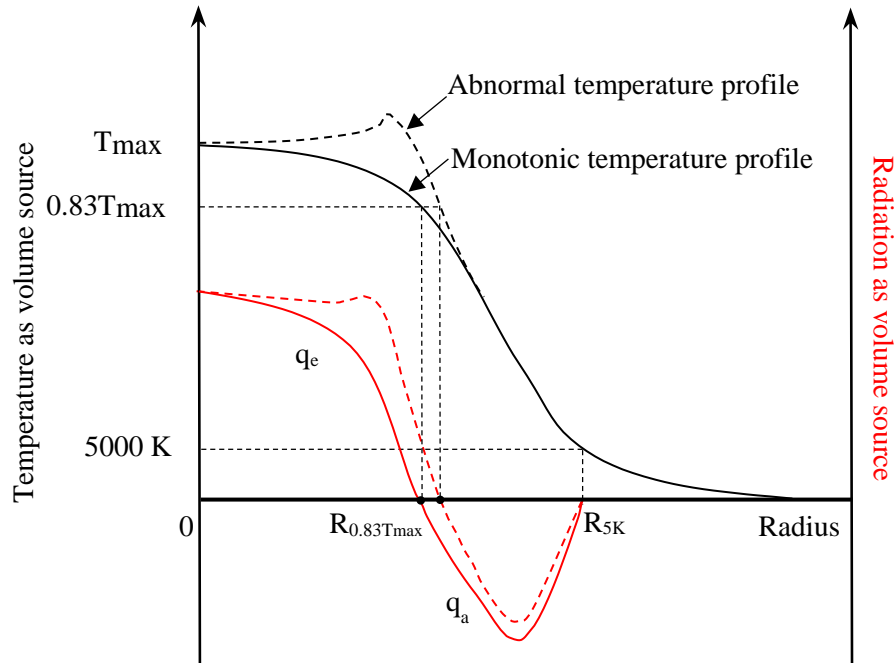


Figure 4.5 Possible arc radial temperature profiles and the emission ($0 \sim R_{83}$) and re-absorption ($R_{83} \sim R_{5K}$) regions. Black lines: (Solid) Monotonic temperature profile; (Dashed) Non-monotonic temperature profile; Red lines: Net radiation loss per unit and time.

The amount of radiation used for nozzle ablation significantly influences the arc voltage. Based on the simulation results [37], the re-absorption factor α_r is empirically related to instantaneous arcing current and nozzle cross section by:

$$\alpha_r = \frac{0.8(1 - C^N) + 6C}{1 + 6C} \quad (4.3.31)$$

where C is the percentage of ablated PTFE vapor injected into the arc column and N is adjusted with the experiment.

In the radiation model, q in Eq. (4.3.1) represents the net radiation loss per unit volume and time. It is determined by the NEC which describes power radiated per unit volume, expressed as [38],

$$\varepsilon_N = \int_0^\infty B_\nu K'_\nu G_l(K'_\nu R) d\nu \quad (4.3.32)$$

where B_ν is the Planck constant; K'_ν is the monochromatic absorption coefficient and G_l is a function for the cylindrical geometry.

Therefore, the total radiation used for nozzle ablation is determined by:

$$Q_{ablation} = (1 - \alpha) \int_{z_1}^{z_2} \int_0^{R_{0.83T_{max}}} q \cdot \xi \cdot 2\pi r_{arc} dr_{arc} dz \quad (4.3.33)$$

where ξ is the coefficient determined by ablation surface incline; $z_2 - z_1$ represents the axial distance of the ablation surface. The total mass ablated from PTFE nozzle surface is thus calculated by:

$$m_{PTFE} = \frac{\int_0^{t_{arc}} Q_{ablation} dt}{h_{v,PTFE}} \quad (4.3.34)$$

where $h_{v,PTFE}$ is the total ablation energy of PTFE material for changing from solid to vapor at 3,400 K, which equals to 11.9 MJ/kg.

The net emission coefficient of different mixtures has been calculated and the arc radii under different pressures, e.g. N₂-SF₆ mixture [38], air and SF₆. The NECs of different gaseous medium such as pure SF₆-Cu [39], SF₆ [40], and SF₆-PTFE [41] are illustrated in Figure 4.6, 4.7 and 4.8. In the present model, the NECs are tabulated from the related publications.

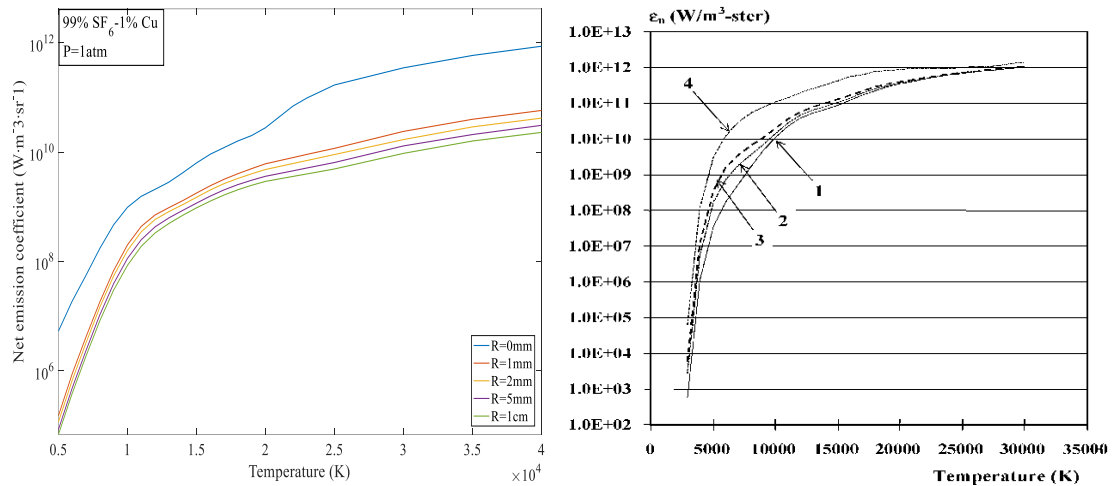


Figure 4.6 Net emission coefficient of SF_6 and copper mixture. Left: NEC as a function of temperature with different arc radii at atmospheric pressure. Right: NEC as a function of temperature and copper vapor concentration at 8atm. 1: 1%; 2: 5%; 3: 10%; 4: 50% [39].

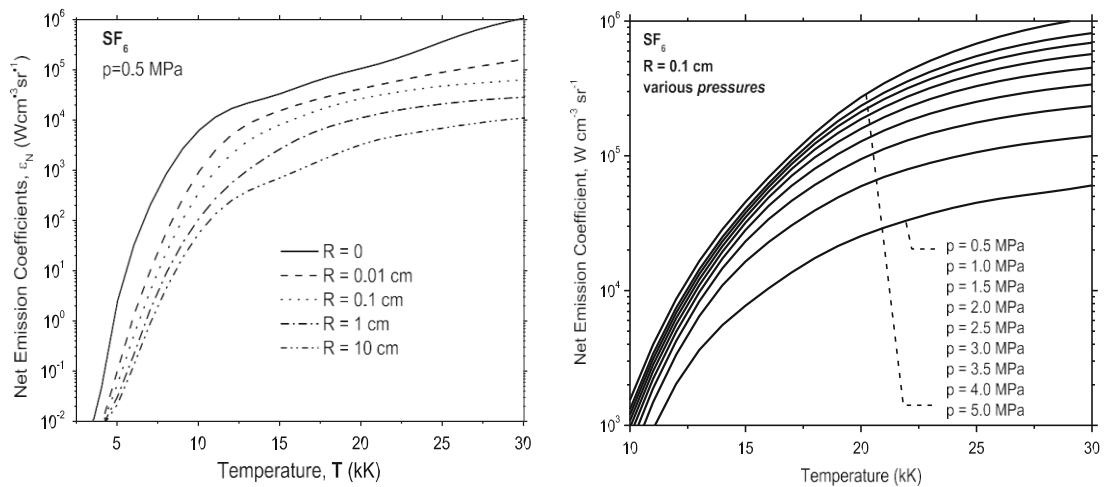


Figure 4.7 Net emission coefficient of SF_6 plasma as a function of temperature with different arc radius and pressure [40].

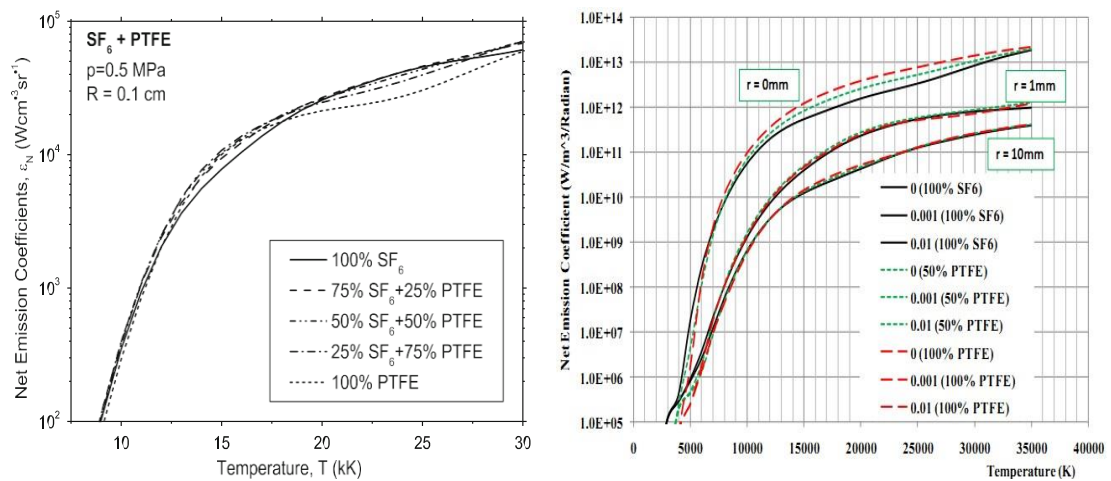


Figure 4.8 Net emission coefficient of SF_6 and PTFE mixture as a function of temperature [41].

In the radiation energy transport process, the total radiative energy flux per unit length Q_{ab} of the arc column is calculated using the radiation model described above. A quasi-steady process is assumed for PTFE nozzle ablation where the amount of ablated mass is proportional to the radiation energy reaching the nozzle surface. To determine the radiation energy flux, coefficient ξ need to be calculated by the axial surface inclination. In PHOENICS, ablative nozzle surface of each cell in an axis-symmetric computational domain of the model is regarded as a circular truncated cone and thus the lateral area of this circular truncated cone is the actual ablation surface area as presented in Figure 4.9, which is calculated by:

$$S = \pi(r_0 + r_i)\sqrt{(r_0 - r_i)^2 + (z_0 - z_i)^2} \quad (4.3.35)$$

and the radiation flux on the cell surface could be determined:

$$q_{ablation} = \frac{|z_0 - z_i|Q_{ab}}{S} \quad (4.3.36)$$

where the coefficient ξ depends on the grid system and the cell coordinates,

$$\xi = \frac{|z_0 - z_i|}{S} \quad (4.3.37)$$

and the mass flux injected into the flow in the direction normal to the ablating surface is:

$$\dot{m} = \frac{\xi Q_{ab}}{h_v} \quad (4.3.38)$$

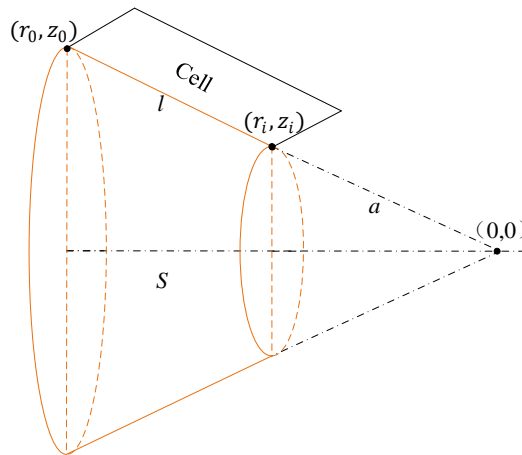


Figure 4.9 nozzle surface area diagram.

In the conservation equations, the momentum source carried by the vapour is calculated as \dot{m}/ρ_{cell} where ρ_{cell} is the density of the mixture in the ablating cell and the energy source is determined by $\dot{m}h_{va}$ where h_{va} is the enthalpy of the vapour at vaporization temperature.

4.4 Numerical Prediction of Nozzle Ablation

4.4.1 Short line fault----L90

The mathematic model that is used for the 145 kV/40 kA auto-expansion circuit breaker has been verified in the previous work including that reported in [3]. According to the international standard [42], [43], different test duties for different fault types (e.g. short line fault and terminal fault) have to be performed on the circuit breaker. Development tests show that the 145 kV/40 kA auto-expansion circuit breaker under the investigation passed the Short Line Fault L90 after a total of three test rounds. During the tests, the circuit breaker needs to be disassembled and overhauled with some new components such as PTFE nozzle(s) after a failed round.

In the present work, a comparative study of nozzle ablation is performed for tests in the first test round. It includes three tests, namely Test 92, Test 93 and Test 98 with different arc durations (Table 4.3). The travel curves of the solid contact and current waveforms for different tests are shown in Figure 4.10. In the first test round, Test 92 and Test 93 are short arc duration cases performed to confirm the shortest possible arc duration with which the circuit breaker can interrupt successfully. Test 98 is a long arc duration case.

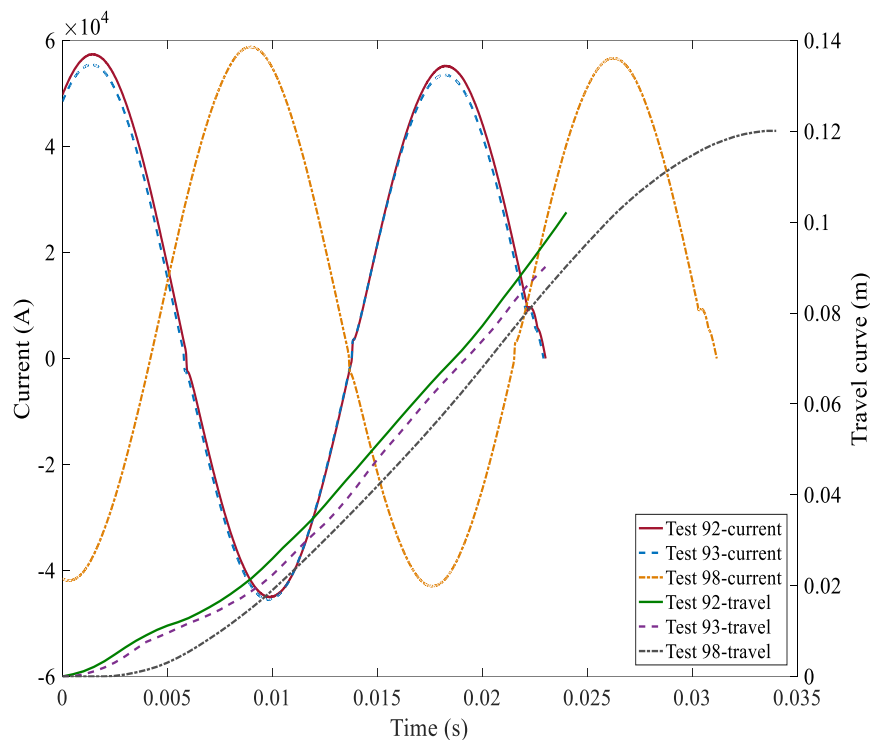


Figure 4.10 Travel curves of the solid contact and the current waveforms of Test 92, 93 and 98 respectively.

Table 4.3 Arc durations of the three tests in the first test round of L90.

Test	Arc duration (ms)	
	Prediction	Actual
92	13	13.6
93	12	12.3
98	20.5	20.1

Figure 4.11 shows the simplified geometry of the 145 kV/40 kA auto-expansion circuit breaker with the specified ablation surfaces (red lines). It should be mentioned that the semi-empirical radiation model applied in the present work assumes that radiation only travels in the radial direction of the axis-symmetric arc column. In other words, the cell on the nozzle surface which is radially shadowed by a solid object receives no radiation from the arc column, as shown in Figure 4.12.

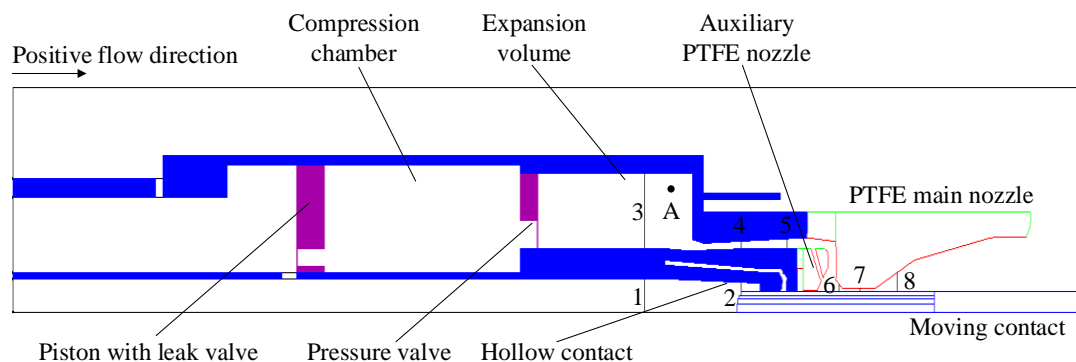


Figure 4.11 Simplified geometry of 145kV auto-expansion circuit breaker. The red lines represent for the specified ablation surfaces.

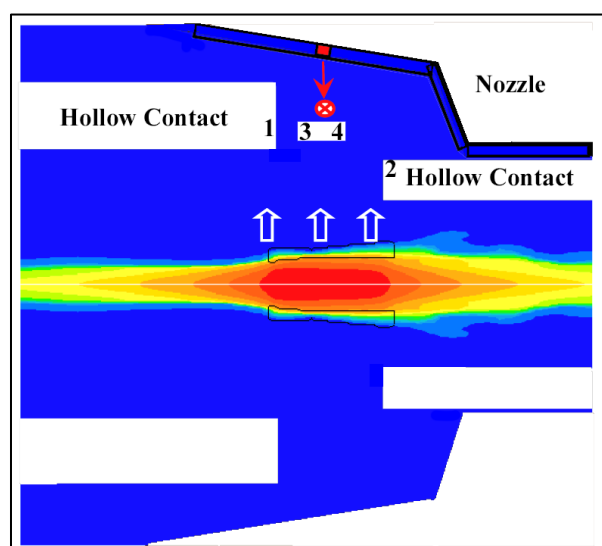


Figure 4.12 Diagram of a simple nozzle with designed solid objects [44].

The cell in red receives no radiation from the arc since the solid block from (3) to (4) stops the radiation from reaching this red cell. According to this description, the nozzle surface which is visible to the arc column is thus defined as the ablation surface.

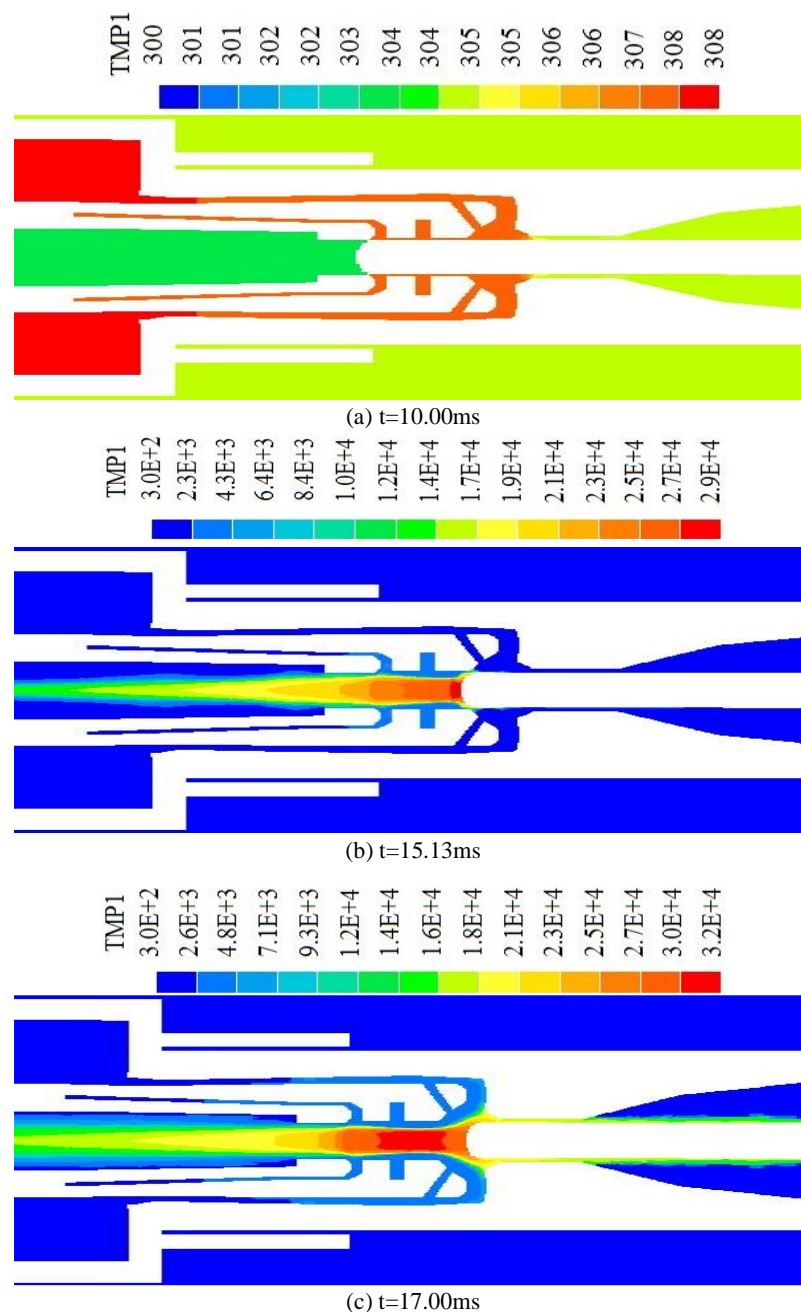
Furthermore, the arc rooting in the hollow contact of the circuit breaker is a complicated phenomenon. Despite the effects of the thin non-LTE layer in front of contact surface, the position of the arc root is also affected by the magnetic field induced by arc current. At present, it is not possible to predict the location and size of the arc root. In the present model, a transparent contact that has a high electrical conductivity (10^5 S/m) is assumed to exist in the hollow contact to sustain the current flow, as shown in Figure 4.1.

4.4.1.1 First short arc duration---Test 92 (13.6ms arcing time)

During the current interruption process, the arc is initiated at 12.2 ms. The temperature distribution in the arcing chamber with different positions of the solid contact are shown in Figure 4.13. The initial temperature inside the arcing chamber is set to 300 K. At the initial stage before the two arcing contacts separate, the solid contact travels inside the hollow contact. The hollow contact is blocked until $t=10.00$ ms as shown in Figure 4.13 (a). In the simulation, the arc is not initiated until the contacts separate with a distance of 5~8 mm. The arcing current is held at ± 3 kA depends on the current polarity when the current falls below this value to change its polarity at the current zero. Besides that, if the instantaneous current at the arc initiation is high (> 10 kA), the current is set to increase from 3 kA linearly to the value of actual current in approximately 0.2 ms [44]. These assumptions are necessary in the simulation to avoid computational difficulties since it is difficult to start an arc from a thin hot column with high instantaneous current. It takes time for the initial column to adjust its temperature and size to match the initial current.

As shown in Figure 4.13 (b), before the solid contact tip clears the auxiliary nozzle flat throat at 15.67 ms with a current of 32.7 kA, the produced PTFE vapour from auxiliary nozzle surface does not flow in large quantity towards the expansion volume since there is only a small gap (0.68mm) between the solid contact and auxiliary nozzle flat throat. The arc temperature in front of the solid contact reaches 29,000 K. With the movement of the solid contact, the current increases to its peak at 18.2 ms and the produced vapour

flows into the expansion volume due to the increased pressure in the contact gap. The temperature in the cross section between the expansion volume and main nozzle which is named “heating channel” is slightly increased as shown in Figure 4.13 (c) and (d). In addition, less amount of vapour flows out through the main nozzle flat throat towards the downstream because of the small gap (1.68mm) between the solid contact and main nozzle flat throat. The solid contact travels into the main nozzle flat throat at 18.96 ms. From Figure 4.13 (e), it is observed that at the end of the high current phase (>15 kA), the main nozzle is still blocked by the solid contact tip and there is a stagnation area in front of the solid contact where the thermal energy generated by ohmic heating could not be removed efficiently.



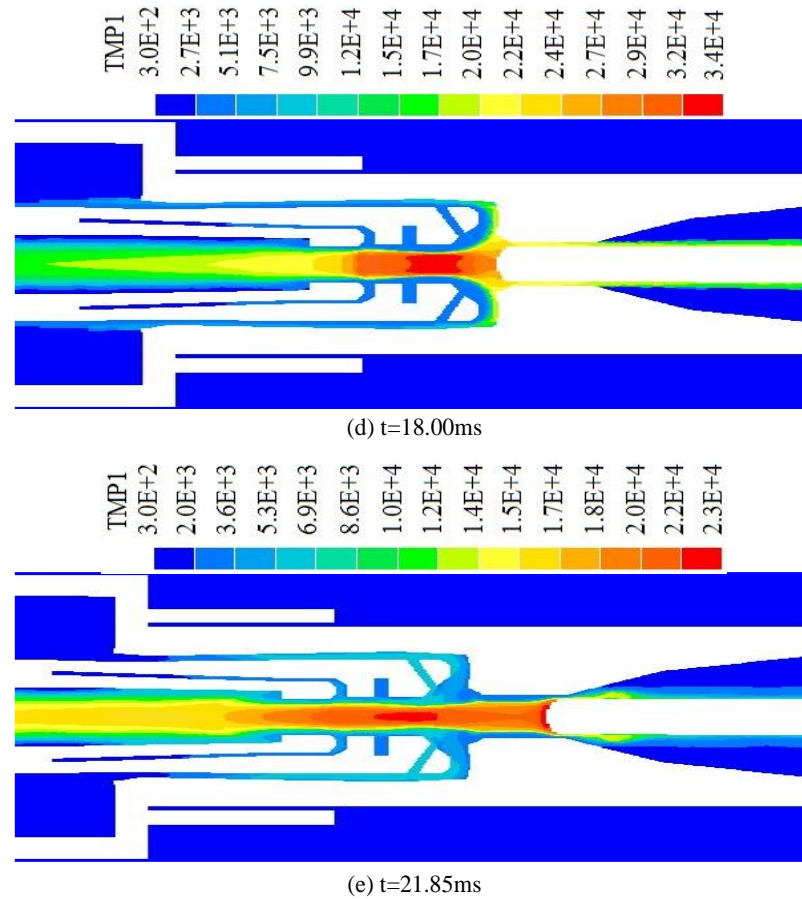


Figure 4.13 Arc temperature distributions at several typical time instants during the arcing period (Test 92).

The material of the nozzles in the 145 kV/40 kA auto-expansion circuit breaker consists of 98% PTFE and 2% MoS₂. The auxiliary nozzle surface starts to be vaporized roughly at 13.14 ms and the PTFE concentration inside the hollow contact is lower at this initial stage. When the solid contact moves through the auxiliary nozzle flat throat, the arc is burning in an ablation dominated mode with higher PTFE concentration, as illustrated in Figure 4.14. Large amount of injected PTFE vapour generates a high pressure region at the auxiliary nozzle flat throat (Figure 4.15 (b)). It is observed that the pressure in the expansion volume is around 0.68 MPa before the arc formation and it is increased to approximately 0.77 MPa at 15.13 ms. With the movement of solid contact, the arc is drawn between the flat throats of the main nozzle and auxiliary nozzle, and the pressure in the expansion volume has a significant increase after the solid contact tip completely clears the auxiliary nozzle flat throat, as shown in Figure 4.15 (c) and (d). The pressure in the expansion volume continuously increases during the high current phase. Besides that, although the produced vapour does not yet reach the interior of expansion volume, the pressure has been substantially increased as a result of the SF₆ gas being compressed

and heated up by the hot PTFE vapour. The pressure increases to a maximum of 2.9 MPa at 21.85 ms. Such a high pressure is to generate a high speed flow to effectively extinguish the arc when the current passes its final zero.

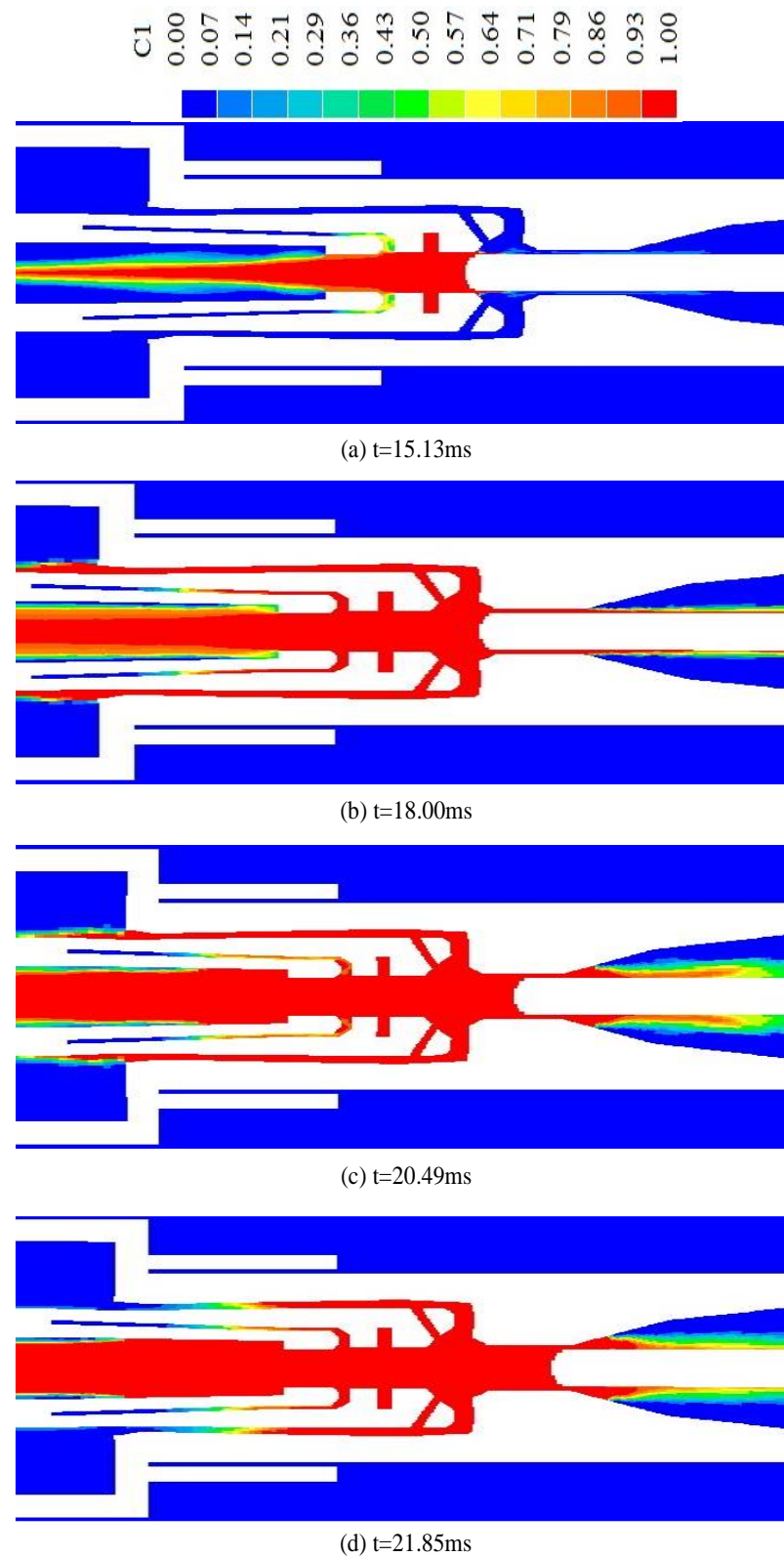


Figure 4.14 Concentration distributions of the produced PTFE vapour at typical time instants during the arcing period (Test 92).

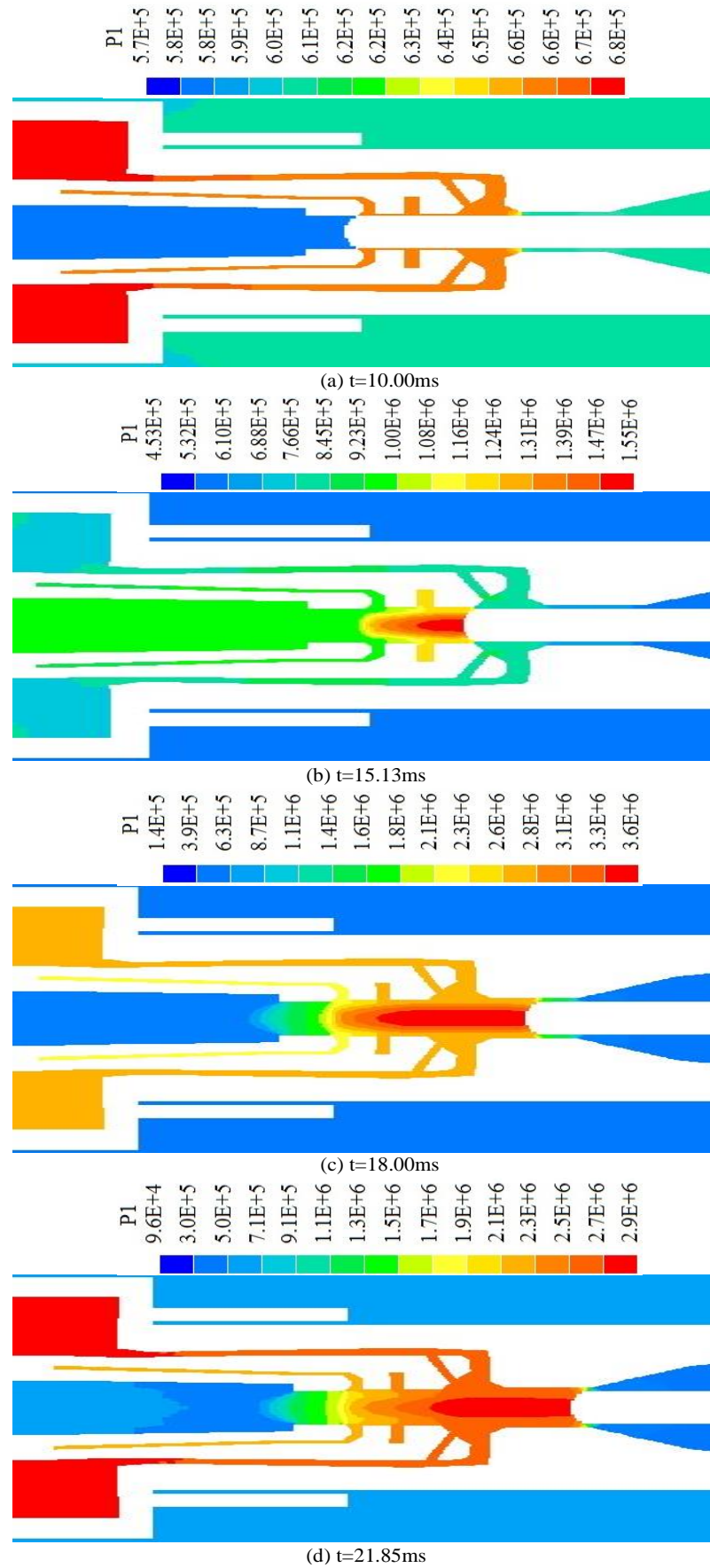


Figure 4.15 Pressure distribution at several typical time instants during the arcing period (Test 92).

Figure 4.16 presents the typical positions of the solid contact tip in the arcing chamber and also the corresponding current. It can be seen that the current starts to reduce from its peak when the solid contact travels from P3 to P4. The main nozzle flat throat starts to vaporize around 18.96 ms and only a moderate amount of vapour is produced from the main nozzle flat throat as a result of the reduced current (Figure 4.17). For Test 92, the vapour produced from the auxiliary nozzle surface takes a larger proportion (77%) in comparison with that from the main nozzle (23%). During the current zero phase (15 kA~0 A) after the solid contact entirely leaves the main nozzle flat throat, the ablation rate of nozzle material becomes lower. The current waveform and predicted arc voltage are shown in Figure 4.18. No measured arc voltage is available for comparison. In the arcing chamber, the solid contact tip blocks gas flow immediately in front of the contact surface where the gas is stagnant. This helps to stabilize the arc root and contributes to a stable arc voltage. In addition, the produced vapour affects the electrical conductivity of the gas mixture especially at high temperatures and it changes the arc voltage.

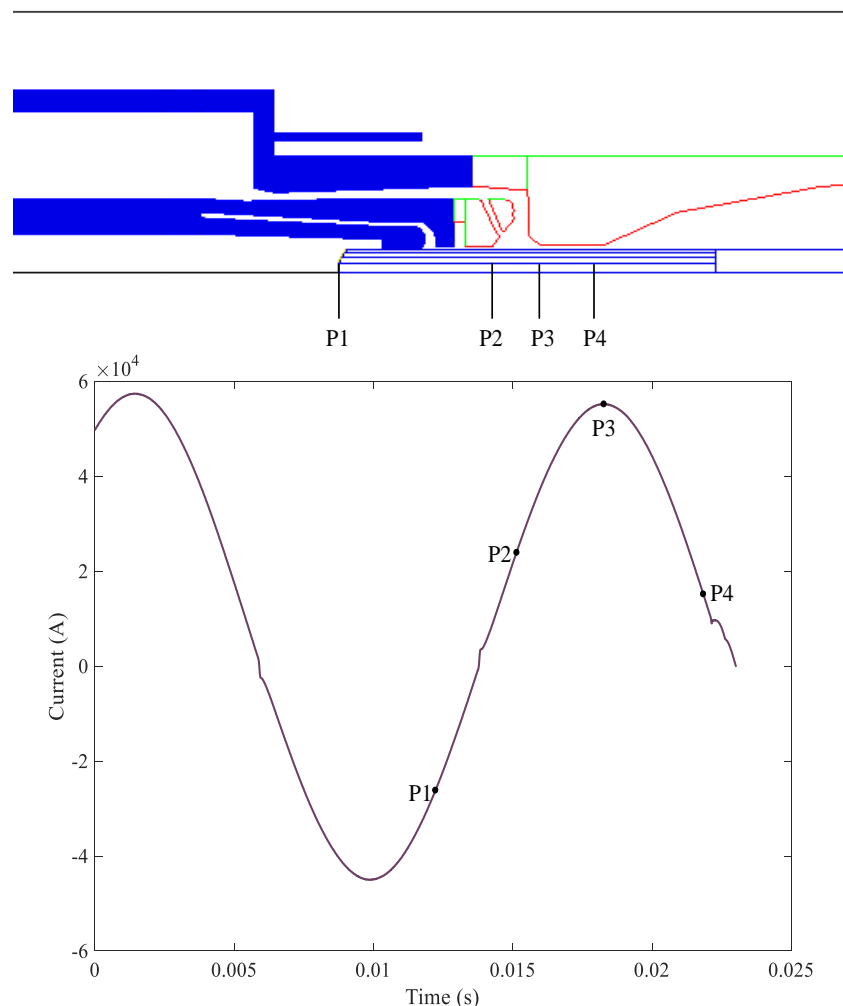


Figure 4.16 Positions of the solid contact tip in the arcing chamber corresponded to the current waveform of Test 92.

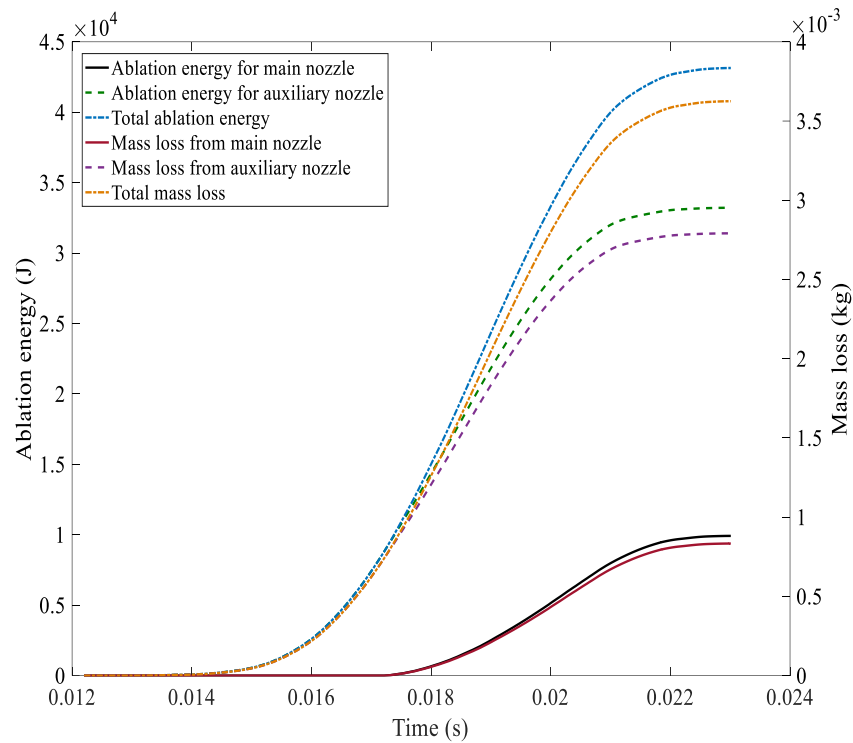


Figure 4.17 Predicted ablation energy and mass loss on the main and auxiliary nozzles of Test 92 with the original nozzle size.

In the present work, the radiation energy is calculated by the NEC data of pure SF_6 gas because of the similarity of NECs between the SF_6 gas and PTFE vapour especially at high temperatures when arc radiation radius larger than 1mm and they both contain an considerable proportion of the fluorine element as well [45].

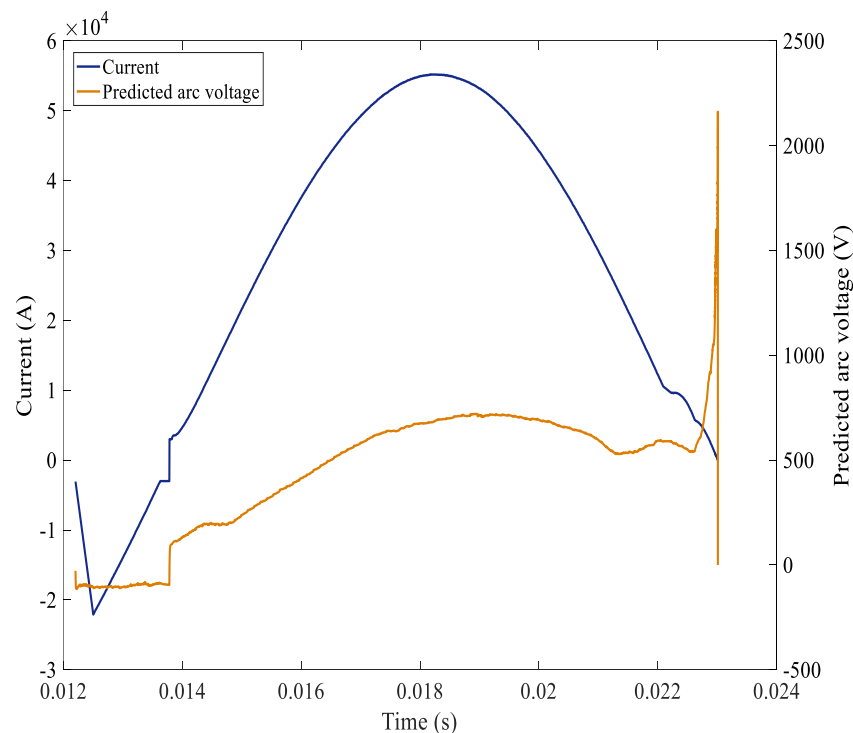


Figure 4.18 Current and the predicted arc voltage between two contacts of Test 92.

4.4.1.2 Second short arc duration---Test 93 (12.3 ms arcing time)

Based on the results of first test round, the 145 kV/40 kA auto-expansion circuit breaker passed Test 92 with a suggested arc duration 13 ms. To determine the effective shortest arc duration, the suggested arc duration of Test 93 is reduced to 12 ms. Nevertheless, this circuit breaker fails to thermally recover under the stress of the transient recovery voltage imposed by the system after the final current zero (Figure 4.19), which means that the short arc duration of L90 for this circuit breaker is 13 ms.

To analyse the circuit breakers interruption capacity, the post arc current after the final current zero is calculated. The arc resistance is determined by integrating the electrical conductivity over the arc column cross section and length. For the short line fault L90, the critical rate of rise of recovery voltage (RRRV: kV/us) is much higher especially at the initial stage in comparison with other test duties. Detailed descriptions are presented in Chapter 5.

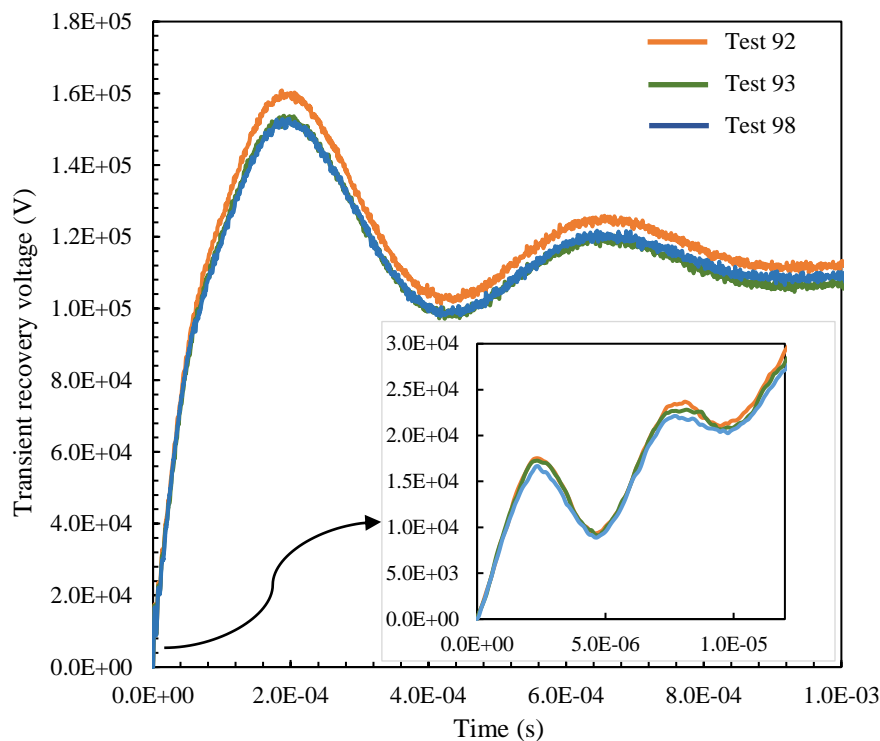


Figure 4.19 Imposed transient recovery voltages of Test 92, 93 and 98.

The determined radiation energy and the ablated mass from the nozzles of Test 93 are shown in Figure 4.20 which have similar profiles in comparison with Test 92. With the consideration of nozzle ablation resulted from Test 92, the mass loss from the auxiliary nozzle occupies 82% of the total ablated mass while main nozzle only takes 18%.

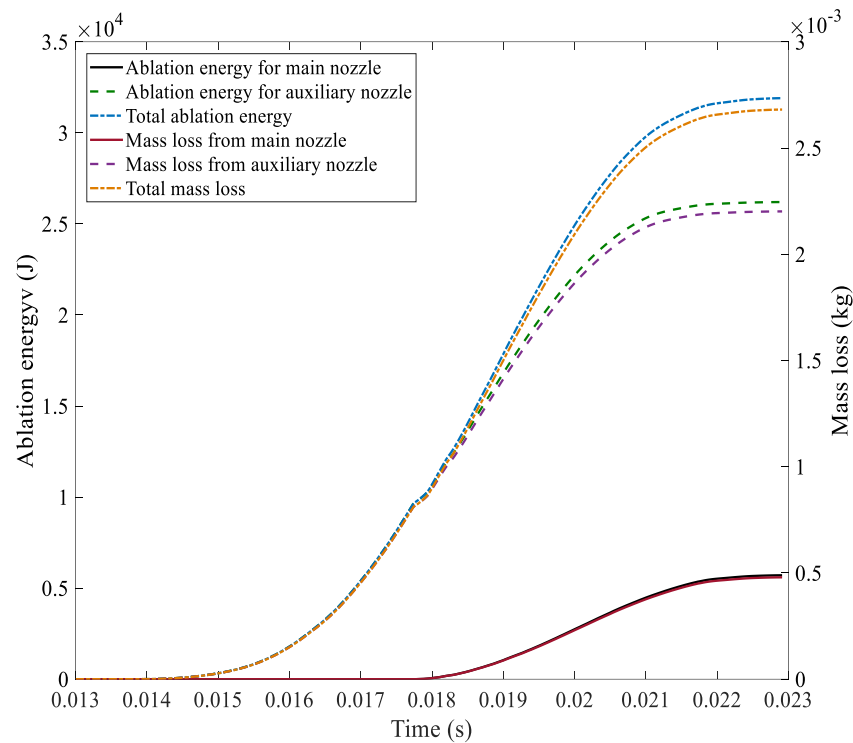


Figure 4.20 Predicted ablation energy and mass loss on the main and auxiliary nozzles with the consideration of nozzle flat throat diameter variation resulted from Test 92.

4.4.1.3 Long arc duration---Test 98 (20.1 ms arcing time)

The long arc duration case (Test 98) is somewhat different in comparison with Test 92 and Test 93. The arc is initiated at 13.8ms. From P1 to P2 where the current increases (Figure 4.21), a total of 0.2 g is ablated from auxiliary nozzle flat throat. When the solid contact moves towards the main nozzle downstream, the current reduces to its zero in the first half cycle and then rises to its positive maximum when the solid contact arrives at P6. From Figure 4.22, the PTFE concentration within the arcing space has a reduction which is due to the SF₆ gas flowing out from the expansion volume into the contact gap and mixes with the produced vapour. It is found that the solid contact has completely cleared the main nozzle flat throat before the final current zero. It leads to a larger cross section of the main nozzle surface exposes to the hot arc column, and eventually brings more vapour ablated from the main nozzle surface (Figure 4.23). The total mass loss from main nozzle surface is substantially increased around 23 ms when the solid contact moves across the middle of main nozzle flat throat. The mass ablated from the auxiliary nozzle surface takes 35% of the total ablated mass while the main nozzle takes a larger proportion of 65%. From the comparison of different arc duration cases, the auxiliary nozzle has a larger contribution for the pressurisation in expansion volume for the short arc duration case while the main nozzle becomes dominant for long arc duration case.

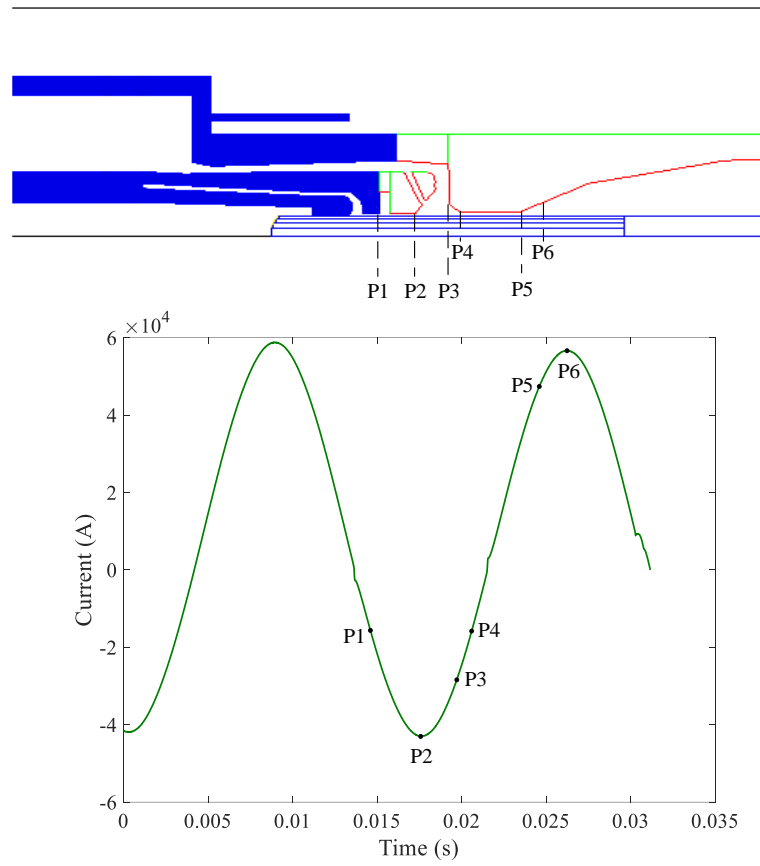


Figure 4.21 Positions of the solid contact tip in the arcing chamber corresponded to the current of Test 98.

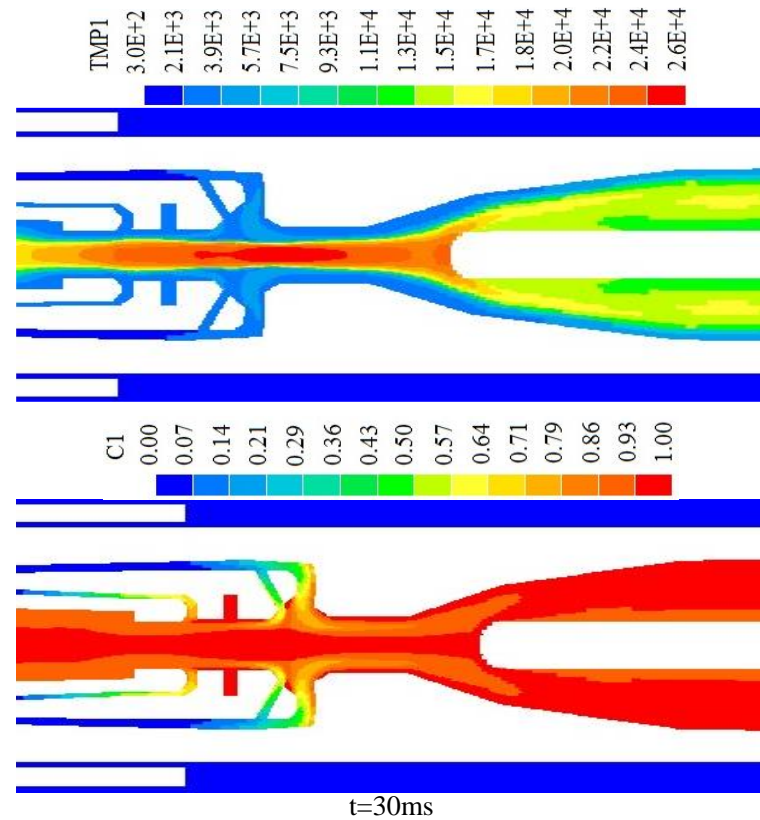


Figure 4.22 Temperature and PTFE concentration distributions approximately at the end of the high current phase of Test 98.

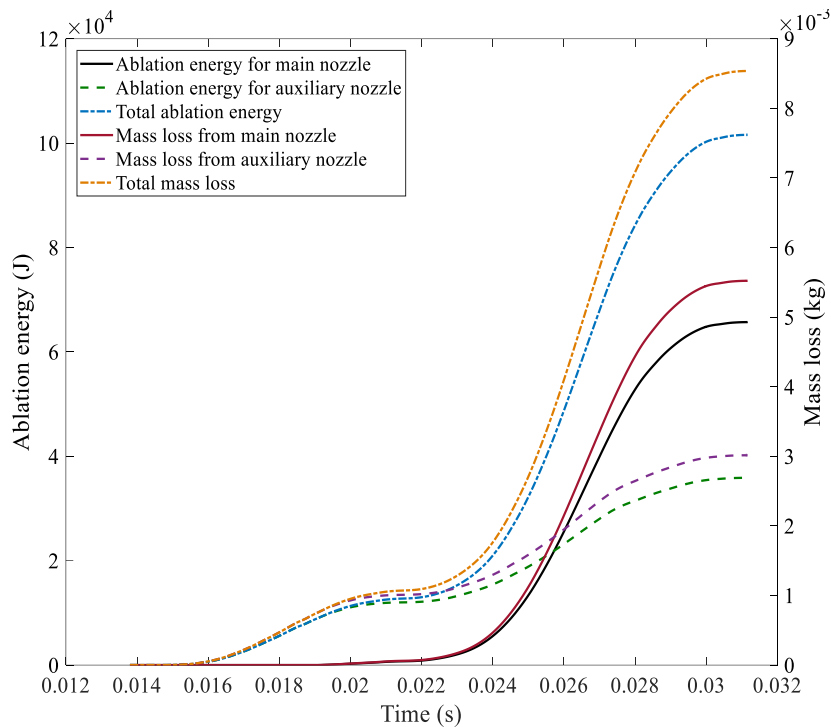


Figure 4.23 Predicted ablation energy and mass loss on the main and auxiliary nozzles with the consideration of nozzle flat throat diameter variation resulted from Test 93.

4.4.2 Associated experimental results of the mass loss from PTFE nozzle(s)

To study the characteristics of nozzle ablation in the high voltage auto-expansion circuit breaker, some investigations have been carried out experimentally by Seeger *et al* [46], [47] using a circuit breaker test device and a commercial circuit breaker to consider the PTFE ablation with different current levels, arc durations and nozzle geometries. The details of the experiment conditions are listed in Table 4.4.

Table 4.4 Experiment conditions on the test device and commercial circuit breaker [46], [47].

Conditions	Test device	Commercial circuit breaker
Test current (rms, kA)	3-45	6-63
Arcing time (ms)	5, 10, 15	10-20
Operating frequency (Hz)	29, 50	-
Arcing contact	Cu/W	Cu/W
Filling pressure (atm)	5	5

Theoretically, the extent of the ablation is determined by the total electrical energy input. Therefore, a reasonable quantity defined as the “specific ablation” is used to describe a time-averaged ablation:

$$\delta = \frac{\Delta m}{\int_{t=0}^{t_{arc}} U_i(t) \cdot I_i(t) dt} \quad (4.4.1)$$

where Δm is the total PTFE mass loss both from the main and auxiliary nozzles; U_i and I_i are the measured voltage and current. For the circuit breaker test device, the specific ablation with different current density ranges are:

$$\begin{cases} \delta = 8.50 \pm 1 \text{ mg/kJ} & j_{peak} < 0.55 \times 10^8 \text{ A/m}^2 \\ \delta = 26 \pm 2.5 \text{ mg/kJ} & j_{peak} > 0.80 \times 10^8 \text{ A/m}^2 \end{cases}$$

where $0.55 \times 10^8 \text{ A/m}^2$ is regarded as the transition current density to describe the arc burning mode (axial blown and ablation controlled).

For the commercial circuit breaker, the specific ablation with different current density ranges are:

$$\begin{cases} \delta = 29 \pm 3 \text{ mg/kJ} & j_{peak} > 1.20 \times 10^8 \text{ A/m}^2 \\ \delta \approx 20.0 \text{ mg/kJ} & j_{peak} < 1.00 \times 10^8 \text{ A/m}^2 \end{cases}$$

and the average peak current densities of the test device and commercial circuit breaker are respectively defined by:

$$j_{peak} = \frac{I_{peak}}{A_n} \quad (4.4.2)$$

$$j_{peak} = \frac{\sum_{i=1}^n Q_i \cdot j_{peak,i}}{\sum_{i=1}^n Q_i} \quad (4.4.3)$$

where A_n is the nozzle throat cross section; n is the total number of current applications of each test; Q_i is the total energy input and I_{peak} is the peak value of applied current.

From the experiments, the amount of PTFE mass loss was measured using two different methods: weigh the mass loss and analyse the geometry change. The former method is performed with an uncertainty of less than 2%. When the mass ablated from the nozzle throat is determined, the latter method is adopted. The volume loss is simply determined from the average of radial burn-off for a circuit breaker test device while a comparison of the contours of ablated nozzle with a new one is carried out on a commercial circuit breaker. From the comparison, the method used for commercial circuit breaker is more precise with smaller error bar. Following the experiments, the specific ablation for the axial blown arc is $(8.5 \pm 1 \text{ mg/kJ})$ much smaller than the ablation dominated arc $(23\text{-}32 \text{ mg/kJ})$. In addition, experimental research of the ablation dominated arc in a cylindrical PTFE tube demonstrates that the estimated specific ablation is roughly constant when

the current density exceeds 1.5×10^8 A/m² [40]. From another experiment on a smaller scale test device, the estimated specific ablation at the arc confining wall (10-20 mg/kJ) is in accordance with small PTFE tube experiments [47]. In reality, an accurate method to quantitatively determine the mass loss especially from nozzle throat is more difficult because the ablation is not evenly distributed on nozzle surface which becomes rough after a number of operations. The experiment results of 145 kV/40 kA auto-expansion circuit breaker are obtained from the measurement of the nozzle surface deformation using Vernier scale (Table 4.5) which is for reference only.

In the first test round, three tests (92, 93, 98) are performed in sequence. The predictions of the mass loss from the main and auxiliary nozzles with and without considering the variations of the nozzle flat throat diameter after the first test round are shown in Table 4.6 and 4.7. Table 4.8 gives detailed results of the nozzle flat throat dimension changes after each test and Table 4.9 shows the calculated specific ablation which are reasonably close to the experiment results.

Table 4.5 Experimental result of the 145 kV/40 kA auto-expansion circuit breaker nozzle flat throat mass loss and changed flat throat radius after the first test round.

Nozzle	Measurement from experiments	
	Mass loss (g)	Nozzle throat radius (mm)
Main nozzle flat throat	1.84	11.05
Auxiliary nozzle flat throat	1.52	10.65

Table 4.6 Predicted mass loss and changed nozzle flat throat radius after the first test round (3 tests) with the consideration of radius variation resulted from each test.

Nozzle	Predicted value from computation	
	Mass loss (g)	Nozzle flat throat radius (mm)
Main nozzle flat throat	3.79	11.60
Auxiliary nozzle flat throat	4.26	12.40

Table 4.7 Predicted mass loss and changed nozzle flat throat radius after the first test round without the consideration of radius variation resulted from each test.

Nozzle	Predicted value from computation	
	Mass loss (g)	Nozzle throat radius (mm)
Main nozzle flat throat	3.34	11.50
Auxiliary nozzle flat throat	1.65	10.70

Table 4.8 Predicted PTFE mass loss and nozzle throat diameter variation after each test in the first test round.

Nozzle		Predicted value from computation					
		Mass loss (g)			Nozzle flat throat radius (mm)		
		Test 92	Test 93	Test 98	Test 92	Test 93	Test 98
Main nozzle	Flat throat	0.31	0.14	3.34	10.6	10.6	11.6
	Total	0.83	0.48	5.51			
Auxiliary nozzle	Flat throat	1.50	1.21	1.55	10.6	11.4	12.4
	Total	2.78	2.20	3.02			
Total mass loss from nozzle surface		3.61	2.68	8.53			

Table 4.9 Predicted specific ablation for the three tests in the first test round.

Tests	Q_i (kJ)	I_{peak} (kA)	j_{peak} (A/m ²)	δ (mg/kJ)
Test 92	183	55.7	1.61×10^8	19.7
Test 93	146	53.9	1.53×10^8	18.4
Test 98	392	57.3	1.62×10^8	21.8

4.4.3 Variation of the nozzle flat throat dimension as a result of ablation

The objective of work in this section is to study the severity of nozzle ablation relating to electrical endurance. To obtain a thorough understanding of the nozzle ablation and its effects on arc behaviour, three computations correspond to the current interruption process of each test in the first test round with considering the variations of nozzle flat throat diameters resulted from the prior computation are performed in sequence. The changed diameters of main and auxiliary nozzle holes are obtained from the predicted mass loss with PTFE material density of 2.2 g/cm³. The results are presented in Table 4.10, 4.11 and 4.12.

The predicted total mass loss from the nozzle flat throat occupies approximately 50% of the total mass loss which has been proved from the experiment mentioned previously. From the calculation, the variations present similar manner after each computation for Test 92 and 93. The total mass loss is decreased with the enlarged nozzle holes and the proportion from the auxiliary nozzle is roughly 3~5 times higher than the main nozzle.

However, the ablated mass from auxiliary nozzle surface presents an increase when the radii of main and auxiliary nozzle flat throats are respectively enlarged to 11.5 mm and 10.7 mm Test 98. The mass loss from the main nozzle is decreased under this condition. Overall, the total ablated mass from the nozzle flat throat shows a reduction due to the enlargement of the nozzle holes. Detailed explanations of Test 98 with test duty T60 are described in Chapter 5.

Table 4.10 Predicted PTFE mass loss due to the nozzle ablation after each computation of Test 92 with the consideration of nozzle diameter variation.

Nozzle		Predicted value from computation					
		Mass loss (g)			Nozzle throat radius (mm)		
		Com. 1	Com. 2	Com. 3	Com. 1	Com. 2	Com. 3
Main nozzle	Throat	0.31	0.31	0.29	10.6	10.7	10.8
	Total	0.83	0.81	0.78			
Auxiliary nozzle	Throat	1.50	1.34	1.22	10.6	11.5	12.3
	Total	2.78	2.49	2.25			
Total mass loss from nozzle surface		3.61	3.30	3.02			

Table 4.11 Predicted PTFE mass loss due to the nozzle ablation after each computation of Test 93 with the consideration of nozzle diameter variation.

Nozzle		Predicted value from computation					
		Mass loss (g)			Nozzle throat radius (mm)		
		Com. 1	Com. 2	Com. 3	Com. 1	Com. 2	Com. 3
Main nozzle	Throat	0.14	0.14	0.14	10.5	10.5	10.5
	Total	0.52	0.49	0.48			
Auxiliary nozzle	Throat	1.38	1.26	1.13	10.5	11.4	12.1
	Total	2.53	2.31	2.06			
Total mass loss from nozzle surface		3.08	2.80	2.54			

Table 4.12 Predicted PTFE mass loss due to the nozzle ablation after each computation of Test 98 with the consideration of nozzle diameter variation.

Nozzle		Predicted value from computation					
		Mass loss (g)			Nozzle throat radius (mm)		
		Com. 1	Com. 2	Com. 3	Com. 1	Com. 2	Com. 3
Main nozzle	Throat	3.34	2.86	2.63	11.5	12.3	13.0
	Total	5.51	4.90	4.68			
Auxiliary nozzle	Throat	1.65	2.01	1.75	10.7	12.0	13.1
	Total	3.24	3.88	3.31			
Total mass loss from nozzle surface		8.75	8.78	7.99			

4.5 Gas Flow Environment Considering Dimensional Change due to the Nozzle Ablation

The flow field conditions inside the arcing chamber, e.g. in hollow contact, in upstream expansion volume, main nozzle and its downstream are analysed by assigning 8 cross sections in the model as presented in Figure 4.11. In the present work, the enthalpy and mass flow conditions are discussed. The corresponded enthalpy and mass flow rates are respectively determined by:

$$\dot{m}_h = \int \rho w h \cdot 2\pi r dr \quad (4.5.1)$$

$$\dot{m}_{h,PTFE} = \int \rho w h c \cdot 2\pi r dr \quad (4.5.2)$$

$$\dot{m}_{h,SF_6} = \int \rho w h (1 - c) \cdot 2\pi r dr \quad (4.5.3)$$

$$\dot{m} = \int \rho w \cdot 2\pi r dr \quad (4.5.4)$$

$$\dot{m}_{PTFE} = \int \rho w c \cdot 2\pi r dr \quad (4.5.5)$$

$$\dot{m}_{SF_6} = \int \rho w (1 - c) \cdot 2\pi r dr \quad (4.5.6)$$

where ρ is the gas mixture density; w is the axial velocity component; h is the mixture enthalpy; c is the concentration of PTFE vapour and r represents for the radial direction.

For Test 92, the auxiliary nozzle starts to vaporize after the arc initialisation (13.14 ms). The less amount of produced PTFE vapour at the initial stage carries negligible enthalpy and mass fluxes through cross sections 1 and 2 towards the hollow contact, as presented in Figure 4.24. When the solid contact completely clears the auxiliary nozzle flat throat at 13.86 ms, the interrupting current increases from 3.5 kA to its positive peak 55.2 kA at 18.20 ms before the solid contact enters the main nozzle flat throat. The PTFE vapour starts to be produced in large quantity from the auxiliary nozzle during this period. The total enthalpy and mass fluxes have considerable increase with high flow rates as well. Nevertheless, the increased enthalpy is due to the PTFE vapour while the SF₆ gas is the main contributor for the mass flow. The total enthalpy passing through cross section 1 is slightly less than that through cross section 2 which is a result of the decreased PTFE and SF₆ fluxes. The total mass enters through cross section 1 is higher than that through cross section 2 which is determined by the increased SF₆ mass flow. Besides that, total mass carried by PTFE vapour flows towards the hollow contact takes 32% of the total ablated mass (3.61 g) from the nozzles.

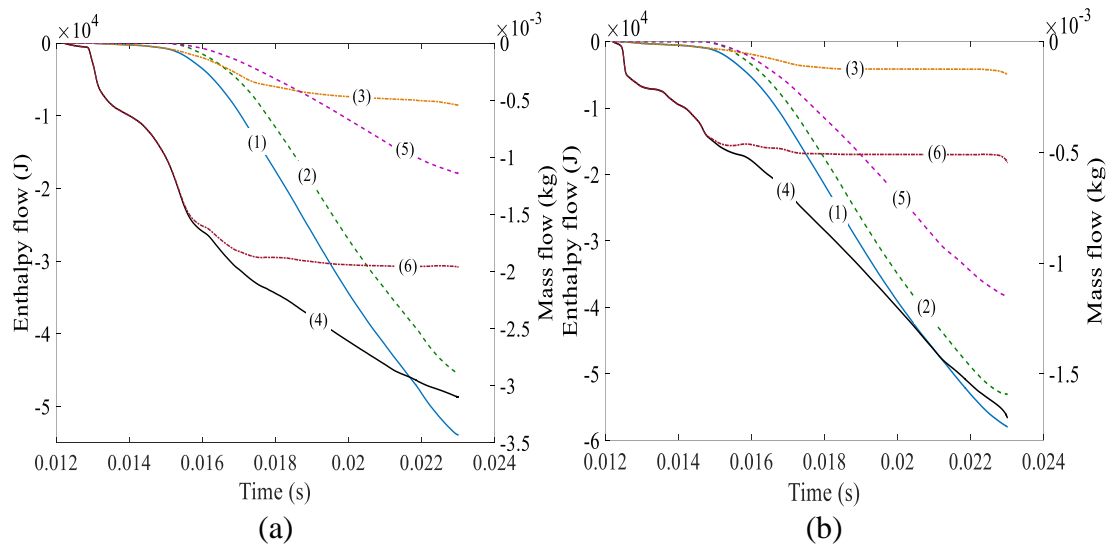
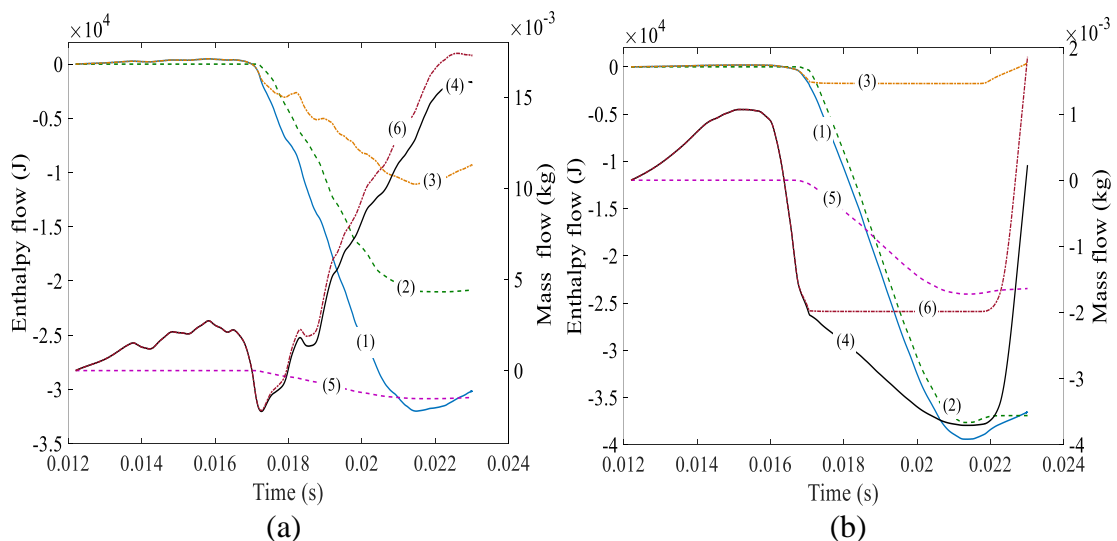


Figure 4.24 Predicted enthalpy and mass flow through the cross sections 1 (a) and 2 (b) in the hollow contact of Test 92 (Com.1). The six curves respectively represent (1): total enthalpy flow; (2): enthalpy flow carried PTFE vapor; (3): enthalpy flow carried by SF₆ gas; (4): total mass flow; (5): mass flow carried by PTFE vapor; (6): mass flow carried by SF₆ gas.

Figure 4.25 (a) describes the flow field distribution inside the expansion volume during the whole arcing period. As discussed previously, before the solid contact totally clears the auxiliary nozzle flat throat, the gaseous mixture is largely blocked inside the hollow contact and less amount of vapour is flowed out through the smaller gap between solid contact and auxiliary nozzle flat throat. Roughly at 17 ms, the thermal energy is largely

brought into the expansion volume by the hot PTFE vapour as a consequence of strong ablation from the nozzles especially the auxiliary one with the increased current. A total of 32 kJ enthalpy, which PTFE vapour contributes 66%, enters through cross section 3 during the whole arcing period. However, it is observed that only 1.54 g ablated mass is driven into the interior of the expansion volume, which contributes to 9.7% of the total mass flow. As explained before, although the produced PTFE vapour does not yet reach the interior of expansion volume, the pressure has been considerably increased as shown in Figure 4.15. This pressurisation is resulted from the thermal energy brought by the vapour which heats up the gaseous mixture in expansion volume while the effect of mass flow is smaller due to the less amount of PTFE vapour in the expansion volume. At 18.37 ms, the total enthalpy flow rate rises to maximum (-13.6 MJ/s). At 17.99 ms, the mass starts to flow out towards heating channel and reaches its maximum of 15.9 g at 22.62 ms which contains 17.4 g SF₆ gas and 1.5 g PTFE vapour.

Through the heating channel, the mass flux carried by SF₆ gas presents an insignificant change from 17 ms to 22 ms while the total enthalpy towards the expansion volume has a substantial increase as shown in Figure 4.25 (b) and (c). During this period, the main nozzle is clogged by the solid contact which makes the produced vapour flow towards the expansion volume. When the solid contact entirely clears the main nozzle flat throat at 22.83 ms, the current has dropped to 3.6 kA and the produced vapour becomes much less, the total mass flows out through the heating channel with a comparative high rate for the final arc cooling. In addition, the flow conditions around main nozzle flat throat present similar manner (Figure 4.26) in comparison with that through hollow contact and the detailed description is shown in the following contents.



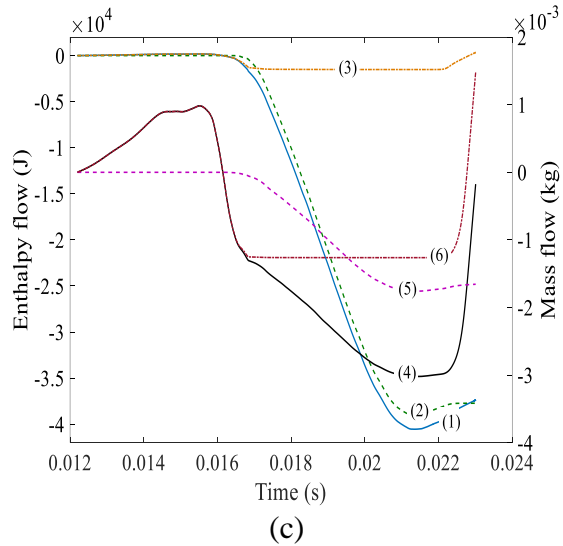


Figure 4.25 Predicted enthalpy and mass flow through the cross sections 3 (a), 4 (b) and 5 (c), each curve has the same meaning explained in Figure 4.24.

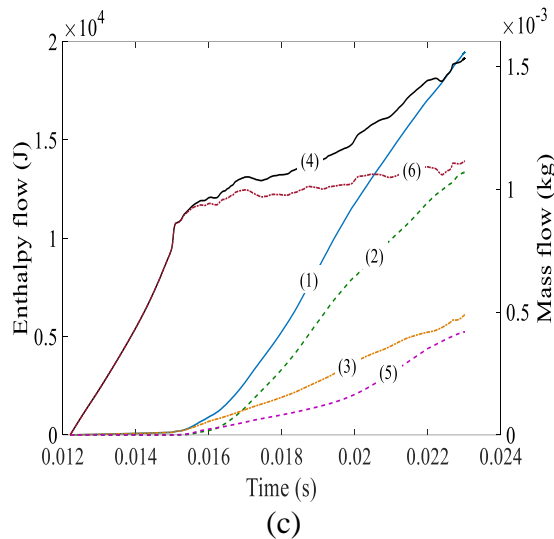
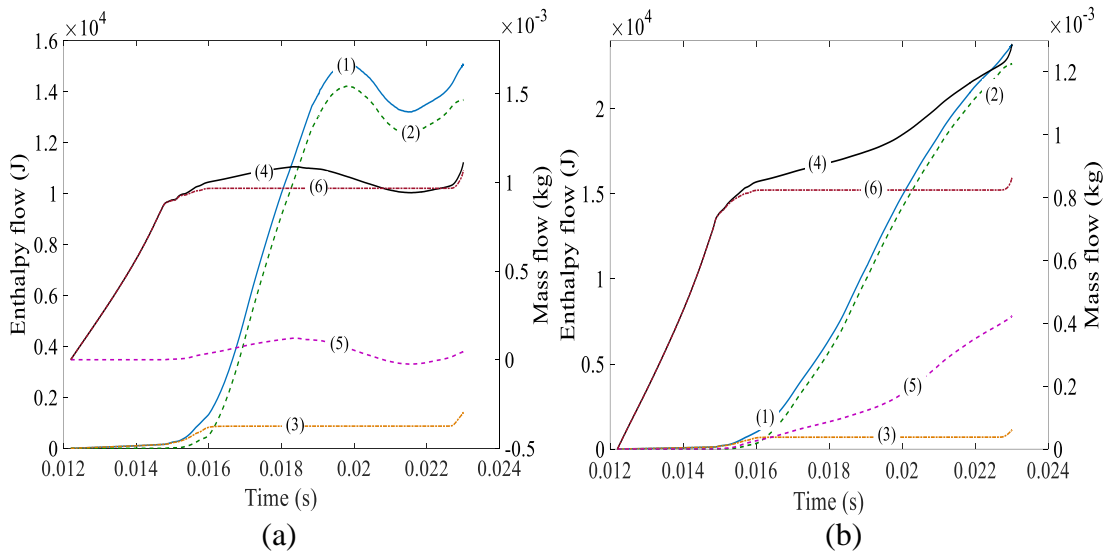


Figure 4.26 Predicted enthalpy and mass flow through cross sections 6 (a), 7 (b) and 8 (c) towards downstream, each curve has same meaning explained in Figure 4.24.

For Test 98, the arc is initialised at 13.8 ms and the solid contact starts to travel through the auxiliary nozzle at 14.85 ms. As shown in Figure 4.27, the flow field distribution in the hollow contact is similar to Test 92. A total of 102.3 kJ enthalpy flows through cross section 1 with a maximum flow rate of -9.41MJ/s and a total of 3.04 g mass.

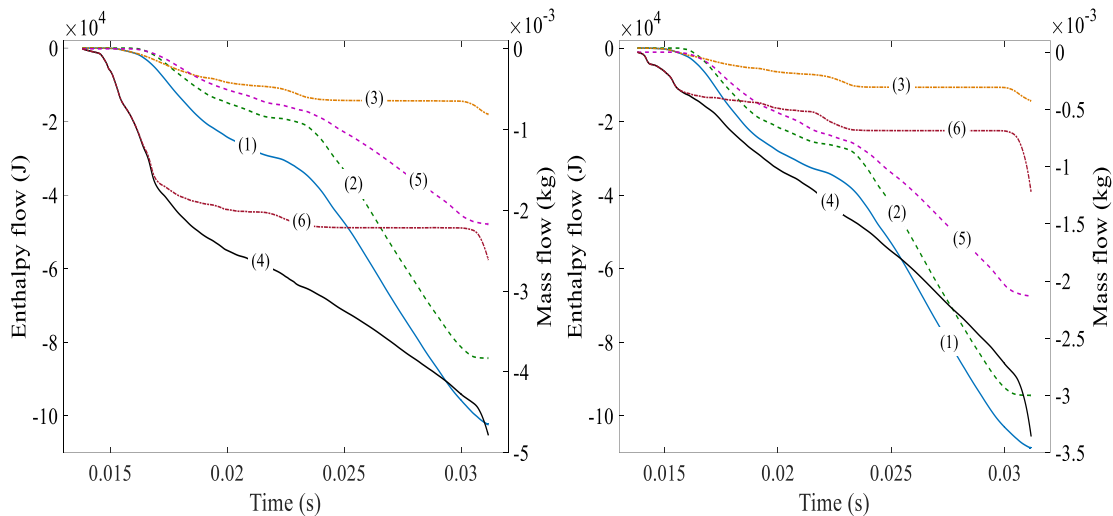


Figure 4.27 Predicted enthalpy and mass flow through cross sections 1 (a) and 2 (b) in hollow contact of Test 98 (Com.1), each curve has same meaning explained in Figure 4.24.

However, the flow field condition inside the expansion volume is somewhat different as shown in Figure 4.28 (a). From 17.72 ms to 20.22 ms when the solid contact travels through P2 to P4 (Figure 4.21), only 5.44 kJ enthalpy flows into the expansion volume through cross section 3 with a relatively slow rate. It is caused by a decreased electrical power supply from the arc column as a result of current decrease. Insufficient electrical energy stops the gaseous mixture flow towards the expansion volume until the current passes its zero in the first half cycle. When the solid contact just clears the main nozzle flat throat at 24.60 ms (P5), the arc is drawn into the main nozzle flat throat and larger cross section of the nozzle is exposed to the arc column, but only small amount of PTFE vapour (1.50 g in total) is produced from the nozzles with 0.47 g pumps into expansion volume. This is because the steeply increased current brings a strong thermal energy so that the produced vapour is largely discharged. From 25.0 ms to 26.15 ms when the current increases to its positive peak of 56.64 kA, a total of 4.6 g mass is ablated from the nozzles, and the flat throats of main and auxiliary nozzles respectively contribute 51.1% and 25.7%. But the proportion of mass of PTFE vapour in the expansion volume remains low (14.6% of the total mass). Around 23.35ms when the solid contact moves around the middle of main nozzle flat throat, the total enthalpy has a substantial increase

and reaches its maximum 42.2 kJ at 27.85 ms. From the calculation, the results indicate that the produced vapour only results in a smaller pressurisation (1.33 MPa) inside the expansion volume due to compression of SF_6 gas until the solid contact moves through the middle of main nozzle flat throat as demonstrated in Figure 4.29. After the clearance of main nozzle flat throat, the pressure increases to its maximum of 4.10 MPa.

Outside the expansion volume, the total mass flows through heating channel towards the expansion volume shows a decrease from 20.48 ms which is also determined by the reduced electrical power supply. In addition, large amount of mass rushes out from the heating channel towards the arcing space with a steeply increased mass flow rate before the final current zero which is resulted from the significant pressure difference between the upstream expansion volume and the contact gap.

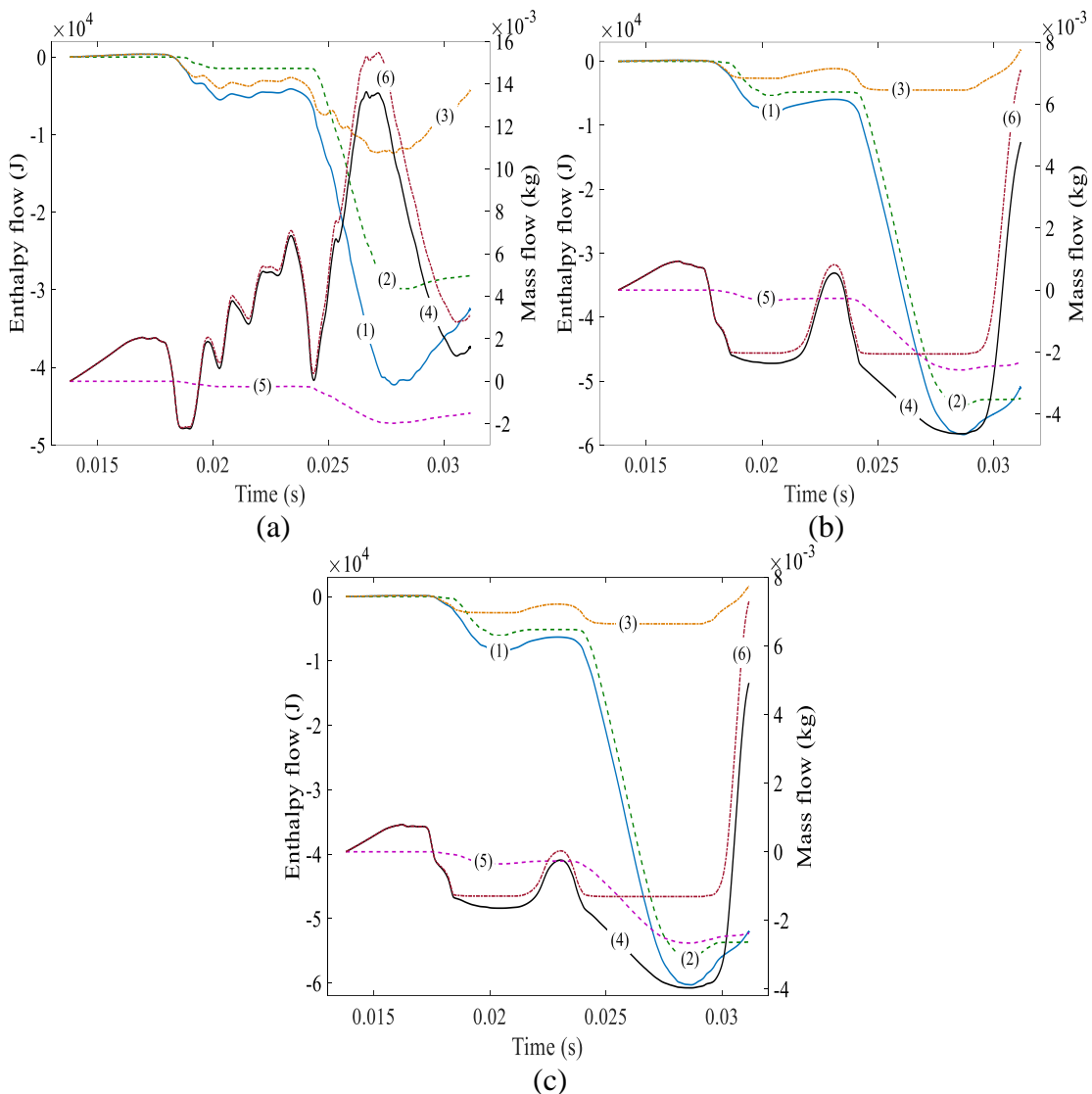


Figure 4.28 Predicted enthalpy and mass flow through the cross sections 3 (a), 4 (b) and 5 (c), each curve has the same meaning explained in Figure 4.24.

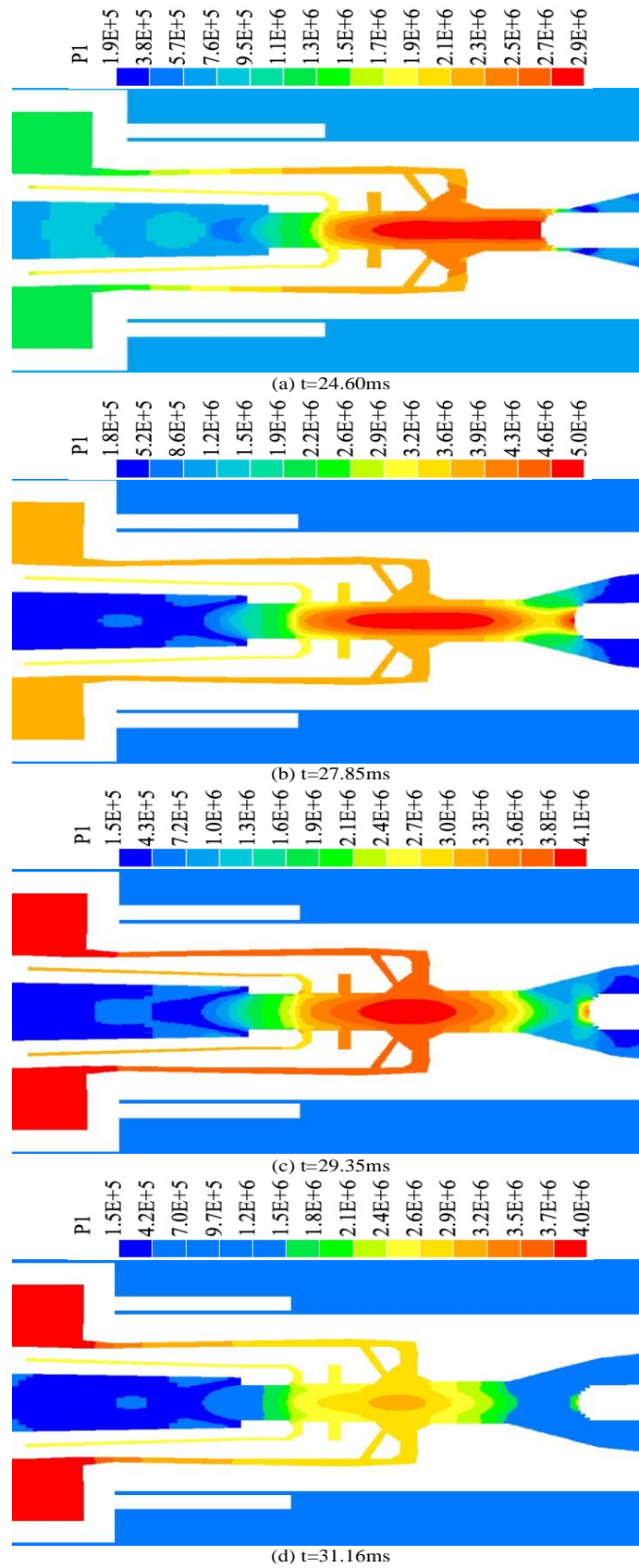
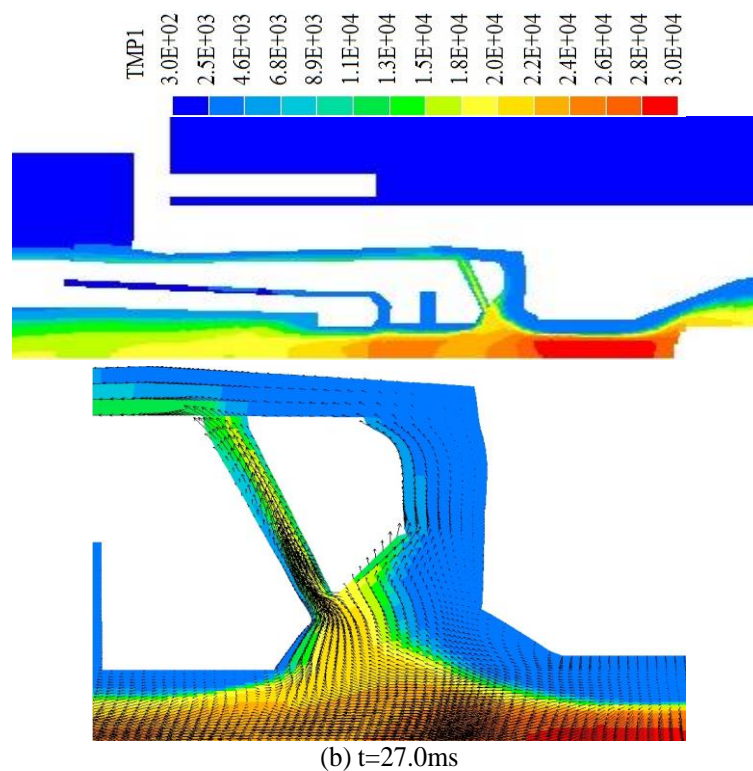
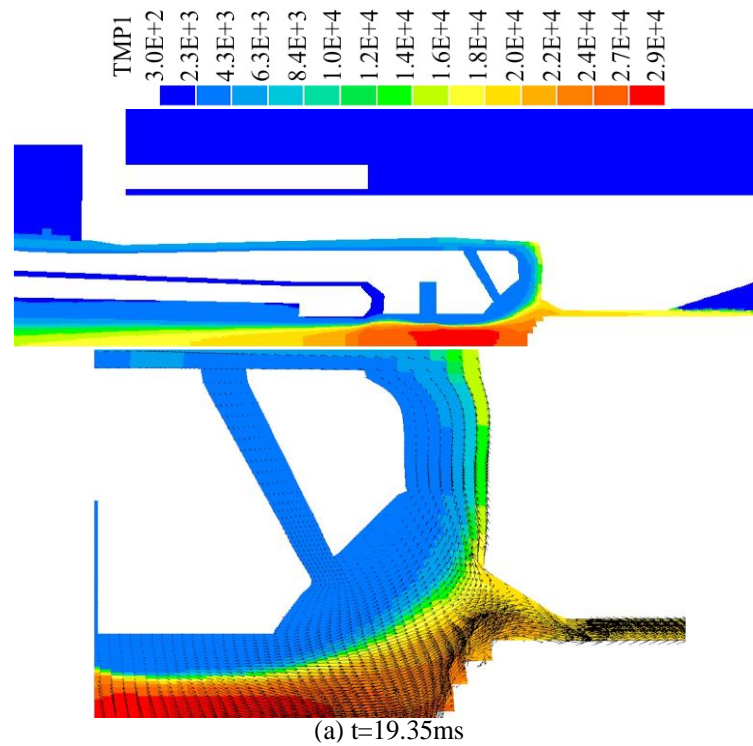


Figure 4.29 Pressure distribution at several typical time instants (Test 98: Com.1).

The temperature distribution with velocity vector that helps to explain the flow reversal in the arcing chamber are shown in Figure 4.30. When the solid contact moves through

main nozzle flat throat, the arc core temperature is slightly increased from 29,000 K to 30,000 K. During this period, the gaseous mixture is driven into the expansion volume. After the current decreases, the temperature decreases from 30,000 K to 26,000 K and insufficient electrical power supply from the arc column fails to trigger the gas flow towards the expansion volume, and eventually the mixed gas flows out through heating channel into the arcing space with two directions (Figure 4.30 (c)).



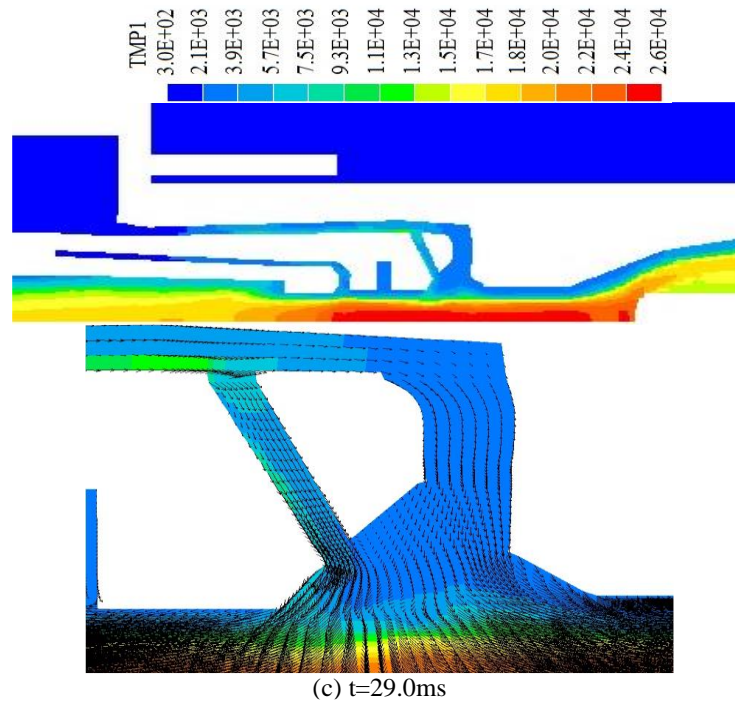
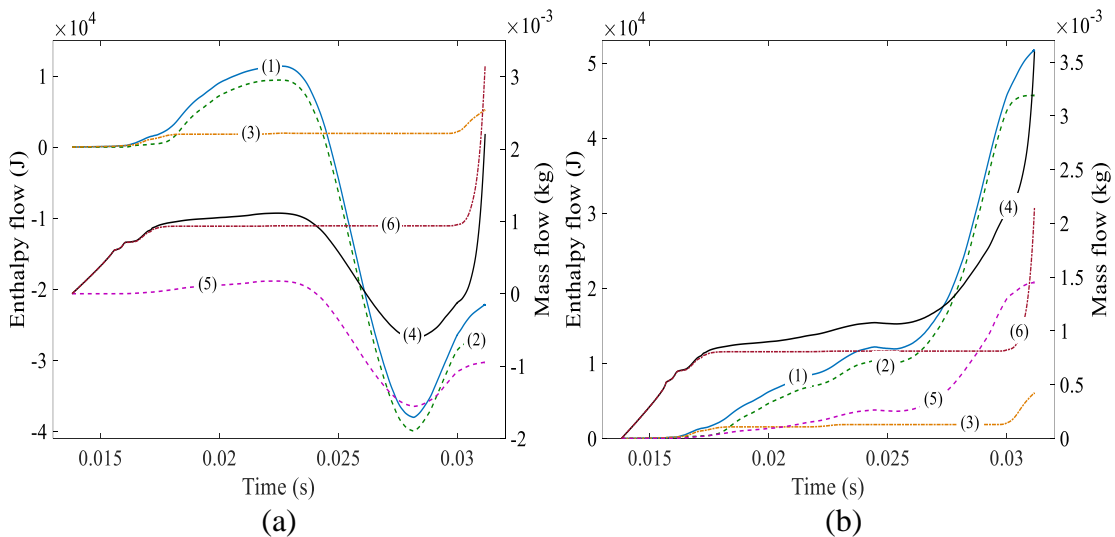


Figure 4.30 Temperature distributions at typical time instants with velocity vector (Test 98: Com.1). The arrow represents for the direction of the flow field.

The flow field distribution around the main nozzle of Test 98 which is similar to Test 92 is presented in Figure 4.31. In front of the main nozzle flat throat, the flow is partially driven towards the downstream exit through the smaller gap as presented in Figure 4.30 (a). When the arc burns in main nozzle flat throat, a stagnation region is formed inside the main nozzle and the gas within the main nozzle is split by the flow stagnation point towards the expansion volume and the downstream exit (Figure 4.30 (b)). The gaseous mixture in front of the main nozzle flat throat starts to flow reversely towards expansion volume through cross section 6 at 24.06 ms while the mixture around the main nozzle downstream continuously flows out towards the exit (Figure 4.31 (b) and (c)).



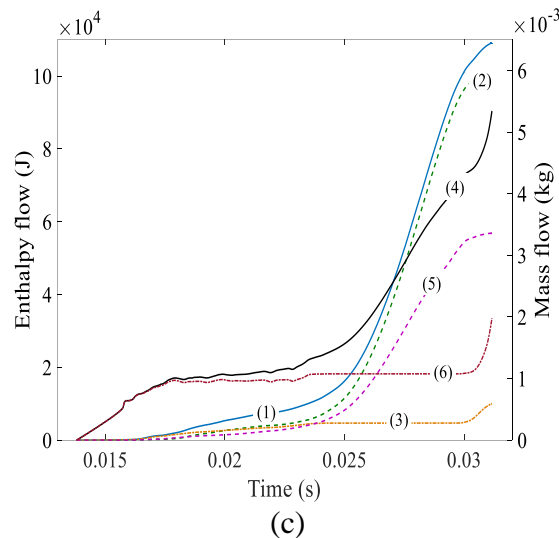


Figure 4.31 Predicted enthalpy and mass flow through cross sections 6 (a), 7 (b) and 8 (c) towards the downstream, each curve has same meaning explained in Figure 4.24.

From the calculation with the consideration of nozzle ablation, the results indicate that the flow field environment is sensitively influenced by the increased diameter of nozzle flat throat as presented in Figure 4.32 and 4.34. For the short arc duration case Test 92, less amount of PTFE vapour is produced due to the enlarged nozzle holes which leads to a decrease of the thermal energy brought into the expansion volume by the hot vapour, respectively from 32 kJ to 28.2 kJ to 25.2 kJ after each computation (Figure 4.32 (b)), corresponding to a drop of maximum pressure in the expansion volume from 2.9 MPa to 2.77 MPa to 2.57 MPa (Figure 4.33). In reality, the arc voltage between the contacts is decreased due to the enlarged nozzle hole and it decreases the electrical power supply from the hot arc column which makes the gaseous mixture driven into the expansion volume insufficiently.

As presented in Figure 4.32 (c) and (d), the total enthalpy and mass flow through main nozzle towards the downstream are largely increased before the solid contact arrives in front of the main nozzle flat throat since the enlarged nozzle holes increase the effective flow area between the main nozzle flat throat and solid contact. Furtherly with the solid contact movement, the mass flow rate which is determined by the velocity and density of the gaseous mixture changes gradually before the final current zero. It is because the reduced amount of vapour decreases the pressure formed in the nozzle flat throat which lowers the mixture density. Besides that, the increased gas flow through the main nozzle towards the downstream results in a decrease of the gas flow towards the hollow contact (Figure 4.32 (a)).

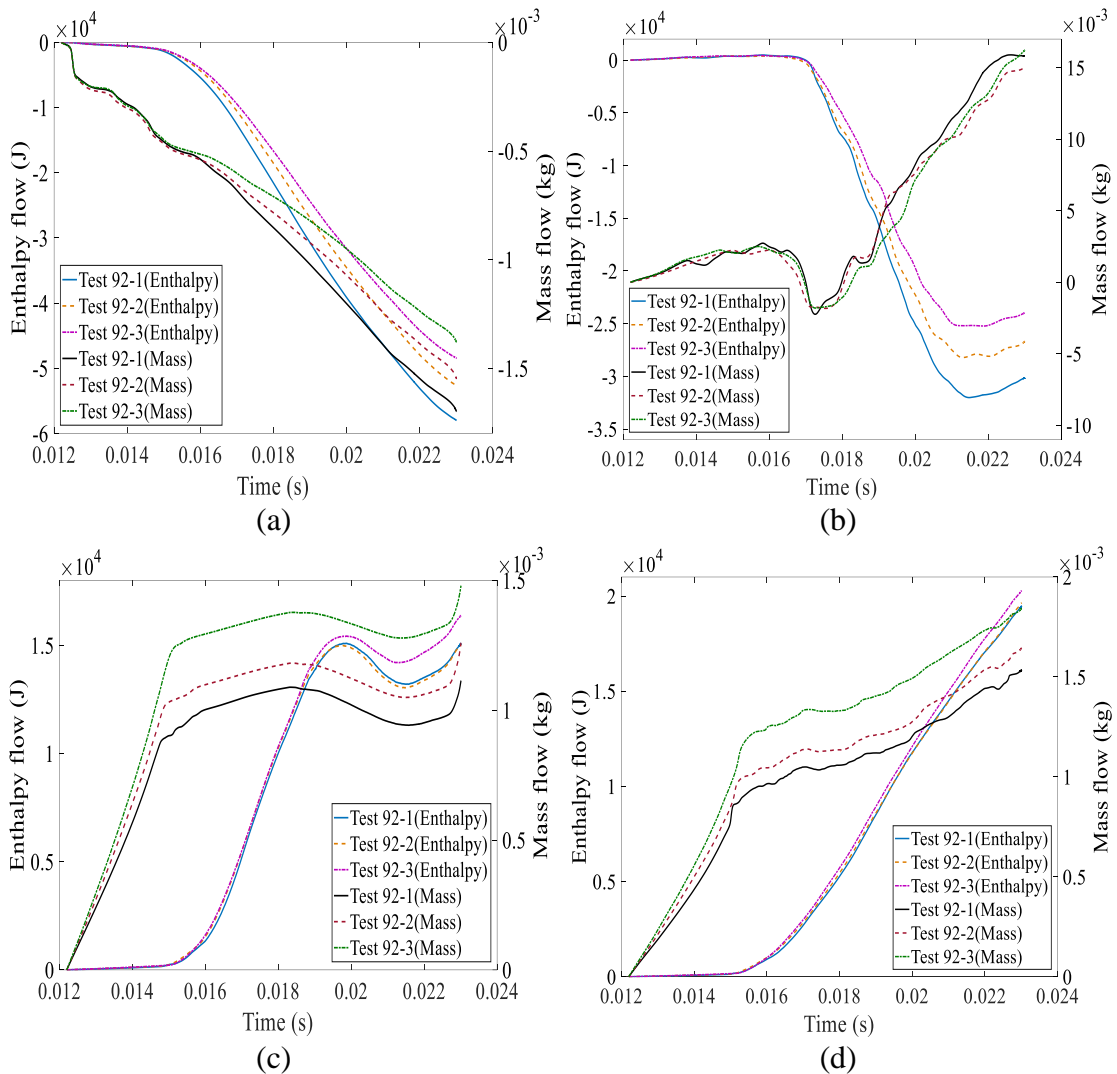


Figure 4.32 Predicted enthalpy and mass flow into (a) hollow contact, (b) expansion volume, (c) in front of main nozzle flat throat and (d) at the downstream respectively through cross sections 2 (a), 3 (b), 6 (c) and 8 (d) with considering the variations of nozzle flat throat diameter of Test 92.

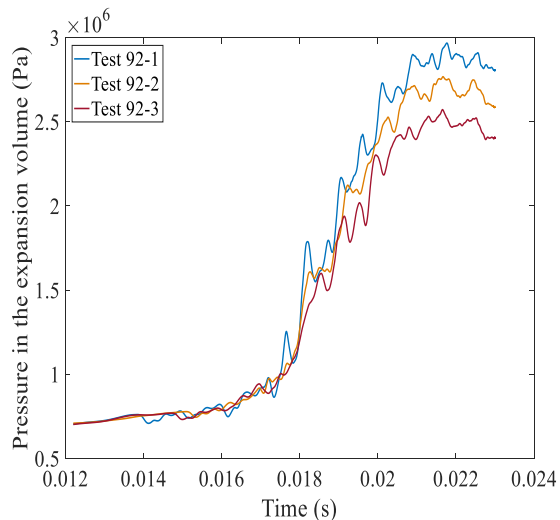


Figure 4.33 Pressure distribution in the expansion volume at position A (in Figure 4.11) with considering nozzles flat throats radii variation after each computation.

The variation of flow field distribution becomes considerable for the long arc duration case (Test 98) as presented in Figure 4.34. From Table 4.12, the total ablated mass has an increase when the radii of main and auxiliary nozzle flat throats enlarge to 11.5 mm and 10.7 mm. It differs from Test 92 which the total ablated mass from nozzle surface presents a decrease with the enlarged nozzle holes. The different flow field conditions of Test 98 are caused by the excessive enlargement of nozzle holes and changed ablated mass from the nozzle surface especially the auxiliary nozzle.

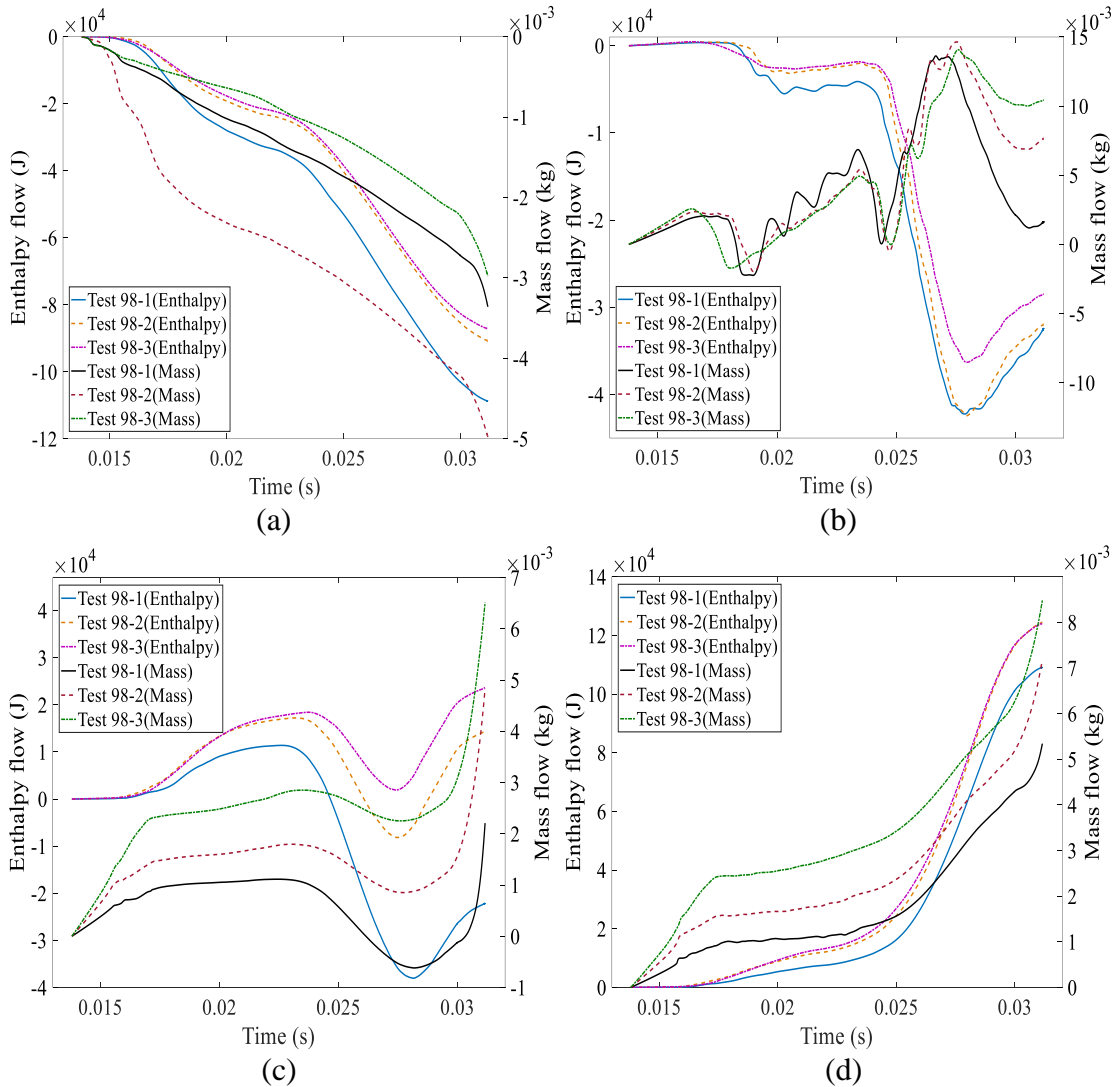


Figure 4.34 Predicted enthalpy and mass flow through cross section 2 (a), 3 (b), 6 (c) and 8 (d) with considering nozzles flat throat diameter variation after each computation of Test 98.

A total of 1.98 g ablated mass flows into the expansion volume when there is no any ablation occurred on the nozzle surface while it decreases to 1.92 g and 1.70 g with the enlarged nozzle holes. Nevertheless, the increased mass of PTFE vapour from auxiliary nozzle surface especially the flat throat as a result of that excessive enlargement results

in an increase of the total enthalpy flows into the expansion volume (42.4 kJ) which is 0.2 kJ higher than the first computation and it also increases the total mass flowing into the hollow contact, but the discrepancy has negligible effect on the flow field conditions through the main nozzle flat throat. As shown in Figure 4.35, the enlargements of nozzle holes result in the decrease of the pressure inside the expansion volume for Test 98 even though the total mass loss from the nozzle surface is contrarily increased for the second computation due to an excessive enlargement of the nozzle hole in comparison with the prior case. It could be concluded that the thermal energy brought by PTFE vapour which produced from nozzle flat throat plays a dominant role in determining the pressurisation in the expansion volume.

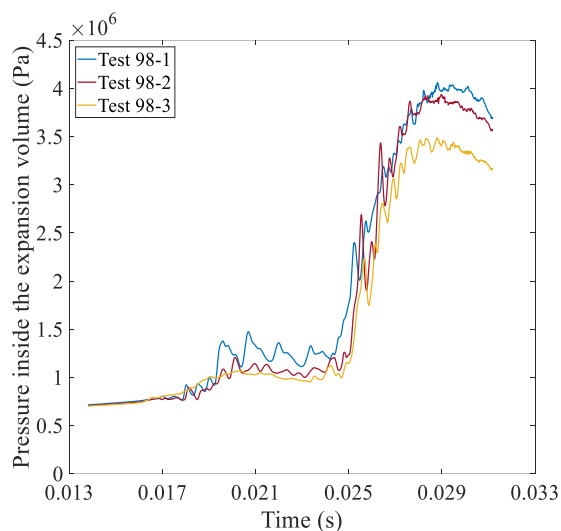


Figure 4.35 Pressure distribution in the expansion volume at position A (in Figure 4.11) with considering nozzles flat throats radii variation after each computation.

4.6 Conclusion

The arc behaviour of the 145 kV/40 kA auto-expansion circuit breaker with considering the nozzle flat throat diameter change due to PTFE ablation is computationally studied. The ablated mass from the nozzle surface is predicted based on the generally accepted theory that nozzle ablation is caused by radiation from arc column. Several conclusions could be drawn from the calculation:

- (1) The auxiliary nozzle plays a significant role in the arcing process especially for the pressurisation process in the expansion volume for the short arc duration case, since the ablated mass from the auxiliary nozzle surface takes a considerable proportion of the total mass loss which carries more thermal energy into the expansion volume.

- (2) The pressurisation in the expansion volume is dominantly determined by the surged enthalpy flux (thermal energy) carried by the hot PTFE vapour. The ablated mass is reduced with an increased nozzle flat throat for the short arc duration case which is due to the decreased radiation energy reaching at the nozzle wall. Furthermore, the reduced ablated mass decreases the total enthalpy flow pumped into the expansion volume and lowers the pressurisation. The mass flow has insignificant influence on the pressurisation. Due to the enlarged nozzle holes, the maximum pressure in the expansion volume drops from 2.9 MPa to 2.77 MPa to 2.57 MPa for Test 92 while it decreases from 4.1 MPa to 3.93 MPa to 3.45 MPa for Test 98. It can be concluded that the thermal energy brought by the PTFE vapour has dominant influence on the pressurisation in the expansion volume and the energy is mainly determined by the ablated mass from the nozzle surface.
- (3) For long arc duration case (Test 98), the main nozzle contributes a large proportion of the ablated mass than the auxiliary nozzle. After an excessive enlargement of the nozzle flat throat, the ablated mass from auxiliary nozzle surface especially the flat throat shows an increase which is somewhat different in comparison with the short arc duration case.
- (4) Flow reversal is a specifically designed physical mechanism in the auto-expansion circuit breaker to achieve the pressurisation in the expansion volume by the surged enthalpy flux. With the current increase, a high pressure region is formed within the arcing space and sufficient electrical energy from the arc column triggers the gas flows through the heating channel into the expansion volume. After the solid contact clears the main nozzle flat throat, the significant pressure difference between the expansion volume and contact gap drives the high pressure gas inside the expansion volume rush out towards the arcing space for the final arc quenching. The pressure build up process determined by nozzle ablation is essential to establish the effective flow field conditions for the arc cooling.

The computation results of the nozzle ablation and its effects on the flow environment can be regarded as the important reference and indicators for the optimum design of the auto-expansion circuit breakers. The relative positions of the main nozzle and auxiliary nozzle, and their dimensions especially the flat throats should be considered carefully.

References

- [1] M. T. C. Fang, Q. Zhuang, and X. J. Guo, “Current-zero behaviour of an SF₆ gas-blast arc. II. Turbulent flow,” *J. Phys. D. Appl. Phys.*, vol. 27, no. 1, pp. 74–83, Jan. 1994.
- [2] J. D. Yan, M. T. C. Fang, and W. Hall, “The development of PC based CAD tools for auto-expansion circuit breaker design,” *IEEE Trans. Power Deliv.*, vol. 14, no. 1, pp. 176–181, 1999.
- [3] Y. Pei, “Computer Simulation of Fundamental Processes in High Voltage Circuit Breakers Based on an Automated Modelling Platform,” University of Liverpool, 2014.
- [4] J. A. Shercliff, *A textbook of magnetohydrodynamics*. Oxford, New York: Pergamon Press, 1965.
- [5] J. L. Zhang, J. D. Yan, and M. T. C. Fang, “Electrode Evaporation and Its Effects on Thermal Arc Behavior,” *IEEE Trans. Plasma Sci.*, vol. 32, no. 3, pp. 1352–1361, Jun. 2004.
- [6] B. E. Launder and D. B. Spalding, “The numerical computation of turbulent flows,” *Comput. Methods Appl. Mech. Eng.*, vol. 3, no. 2, pp. 269–289, Mar. 1974.
- [7] T.-H. Shih, W. W. Liou, A. Shabbir, Z. Yang, and J. Zhu, “A new k - ϵ eddy viscosity model for high reynolds number turbulent flows,” *Comput. Fluids*, vol. 24, no. 3, pp. 227–238, Mar. 1995.
- [8] Y. S. Chen and S. W. Kim, “Computation of turbulent flows using an extended k -epsilon turbulence closure model,” Alabama, 1987.
- [9] N. C. Markatos, “The mathematical modelling of turbulent flows,” *Appl. Math. Model.*, vol. 10, no. 3, pp. 190–220, Jun. 1986.
- [10] M. Nallasamy, “Turbulence models and their applications to the prediction of internal flows: A review,” *Comput. Fluids*, vol. 15, no. 2, pp. 151–194, Jan. 1987.
- [11] N. P. T. Basse, R. Bini, and M. Seeger, “Measured turbulent mixing in a small-scale circuit breaker model,” *Appl. Opt.*, vol. 48, no. 32, pp. 6381–6391, Nov. 2009.
- [12] X. Ye and M. Dhotre, “CFD Simulation of Transonic Flow in High-Voltage Circuit Breaker,” *Int. J. Chem. Eng.*, vol. 2012, pp. 1–9, 2012.
- [13] J.-C. Lee, “Numerical Study of SF₆ Thermal Plasmas Inside a Puffer-assisted

- Self-blast Chamber,” *Phys. Procedia*, vol. 32, no. August 2010, pp. 822–830, 2012.
- [14] K. Y. Park, X. J. Guo, R. E. Blundell, M. T. C. Fang, and Y. J. Shin, “Mathematical modeling of SF₆ puffer circuit breakers. II. Current zero region,” *IEEE Trans. Plasma Sci.*, vol. 25, no. 5, pp. 967–973, 1997.
- [15] Q. Zhang, J. D. Yan, and M. T. C. Fang, “The modelling of an SF 6 arc in a supersonic nozzle: I. Cold flow features and dc arc characteristics,” *J. Phys. D. Appl. Phys.*, vol. 47, no. 21, p. 215201, May 2014.
- [16] R. Bini, N. T. Basse, and M. Seeger, “Arc-induced turbulent mixing in an SF 6 circuit breaker model,” *J. Phys. D. Appl. Phys.*, vol. 44, no. 2, p. 25203, Jan. 2011.
- [17] J. D. Yan, K. I. Nuttall, and M. T. C. Fang, “A comparative study of turbulence models for SF 6 arcs in a supersonic nozzle,” *J. Phys. D. Appl. Phys.*, vol. 32, no. 12, pp. 1401–1406, Jun. 1999.
- [18] L. Niemeyer and K. Ragaller, “Development of Turbulence by the Interaction of Gas Flow with Plasmas,” *Zeitschrift für Naturforsch. A*, vol. 28, no. 8, Jan. 1973.
- [19] L. Niemeyer, “Measurement of turbulent flow in a supersonic nozzle arc,” in *11th International Conference on Phenomena in Ionized Gases*, 1973, p. 219.
- [20] W. Hermann, U. Kogelschatz, L. Niemeyer, K. Ragaller, and E. Schade, “Experimental and theoretical study of a stationary high-current arc in a supersonic nozzle flow,” *J. Phys. D. Appl. Phys.*, vol. 7, no. 12, pp. 1703–1722, Aug. 1974.
- [21] H. Versteeg and W. Malalasekera, *An Introduction to Computational Fluid Dynamics: The Finite Volume Method*, 2nd ed. Prentice Hall, 2007.
- [22] F. G. Schmitt, “About Boussinesq’s turbulent viscosity hypothesis: historical remarks and a direct evaluation of its validity,” *Comptes Rendus Mécanique*, vol. 335, no. 9–10, pp. 617–627, Sep. 2007.
- [23] M. Woelke, “Eddy Viscosity Turbulence Models Employed by Computational Fluid Dynamics,” *Trans. Inst. Aviat.*, vol. 191, no. 4, pp. 92–113, 2007.
- [24] “POLIS, the PHOENICS On-Line Information System.” [Online]. Available: http://www.cham.co.uk/phoenics/d_polis/d_lecs/general/turb.htm.
- [25] J.D.Yan, S.M.Han, Y. Y. Zhan, H. F. Zhao, and M. T. C. Fang, “Computer simulation of the arcing process in high voltage puffer circuit breakers with hollow contacts,” in *Proceedings of XVIII Symposium on Physics of Switching*

- Arc*, 2009, pp. 99–108.
- [26] M. T. C. Fang, Q. Zhuang, and X. J. Guo, “Current-zero behaviour of an SF₆ gas-blast arc. II. Turbulent flow,” *J. Phys. D. Appl. Phys.*, vol. 27, no. 1, pp. 74–83, Jan. 1994.
- [27] A. B. Murphy and P. Kovitya, “Mathematical model and laser-scattering temperature measurements of a direct-current plasma torch discharging into air,” *J. Appl. Phys.*, vol. 73, no. 10, pp. 4759–4769, May 1993.
- [28] “ABB Private communication.”
- [29] X. Wang, L. Zhong, Y. Cressault, A. Gleizes, and M. Rong, “Thermophysical properties of SF₆-Cu mixtures at temperatures of 300–30,000 K and pressures of 0.01–1.0 MPa: part 2. Collision integrals and transport coefficients,” *J. Phys. D. Appl. Phys.*, vol. 47, no. 49, p. 495201, 2014.
- [30] X. Wang, L. Zhong, Y. Cressault, A. Gleizes, and M. Rong, “Thermophysical properties of SF₆-Cu mixtures at temperatures of 300–30,000 K and pressures of 0.01–1.0 MPa: part 2. Collision integrals and transport coefficients,” *J. Phys. D. Appl. Phys.*, vol. 47, no. 49, p. 495201, Nov. 2014.
- [31] S. D. Eby, J. Y. Trépanier, and X. D. Zhang, “Modelling radiative transfer in circuit-breaker arcs with the P-1 approximation,” *J. Phys. D. Appl. Phys.*, vol. 31, no. 13, pp. 1578–1588, Jul. 1998.
- [32] V. Aubrecht and J. J. Lowke, “Calculations of radiation transfer in SF₆ plasmas using the method of partial characteristics,” *J. Phys. D. Appl. Phys.*, vol. 27, no. 10, pp. 2066–2073, Oct. 1994.
- [33] J. F. Zhang, M. T. C. Fang, and D. B. Newland, “Theoretical investigation of a 2 kA DC nitrogen arc in a supersonic nozzle,” *J. Phys. D. Appl. Phys.*, vol. 20, no. 3, pp. 368–379, Mar. 1987.
- [34] P. J. Shayler and M. T. C. Fang, “Radiation transport in wall-stabilised nitrogen arcs,” *J. Phys. D. Appl. Phys.*, vol. 11, no. 12, pp. 1743–1756, Aug. 1978.
- [35] C. M. Dixon, J. D. Yan, and M. T. C. Fang, “A comparison of three radiation models for the calculation of nozzle arcs,” *J. Phys. D. Appl. Phys.*, vol. 37, no. 23, pp. 3309–3318, Dec. 2004.
- [36] Y. Pei, J. Zhong, J. Zhang, and J. D. Yan, “A comparative study of arc behaviour in an auto-expansion circuit breaker with different arc durations,” *J. Phys. D. Appl. Phys.*, vol. 47, no. 33, p. 335201, Aug. 2014.
- [37] J.L. Zhang, J.D. Yan, A. B. Murphy, W. Hall, and M. T. C. Fang,

- “Computational investigation of arc behavior in an auto-expansion circuit breaker contaminated by ablated nozzle vapor,” *IEEE Trans. Plasma Sci.*, vol. 30, no. 2, pp. 706–719, Apr. 2002.
- [38] A. Gleizes, B. Rahmani, J. J. Gonzalez, and B. Liani, “Calculation of net emission coefficient in N₂, SF₆ and SF₆-N₂ arc plasmas,” *J. Phys. D. Appl. Phys.*, vol. 24, no. 8, pp. 1300–1309, Aug. 1991.
- [39] A. Gleizes, J. J. Gonzalez, B. Liani, and G. Raynal, “Calculation of net emission coefficient of thermal plasmas in mixtures of gas with metallic vapour,” *J. Phys. D. Appl. Phys.*, vol. 26, no. 11, pp. 1921–1927, Nov. 1993.
- [40] V. Aubrecht and M. Bartlova, “Net Emission Coefficients of Radiation in Air and SF₆ Thermal Plasmas,” *Plasma Chem. Plasma Process.*, vol. 29, no. 2, pp. 131–147, Apr. 2009.
- [41] R. W. Liebermann and J. J. Lowke, “Radiation emission coefficients for sulfur hexafluoride arc plasmas,” *J. Quant. Spectrosc. Radiat. Transf.*, vol. 16, no. 3, pp. 253–264, Mar. 1976.
- [42] IEC, “IEC 62271-100: 2008 High-Voltage Switchgear and Controlgear-Part 100: Alternating current circuit breakers.” p. 695, 21-Apr-2008.
- [43] IEEE Standards, “IEEE Std C37.06-2009 - IEEE Standard for AC High-Voltage Circuit Breakers Rated on a Symmetrical Current Basis - Preferred Ratings and Related Required Capabilities for Voltages Above 1000 V.” pp. 1–46, 2009.
- [44] J. D. Yan, “COMPUTER SIMULATION OF SWITCHING ARCS AND MODEL IMPLEMENTATION IN PHOENICS,” Liverpool, 2010.
- [45] “Private communication with Professor Vladimir Aubrecht.” .
- [46] M. Seeger, J. Tepper, T. Christen, and J. Abrahamson, “Experimental study on PTFE ablation in high voltage circuit-breakers,” *J. Phys. D. Appl. Phys.*, vol. 39, no. 23, pp. 5016–5024, Dec. 2006.
- [47] M. Seeger, L. Niemeyer, T. Christen, M. Schwinne, and R. Dommerque, “An integral arc model for ablation controlled arcs based on CFD simulations,” *J. Phys. D. Appl. Phys.*, vol. 39, no. 10, pp. 2180–2191, May 2006.

Chapter 5

Prediction of the Critical Rate of Rise of Recovery Voltage Considering Nozzle Diameter Change due to PTFE Material Ablation

5.1 Introduction

Electrical power system is rapidly developing in structural complexity and intelligent operations. However, types of faults in electrical power systems especially under high voltage and current environment causes damage to the electrical apparatuses, results in serious economic consumption and jeopardizes system safety and reliability. Normally, the types of faults can be classified by their common characteristics, which two of them are considered in present work for analysing the interruption capability of high voltage circuit breakers, i.e. terminal fault and short line fault. Terminal fault takes place at the terminals of circuit breakers and short line fault always occurs at a short distance down a transmission line from the circuit breaker [1].

Transient recovery voltage (TRV), which appears across circuit breaker terminals after current interruption, is one of the crucial factors to evaluate circuit breaker interruption capability. It highly correlates with the fault types and grid system characteristics. TRV of a terminal fault is described by the single-frequency or double-frequency waveform while the short line fault has a more complicated TRV which is described by the multi-frequency waveform that includes a saw-tooth waveform component [2]. The imposed TRV has a significant effect on the final recovery process of a circuit breaker after the arc extinction. There are two recovery processes after the current passes its final zero: thermal recovery and dielectric recovery. Thermal recovery occurs roughly in the first few microseconds after the final current zero and the TRV withstand capacity is defined as a function of energy balance in the residual arc. Dielectric recovery occurs after the successful thermal recovery describes the dielectric withstand capacity between arcing contacts [3]. Three important factors need to be considered to analyse TRV withstand capability: maximum withstand voltage, time to reach the maximum voltage and initial

Rate of Rise of Recovery Voltage (RRRV), as shown in Figure 5.1. The TRV obtained by these factors may lead to successful or failed (re-ignition/restrike) interruptions.

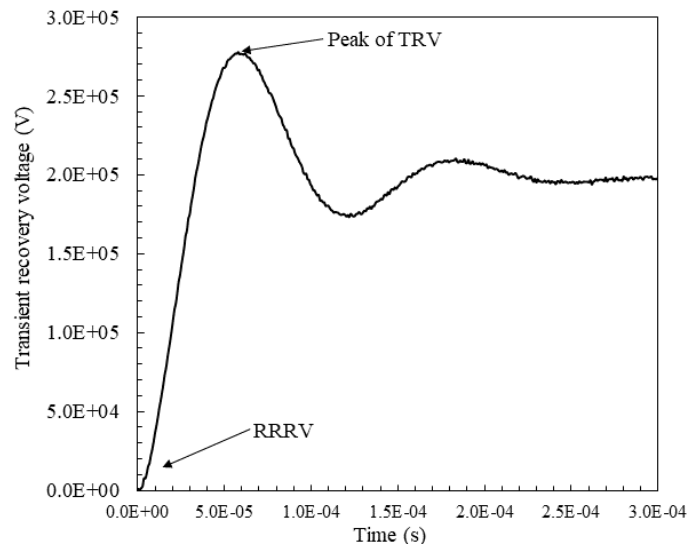


Figure 5.1 Example of TRV waveform.

Critical RRRV is a threshold value to describe the TRV withstand capability of a circuit breaker. A value higher than this critical RRRV will result in the unsuccessful thermal recovery. In this chapter, the consequence of nozzle ablation will be studied to build up correlation between interruption duties and lifetime of nozzle. A successful interruption is achieved if the post arc current drops to a negligible low value in a few microseconds. The variation of critical RRRV resulting from nozzle ablation is studied for different type test duties, including test peak current and arc duration. The results obtained in the chapter contribute to the development of intelligent circuit breakers.

5.2 Synthetic Testing Methods of High Voltage Circuit Breaker tests

To ensure the power system safety and reliability, different tests are required to confirm that the circuit breaker could reasonably operate with the expected protection purposes. Based on the international electrical standards such as IEEE[®] C37 and IEC 62271 (e.g. -100, -200), the tests are categorised into different duties examining the circuit breaker operation performance, e.g. mechanical, thermal, dielectric and short circuit test [4], [5].

For the short-circuit current making and breaking tests, the test methods are classified into direct test and indirect (synthetic) test. Direct test is performed using a circuit with single power source to provide required voltage, current and transient recovery voltage. Synthetic test is an alternative method in which the required current and voltage are

provided from different power sources. The values of the components in the associated test circuit (e.g. resistance, capacitance, inductance). should be determined reasonably since the measurements of the prospective TRV during the tests are carried out with the artificial line connected to the circuit.

To describe the rated characteristics of circuit breakers, rated operating sequence need to be determined. Following IEC62271-100 [4], there are two rated operating sequences: O-t-CO-t'-CO and CO-t''-CO. The rated operating sequence of the 145 kV /40 kA auto-expansion circuit breaker assigned according to the experiment is O-0.3s-CO-3min-CO. "O" and "CO" respectively represent the opening and closing-opening operations. This rated operating sequence includes three valid breaking operations with different arcing time: short, medium and long. The first valid breaking operation is performed with the arcing time as short as possible and the resultant arcing time is defined as the shortest arc duration ($t_{arc, min}$). The second valid breaking operation should be carried out with the arcing time as long as possible ($t_{arc, max}$) and the third valid breaking operation should be performed with the medium arcing time which is determined by:

$$t_{arc, med} = \frac{(t_{arc, min} + t_{arc, max})}{2} \quad (5.2.1)$$

The short-circuit making and breaking test consists of test duties such as T10, T30, T60, T100s, OP1, OP2, L90, L60 and L75. Numbers of 10, 30, 60, 75, 90 and 100 represent the percentage of the rated operating short-circuit breaking current. "T", "L" and "OP" represent different fault types: terminal fault, short line fault and out-of-phase fault.

After the breaking operation, the recovery voltage that applies across the terminals of a circuit breaker contains two successive segments, transient recovery voltage and power frequency voltage. Following IEEE Std C37.011, the TRV waveform could be obtained by two envelopes, i.e. two-parameter and four-parameter. The two-parameter envelope is used to define the oscillatory (underdamped) TRV for the circuit breakers with rated voltage less than 100 kV at all possible breaking currents or the voltage rated 100 kV and above with short circuit current up to 30% of the rated value. The two parameters are specified as reference voltage (TRV peak value) u_c and time t_3 for voltage increases to u_c . The four-parameter envelope is adopted for the overdamped (exponential) TRV with circuit breakers voltage rated 100 kV and above if the short circuit current is higher

than 30% of the rated value. The first reference voltage u_1 , time t_1 to reach u_1 , second reference voltage (TRV peak value) u_c and time t_2 to reach u_c are specified as the four parameters. Examples of these two envelopes are shown in Figure 5.2 [6], [7].

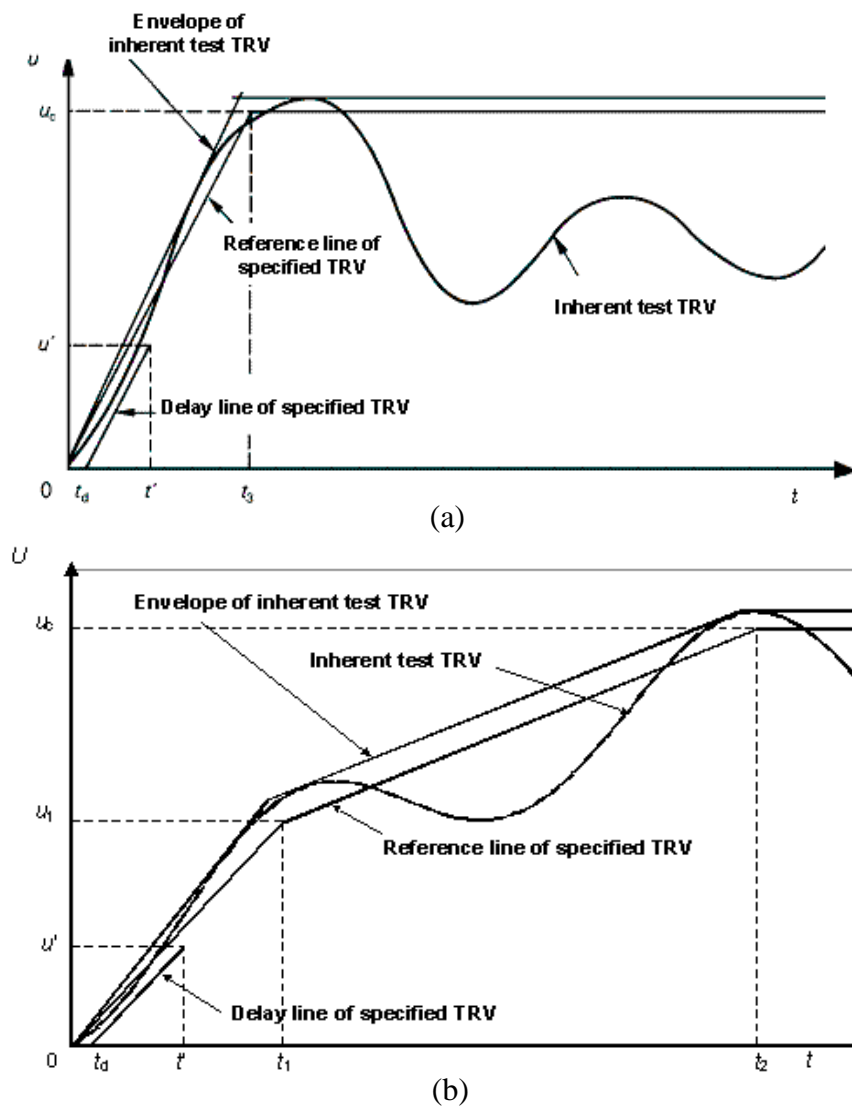


Figure 5.2 Examples of inherent test TRV with the two-parameter envelope (a) and four-parameter waveform (b) that satisfies the conditions to be met during the type test. t_d is a time delay in microseconds. [6].

Different from the terminal fault, the TRV of short line fault is defined using a triangular waveform which contains a saw-tooth component as shown in Figure 5.3. The related RRRV of the saw-tooth shaped TRV, which is determined by the line surge impedance and slope of the interrupted current before its final zero, is higher than the terminal fault. The rated value of line surge impedance is 450Ω . The voltage of short line fault is the sum of voltage at the source side and that at the line side in which the line side voltage exhibits the triangular shape. The variation of the source side voltage is slower than the line side.

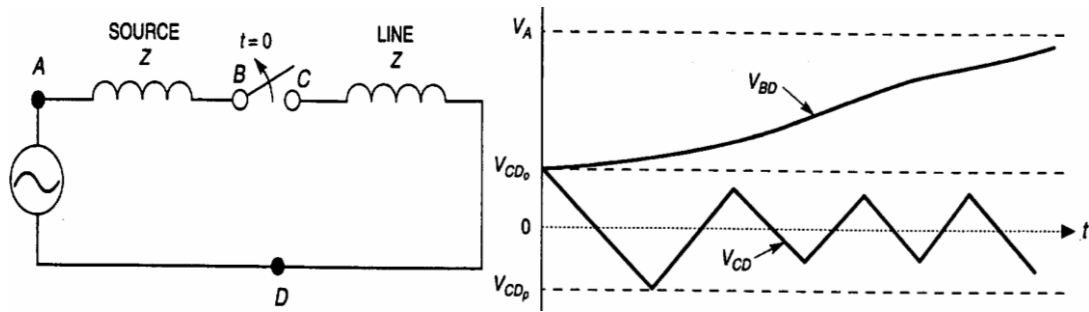


Figure 5.3 Examples of inherent test TRV for short line fault that satisfies the conditions to be met during type test [6].

The TRV ratings are designed to determine a withstand boundary of the circuit breakers relating to its interruption capability. To predict the interruption capability of the auto-expansion circuit breaker comparatively, three different test duties (T30, T60 and L90) are considered in the present work. The corresponding experiments on the commercial 145 kV/ 40 kA auto-expansion circuit breaker are carried out at KEMA high-power laboratory. The arc durations of tests T30 and T60 are described in Table 5.1 and typical parameters are listed in Table 5.2 [8].

Table 5.1 Tested arc durations of different test duties for 145 kV/40 kA auto-expansion circuit breaker.

Test Types	Arc duration (ms)		
	Short	Medium	Long
T30	13.8	16.5	20.2
T60	12.3	14.7	18.5

Table 5.2 Typical parameters of T30 and T60 tests with different arc durations.

Parameters		di/dt at last current zero (A/ μ s)	Peak current at last loop (kA)
T30	Short	6.65	17.6
	Medium	6.70	17.7
	Long	6.58	18.9
T60	Short	12.8	34.7
	Medium	12.6	34.8
	Long	12.8	39.1

5.3 Prediction of Nozzle Ablation with Different Test Duties

5.3.1 Terminal fault T30

As discussed in the previous chapter, nozzle ablation is a dominant mechanism to create a sufficient pressurisation especially in the expansion volume of auto-expansion circuit breaker. At different interrupting currents, the arc is burned in different modes: axial blown arc (SF_6 dominates) and ablation controlled arc (ablated PTFE dominates), as shown in Figure 5.4. It is observed that the arc is burned in axial blown mode at low peak current densities ($<0.55 \times 10^8 \text{ A/m}^2$) while at high peak current densities, the arc is burned in ablated PTFE controlled mode.

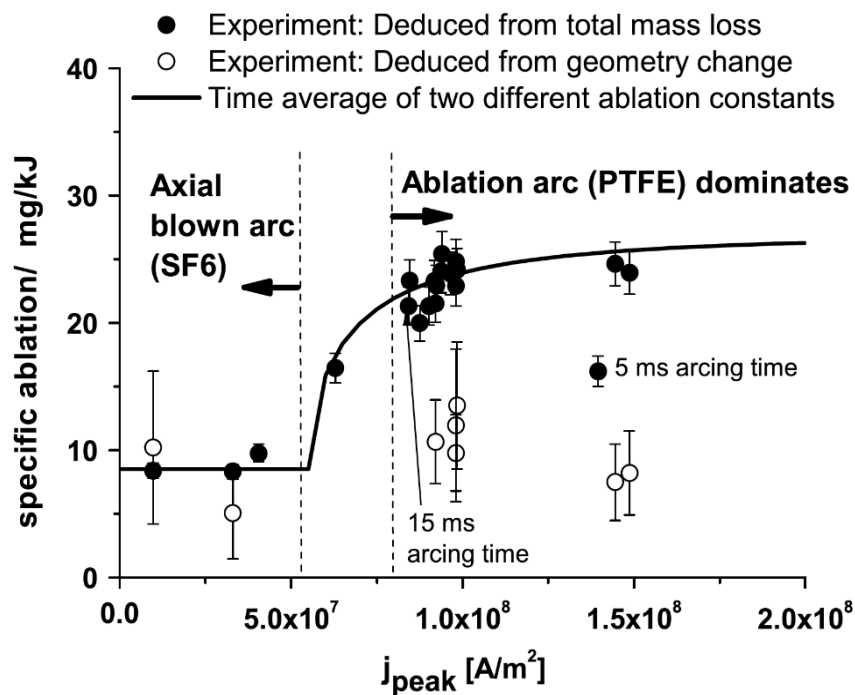


Figure 5.4 Specific ablation in the circuit breaker test device versus peak current density. Applied peak currents amounted from 4 to 64 kA and the arcing times are 5, 10 and 15 ms respectively [9].

The current waveforms and contact travel curves of T30 cases are shown in Figure 5.5. The applied peak currents are less than 20 kA. In addition, the TRVs of T30 imposed by the network are drawn in Figure 5.6. Similar to the short line fault, the interruption of the short arc duration case is the most difficult in comparison with medium and long arc duration cases. The peak current densities of the three cases are lower than $0.55 \times 10^8 \text{ A/m}^2$ and the arc is thus burned in axial blown mode. The arcs of different arc duration cases are respectively initiated at 12.84 ms (short), 13.40 ms (medium) and 13.76 ms (long).

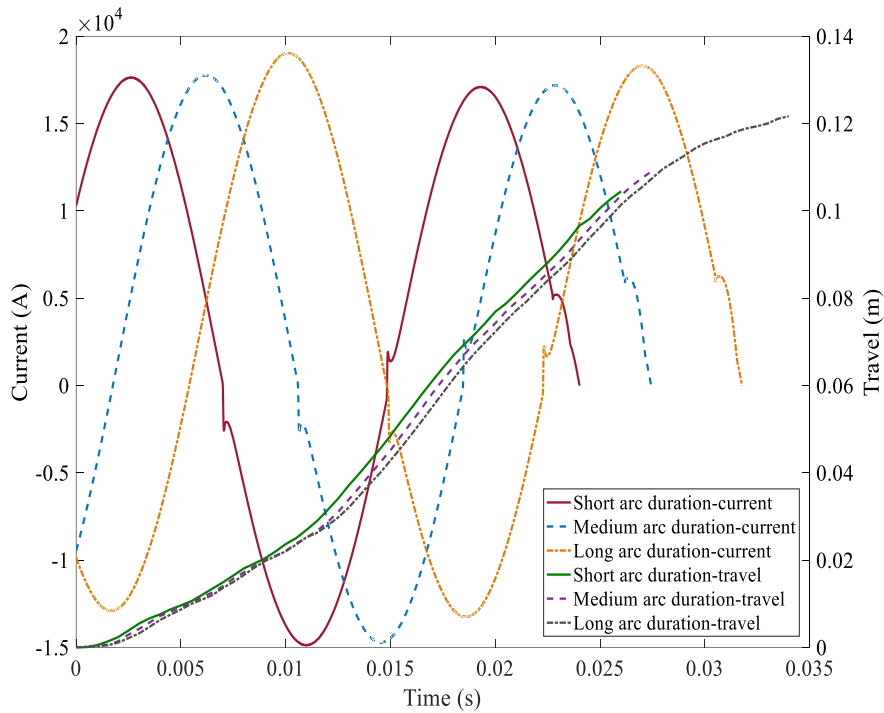


Figure 5.5 Current waveforms and contact travel curves of T30 tests of 145 kV/40 kA auto-expansion circuit breaker.

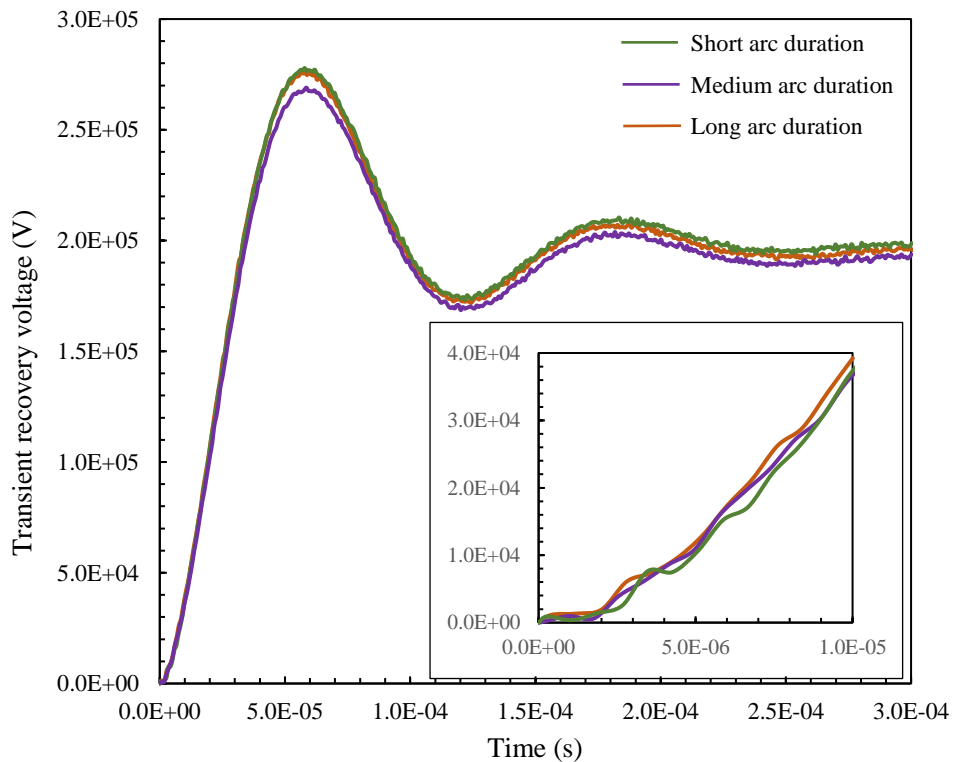


Figure 5.6 Transient recovery voltages of T30 tests with different arc durations.

The predicted mass loss respectively from main and auxiliary nozzle surfaces especially from the nozzle flat throat with the consideration of dimensional variation of the nozzle holes after each valid breaking operation in the rated operation sequence are shown in

Table 5.3. From the calculation, it is found that such a low current causes small amount of mass ablated from the nozzle surface especially for the short arc duration case which the ablated mass from the main nozzle flat throat has a negligible influence on changing the throat diameter (Table 5.4) but the ablation becomes intensified with the increased arc duration. For the medium and long arc duration cases, the nozzle holes are enlarged uniformly when considers the effects of nozzle ablation resulted from the prior current interruptions (Table 5.5 and 5.6). The total ablated mass from nozzle surface presents a decrease as a result of the nozzle hole enlargement.

Table 5.3 Predicted PTFE mass loss due to nozzle ablation after each valid breaking operation of rated operation sequence of T30 with considering the variation of nozzle flat throat diameter.

Nozzle		Prediction					
		Mass loss (g)			Nozzle throat radius (mm)		
		Short	Long	Medium	Short	Long	Medium
Main nozzle	Flat throat	0.10	0.51	0.34	10.5	10.7	10.8
	Total	0.22	0.92	0.52			
Auxiliary nozzle	Flat throat	0.20	0.36	0.24	9.7	10.0	10.2
	Total	0.39	0.69	0.47			
Total mass loss from nozzle surface		0.61	1.61	0.99			

Table 5.4 Predicted PTFE mass loss due to nozzle ablation after each computation of T30 short arc duration case with considering the variation of nozzle flat throat diameter.

Nozzle		Prediction					
		Mass loss (g)			Nozzle throat radius (mm)		
		Com. 1	Com. 2	Com. 3	Com. 1	Com. 2	Com. 3
Main nozzle	Flat throat	0.10	0.10	0.10	10.5	10.5	10.5
	Total	0.22	0.22	0.22			
Auxiliary nozzle	Flat throat	0.20	0.19	0.19	9.7	9.8	9.9
	Total	0.39	0.38	0.38			
Total mass loss from nozzle surface		0.61	0.60	0.60			

Table 5.5 Predicted PTFE mass loss due to nozzle ablation after each computation of T30 medium arc duration case with considering the variation of nozzle flat throat diameter.

Nozzle		Prediction					
		Mass loss (g)			Nozzle throat radius (mm)		
		Com. 1	Com. 2	Com. 3	Com. 1	Com. 2	Com. 3
Main nozzle	Flat throat	0.34	0.34	0.34	10.6	10.7	10.8
	Total	0.52	0.52	0.51			
Auxiliary nozzle	Flat throat	0.25	0.24	0.24	9.7	9.9	10.1
	Total	0.48	0.47	0.47			
Total mass loss from nozzle surface		1.00	0.99	0.98			

Table 5.6 Predicted PTFE mass loss due to nozzle ablation after each computation of T30 long arc duration case with considering the variation of nozzle flat throat diameter.

Nozzle		Prediction					
		Mass loss (g)			Nozzle throat radius (mm)		
		Com. 1	Com. 2	Com. 3	Com. 1	Com. 2	Com. 3
Main nozzle	Flat throat	0.52	0.51	0.51	10.7	10.9	11.1
	Total	0.92	0.92	0.92			
Auxiliary nozzle	Flat throat	0.37	0.36	0.34	9.8	10.1	10.4
	Total	0.71	0.69	0.67			
Total mass loss from nozzle surface		1.63	1.61	1.59			

For the short arc duration case, the mass loss from the main nozzle occupies 36% of the total ablated mass while that from auxiliary nozzle surface takes 64%. With arc duration increase, the proportion of ablated mass from main nozzle surface grows to 56.5% and 52.5% respectively correspond to the long and medium arc duration tests in the rated operating sequence. The variations of enthalpy and mass flow inside the hollow contact, expansion volume and towards the main nozzle downstream resulted from the enlarged nozzle flat throat of the short arc duration case are presented in Figure 5.9. It is observed that the PTFE vapour starts to flow into the expansion volume roughly at 20.05 ms and

the occupied proportion is smaller, no more than 3.8% enthalpy and 2.1% mass of the total (Figure 5.7 (c) and (d)). Due to the less contribution of the ablated PTFE vapour, the pressure inside the expansion volume remains lower, with a maximum of 1.0 MPa (Com.1). Furthermore, the less amount of ablated mass from nozzle surface only results in an inconsequential variation of pressure after each computation. The pressurisation inside the expansion volume is determined by the coupled effect of arc formation, gas compression due to the piston movement, and produced hot vapour. The initial pressure in expansion volume is 0.6 MPa. The pressure increases to 0.71 MPa at the time instant of arc initialisation and before the produced vapour flows into the expansion volume, the pressure grows to 0.93 MPa and the vapour only contributes a 0.07 MPa increase.

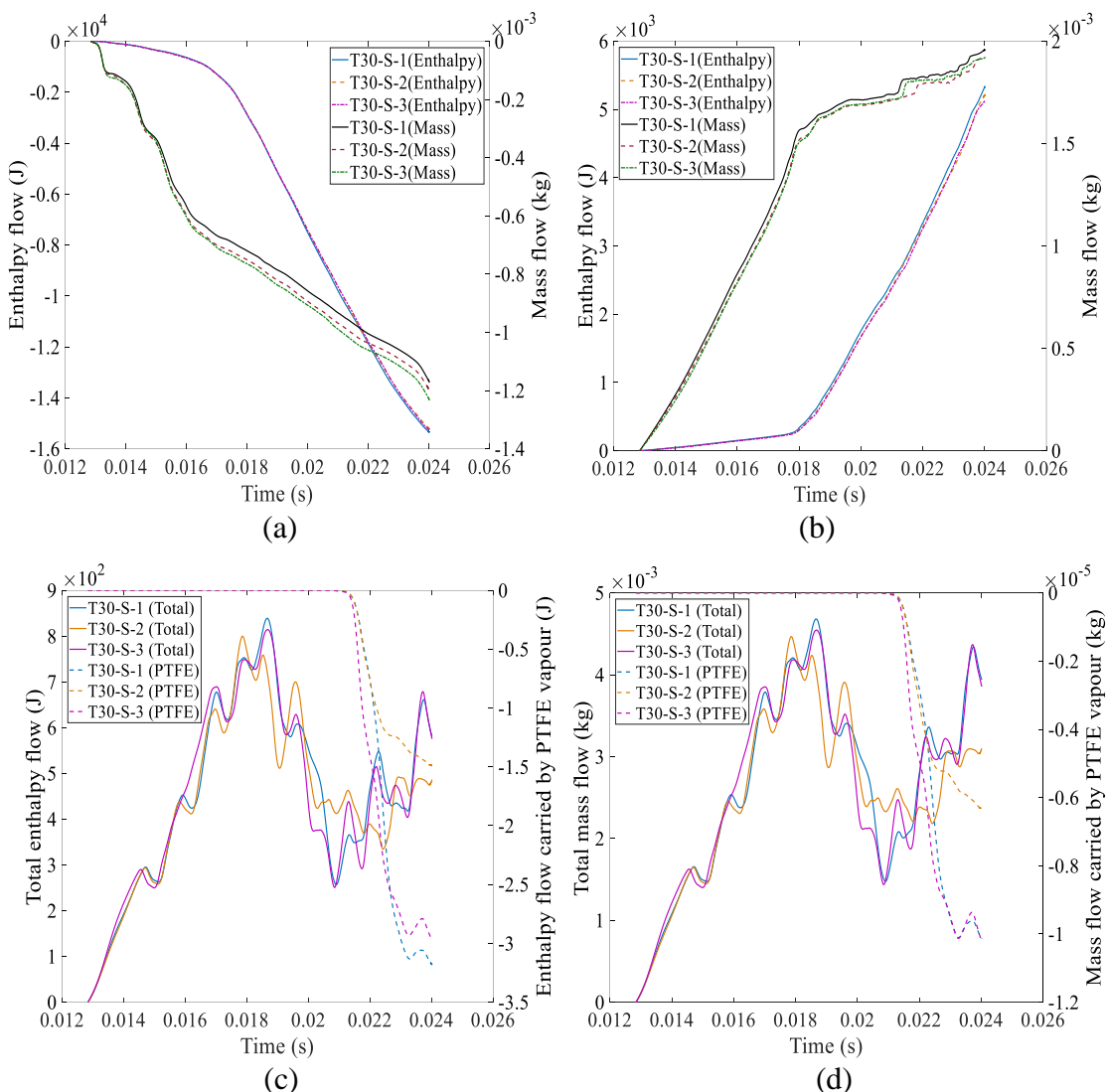


Figure 5.7 Predicted total enthalpy and mass flow in the hollow contact (a), towards the main nozzle downstream (b) and inside the expansion volume (c), (d) through cross sections 2 (a), 3 (b) and 6 (c) (d) respectively (Figure 4.11) with considering the diameter variation of nozzle flat throat. “S” represents for the short arc duration and “1, 2, 3” represent for the three computations.

For medium and long arc duration cases, the maximum enthalpy flows outwards from the expansion volume respectively increases to 1.2 kJ and 1.4 kJ with increased ablated mass of Com.1 (Figure 5.8 (a) and (c)). The total mass flows outwards from expansion volume is less than 7 g and 9 g (Figure 5.8 (b) and (d)). The gas in the expansion volume constantly flows out because of the extremely less amount of ablated mass flows into the expansion volume. Such a lower current of T30 results in a smaller electrical power supply from arc column so that the insufficient gas mixture is driven into the expansion volume. It means the pressurisation in expansion volume is principally determined by the coupled effect of piston movement and thermal energy carried by the PTFE vapour for low interrupting current case while the produced vapour is the dominant contributor for the high interrupting current case, e.g. L90.

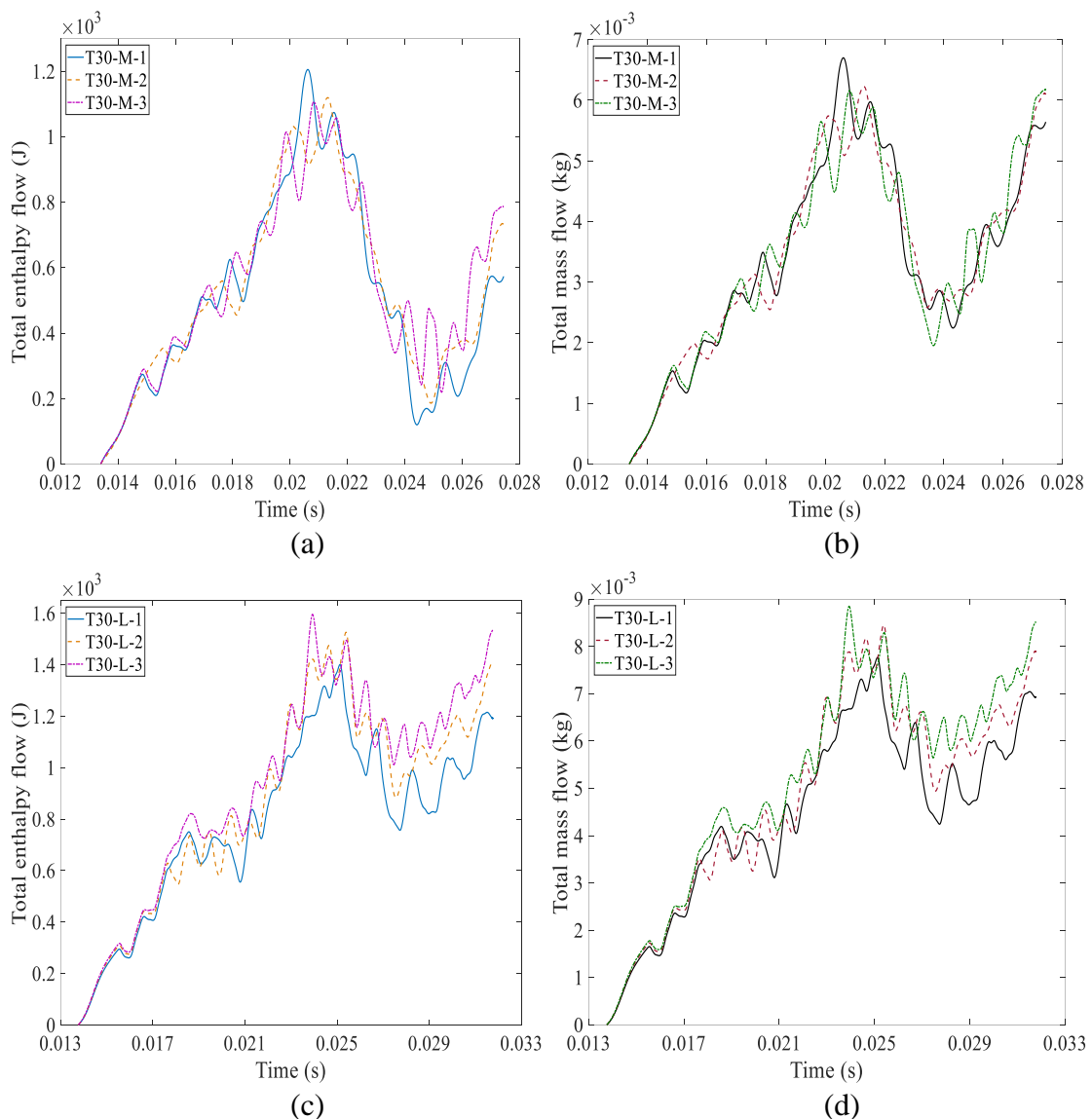


Figure 5.8 Predicted total enthalpy and mass flow inside the expansion volume through cross section 3 (Figure 4.11) of medium (“M”) and long (“L”) arc duration cases with considering the diameter variation of nozzle flat throat.

5.3.2 Terminal fault T60

Figure 5.9 draws the current waveforms and contact travel curves of T60 with different arc durations and the TRVs imposed from the system across circuit breaker terminals after the final current zero are shown in Figure 5.10. The peak current densities of T60 tests are higher than $1.0 \times 10^8 \text{ A/m}^2$ and larger amount of vapour would be produced of this kind of ablation dominated mode arc in comparison with T30 (Table 5.7-5.10).

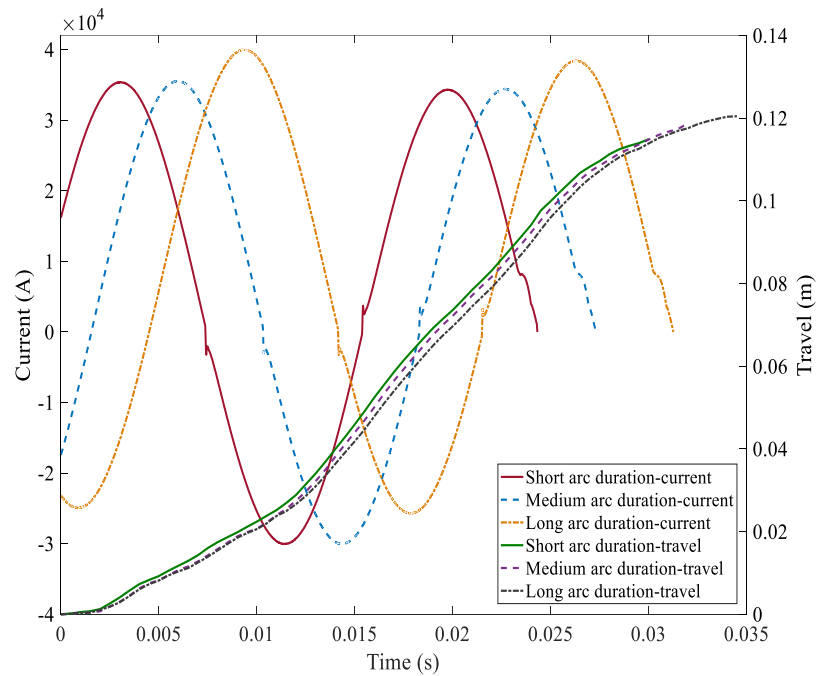


Figure 5.9 Current waveforms and travel curves of T60 tests.

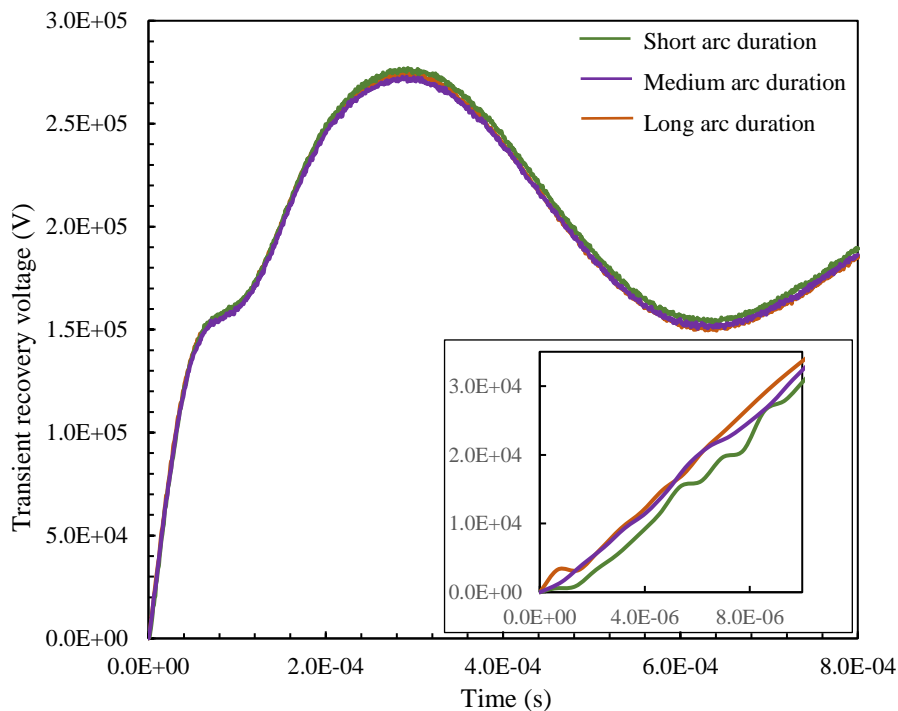


Figure 5.10 Transient recovery voltages of T60 tests with different arc durations.

Table 5.7 Predicted PTFE mass loss due to nozzle ablation after each valid breaking operation of rated operation sequence of T60 with considering the variation of nozzle flat throat diameter.

Nozzle		Prediction					
		Mass loss (g)			Nozzle throat radius (mm)		
		Short	Long	Medium	Short	Long	Medium
Main nozzle	Flat throat	0.24	1.73	0.76	10.6	11.1	11.3
	Total	0.54	2.90	1.27			
Auxiliary nozzle	Flat throat	0.66	0.81	0.60	10.0	10.6	11.0
	Total	1.25	1.73	1.22			
Total mass loss from nozzle surface		1.80	4.63	2.49			

Table 5.8 Predicted PTFE mass loss due to nozzle ablation after each computation of T60 short arc duration case with considering the variation of nozzle flat throat diameter.

Nozzle		Prediction					
		Mass loss (g)			Nozzle throat radius (mm)		
		Com. 1	Com. 2	Com. 3	Com. 1	Com. 2	Com. 3
Main nozzle	Flat throat	0.24	0.24	0.23	10.6	10.7	10.8
	Total	0.54	0.54	0.54			
Auxiliary nozzle	Flat throat	0.66	0.61	0.59	10.0	10.5	10.9
	Total	1.25	1.17	1.13			
Total mass loss from nozzle surface		1.80	1.71	1.67			

Table 5.9 Predicted PTFE mass loss due to nozzle ablation after each computation of T60 medium arc duration case with considering nozzle flat throat diameter variation.

Nozzle		Prediction					
		Mass loss (g)			Nozzle throat radius (mm)		
		Com. 1	Com. 2	Com. 3	Com. 1	Com. 2	Com. 3
Main nozzle	Flat throat	0.83	0.78	0.75	10.8	11.0	11.2
	Total	1.33	1.29	1.26			
Auxiliary nozzle	Flat throat	0.64	0.62	0.61	10.0	10.5	10.9
	Total	1.28	1.24	1.22			
Total mass loss from nozzle surface		2.61	2.53	2.48			

Table 5.10 Predicted PTFE mass loss due to the nozzle ablation after each computation considering the variation of nozzle flat throat diameter of T60 long arc duration case.

Nozzle		Prediction					
		Mass loss (g)			Nozzle throat radius (mm)		
		Com. 1	Com. 2	Com. 3	Com. 1	Com. 2	Com. 3
Main nozzle	Flat throat	1.73	1.64	1.49	11.0	11.5	11.9
	Total	2.90	2.77	2.66			
Auxiliary nozzle	Flat throat	0.84	0.81	1.00	10.2	10.8	11.5
	Total	1.67	1.64	1.95			
Total mass loss from nozzle surface		4.58	4.40	4.60			

The ablation from nozzle surface becomes more serious with the increased interrupting current. After the rated operating sequence of T60, ablation causes 0.8 mm and 1.5 mm dimension changes on the main and auxiliary nozzle flat throats while a smaller increase (0.5 mm and 0.7 mm) is obtained if the effects of ablation are not considered during the breaking operation with short and long arc durations. Furthermore, the increased arcing time also makes the ablation intensified which is related to the electrical power supply from the arc column, as shown in Figure 5.11.

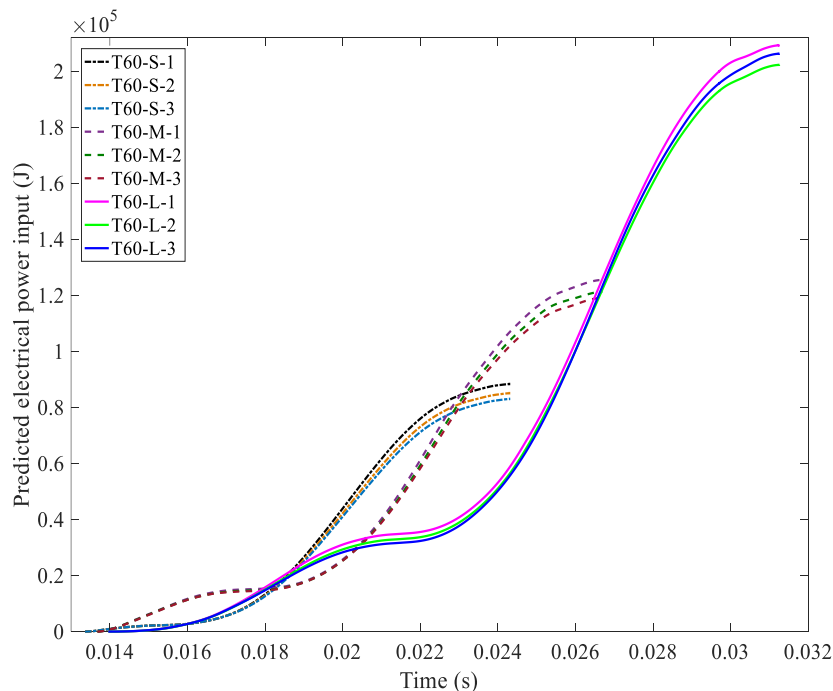


Figure 5.11 Electrical energy input for different arc durations while “S, M, L” represent for the short, medium, long arc duration and “1,2,3” represent for the three computations with the consideration of nozzle flat throat diameter variation.

The present work addressed in this chapter attempts to investigate the effect of nozzle ablation on the pressure distribution in particular in the expansion volume. In the circuit breaker, the pressure inside the expansion volume (A), at the middle of main nozzle flat throat (B) and towards the downstream exit (C) are respectively recorded as labelled in Figure 5.12 and the pressure variation resulted from flat throat enlargement is presented in Figure 5.13.

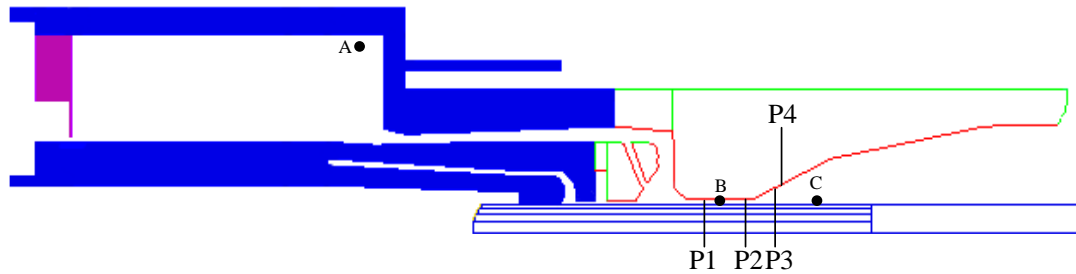
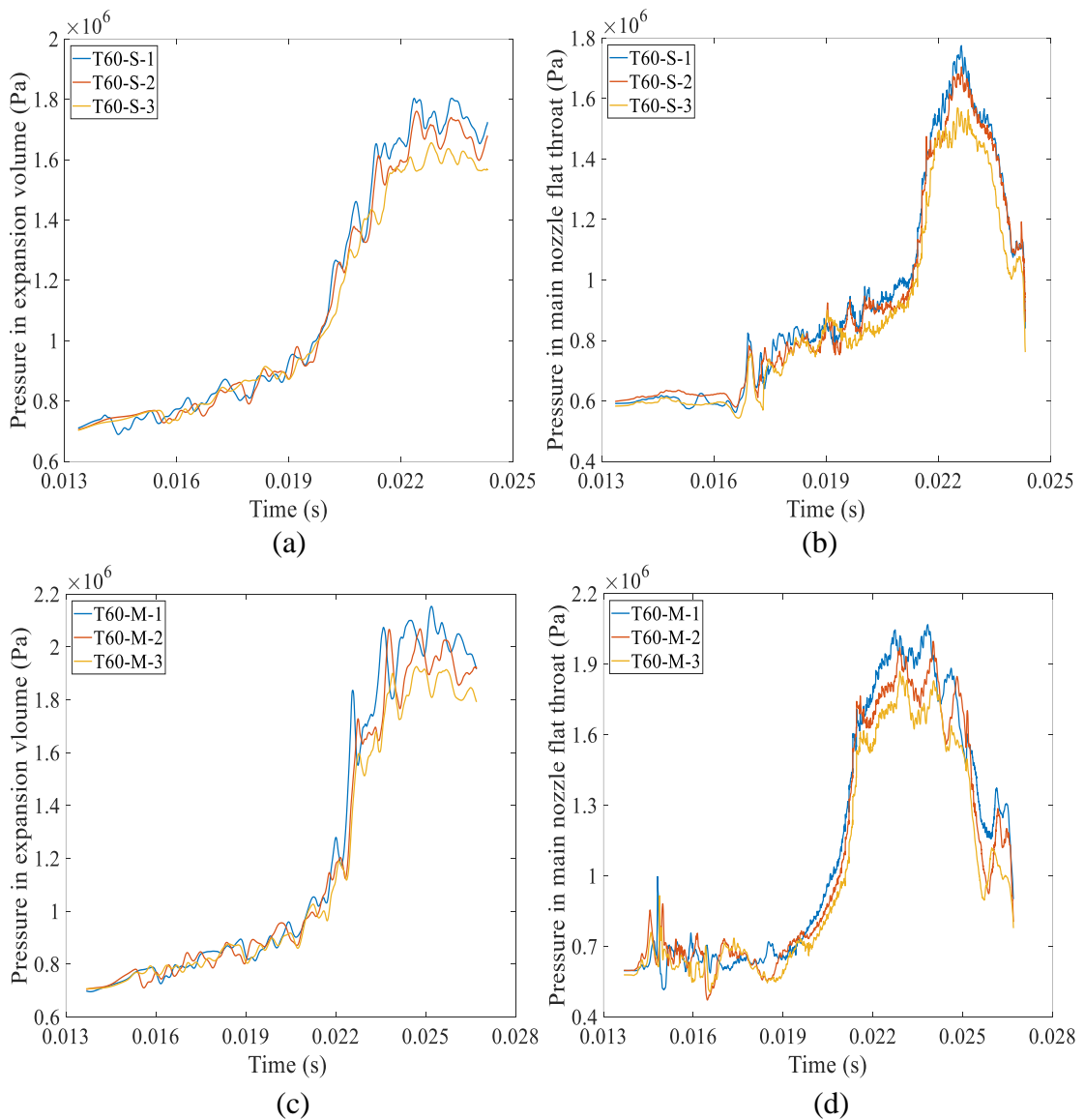


Figure 5.12 Three monitor positions for the pressures in expansion volume, middle of main nozzle flat throat and the downstream.



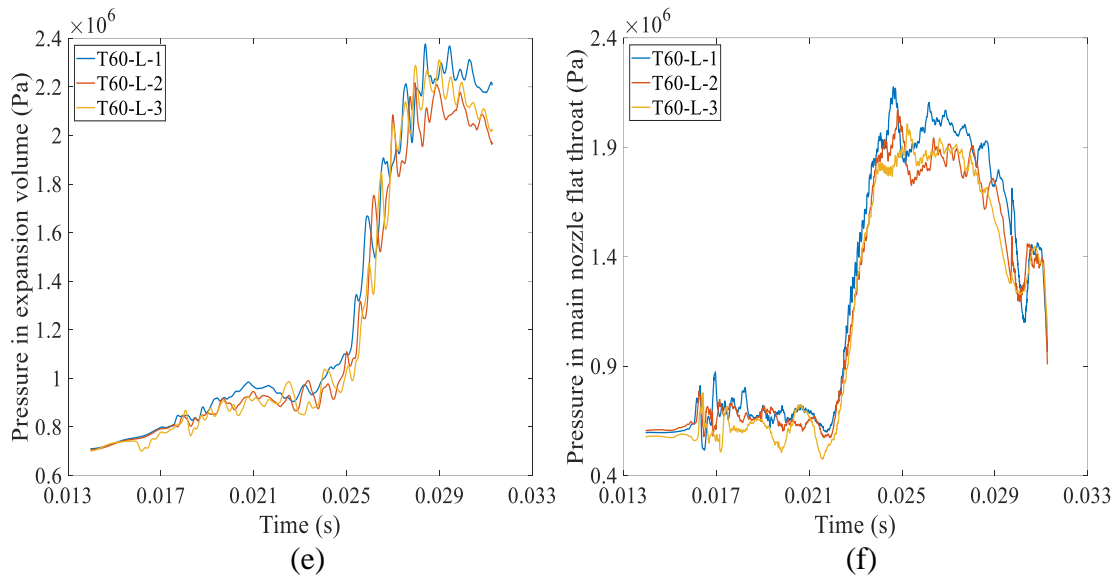


Figure 5.13 Pressure in the expansion volume (a), (c), (e) and at the middle of the main nozzle flat throat (b), (d), (f) with the consideration of nozzle flat throat diameter variation after each computation while “S, M, L” and “1, 2, 3” have the same meaning explained in Figure 5.11.

The pressure inside the expansion volume shows a gradual rise until 19 ms (T60-S), 22 ms (T60-M) and 25 ms (T60-L) due to the arc formation and piston movement. Thermal energy brought into expansion volume by hot vapour becomes the dominant contributor on the further steep increase of pressure. From the overall calculation, pressure decrease is normally expected with broadened nozzle holes. If the dimension alteration of nozzle flat throat is not considered during the rated operating sequence, the pressure inside the expansion volume reaches its maximum of 1.8 MPa, 2.15 MPa and 2.4 MPa while with the consideration of enlarged flat throat, the pressure is relatively low, 1.93 MPa (T60-M) and 2.31 MPa (T60-L).

It is worth to notice that the long arc duration case is somewhat different with respect to the ablated mass from the nozzle surface and its influence on the pressurisation inside the expansion volume. As shown in Table 5.10, the vaporised mass from the auxiliary nozzle surface especially the flat throat has an increase when the flat throats of the main and auxiliary nozzle enlarge to 11.5 mm and 10.8 mm. A similar situation can be found in Test 98 as mentioned in Chapter 4. By comparing the three computations of T60-L, the total ablated mass from the auxiliary nozzle flat throat in Com.3 shows a substantial increase when the solid contact fully clears the main nozzle flat throat at approximately 25 ms, even higher than that in the prior computations. It is resulted from a much higher mass ablation rate with a maximum of 0.15 kg/s as shown in Figure 5.14. The increased

ablation rate is affected by the radiation energy reaching at the nozzle surface. After an excessive enlargement of the nozzle holes, the electrical power supply becomes higher with current increase and brings a stronger radiation (Figure 5.11) to vaporise the nozzle surface.

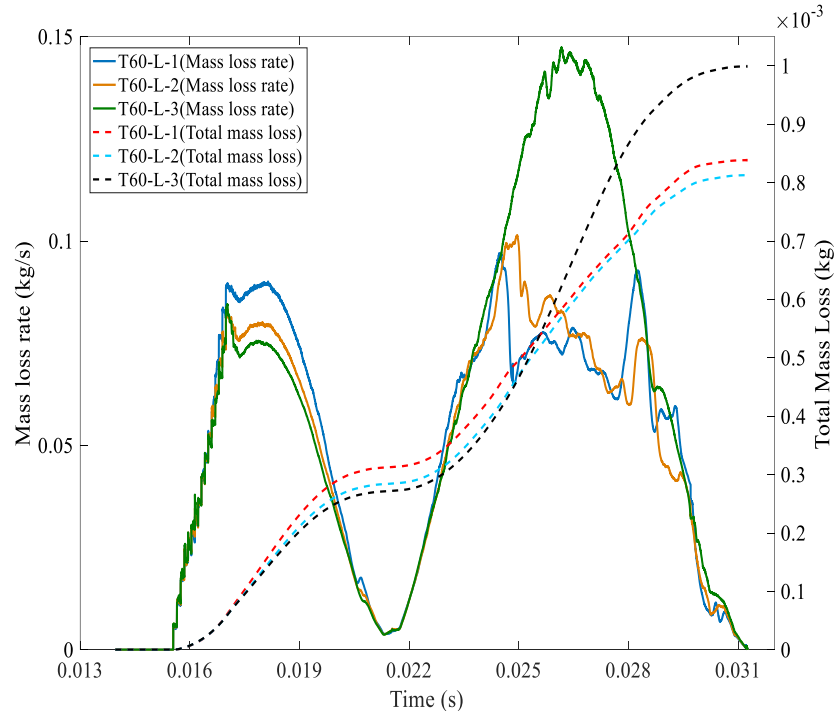


Figure 5.14 Mass loss rate and total mass loss from auxiliary nozzle flat throat after each computation with considering nozzle flat throat diameter variation of T60 long arc duration case and “L” and “1, 2, 3” have same meaning explained in Figure 5.11.

The axial temperature distribution at typical time instants are presented in Figure 5.15. In the geometric design of the auto-expansion circuit breaker model, the flat throats of the auxiliary and main nozzles respectively lie within 53.18~54.13 cm and 55.82~58.06 cm. Around 21.68 ms, the solid contact tip arrives at P1 of the main nozzle flat throat as shown in Figure 5.12. A stagnation region is formed between the two flat throats and the gaseous mixture flows out from expansion volume splits into two directions: hollow contact and main nozzle downstream, as illustrated in Figure 5.16 (a). When the solid contact travels to P2 at 23.88 ms, the gas flow in front of the solid contact changes its direction, into the expansion volume and through hollow contact as well (Figure 5.16 (b)). During this period, the enlarged nozzle flat throat only results in an insignificant change of axial temperature. In the vicinity of the solid contact, there is also a stagnation area where the thermal energy produced from ohmic heating could not be sufficiently removed by the slower gas flow so that the temperature becomes very high. However, the temperature shows a significant change especially around the auxiliary nozzle flat

throat when solid contact arrives at P3. The local axial temperature (Com.3) becomes higher and such a higher temperature causes much more mass ablated from the auxiliary nozzle surface.

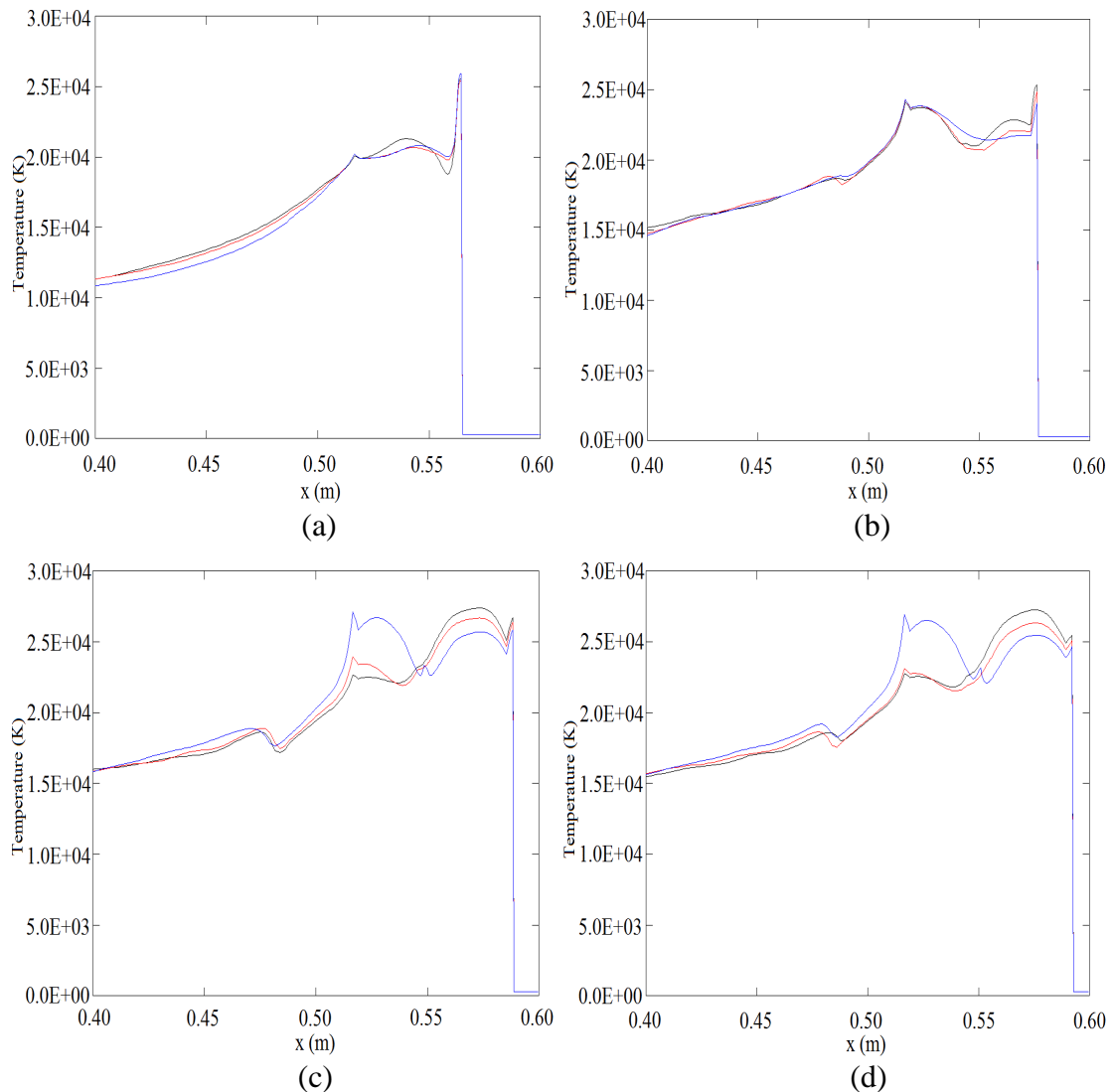
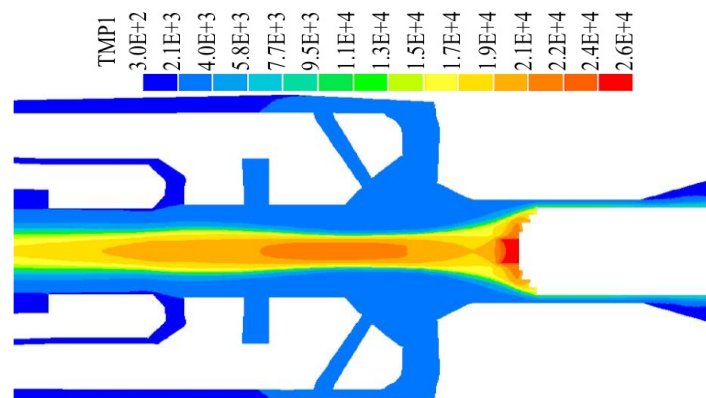


Figure 5.15 Temperature distribution in the arcing space when the solid contact arrives at four positions (Figure 5.12): (a) $t=21.68\text{ms}$; (b) $t=23.88\text{ms}$; (c) $t=26.08\text{ms}$; (d) $t=27.05\text{ms}$; The three curves respectively represent for the three computations of T60 long arc duration case: black-Com.1; red-Com.2; blue-Com.3.



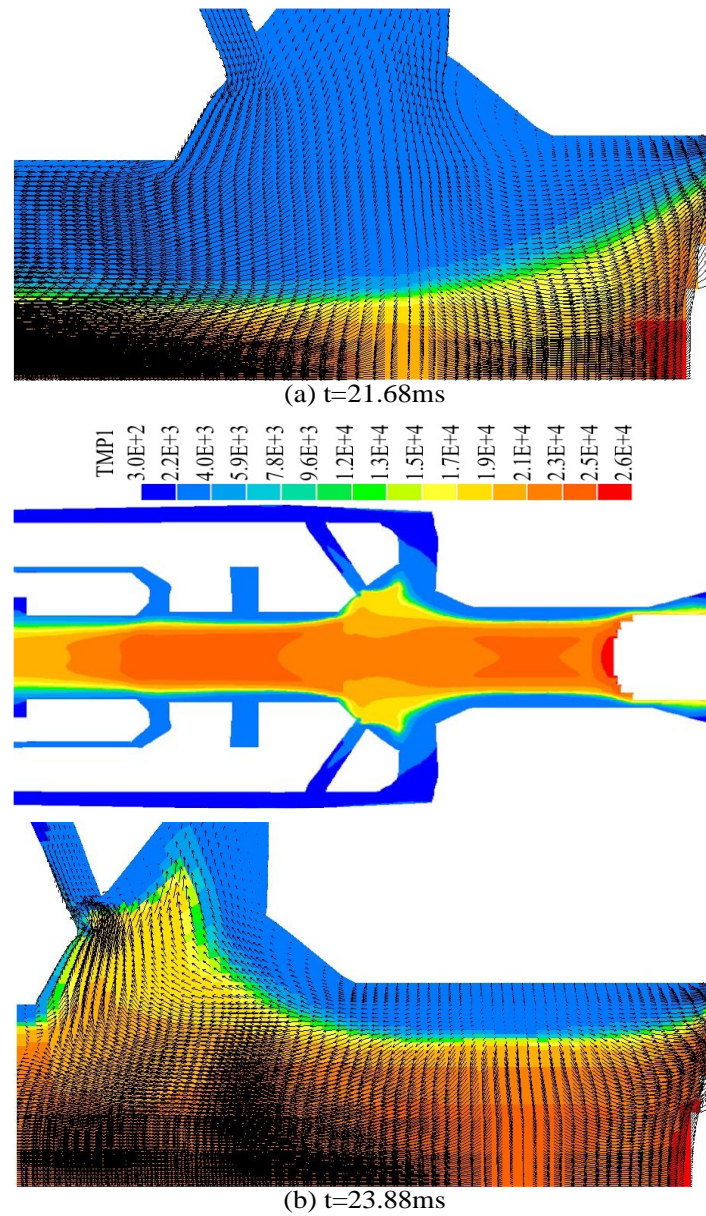


Figure 5.16 Temperature distribution with the velocity vector at (a) $t=21.68\text{ms}$; (b) $t=23.88\text{ms}$ of T60 long arc duration case (Com.1).

Figure 5.17 shows the temperature distributions within the arcing space. In reality, arc temperature is determined by the energy transfer process during the current interruption. Such a higher temperature around the auxiliary nozzle flat throat is due to the stronger ohmic heating and radiation, which are the dominant mechanism for the energy transfer during the high current phase as shown in Figure 5.18 (a) and (b). Furthermore, the arc radius as the radiation emission boundary that from the axis to the temperature isotherm of $0.83T_{\max}$ is comparatively smaller as a result of vapour compression (Figure 5.18 (c)). Besides that, the compressed arc column also leads to a larger effective flow area when the arc is drawn towards the downstream.

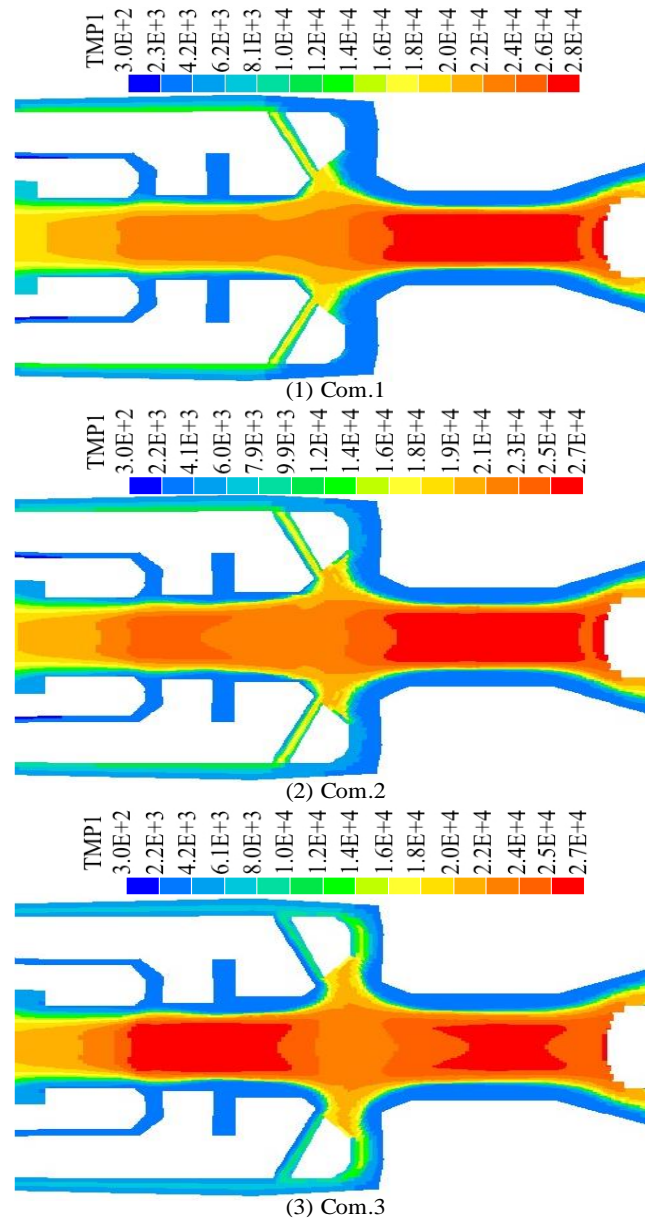
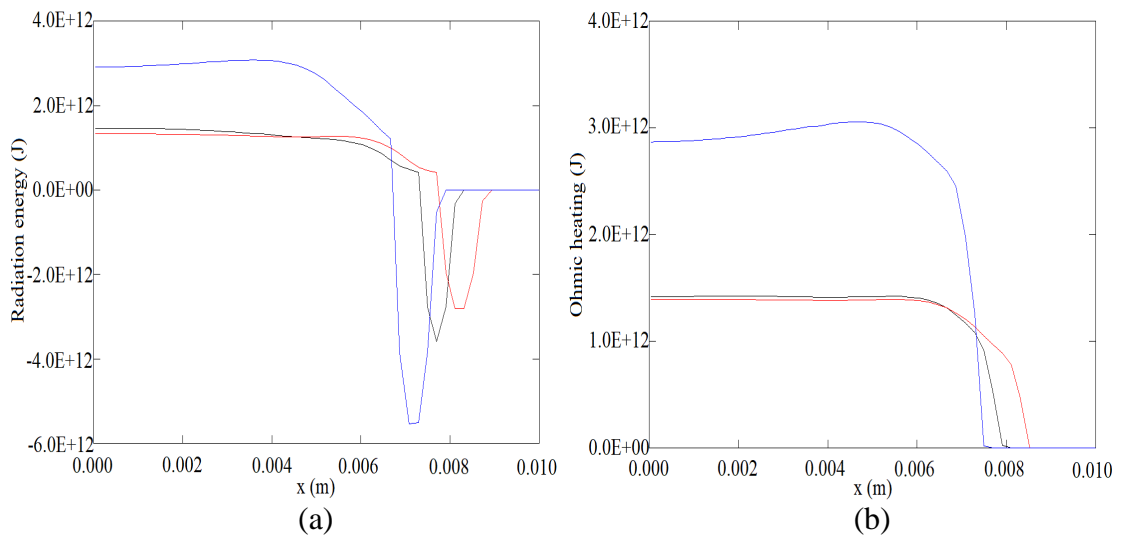


Figure 5.17 Temperature distribution within the arcing space at $t=26.08$ ms after the solid contact clears the main nozzle.



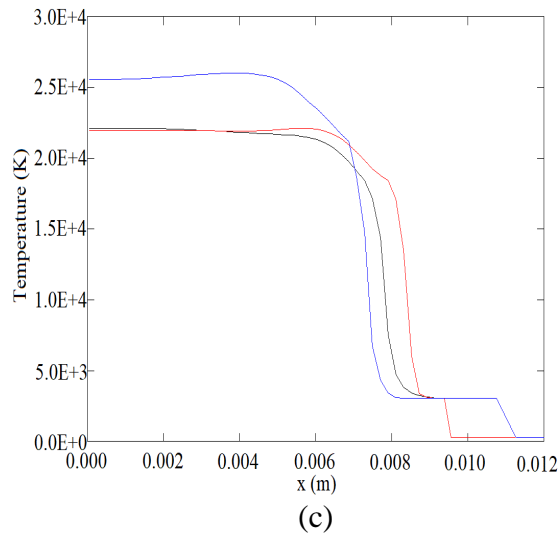
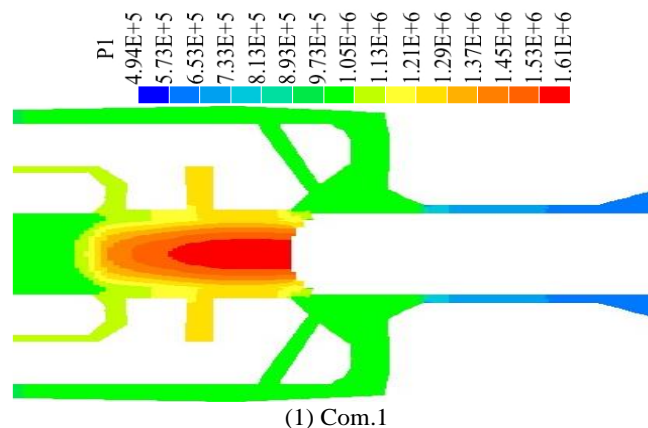


Figure 5.18 Radiation energy (a), ohmic heating (b) and the temperature distribution (c) in the radial direction at the middle of auxiliary nozzle flat throat at $t=26.08$ ms (T60-L-3); Each curve has same meaning explained in Figure 5.15.

As explained previously, before the solid contact leaves the auxiliary nozzle flat throat, a high pressure region is formed in the auxiliary nozzle stagnation area by the produced PTFE vapour (Figure 5.19) and the maximum pressure is slightly decreased (1.61 MPa, 1.51 MPa and 1.47 MPa) due to the enlarged flat throats. However, although the gap between solid contact and flat throat becomes larger, the enlargement of the nozzle hole lowers the pressure in the heating channel since the ablated mass is reduced. When the solid contact travels into the divergent section of main nozzle, the maximum pressure in the arcing space grows 0.1 MPa higher than Com.2, by virtue of the increased total ablated mass from the nozzle surface although the proportion from the main nozzle flat throat drops (Figure 5.20). At this instant, the gas mixture still flows reversely towards the expansion volume and through the hollow contact since current grows to its positive peak until 26.34 ms. Additionally, a slightly higher pressurisation inside the expansion volume is obtained as well (Figure 5.13 (e)).



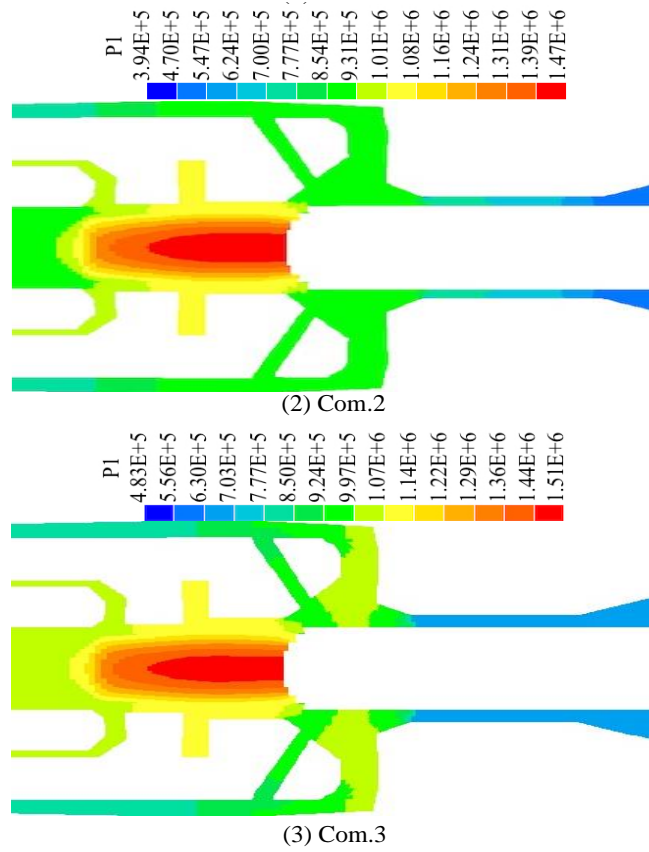
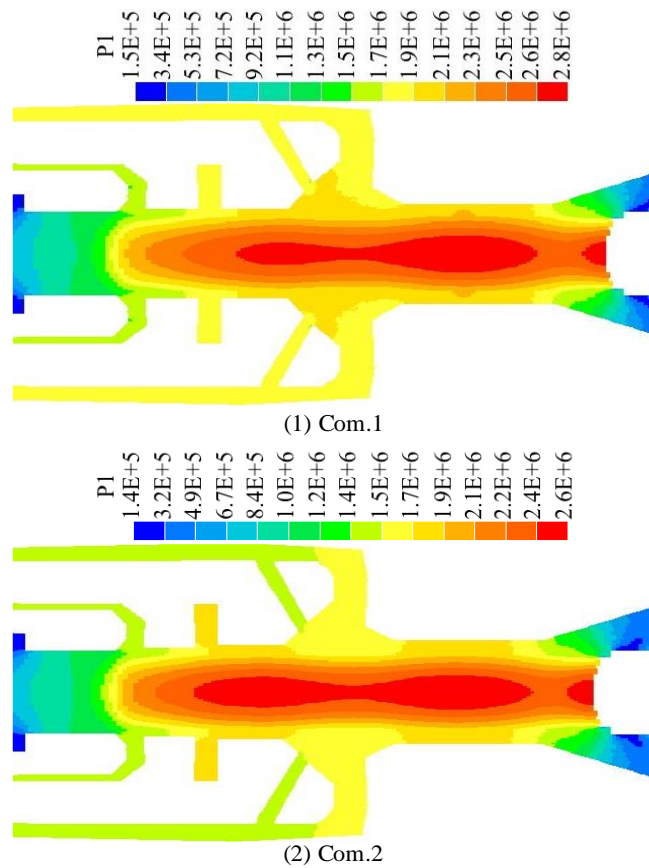


Figure 5.19 Pressure distributions when the solid contact just clears the auxiliary nozzle flat throat of T60 long arc duration cases with considering the diameter variation of nozzle flat throat after each computation.



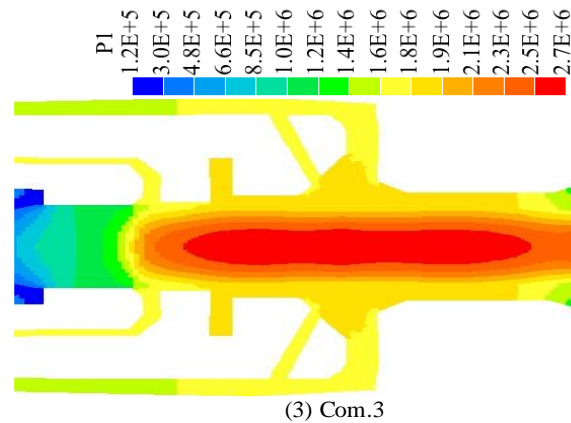


Figure 5.20 Pressure distribution within the arcing space after the solid contact leaves the main nozzle flat throat at $t=26.08$ ms.

The positions of solid contact tip at typical time instants corresponds to the interrupting current is given in Figure 5.21. Solid contact moves through the flat throats of auxiliary and main nozzles respectively between 15.50~17.15 ms (P1~P2) and 20.0~24.85 ms (P3~P4). The corresponded current decreases towards the first zero when solid contact moves through the auxiliary nozzle flat throat while it grows towards the positive peak with the solid contact movement from P3 to P4, and it reaches peak at 26.34 ms.

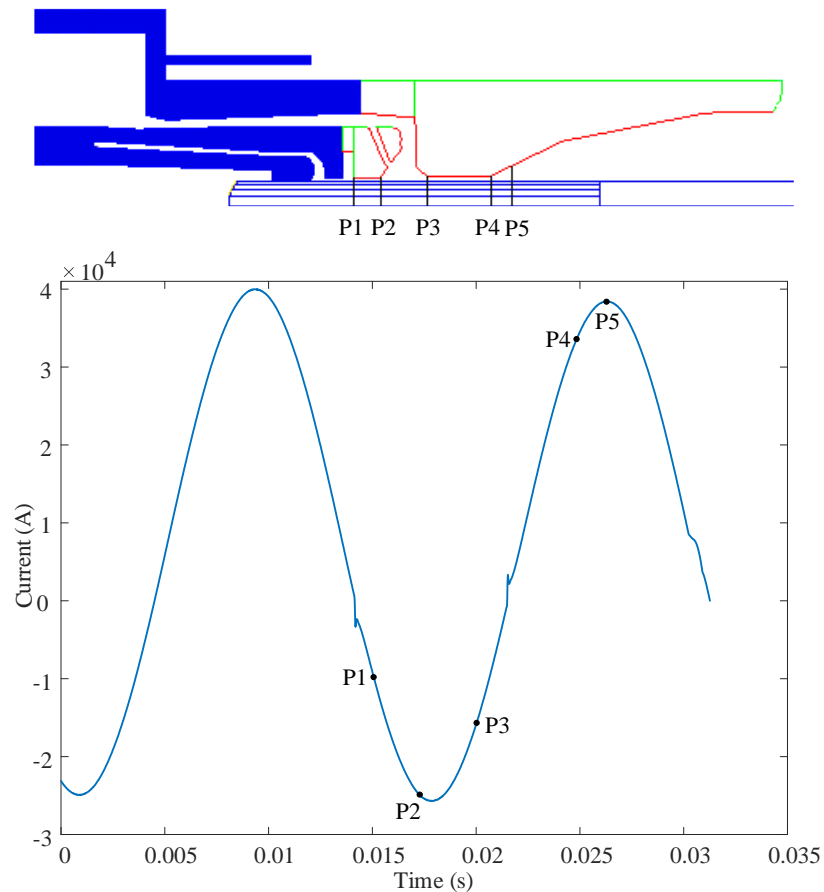


Figure 5.21 Positions of the solid contact in the arcing chamber corresponded to the current waveform for T60 long arc duration case.

Figure 5.22 describes the flow field conditions inside the expansion volume of T60 long arc duration cases (T60-L-1/2/3). The current decreases from -5.2 kA at 21.08 ms to its zero at 21.49 ms and rises again to 18.99 kA at 23.18 ms. The arc is mainly burned in the auxiliary nozzle and a considerable length of the main nozzle flat throat. However, for T60-L-1, only 0.72 g mass is ablated from the nozzle surface with ablation energy of 8.58 kJ until 23.18 ms. Due to the insufficient produced vapour and electrical power supply, the total enthalpy flows into the expansion volume shows a decrease (Figure 5.22 (1)). It stops flow into the expansion volume at 23.18 ms and furtherly flows out with a smaller value (<10 J) until 23.33 ms. In comparison with T60-L-1, the proportion of total enthalpy flows into the expansion volume is smaller for T60-L-2 while for T60-L-3, the total enthalpy is continuously flowing out from the beginning until 25.14 ms. The corresponded times for the enthalpy re-flows into the expansion volume are 24.91 ms (T60-L-2) and 25.13 ms (T60-L-3).

After the solid contact leaves the main nozzle flat throat, the effective cross section of main nozzle surface exposed to the arc column becomes larger, the current increases to its positive peak (38.43 kA) and the enthalpy flows into expansion volume substantially increases with a higher flow rate. The maximum enthalpy of the three computations is respectively 18.14 kJ, 16.29 kJ and 16.39 kJ. In T60-L-3, the 0.1 kJ enthalpy increase is responsible for the corresponded higher pressure. After the enthalpy re-flows into the expansion volume, the enthalpy carried by PTFE vapour becomes larger. At 26.56 ms, due to the increased amount of ablated mass from auxiliary nozzle surface by the higher radiation energy in T60-L-3, it continuously increases and even exceeds that of T60-L-2. The maximum enthalpy carried by the PTFE vapour is 11.07 kJ, 9.49 kJ and 10.24 kJ for the three computations.

Furthermore, the total mass rushes out towards the downstream through cross section 7 (Figure 4.11) shows a steeply increased flow rate when the current drops to 11.5 kA after 30.0 ms (Figure 5.23). The decreased current lowers the pressure around the main nozzle and the generated high pressure difference between the expansion volume and downstream exit drives the gaseous mixture out from the expansion volume. Excessive enlargement of the nozzle holes leads to a higher mass flow rate before the final current zero with a maximum of 2.3 kg/s (T60-L-3) which is higher than the prior computations. However, it only shows a negligible effect on the mass flow towards the hollow contact.

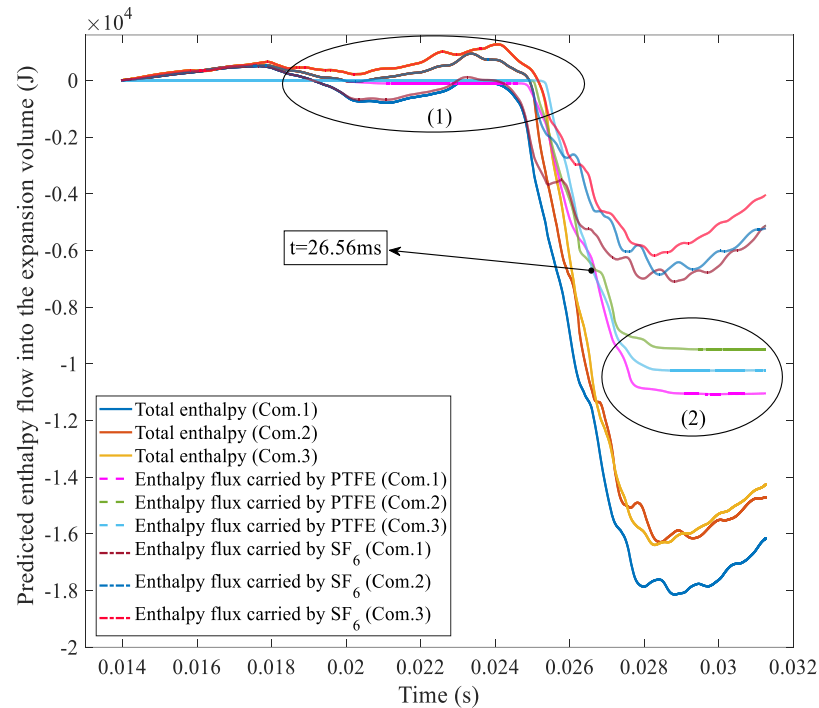


Figure 5.22 Predicted enthalpy flowed into the expansion volume through cross section 3 as shown in Figure 4.11 with considering the diameter variation of the nozzle flat throat after each computation (T60-L-1/2/3).

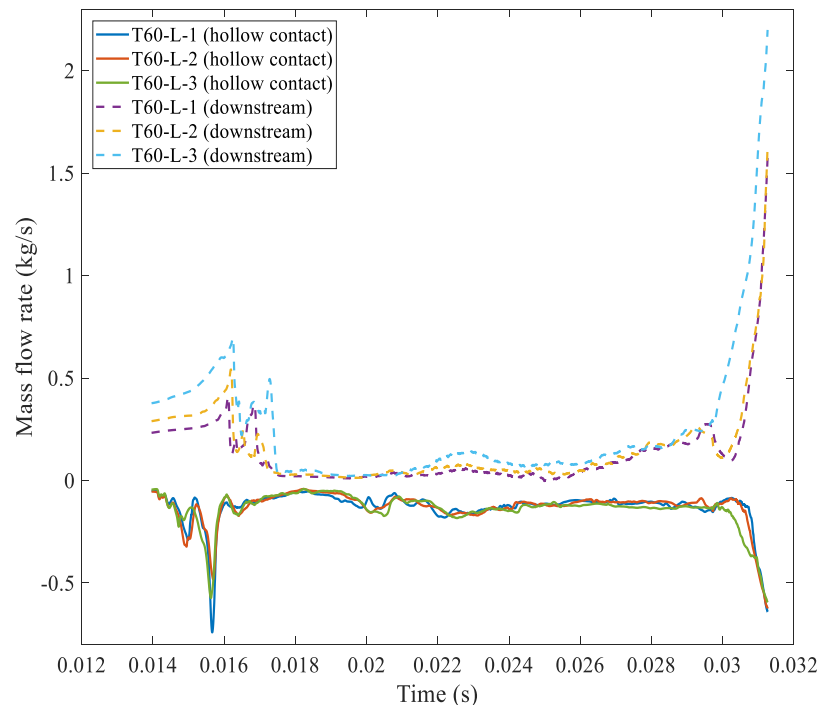


Figure 5.23 Predicted mass flow rate outwards the main nozzle downstream and into the hollow contact respectively with considering the diameter variation of the nozzle flat throat after each computation (T60-L-1/2/3).

Figure 5.24 illustrates the mass ablation rate of the three computations of Test 98. The variation also occurs after the solid contact clears the main nozzle flat throat, resulting

in a higher local temperature around the auxiliary nozzle flat throat although the ablated mass from the auxiliary nozzle surface is comparatively decreased again when the main and auxiliary flat throats enlarge to 12.3 mm and 12.0 mm respectively.

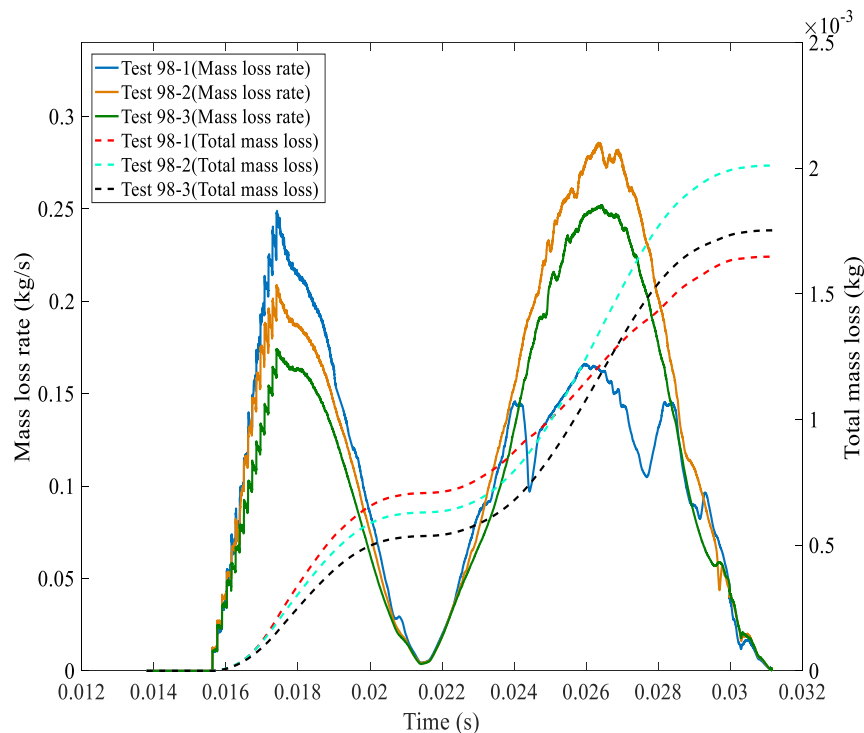


Figure 5.24 Mass ablated rate and the total mass loss from auxiliary nozzle flat throat with considering the diameter variation of nozzles flat throats of Test 98.

To comparatively investigate whether the dimension change of main nozzle or auxiliary nozzle flat throat is the primary cause of the flow field environment variation, another two groups of a total of five computations are performed. Since the variation is occurred when the main and auxiliary nozzle flat throats enlarge to 11.5 mm and 10.8 mm, these new computations are specified the radii of flat throats to be ± 0.5 mm of the respective flat throats enlargement. The first group is designed with setting the radius of the main nozzle flat throat to 11.0 mm and changing the radius of auxiliary nozzle flat throat to 10.3 mm (T60_1) and 11.3 mm (T60_2). The second group keeps the auxiliary nozzle flat throat to 10.8 mm while enlarges the main nozzle to 11.1 mm (T60_3), 11.2 mm (T60_4) and 11.3 mm (T60_5) respectively.

The detailed calculation results are shown in Table 5.11. It is observed that the variation of the auxiliary nozzle flat throat only has an insignificant effect on the nozzle material mass loss rate of main nozzle. In addition, the maximum mass loss rate is reduced after solid contact clears the main nozzle flat throat by the uniformly enlarged main nozzle

flat throat. Although the total ablated mass is increased, the decrease of the proportion occupied by the main nozzle flat throat is expected with the broadened flat throat.

However, there is a considerable change on the mass ablation rate when the main nozzle flat throat increases larger than 11.2 mm as presented in Figure 5.26. The calculation results indicate that the flow field conditions of long arc duration case especially around the auxiliary nozzle flat throat are sensitively influenced by the dimension change of nozzle flat throat and the variation of main nozzle flat throat is the dominant contributor.

Table 5.11 Predicted PTFE mass loss due to the nozzle ablation with different nozzles dimensions of T60 long arc duration case.

Nozzle		Prediction					
		Mass loss (g)		Nozzle throat radius (mm)			
		T60_1	T60_2	T60_1	T60_2		
Main nozzle	Flat throat	1.64	1.65	11.5	11.5		
	Total	2.79	2.81				
Auxiliary nozzle	Flat throat	0.82	0.79	10.9	11.8		
	Total	1.64	1.58				
Total mass loss from nozzle surface		4.43	4.39				
Nozzle		Prediction					
		Mass loss (g)			Nozzle throat radius (mm)		
		T60_3	T60_4	T60_5	T60_3	T60_4	T60_5
Main nozzle	Flat throat	1.61	1.55	1.53	11.6	11.6	11.7
	Total	2.75	2.70	2.70			
Auxiliary nozzle	Flat throat	0.84	0.98	0.99	11.4	11.5	11.5
	Total	1.67	1.94	1.95			
Total mass loss from nozzle surface		4.42	4.64	4.65			

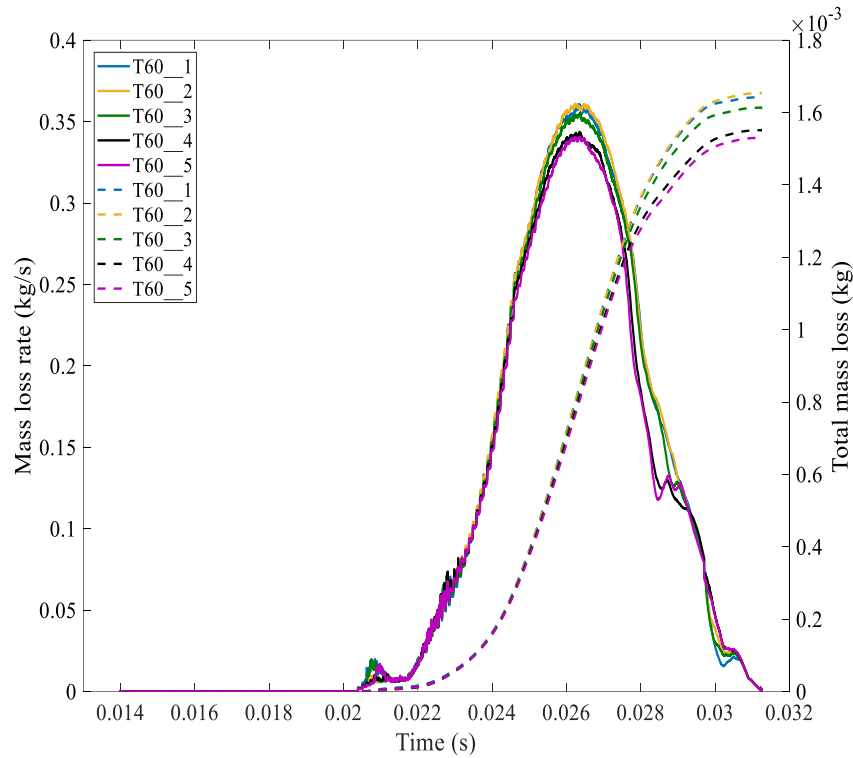


Figure 5.25 Mass ablated rate and the total mass loss from main nozzle flat throat with considering the nozzles flat throats diameter variation for T60_1/2/3/4/5. The solid lines represent for the mass loss rate while the dashed lines represent for the total mass loss.

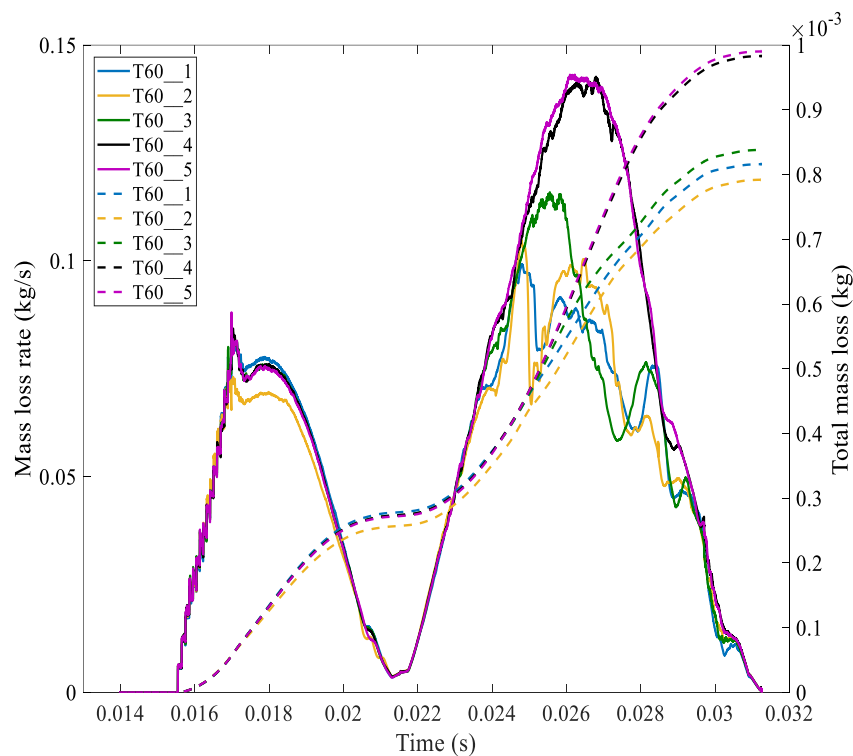


Figure 5.26 Mass ablated rate and the total mass loss from auxiliary nozzle flat throat with considering the nozzles flat throats diameter variation for T60_1/2/3/4/5. The solid lines represent for the mass loss rate while the dashed lines represent for the total mass loss.

5.4 Critical RRRV Affected by Nozzle Ablation

5.4.1 Calibration of turbulence parameter in Prandtl mixing length model

When the interrupted current approaches its final zero, turbulence cooling becomes a dominant mechanism to remove thermal energy generated in the residual arc between the arcing contacts. The post arc current flowing between the arcing contacts is obtained to predict the successful or failed thermal recovery process after the current interruption process. In the present work, the Prandtl mixing length model described in Chapter 4 is adopted to predict the turbulence cooling effect [10], where a calibration of turbulence parameter c is required during the calculation .

A range of turbulence parameters used for the current zero phase calculation (T_{p10}) is chosen. From the calculation, a reasonable value of the turbulence parameter c is 0.32 for the 145 kV/40 kA auto-expansion circuit breaker, producing agreement with tests. As shown in Figure 5.27 and 5.28, the circuit breaker can sustain the transient recovery voltage imposed from the network when c sets to 0.32 and above (Test 92) while the circuit breaker could successfully interrupt T60 short arc duration case for all values of c . For the successful case, the predicted post arc current eventually decreases to a much smaller value.

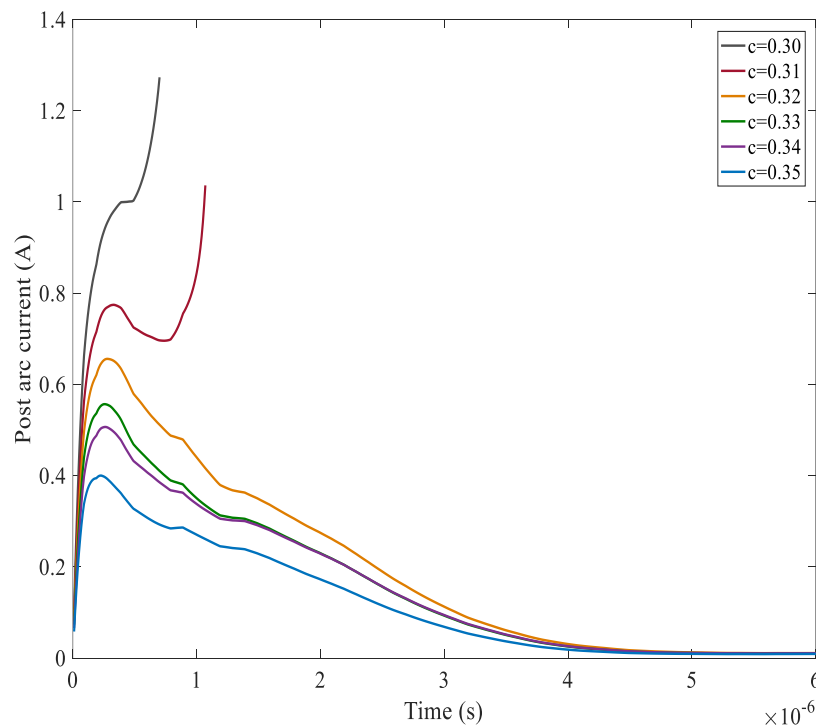


Figure 5.27 Post arc current calculated using different turbulence parameter c of Test 92 (Com.1).

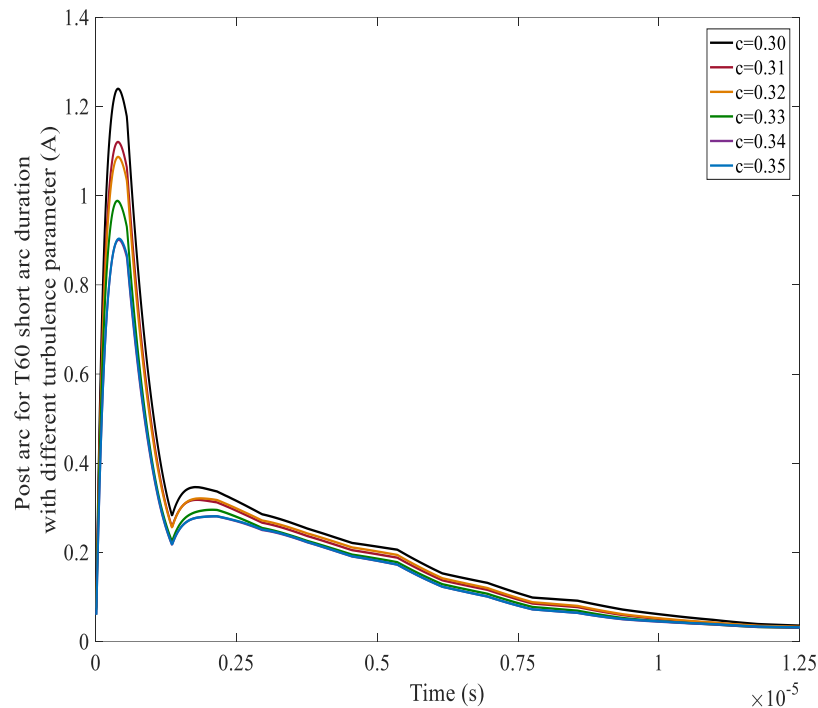


Figure 5.28 Post arc current calculated using different turbulence parameter c for T60 short arc duration test (Com.1).

Test 93, which is performed to determine the shortest arc duration, is a typical thermal failure case. For different test duties, the first effective interruption is designed with the arc duration as short as possible. For short line fault L90, the new arc duration is reduced 1 ms in comparison with the predicted arc duration of Test 92 and the actual arcing period of Test 93 is 12.3 ms. From the calculation, it is observed the main nozzle flat throat is still blocked by the solid contact tip when the current drops to the final zero (Figure 5.29). The final position of the solid contact is affected by the arc duration and contact travel curve, it differs the effective flow area around main nozzle downstream. As a result of nozzle clogging, the hot gas could not be flowed out through the main nozzle flat throat towards the downstream sufficiently. Furthermore, the ablated mass from the nozzle surface is less than the case of Test 92, which leads to a relatively lower pressurisation in the expansion volume and wider arc column. Due to a smaller pressure difference between upstream expansion volume and main nozzle downstream, the thermal energy removed by the gas flow becomes insufficient. In addition, there is also a stagnation region between the two flat throats where the hot gas cannot be effectively cool down. As presented in Figure 5.30, Test 93 shows a failed thermal recovery when $c=0.35$. Therefore, it can be concluded that 0.32 is a reasonable value of the turbulence parameter to provide satisfactory prediction of the thermal recovery process of 145 kV/40 kA circuit breaker.

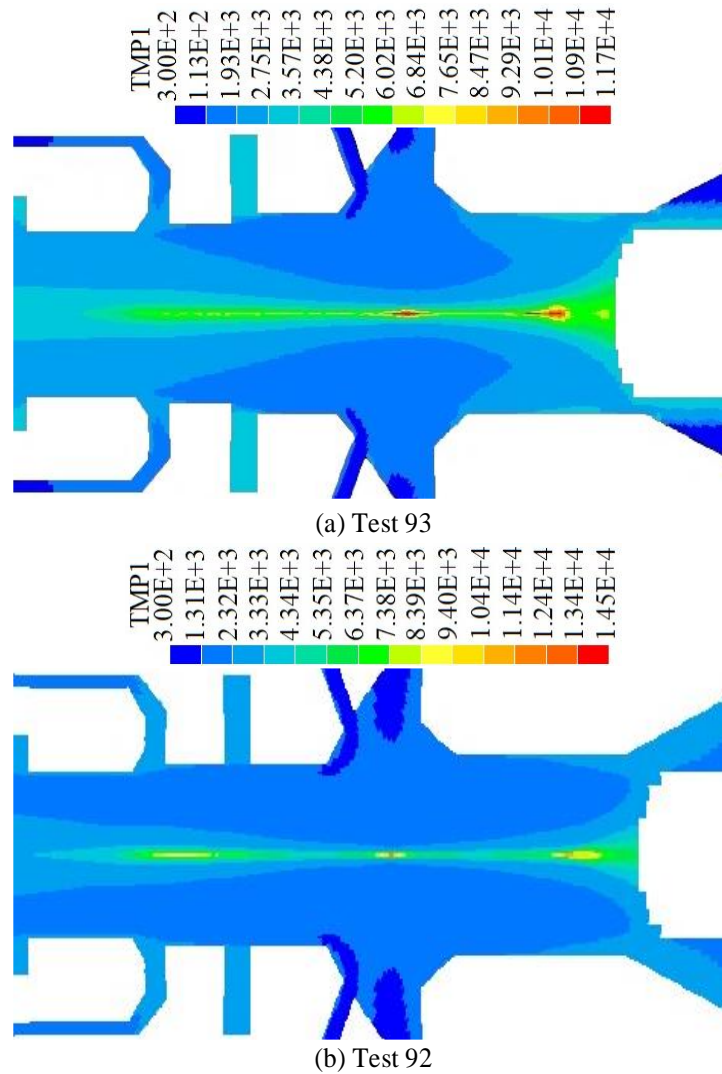


Figure 5.29 Temperature distribution at the final current zero for Test 93 (a) with the consideration of nozzle flat throats diameter variation resulted from Test 92 (b).

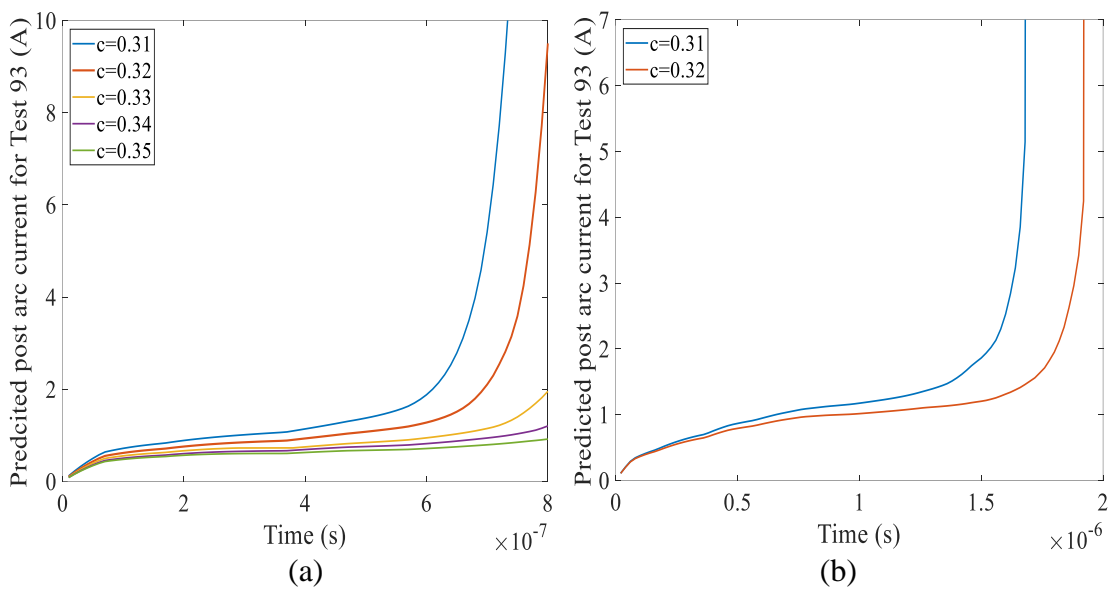


Figure 5.30 Predicted post arc current with different c for Test 93 without (a) and with (b) the consideration of the nozzle flat throat diameter variation resulted from Test 92.

5.4.2 Critical rate of rise of recovery voltage

The critical RRRV is used to predict the interruption capability of circuit breakers. The rated RRRVs of different test duties are given in Table 5.12 [11].

Table 5.12 Applicable RRRV values for different test duties introduced in the standards.

Test duty	RRRV (kV/us)	Operation frequency
T10	7	50/60
T30	5	50/60
T60	3	50/60
T100s	2	50/60
L90 40kA	8.64	60
L90 50kA	9	50
L90 50kA	10.8	60

For the 145 kV/40 kA auto-expansion circuit breaker, the corresponded TRV waveform of SLF L90 is determined based on the standards using the four-parameter method and the corresponded symbols are determined by [5]–[7]:

$$u_1 = 0.75 \times k_{pp} \times \sqrt{2/3} \times U_r \quad (5.4.1)$$

$$u_c = k_{pp} \times k_{af} \times \sqrt{2/3} \times U_r \quad (5.4.2)$$

$$u_1/t_1 = 2 \quad (5.4.3)$$

where U_r is the rated maximum voltage and k_{pp} is the first pole to clear factor where 1.0 is used for short line fault. The ratio between u_1 and t_1 is defined to 2 while k_{af} is the amplitude factor with value of 1.40.

The short line fault TRV ratings with rated 145 kV is determined as followed [6]:

$$u_T = u_L + u_S \quad (5.4.4)$$

$$u_L = d(1 - M)\sqrt{2/3}U_r \quad (5.4.5)$$

$$u_S = 2M(t_L - t_d) \quad (5.4.6)$$

$$\frac{du_L}{dt} = \sqrt{2}\omega MIZ_{eff} \times 10^{-6} = sI_L \quad (5.4.7)$$

$$t_L = \frac{u_L}{\frac{du_L}{dt}} \quad (5.4.8)$$

$$\omega = 2\pi f \quad (5.4.9)$$

where u_T is the first peak value of TRV; u_L is the line-side contribution to TRV; u_S is the source-side contribution to TRV; $\frac{du_L}{dt}$ is the RRRV and t_L is the time to peak; d and Z_{eff} are the transmission line parameters (1.6 and 450 Ω); M is the ratio of fault current to the rated short-circuit current (I_L/I); the time delay t_d is defined to $2\mu s$; f is the power frequency and s is 0.24 for 60 Hz system and 0.20 for 50 Hz system.

Based on the calculation, the corresponding value of RRRV for the rated 145 kV circuit breakers short line fault is 8.64 kV/ μs with the time to peak of 2.19 μs . For different test duties, the reference parameters used to determine the TRV envelope are given in Table 5.13. The parameters u_L and t_L are additional to the four-(two-) parameters to describe the TRV envelope.

Table 5.13 Parameters used to define the TRV envelope for different test duties.

Test duty	Parameters	
T30	u_c	237 kV
	t_3	47 μs
T60	u_1	133 kV
	t_1	44 μs
	u_c	266 kV
	t_2	132 μs
L90	u_1	89 kV
	t_1	44 μs
	u_c	166 kV
	t_2	178 μs

To comparatively study the circuit breakers interruption capability, a range of RRRV values are chosen to calculate the post arc current with the consideration of the enlarged nozzle holes. A threshold value is determined through the calculation which represents the largest RRRV a circuit breaker could withstand. The computational uncertainty of this threshold value is less than 0.5 kV/ μs .

From the calculation, the critical RRRV is largely affected by the flow field conditions established before the final current zero. For the short arc duration case Test 92 without

considering the effects of ablation, the predicted critical value of RRRV (9.0 kV/us) is higher than that described in the standard, as shown in Figure 5.31. As the most difficult test duty to interrupt, the result indicates that the 145 kV/40 kA auto-expansion circuit breaker is designed with sufficient interruption capability.

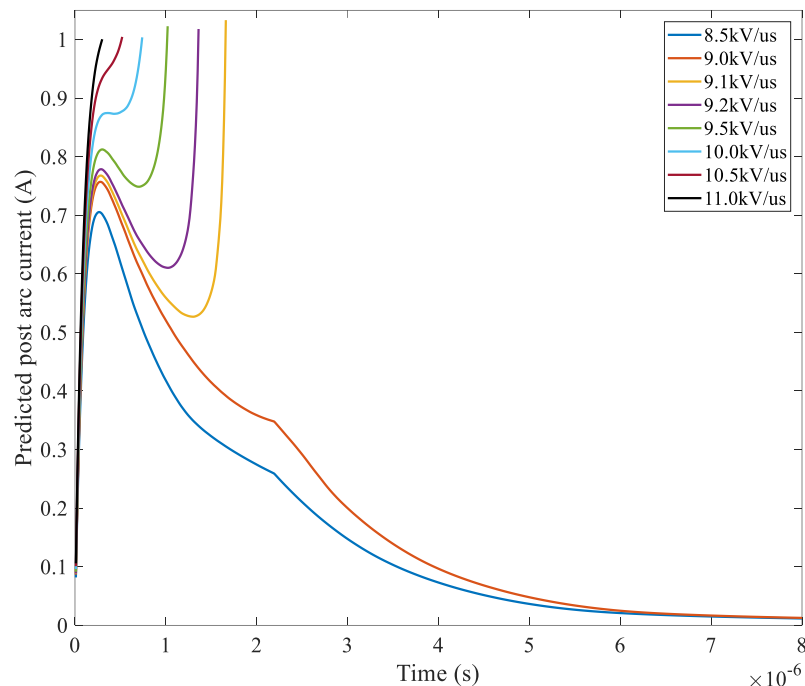


Figure 5.31 Predicted post arc current with different RRRV of the short arc duration case Test 92 (Com.1).

To determine the effects of nozzle flat throat diameter variation on the circuit breakers interruption capability, the critical RRRVs for the test duties with different arc durations are predicted after each computation with considering the nozzle flat throat increasing. As is recognised from previous study, the turbulence cooling has the strongest influence for the long arc duration case and thus the predicted critical RRRV is the highest. From the calculation, the decreased critical RRRV is expected with the enlarged nozzle flat throat. However, for the long arc duration case, the critical RRRV of T60-L-3 is slightly higher than T60-L-2, which is due to the increased pressurisation inside the expansion volume. It should be emphasised that the critical RRRV of Test 98 illustrates a decrease although the nozzle flat throats are enlarged excessively which leads to the variation of local flow field conditions. It is because significantly larger mass is ablated from nozzle surface especially from the main nozzle flat throat in comparison with other cases. The increased ablated mass from the auxiliary nozzle flat throat is not enough to compensate the reduced amount from the main nozzle flat throat. Due to the overall reduced mass ablated from the flat throats, the pressurisation inside the expansion volume becomes

lower so that the corresponding critical RRRV is decreased. The predicted total ablated mass from the two nozzle surfaces is given in Table 5.16.

Table 5.14 Predicted critical RRRV values of Test 92 and 98 with the consideration of nozzle flat throat diameters variation.

Critical RRRV (kV/us) Case	Com.1	Com.2	Com.3
Test 92	9.0	7.6	5.9
Test 98	14.2	11.1	9.2

Table 5.15 Predicted critical RRRV values for the T60 test under different arc durations with the consideration of nozzle flat throat diameters variation.

Critical RRRV (kV/us) Case	Com.1	Com.2	Com.3
Short arc duration	3	2.6	2.2
Medium arc duration	9.6	9.5	9.4
Long arc duration	11	9.5	9.6

Table 5.16 Predicted total mass loss from the flat throats of main and auxiliary nozzles for different test duties with different arc durations.

Total mass loss Test duty	Com.1	Com.2	Com.3
Test 92	1.81	1.65	1.53
Test 93	1.52	1.40	1.27
Test 98	4.99	4.87	4.38
T30-S	0.30	0.29	0.29
T30-M	0.59	0.58	0.58
T30-L	0.89	0.87	0.85
T60-S	0.90	0.85	0.82
T60-M	1.47	1.40	1.36
T60-L	2.57	2.46	2.49

5.4.3 Comparative study of nozzle ablation and its effects

From the calculation, it can be concluded that the critical RRRV is affected by coupled factors, e.g. interrupting current, arc duration, pressure, temperature and the dimension of nozzle. Despite the difference of the arc durations, the pressures inside the expansion volume and at the main nozzle flat throat are significantly increased with higher current, as shown in Figure 5.32.

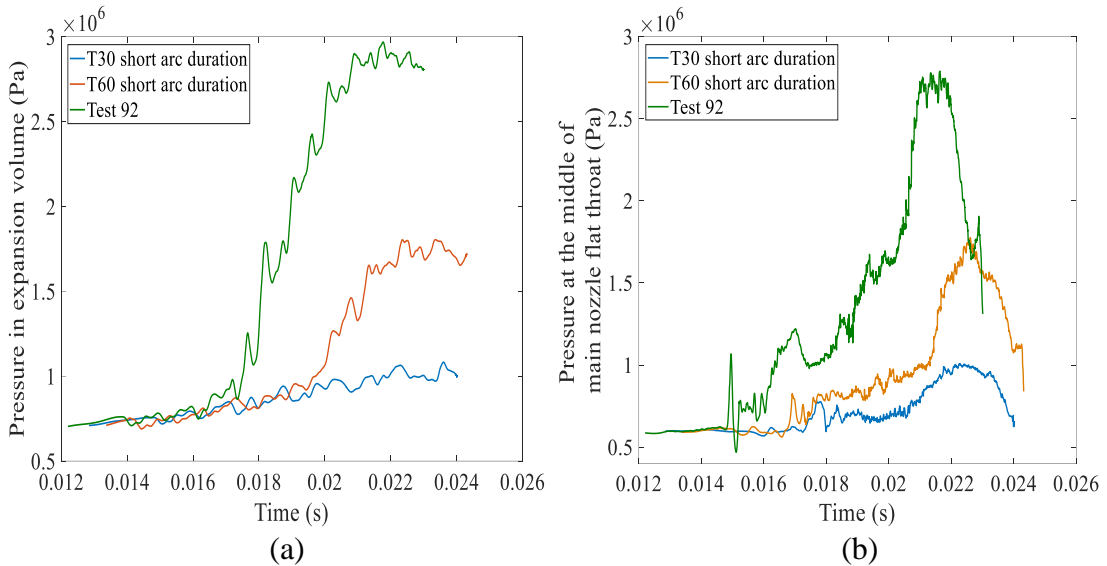


Figure 5.32 Pressure variation (a) in expansion volume and (b) at the middle of main nozzle flat throat of the short arc duration cases;

The fluctuation of the pressure curve is due to the propagated pressure waves from the arcing space towards expansion volume. Theoretically, the pressure waves could not be propagated instantaneously from one position to another and the waves propagation is affected by the factors such as frequency and transmission medium. The compressible characteristics of the fluid inside the arcing chamber results in the disturbances during the pressure wave propagation and reflection.

Additionally, despite the difference of the interrupted current level, the arc duration also affects the nozzle ablation and pressure distribution. The arc duration correlated to the contact travel curve determines the final position of the solid contact within the main nozzle and the effective flow area around the main nozzle downstream. As illustrated in Figure 5.33, the longer arc duration results in a higher pressure inside the expansion volume and at the main nozzle flat throat. It also leads to more ablation from the nozzle surface which makes the arc column thinner in comparison with the short and medium arc duration cases.

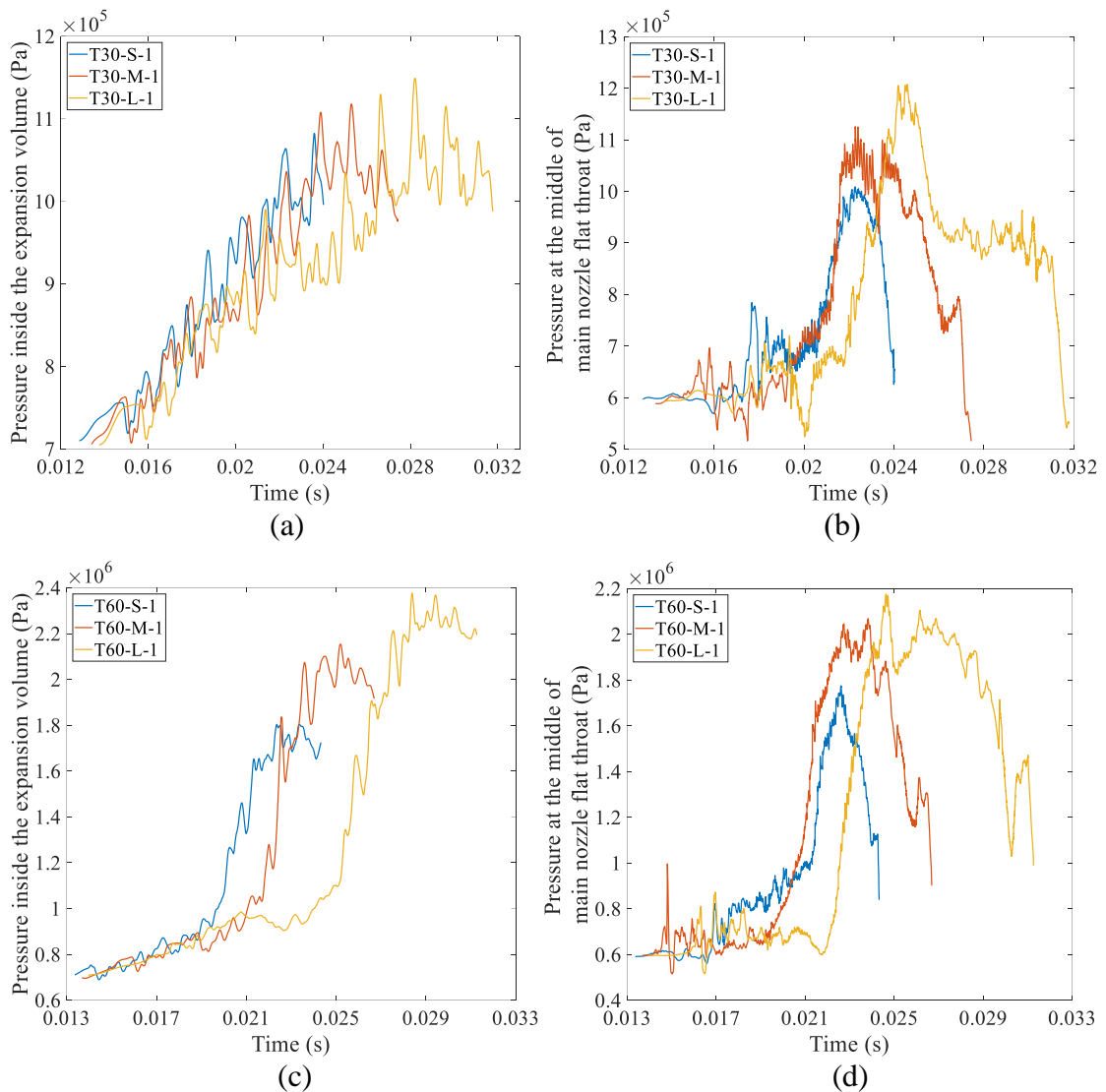


Figure 5.33 Pressure variation inside the expansion volume (a) (c) and at the middle of main nozzle flat throat (b) (d) for T30 and T60 cases with different arc durations.

During the final current zero phase, the arc temperature within the arcing space between the contacts in particular in the stagnation area is considerably affected by the enlarged nozzle holes as well. The pressure within the arcing space between the arcing contacts drops lower since the electrical power supply is insufficient when the current decreases below 15 kA, and eventually the gaseous mixture inside the expansion volume rushes out into the arcing space with a higher mass flow rate compared with the high current phase to cool down the arc column and surrounding gas. Furthermore, as the dominant mechanism for the arc cooling during the current zero phase, turbulence is affected by the mass flow rate and corresponded flow velocity around the main nozzle downstream exit. As a result of turbulence cooling, the arc column size is compressed by the cold gas flow and the temperature is thus decreased by interacting with surrounding cold gas

(energy exchange). As two typical examples, the temperature distributions at the final current zero of Test 92 and 98 are demonstrated in Figure 5.34 and 5.35. In Test 92, the effective flow area of main nozzle divergent section is smaller and the gas temperature around the arc column is higher than Test 98. Because of the smaller pressure difference between the expansion volume and the main nozzle downstream, the gas flows out from the expansion volume towards hollow contact and downstream exit with a smaller flow rate, as shown in Figure 5.36. Besides that, the mass flow rate of the short arc duration case in current zero phase is the smallest and it increases with the arc duration.

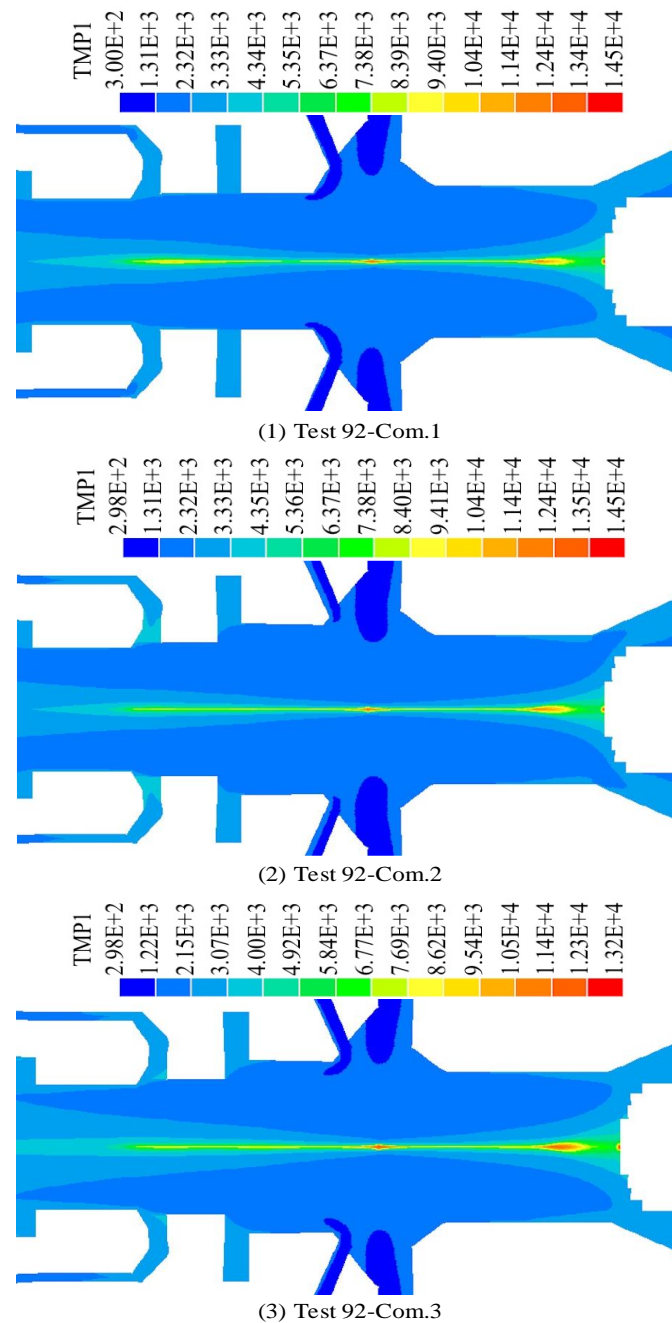


Figure 5.34 Temperature distribution at the final current zero for Test 92 with the consideration of nozzle flat throats diameters variation.

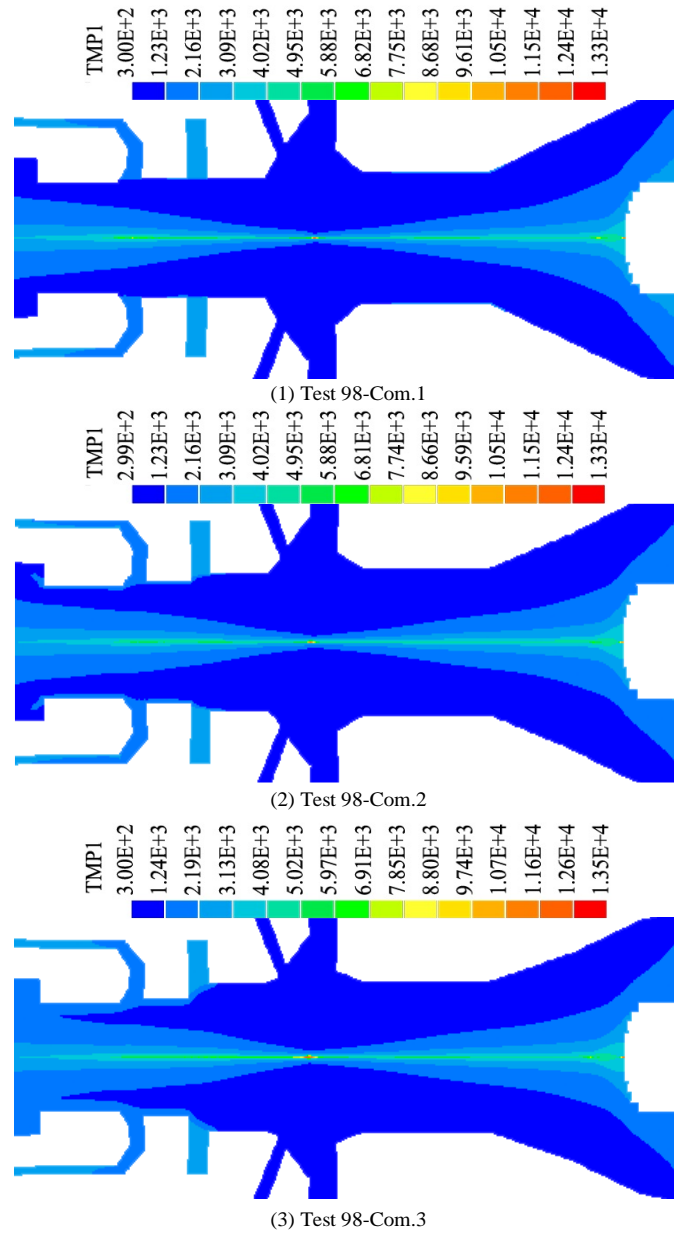
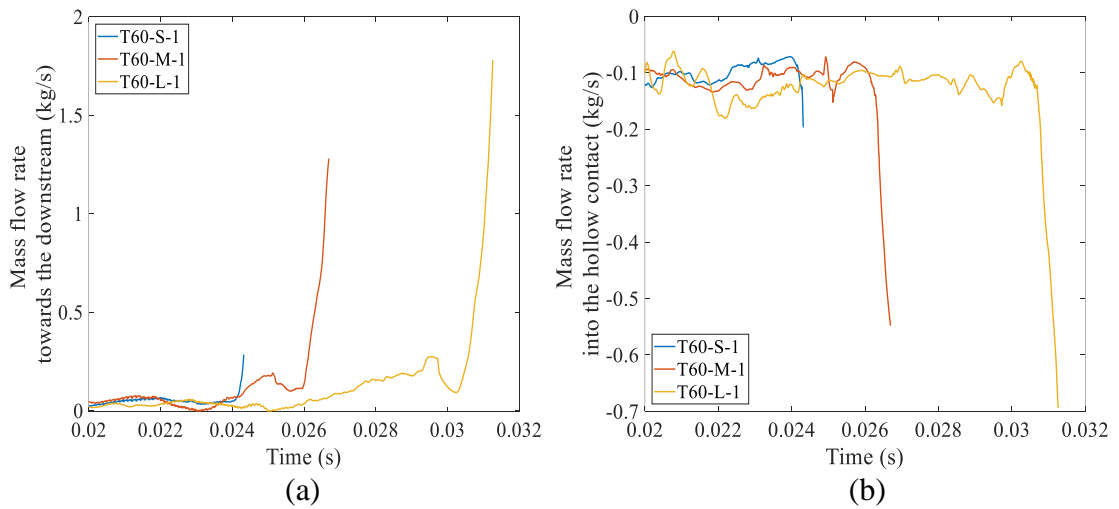


Figure 5.35 Temperature distribution at the final current zero for Test 98 with the consideration of nozzle flat throats diameters variation.



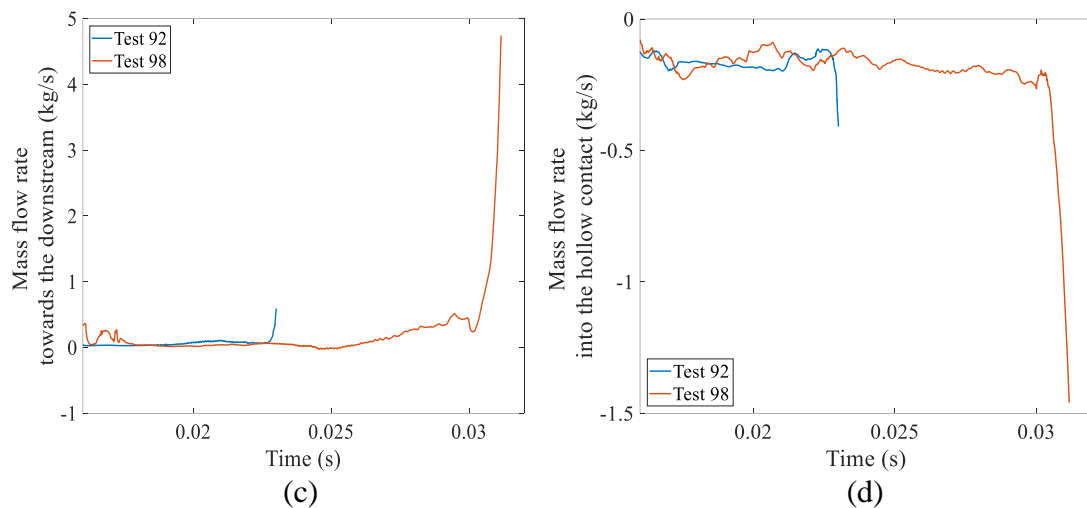


Figure 5.36 Mass flow rate towards the main nozzle downstream (a) (c) and into the hollow contact (b) (e) before the final current zero through cross sections 7 and 2 respectively with different arc durations without the consideration of nozzles flat throats diameters variation.

5.5 Conclusion

The present study shows that improvement of the circuit breaker interruption capability by design demands a comprehensive knowledge of the interaction between the hot arc column and the nozzle surface since the dimensional change of nozzle flat throat alters the flow environment, especially within the contact gap. To optimize the circuit breaker design, nozzle ablation is quantitatively determined and its effects on the circuit breaker's interruption capability is discussed as well. In the work of this chapter, the interruption capability is predicted through the determination of the critical RRRV. Some important findings are shown below:

- (1) For the short arc duration case T30 with a considerable lower current level, nozzle ablation has a smaller effect on the pressure build up process inside the expansion volume due to less amount of vapour produced from the nozzle surface. It is not a limiting factor for the lifetime of the nozzle.
- (2) With increased current level, the arc is burned in an PTFE ablation dominated mode with high PTFE concentration and nozzle ablation becomes a dominant mechanism to establish the effective flow field condition at the final current zero. However, the enlarged nozzle flat throat lowers the pressurisation in the expansion volume in the subsequent operation since the amount of produced vapour from the nozzle surface

is reduced. At a long arc duration, with an excessive enlargement of the nozzle flat throat, local flow condition at the auxiliary nozzle flat throat is adversely affected, leading to an increase of the ablated mass from the auxiliary nozzle flat throat. Since the main nozzle ablation contributes a significant proportion of pressurisation inside the expansion volume at high interrupted current level, this excessive enlargement of the nozzle holes leads to a rapid reduction in the interruption capability of circuit breakers.

- (3) The turbulence parameter c of Prandtl mixing length model is calibrated to predict the turbulence cooling effect especially during the current zero phase. It is observed that 0.32 is a reasonable value which produces results agreeing with the test results. This value reconfirms the value of turbulence parameter of 0.3 for the puffer type circuit breakers.
- (4) Interruption capability of the auto-expansion circuit breaker presents a deterioration with the consideration of the nozzle enlargement. As a more serious fault type, the deterioration of the interruption capacity of breaker can be explained by a reduction of approximately 19% in the predicted RRRV. It is mainly caused by dimensional variation of the main and auxiliary nozzles. For the long arc duration case (Test 98), the 2.4 mm/2.6mm (auxiliary nozzle) and 2 mm/1.6 mm (main nozzle) enlargement of the nozzle flat throat leads to the reduction of approximately 20% in the predicted RRRV.

References

- [1] D. F. Peelo, Ed., *Current Interruption Transients Calculation*. Chichester, United Kingdom, United Kingdom: John Wiley & Sons, Ltd, 2014.
- [2] R. D. Garzon, *HIGH VOLTAGE CIRCUIT BREAKERS: Design and Applications*, Second. New York, NY: Marcel Decker, 2002.
- [3] D. Dufournet and R. K. Smith, “Transient Recovery Voltages (TRVs) for High Voltage Circuit Breakers.” 2008 PES General Meeting, p. 139, 2008.
- [4] IEC, “IEC 62271-100: 2008 High-Voltage Switchgear and Controlgear-Part 100: Alternating current circuit breakers.” p. 695, 21-Apr-2008.
- [5] IEEE Standards, “IEEE Std C37.06-2009 - IEEE Standard for AC High-Voltage Circuit Breakers Rated on a Symmetrical Current Basis - Preferred Ratings and Related Required Capabilities for Voltages Above 1000 V.” pp. 1–46, 2009.
- [6] Switchgear Committe, “IEEE Application Guide for Transient Recovery Voltage for AC High-Voltage Circuit Breakers,” *IEEE Std C37.011*. IEEE STANDARDS ASSOCIATION, New York, p. 72, 2006.
- [7] J. G. Jamnani and S. A. Kanitkar, “TRV Rating Concepts and Generation of TRV Envelopes for Synthetic Testing of Extra High Voltage Circuit Breakers,” *Int. J. Comput. Electr. Eng.*, vol. 3, no. 1, pp. 24–29, 2011.
- [8] Private Communication, “Preliminary report of the 145kV/40kA auto-expansion circuit breaker tests,” 2012.
- [9] M. Seeger, J. Tepper, T. Christen, and J. Abrahamson, “Experimental study on PTFE ablation in high voltage circuit-breakers,” *J. Phys. D. Appl. Phys.*, vol. 39, no. 23, pp. 5016–5024, Dec. 2006.
- [10] J. D. Yan, K. I. Nuttall, and M. T. C. Fang, “A comparative study of turbulence models for SF 6 arcs in a supersonic nozzle,” *J. Phys. D. Appl. Phys.*, vol. 32, no. 12, pp. 1401–1406, Jun. 1999.
- [11] D. Dufournet, “Transient Recovery Voltages (TRVs) for High-Voltage Circuit Breakers.” San Antonio, 2013.

Chapter 6

Conclusions and Future Work

6.1 Contributions and Achievements in the Present Work

The work in this thesis is primarily concerned with the “intelligence” of circuit breakers at the physical layer, especially the arc dynamics when it interacts with the contacts and nozzle(s). Realistic predictions of the contact erosion and nozzle ablation are critically important for developing truly intelligent circuit breakers. The operation performance of circuit breakers, especially the interruption capability and lifetime, are significantly affected by these two phenomena. Present work is aimed at a systematic understanding of interaction between the arc and the metallic contacts and the PTFE nozzle.

The thermodynamic properties and transport coefficients of pure copper plasma under LTE and non-LTE conditions are firstly calculated. The chemical composition of pure copper plasma is computed by solving the generalised Saha equations, equation of state and the equation describing the electrical neutrality of the plasma. The thermodynamic properties and transport coefficients are then calculated as function of temperature and pressure. The transport coefficients are calculated using the classical Chapman-Enskog method and the corresponding formulas are derived from Boltzmann nonlinear integro-differential equations assuming a Maxwell-Boltzmann distribution for particle velocity. A mathematical model describing the non-LTE layer in front of the cathode surface is then developed to predict the contact erosion resulted from energy transfer between the non-LTE plasma and the cathode bulk. The predicted mass loss due to the evaporation is smaller than the measured mass loss, which includes solid particles ejected from the contact surface.

Nozzle ablation is a major factor controlling the interruption capability and lifetime of the circuit breaker. The present study shows that nozzle ablation at high current, such as in the L90 type test, leads to significant increase in the size of the main and auxiliary nozzles. The variation in the nozzle size has two consequences. The first is the reduction of the pressure rise in the expansion volume, which is responsible for the generation of

high speed gas flow at current zero. The second consequence is the change in flow field, especially around the nozzle flat throat. The combined effect leads to the reduction in the interruption capability of circuit breakers. The predicted specific ablation falls well within the range of results obtained by ABB.

The last contribution is a study of the influences of nozzle ablation on the interruption capability of the auto-expansion circuit breaker. It is shown that the arc model with a turbulence parameter of 0.32 produce predictions of the critical RRRV that match well with the test results. This value is also very close to the value of 0.30 for puffer circuit breakers, further validating the arc model. Results also show that the critical RRRV of the auto-expansion circuit breaker drops rapidly resulted from the nozzle enlargement by nozzle ablation. Therefore, for realistic modelling of the interruption performance of a circuit breaker, the nozzle ablation at high current must be considered.

6.2 Future Work

In the future, the development of smart grid would be a better answer to satisfy the ever-growing need for the electricity and increased complexity of system management with applying the “intelligent” computerised control and automation to improve the system availability, reliability, and efficacy. It is achieved by improving the real-time dynamic monitoring and controlling as well as bi-directional communication between the control system and the apparatuses. As an important apparatus for protecting power grid system, the idea of intelligent circuit breaker has to be realised by hardware components which could complete intelligent operations not only in the practical application level but also the physical level. Since the contact erosion and nozzle ablation as two decisive factors are difficult to determine from the tests, a satisfactory mathematical model is important to provide the reasonable computation results for the optimum design. Nevertheless, it is difficult to establish an accurate model without the trustable evidence from the tests. Therefore, more trustable data with respect to the tests on the circuit breaker is essential to improve the accuracy of arc modelling.

6.2.1 Modified near cathode non-LTE layer model

For contact erosion, the near cathode non-LTE layer model need to be considered together with the present arc column model to furtherly analyse its effects on the overall

flow field conditions. The assumptions of the total current density and cathode surface temperature could be eliminated through the coupled calculation between the non-LTE layer model and arc model. Furthermore, metallic particles detached from the cathode surface need to be considered in the future work because of it is significant for the total mass loss during the current interruptions. In addition, as is recognised from previous investigations, the non-LTE layer is only presented in a much shorter distance in front of the contacts in comparison with the arc length so that the contact erosion is currently assumed to be neglected during the arc modelling of circuit breakers. Since the injected metallic vapour changes the arc temperature and arc column size especially the arc root attachment on the contact surface, the presence of metallic vapour should be considered in the future works.

6.2.2 Radiation model correlates to the nozzle ablation

Semi-empirical radiation model is adopted in present work with assuming a reasonable proportion of the radiation energy to be absorbed. Therefore, the radiation model also need to be modified using the more accurate method in the future to predict the nozzle ablation with more accuracy.

6.2.3 Thermodynamic properties and transport coefficients of the mixture inside the arcing chamber

Current investigation of thermodynamic properties and transport coefficients of the gas mixture inside the arcing chamber is limited to a pressure of 1~2 MPa. However, with the development of smart grid especially for the apparatuses operate in higher voltage and interrupting current environment, the pressure in the arcing chamber would become higher. This kind of high pressure, as a result of the strong magnetic pinch effect and nozzle ablation, may occur in the arcing chamber when interrupting high current in the order of 100 kA, where experimentally study of circuit breaker operation performance under such conditions is difficult and expensive. The thermodynamic properties and transport coefficients of the gaseous medium in such a higher pressure environment are prerequisite for arc modelling, hence need to be determined accurately. Moreover, the arc characteristics would be more complicated if considering the metallic vapour from

contacts injects into the SF₆-PTFE mixture. To improve the model, the thermodynamic properties and transport coefficients of the ternary mixture also need to be determined.

Appendix A

1. Partial Differentiation form of Saha equation associated with the partial pressure

$$\begin{aligned} \frac{1}{p_e} \frac{\partial p_e}{\partial T_e} + \frac{1}{p_3} \frac{\partial p_3}{\partial T_e} - \frac{1}{p_2} \frac{\partial p_2}{\partial T_e} \\ = \frac{5}{2} \frac{1}{T_e} + \frac{\partial \ln(Q_{Cu^+}(T_e))}{\partial T_e} - \frac{\partial \ln(Q_{Cu}(T_e))}{\partial T_e} + \left(\frac{E_{i,Cu} - \Delta E_{(0)}}{k_B T_e^2} \right) \end{aligned} \quad (A.1)$$

$$= C_1$$

$$\begin{aligned} \frac{1}{p_e} \frac{\partial p_e}{\partial T_e} + \frac{1}{p_4} \frac{\partial p_4}{\partial T_e} - \frac{1}{p_3} \frac{\partial p_3}{\partial T_e} \\ = \frac{5}{2} \frac{1}{T_e} + \frac{\partial \ln(Q_{Cu^{2+}}(T_e))}{\partial T_e} - \frac{\partial \ln(Q_{Cu^+}(T_e))}{\partial T_e} \\ + \left(\frac{E_{i,Cu^+} - \Delta E_{(1)}}{k T_e^2} \right) = C_2 \end{aligned} \quad (A.2)$$

$$\begin{aligned} \frac{1}{p_e} \frac{\partial p_e}{\partial T_e} + \frac{1}{p_5} \frac{\partial p_5}{\partial T_e} - \frac{1}{p_4} \frac{\partial p_4}{\partial T_e} \\ = \frac{5}{2} \frac{1}{T_e} + \frac{\partial \ln(Q_{Cu^{3+}}(T_e))}{\partial T_e} - \frac{\partial \ln(Q_{Cu^{2+}}(T_e))}{\partial T_e} \\ + \left(\frac{E_{i,Cu^{2+}} - \Delta E_{(2)}}{k T_e^2} \right) = C_3 \end{aligned} \quad (A.3)$$

$$\begin{aligned} \frac{1}{p_e} \frac{\partial p_e}{\partial T_e} + \frac{1}{p_6} \frac{\partial p_6}{\partial T_e} - \frac{1}{p_5} \frac{\partial p_5}{\partial T_e} \\ = \frac{5}{2} \frac{1}{T_e} + \frac{\partial \ln(Q_{Cu^{4+}}(T_e))}{\partial T_e} - \frac{\partial \ln(Q_{Cu^{3+}}(T_e))}{\partial T_e} \\ + \left(\frac{E_{i,Cu^{3+}} - \Delta E_{(3)}}{k T_e^2} \right) = C_4 \end{aligned} \quad (A.4)$$

$$\frac{1}{p_e} \frac{\partial p_e}{\partial T_h} + \frac{1}{p_3} \frac{\partial p_3}{\partial T_h} - \frac{1}{p_2} \frac{\partial p_2}{\partial T_h} = 0 \quad (A.5)$$

$$\frac{1}{p_e} \frac{\partial p_e}{\partial T_h} + \frac{1}{p_4} \frac{\partial p_4}{\partial T_h} - \frac{1}{p_3} \frac{\partial p_3}{\partial T_h} = 0 \quad (A.6)$$

$$\frac{1}{p_e} \frac{\partial p_e}{\partial T_h} + \frac{1}{p_5} \frac{\partial p_5}{\partial T_h} - \frac{1}{p_4} \frac{\partial p_4}{\partial T_h} = 0 \quad (A.7)$$

$$\frac{1}{p_e} \frac{\partial p_e}{\partial T_h} + \frac{1}{p_6} \frac{\partial p_6}{\partial T_h} - \frac{1}{p_5} \frac{\partial p_5}{\partial T_h} = 0 \quad (A.8)$$

2. Partial Differentiation form of Saha equation associated with the partial number density

$$\begin{aligned} \frac{1}{n_e} \frac{\partial n_e}{\partial T_e} + \frac{1}{n_{Cu^+}} \frac{\partial n_{Cu^+}}{\partial T_e} - \frac{1}{n_{Cu}} \frac{\partial n_{Cu}}{\partial T_e} \\ = \frac{3}{2} \frac{1}{T_e} + \frac{\partial \ln(Q_{Cu^+}(T_e))}{\partial T_e} - \frac{\partial \ln(Q_{Cu}(T_e))}{\partial T_e} + \left(\frac{E_{i,Cu} - \Delta E_{(0)}}{kT_e^2} \right) \quad (A.9) \\ = D_1 \end{aligned}$$

$$\begin{aligned} \frac{1}{n_e} \frac{\partial n_e}{\partial T_e} + \frac{1}{n_{Cu^{2+}}} \frac{\partial n_{Cu^{2+}}}{\partial T_e} - \frac{1}{n_{Cu^+}} \frac{\partial n_{Cu^+}}{\partial T_e} \\ = \frac{3}{2} \frac{1}{T_e} + \frac{\partial \ln(Q_{Cu^{2+}}(T_e))}{\partial T_e} - \frac{\partial \ln(Q_{Cu^+}(T_e))}{\partial T_e} \\ + \left(\frac{E_{i,Cu^+} - \Delta E_{(1)}}{kT_e^2} \right) = D_2 \quad (A.10) \end{aligned}$$

$$\begin{aligned} \frac{1}{n_e} \frac{\partial n_e}{\partial T_e} + \frac{1}{n_{Cu^{3+}}} \frac{\partial n_{Cu^{3+}}}{\partial T_e} - \frac{1}{n_{Cu^{2+}}} \frac{\partial n_{Cu^{2+}}}{\partial T_e} = \frac{3}{2} \\ = \frac{3}{2} \frac{1}{T_e} + \frac{\partial \ln(Q_{Cu^{3+}}(T_e))}{\partial T_e} - \frac{\partial \ln(Q_{Cu^{2+}}(T_e))}{\partial T_e} \\ + \left(\frac{E_{i,Cu^{2+}} - \Delta E_{(2)}}{kT_e^2} \right) = D_3 \quad (A.11) \end{aligned}$$

$$\begin{aligned} \frac{1}{n_e} \frac{\partial n_e}{\partial T_e} + \frac{1}{n_{Cu^{4+}}} \frac{\partial n_{Cu^{4+}}}{\partial T_e} - \frac{1}{n_{Cu^{3+}}} \frac{\partial n_{Cu^{3+}}}{\partial T_e} \\ = \frac{3}{2} \frac{1}{T_e} + \frac{\partial \ln(Q_{Cu^{4+}}(T_e))}{\partial T_e} - \frac{\partial \ln(Q_{Cu^{3+}}(T_e))}{\partial T_e} \\ + \left(\frac{E_{i,Cu^{3+}} - \Delta E_{(3)}}{kT_e^2} \right) = D_4 \quad (A.12) \end{aligned}$$

$$\frac{1}{n_e} \frac{\partial n_e}{\partial T_h} + \frac{1}{n_{Cu^+}} \frac{\partial n_{Cu^+}}{\partial T_h} - \frac{1}{n_{Cu}} \frac{\partial n_{Cu}}{\partial T_h} = 0 \quad (A.13)$$

$$\frac{1}{n_e} \frac{\partial n_e}{\partial T_h} + \frac{1}{n_{Cu^{2+}}} \frac{\partial n_{Cu^{2+}}}{\partial T_h} - \frac{1}{n_{Cu^+}} \frac{\partial n_{Cu^+}}{\partial T_h} = 0 \quad (A.14)$$

$$\frac{1}{n_e} \frac{\partial n_e}{\partial T_h} + \frac{1}{n_{Cu^{3+}}} \frac{\partial n_{Cu^{3+}}}{\partial T_h} - \frac{1}{n_{Cu^{2+}}} \frac{\partial n_{Cu^{2+}}}{\partial T_h} = 0 \quad (A.15)$$

$$\frac{1}{n_e} \frac{\partial n_e}{\partial T_h} + \frac{1}{n_{Cu^{4+}}} \frac{\partial n_{Cu^{4+}}}{\partial T_h} - \frac{1}{n_{Cu^{3+}}} \frac{\partial n_{Cu^{3+}}}{\partial T_h} = 0 \quad (A.16)$$

Appendix B

1. Ordinary differential forms of the conservation equations of pre-sheath model

$$\begin{aligned} \nabla \cdot \Gamma_e = & - \left(\frac{D_e^T}{m_e T_e} + \frac{m_e n n_e D_{ee}}{\rho T_e} \right) \frac{d^2 T_e}{dx^2} - \frac{d}{dx} \left(\frac{D_e^T}{m_e T_e} + \frac{m_e n n_e D_{ee}}{\rho T_e} \right) \frac{dT_e}{dx} \\ & - \left(\frac{m_e n D_{ee}}{\rho} \right) \frac{d^2 n_e}{dx^2} - \frac{d}{dx} \left(\frac{m_e n D_{ee}}{\rho} \right) \frac{dn_e}{dx} + \left(\frac{m_e n n_e e D_{ee}}{\rho k_B T_e} \right) \frac{d^2 V}{dx^2} \\ & + \frac{d}{dx} \left(\frac{m_e n n_e e D_{ee}}{\rho k_B T_e} \right) \frac{dV}{dx} = \alpha_{rec} n_e^3 \left(\frac{n_a}{n_{a,LTE}} - 1 \right) \end{aligned} \quad (\text{B.1})$$

$$\begin{aligned} \nabla \cdot \Gamma_i = & - \left(\frac{n_a m_a D_{ia}}{\rho} \right) \frac{d^2 n_e}{dx^2} - \frac{d}{dx} \left(\frac{n_a m_a D_{ia}}{\rho} \right) \frac{dn_e}{dx} + \left(\frac{n_e m_i D_{ia}}{\rho} \right) \frac{d^2 n_a}{dx^2} \\ & + \frac{d}{dx} \left(\frac{n_e m_i D_{ia}}{\rho} \right) \frac{dn_a}{dx} - \left(\frac{n^2 n_e m_i D_{ia} e}{P \rho} \right) \frac{d^2 V}{dx^2} \\ & - \frac{d}{dx} \left(\frac{n^2 n_e m_i D_{ia} e}{P \rho} \right) \frac{dV}{dx} = \alpha_{rec} n_e^3 \left(\frac{n_a}{n_{a,LTE}} - 1 \right) \end{aligned} \quad (\text{B.2})$$

$$\begin{aligned} -e \left(\frac{D_e^T}{m_e T_e} + \frac{m_e n n_e D_{ee}}{\rho T_e} \right) \frac{dT_e}{dx} \frac{dV}{dx} - e \left(\frac{m_e n D_{ee}}{\rho} \right) \frac{dn_e}{dx} \frac{dV}{dx} + e \left(\frac{m_e n n_e e D_{ee}}{\rho k_B T_e} \right) \left(\frac{dV}{dx} \right)^2 \\ = - \frac{dk_e}{dx} \frac{dT_e}{dx} - k_e \frac{d^2 T_e}{dx^2} - \frac{5}{2} k_B \alpha \left(\frac{D_e^T}{m_e T_e} + \frac{m_e n n_e D_{ee}}{\rho T_e} \right) \left(\frac{dT_e}{dx} \right)^2 \\ - \frac{5}{2} k_B \alpha \left(\frac{m_e n D_{ee}}{\rho} \right) \frac{dn_e}{dx} \frac{dT_e}{dx} + \frac{5}{2} k_B \alpha \left(\frac{m_e n n_e e D_{ee}}{\rho k_B T_e} \right) \frac{dV}{dx} \frac{dT_e}{dx} \\ + \left(\frac{5}{2} k_B \alpha T_e + E_{ion} \right) \dot{n}_e + W_{eh} \end{aligned} \quad (\text{B.3})$$

$$\begin{aligned} \left(\frac{n_a m_a e D_{ia}}{\rho} \right) \frac{dn_e}{dx} \frac{dV}{dx} - \left(\frac{n_e m_i e D_{ia}}{\rho} \right) \frac{dn_a}{dx} \frac{dV}{dx} + \left(\frac{n^2 n_e m_i e^2 D_{ia}}{P \rho} \right) \left(\frac{dV}{dx} \right)^2 + W_{eh} \\ = - \frac{dk_h}{dx} \frac{dT_h}{dx} - k_h \frac{d^2 T_h}{dx^2} \end{aligned} \quad (\text{B.4})$$

2. Second-order differential forms of the conservation equations of pre-sheath model

$$\begin{aligned} \frac{d^2 n_e}{dx^2} = & - \left(\frac{e^2 D_e^T}{k_B \sigma m_e} \cdot \frac{n_e}{T_e^2} + \frac{n_e}{T_e} \right) \frac{d^2 T_e}{dx^2} - \frac{1}{m_e T_e} \cdot \frac{e^2 n_e}{k_B T_e \sigma} \cdot \frac{d}{dx} (D_e^T) \cdot \frac{dT_e}{dx} \\ & + \frac{D_e^T}{m_e T_e^2} \cdot \frac{e^2 n_e}{k_B T_e \sigma} \cdot \left(\frac{dT_e}{dx} \right)^2 - \frac{n_e}{T_e \sigma} \cdot \frac{dT_e}{dx} \cdot \frac{d\sigma}{dx} - \frac{1}{\sigma} \cdot \frac{dn_e}{dx} \\ & \cdot \frac{d\sigma}{dx} - \frac{1}{T_e} \cdot \frac{dT_e}{dx} \cdot \frac{dn_e}{dx} + \frac{1}{n_e} \cdot \left(\frac{dn_e}{dx} \right)^2 + \frac{n_e e}{k_B T_e} \cdot \frac{d^2 V}{dx^2} \\ & + \frac{e n_e}{k_B T_e \sigma} \cdot \frac{d\sigma}{dx} \cdot \frac{dV}{dx} - \frac{e^2 n_e}{k_B T_e \sigma} \cdot \alpha_{rec} \left(\frac{n_a}{n_{a,LTE}} - 1 \right) \cdot n_e^3 \end{aligned} \quad (\text{B.5})$$

$$\begin{aligned}
\frac{d^2V}{dx^2} = & - \left(\frac{Pn_a m_a}{n^2 n_e m_i e} \cdot \frac{d^2 n_e}{dx^2} \right) - \frac{Pn_a m_a}{n^2 n_e D_{ia} m_i e} \cdot \frac{d}{dx} (D_{ia}) \cdot \frac{dn_e}{dx} \\
& - \frac{Pm_a}{n^2 n_e m_i e} \cdot \frac{dn_a}{dx} \cdot \frac{dn_e}{dx} + \frac{Pn_a m_a}{\rho n^2 n_e m_i e} \cdot \frac{d\rho}{dx} \cdot \frac{dn_e}{dx} + \frac{P}{n^2 e} \\
& \cdot \frac{d^2 n_a}{dx^2} + \frac{P}{n^2 n_e e} \cdot \frac{dn_e}{dx} \cdot \frac{dn_a}{dx} + \frac{P}{n^2 D_{ia} e} \cdot \frac{d}{dx} (D_{ia}) \cdot \frac{dn_a}{dx} \\
& - \frac{P}{n^2 \rho e} \cdot \frac{d\rho}{dx} \cdot \frac{dn_a}{dx} - \frac{2}{n} \cdot \frac{dn}{dx} \cdot \frac{dV}{dx} - \frac{1}{n_e} \cdot \frac{dn_e}{dx} \cdot \frac{dV}{dx} - \frac{1}{D_{ia}} \\
& \cdot \frac{d}{dx} (D_{ia}) \cdot \frac{dV}{dx} + \frac{1}{\rho} \cdot \frac{d\rho}{dx} \cdot \frac{dV}{dx} - \frac{P\rho}{n^2 m_i D_{ia}} \cdot \alpha_{rec} \cdot n_e^2 \\
& \cdot \left(\frac{n_a}{n_{a,LTE}} - 1 \right)
\end{aligned} \tag{B.6}$$

$$\begin{aligned}
\frac{d^2 T_e}{dx^2} = & \frac{1}{k_e} \left[\left(\frac{eD_e^T}{m_e T_e} + \frac{k_B \sigma}{e} \right) \cdot \frac{dT_e}{dx} \cdot \frac{dV}{dx} + \left(\frac{k_B \sigma}{e} \cdot \frac{T_e}{n_e} \cdot \frac{dn_e}{dx} \cdot \frac{dV}{dx} \right) \right. \\
& - \sigma \left(\frac{dV}{dx} \right)^2 - \left(\frac{dk_e}{dx} \cdot \frac{dT_e}{dx} \right) \\
& - \frac{5}{2} k_B \alpha \left(\frac{D_e^T}{m_e T_e} + \frac{k_B \sigma}{e^2} \right) \left(\frac{dT_e}{dx} \right)^2 - \frac{5}{2} k_B \alpha \left(\frac{k_B \sigma}{e^2} \cdot \frac{T_e}{n_e} \right) \\
& \cdot \frac{dn_e}{dx} \cdot \frac{dT_e}{dx} + \left(\frac{5}{2} k_B \alpha \cdot \frac{\sigma}{e} \cdot \frac{dV}{dx} \cdot \frac{dT_e}{dx} \right) \\
& \left. + \left(\frac{5}{2} k_B \alpha T_e + E_{ion} \right) \cdot \dot{n}_e + W_{eh} \right]
\end{aligned} \tag{B.7}$$

$$\begin{aligned}
\frac{d^2 T_h}{dx^2} = & \frac{1}{k_h} \left[- \left(\frac{dk_h}{dx} \cdot \frac{dT_h}{dx} \right) - \left(\frac{n_a m_a e D_{ia}}{\rho} \cdot \frac{dn_e}{dx} \cdot \frac{dV}{dx} \right) \right. \\
& + \left(\frac{n_e m_i e D_{ia}}{\rho} \cdot \frac{dn_a}{dx} \cdot \frac{dV}{dx} \right) - \left(\frac{n^2 n_e m_i e^2 D_{ia}}{P\rho} \right) \cdot \left(\frac{dV}{dx} \right)^2 \\
& \left. - W_{eh} \right]
\end{aligned} \tag{B.8}$$